University of Warsaw
Faculty of Chemistry

Doctor of Philosophy Dissertation

Quantum dynamics and control of ultracold molecules in external fields

by

Michał Tomza

Thesis supervisors:
Prof. Dr. Robert Moszyński, University of Warsaw, Poland
Prof. Dr. Christiane P. Koch, University of Kassel, Germany

Warsaw, March 2014

Contents

Chapter 1

Introduction to ultracold molecules and quantum control

1.1 Quantum matter at ultralow temperatures

The first experiments with temperatures much lower than the room temperature date back to the XIXth century and successful efforts to condensate nitrogen and oxygen from the air are good examples [1]. The experiments with the liquid helium at the temperature of 4 K led to the discovery of the superconductivity by Heike Kamerlingh Onnes in 1911 [2] and further cooling led to the discovery of the helium superfluidity in 1937 [3, 4]. Shortly after the birth of quantum mechanics, Satyendra Nath Bose and Albert Einstein predicted in 1924 that a quantum phase transition occurs in a system consisting of identical bosons when particles, under special conditions, tend to occupy a single quantum state [5, 6, 7]. The Bose-Einstein condensate can be formed only if the thermal de Broglie wavelength of the particles is comparable or even larger to the average distance between them. Such a condition is met at ultralow temperatures. The complexity of cooling to ultralow temperatures is illustrated by the fact that the Bose's and Einstein's prediction had been waiting seventy years until the development of laser cooling and trapping [8, 9, 10] and the first production of the condensate in 1995 [11, 12, 13, 14].

The cold ($< 1\,\mathrm{K}$) and ultracold ($< 1\,\mathrm{mK}$) systems attract great interest because the quantum nature of the world is visibly manifested at ultralow temperatures and research on such systems gives a new insight into the quantum theory of matter and matter-light interaction. Superconductivity, superfluidity, Bose-Einstein condensate, and other more exotic quantum phases are only the tip of the iceberg of the diversity of the quantum world at low and ultralow temperatures. What is more, the trapped ultracold atomic and molecular gases are highly controllable systems that can potentially be engineered to simulate other quantum systems such as solids and used to store and process quantum information.

The ultracold revolution has started in the 1990s and has lasted unit today. In its first years ultracold atoms were in the center of interest, however during the last ten years we witness the increased interest in the research on ultracold molecules. Fueled by the promise of exciting applications [15, 16], the production of ultracold gases of molecules is an important objective for the present day physics and chemistry. In contrast to the manipulation and control over the atomic and ionic as well photonic quantum systems, which reached an unprecedented level [17, 18, 19, 20, 21], the engineering of molecular quantum systems remains still a challenge.

1.2 Production and trapping of ultracold molecules

Molecules are much more complex objects as compared to atoms due to their internal rovibrational structure. For this reason the production of ultracold molecular gases is much more challenging than of the atomic ones [22, 23, 24, 25, 26, 27]. Two approaches to this problem are being used – direct methods, in which molecules are cooled from molecular beam temperatures, typically starting at tens of Kelvin, and indirect methods, in which molecules are formed from pre-cooled atomic gases.

Direct cooling

The laser ablation of a solid target or expansion of the high-pressure gas from a reservoir into vacuum are a source of molecules in direct cooling schemes [28, 29, 30, 31, 32]. There are two distinct regimes of the expansion depending on the relation between the mean free path of the molecules in the reservoir, λ_0, and the diameter of the orifice, D. When $\lambda_0 \gg D$, the effusive beam is generated with the velocity distribution as in the reservoir. In the limit of $D \gg \lambda_0$, the supersonic beam is generated which properties are determined by the flow properties of the gas.

Beam decelerators

The first experiments with molecular beams date back to the beginning of the XXth century with the first demonstrations of the deflection of beams by the magnetic [33] and electric [34] fields in the 1920s. In subsequent years, research was focused on the manipulation and control of beams [35]. Supersonic beams and crossed-beam experiments enormously contributed to the spectroscopic characterization of molecules [36], including Van der Waals complexes, understanding of chemical reactions [37], and intra- and intermolecular forces [38]. Although the molecules in supersonic beams are internally cold, the translational motion is fast.

The first deceleration of a molecular beam was experimentally demonstrated by Gerard Meijer and collaborators in 1999 by using an appropriately designed array of electric fields in a Stark decelerator [39]. This experiment proved that the motion of neutral molecules in a beam can be manipulated and controlled with an inhomogeneous electric field (via the Stark effect) and potentially magnetic field (via the Zeeman effect) [29, 30, 32, 40] and paved the way to decelerate molecular beams to low and ultralow temperatures. The lenses [41] and mirrors [42] for beams of polar molecules have been constructed and molecules cooled down with Stark decelerator to sufficiently low temperatures have been loaded into a quadrupole electrostatic trap [43, 44], storage ring [45], or synchrotron [46, 47]. The molecules such as metastable CO [39], ND_3 [43], OH [48], YbF [49], metastable NH [50], H_2CO [51], and LiH [52] have already been Stark decelerated. The beam deceleration employing the Zeeman effect with pulsed electromagnetic coils was demonstrated for the first time in 2007 for the hydrogen atoms [53, 54] and later to stop a supersonic beam of molecular oxygen [55, 56]. The loading molecules into trap has not been realized yet, but the magnetic trapping of hydrogen atoms after multistage Zeeman deceleration was demonstrated [57].

Recently, a new type of the continuous centrifuge decelerator for polar molecules was demonstrated [58], where the electrically guided molecules are slowed down to near-zero velocities by employing a centrifugal force.

Buffer-gas and sympathetic cooling

In the buffer-gas cooling technique the hot molecules of interest are injected or laser ablated into the bath of cooled to $\sim 1\,\mathrm{K}$ inert buffer gas, typically helium. The method relies on collisions with cold buffer gas atoms to thermalize atoms or molecules to a low temperature [59, 60, 31]. Since helium is chemically inert and effectively structureless, the method is very general and can be applied to nearly any atom and molecule and can be employed to cool molecular beams [61]. For instance Eu [60], Cr [62], Cu/Ag [63], N [64], CaH [65], NH [66], CaF [67], and CrH/MnH [68] have been buffer-gas cooled. The formation of a Bose-Einstein condensate of metastable helium using buffer-gas cooling was also demonstrated [69].

Sympathetic cooling is the method also based on the collisional thermalization between warm molecules and cooled atomic gas. The difference, as compared to the buffer-gas cooling, is that the coolant is the ultracold gas of laser-cooled atoms at lower density [70] and the initial temperature of atoms or molecules to cool is lower (pre-cooled by e.g. beam decelerator or buffer-gas cooling) and the final temperature after cooling can potentially be in the ultracold regime [71]. Since the coolant atoms are less inert than helium the method is less universal and systems with the ratio of elastic to inelastic/reactive collision rates over 100 must be found [72, 73, 74]. Sympathetic cooling of e.g. NH with Rb [75], OH with Rb [76], NH with Mg [77], NH_3/ND_3 with Rb [78], LiH with Li [71, 79], and OH/NH with H [80] has been proposed but not yet realized in any molecular system.

Doppler cooling

The development of the Doppler laser cooling and trapping technique, awarded by the Nobel prize in 1997, was a breakthrough in the atomic and optical physics [8, 9, 10] and led to the birth and rapid advances of the research at ultralow temperatures. Its mechanism is based on the difference of the light frequency experienced by moving atom due to the Doppler effect. The laser frequency is tuned slightly below an electronic transition in an atom (red detuned) and an atom moving away from the laser does not absorb photons whereas an atom moving towards the laser sees photons blue-shifted and absorbs them that slows the atom. The excited atom reemits a photon but because its direction is random, there is no net change in the momentum over many spontaneous emissions. To slow down a particle approximately $10^3 - 10^4$ absorption-emission cycles are needed. Since there are much more states and allowed transitions in molecules the spontaneous emissions can lead to the distribution over many states and repumping scheme may be needed. For this reason the laser cooling of molecules is not as universal as in the atomic case and restricted to molecules with a diagonal structure of the Franck-Condon factors. However, in 2010 the laser cooling of a diatomic molecule was demonstrated for the first time in the case of the polar strontium monofluoride molecule for which the closed cycle of electric transitions exists and only three lasers are needed [81]. Recently, the one- and two-dimensional transverse laser cooling and magneto-optical trapping of the polar yttrium oxide molecule [82], rovibrational cooling of cesium dimer by optical pumping [83], and the deceleration of a beam of strontium monofluoride molecules using laser radiation pressure were realized [84].

Sisyphus cooling

The Sisyphus cooling allows to cool particles below the limit of the Doppler cooling given by the recoil energy of a photon. Particles move through the potential and lose kinetic energy approaching a potential maximum, at which point the optical pumping moves them to a lower-energy state, thus losing the potential energy they had [85]. In 2012 the optoelectrical Sisyphus cooling of polyatomic molecules in suitably tailored electric trapping fields was realized for the first time [86].

Evaporative cooling

The production of the first Bose-Einstein condensate [11, 12] was achieved by using the forced evaporative cooling of atoms in a trap [87, 88] as a final step of cooling. Its mechanism is based on removing from the system particles with the highest kinetic energy by adiabatic ramping the trap depth. In 2012 the microwave-forced evaporative cooling of neutral hydroxyl radicals loaded from a Stark-decelerated beam into an extremely high-gradient magnetic quadrupole trap was demonstrated for the first time and proved that the evaporating cooling of molecules is possible [89]. It is believed that the evaporative cooling should be feasible for most of molecules once they are trapped and initially cooled to ultralow (below 1 mK) temperature by means of other cooling techniques [80, 90].

Indirect methods - associating ultracold atoms

Ultracold dense gases of molecules in the rovibrational ground state ($v'' = 0,\ J'' = 0$) were produced for the first time in 2008 [91, 92]. The KRb molecules were formed by using magnetoassociation via magnetically tunable Feshbach resonance into weakly bound state with

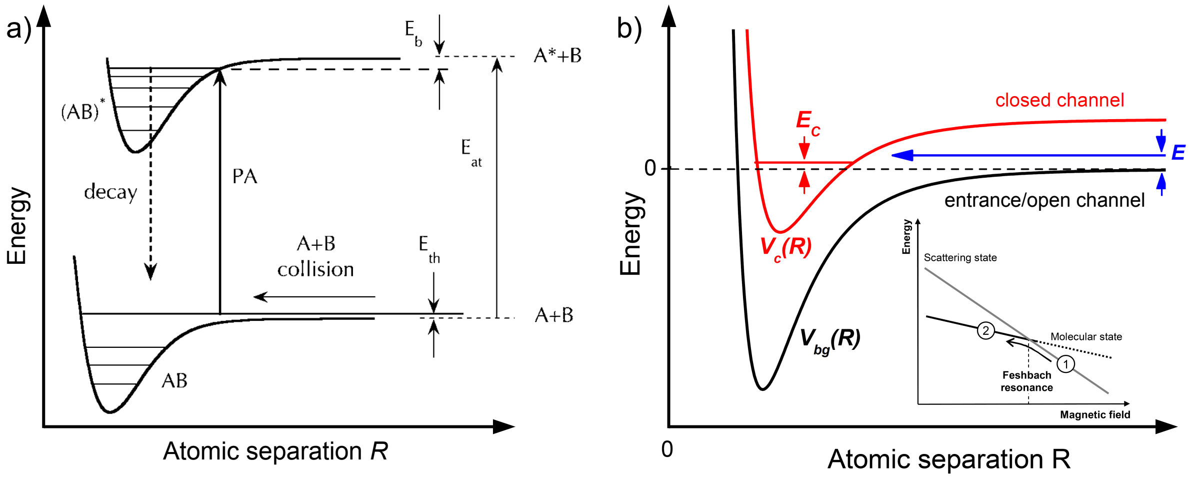

Figure 1.1: A scheme of the photoassociation (a) and magnetoassociation within two-channel model for a Feshbach resonance (b) with the corresponding avoided crossing shown in the inset [23, 24].

subsequent stimulated adiabatic Raman passage (STIRAP) to the absolute ground state [91] whereas the LiCs molecules were formed via a single photoassociation step with spontaneous decay into deeply bound ground state [92]. Until now, the indirect methods of molecular formation, when the laser-cooled atoms are photo- or magnetoassociated into molecules, remain the most efficient ways of producing ultracold molecules.

Photoassociation

Photoassociation is the process in which two colliding atoms absorb one or more photons of the laser field to form a molecule in an excited electronic state [23, 27]. The idea of photoassociation spectroscopy at ultralow temperatures was introduced in 1987 [93] and soon experimentally realized [94], whereas the use of photoassociation to produce ultracold ground state molecules was proposed in 1995 [95] and experimentally realized three years later [96]. The lifetime of molecules in an excited state is finite, therefore photoassociated molecules spontaneously radiate to the electronic ground state either remaining as bound molecules or dissociating back into atoms. The distribution of the spontaneously populated vibrational levels depends on the transition dipole moments and Franck-Condon factors. Therefore to control the vibrational population of formed molecules and to avoid dissociating back to atoms a stabilization laser can be used after the photoassociation to produce molecules in a chosen quantum state. Both continuous wave and pulsed lasers can be used for photoassociation.

All homonuclear alkali-metal molecules (Li_2 [97], Na_2 [94], K_2 [98], Rb_2 [99], Cs_2[96]) have been photoassociated at ultralow temperatures and many heteronuclear alkali-metal dimer (LiK [100], LiCs [92], NaCs [101], KRb [102], RbCs [103]) have been produced by using this technique. Additionally molecules containing closed-shell atoms such as RbYb [104], Sr_2 [105, 106, 107], Ca_2 [108], and Yb_2 [109, 110], that cannot be produced by using magnetoassociation, have been photoassociated.

Feshbach resonances and magnetoassociation

Magnetically tunable Feshbach resonances are commonly employed to associate cold atoms into diatomic molecules [24, 111]. This kind of resonances exists in systems of two interacting particles when there are at least two coupled internal states of the system that are of the open/scattering and closed/bound nature, respectively, and have different magnetic susceptibilities (different magnetic moments) [112]. A Feshbach resonance occurs when the energy of the bound molecular state in the closed channel approaches the energy of the scattering state in the open channel. Even a weak coupling leads to a strong mixing between the two channels and the avoided crossing between the scattering and bound states allows to adiabatically transfer the system between these two states. There are two schemes for the formation of Feshbach molecules. The first one is the adiabatic ramping an external magnetic field across a Feshbach resonance [113] and second one is driving the transition from the scattering state to the molecular state by an oscillatory magnetic field or by radio frequency [114]. The formed molecules are very weakly bound and subsequent stimulated adiabatic Raman passage is needed to produce deeply bound molecules [91, 115]. If there is no natural coupling between the scattering and bound molecular states, it can be induced by electromagnetic field leading to optical Feshbach resonance [116, 117, 118].

Ultracold alkali-metal gases were the first systems where the magnetically tunable Feshbach resonances were observed in 1998 [119, 120]. Since then, homonuclear [113, 121, 115] and heteronuclear [122, 123, 124] alkali-metal molecules have routinely been formed by using magnetoassociation for many different species. Later, Feshbach resonances in collisions between ultracold chromium atoms [125] have been observed. Recently, Feshbach resonances in ultracold gases of highly magnetic erbium [126, 127] and dysprosium [128, 129] atoms have been investigated and erbium dimers were magnetoassociated whereas experiments aiming on the magnetoassociation of lithium-erbium and potassium-dysprosium molecules are ongoing.

Somewhat unexpectedly, Feshbach resonances have also been predicted for mixtures of the open-shell and closed-shell atoms with the corresponding molecules in a $^2\Sigma$ ground electronic state such as RbSr and LiYb [130, 131, 132] but their experimental confirmation is still missing.

Trapping

Production of any ultracold gas and any possible application of ultracold atoms or molecules is not possible without the use of a properly designed trap. To trap ultracold atomic and molecular gases external static or time-dependent magnetic, electric, or electromagnetic fields can be employed. The development of trapping techniques was crucial at the early stage of research on ultracold atoms and now the development of traps for specific applications of ultracold molecules is one of the most important research goals.

Magnetic and magneto-optical traps

The oldest and simplest type of trap used to confine ultracold atoms is a magnetic trap [133]. In this trap atoms with non-zero magnetic moment are situated in the inhomogeneous magnetic field. To achieve a minimum of energy given by the Zeeman effect atoms prefer to occupy the region of the maximum of the magnetic field in the case of the so-called high-field seekers or the minimum of the magnetic field in the case of the low-field seekers. A local maximum cannot be generated in the stationary magnetic field, therefore to confine high-field seekers particles time-dependent fields are used.

The calcium monohydride was the first molecular species magnetically trapped at milliKelvin temperatures in 1998 [65]. Later molecules such as NH [134], OH [135, 89], and CrH/MnH [68] were also magnetically trapped and free radicals are the best candidates for magnetic trapping because of the presence of unpaired electrons.

By combining magnetic trap with the optical field needed for the laser cooling the magneto-optical trap (MOT) is formed. MOTs are essential for producing atomic Bose-Einstein condensates and Fermi gases. The creation of the magneto-optical traps for molecules is now one of the most important research goals. Recently, the 1D and 2D magneto-optical trapping of the YO molecules was demonstrated for the first time [82] promising the 3D molecular magneto-optical trapping in the near future.

Electrostatic and optical dipole traps

To confine charged or polar particles electrostatic traps can be used. Both atomic or molecular ions may be trapped either by using a static electric field and radiofrequency in a Paul trap or a combination of static electric and magnetic fields in a Penning trap [136]. The trapping of neutral particles with the static electric field is based on the Stark effect. The static electric field strength can have a minimum in the free space (maximum is not allowed by the Earnshaw's theorem) and only molecules in the low-field seeking quantum states can thus be trapped with static electric fields [137]. Nevertheless, the trap for the high-field seekers can be realized by a proper switching electric field that has a saddle point [138].

Electrostatic trapping of the ammonia molecules in the excited low-field seeking state was demonstrated for the first time in 2000 [43]. Later, the ac electric trap for the ground state ammonia molecules was also realized [139]. The combined static magnetic and electric fields were used to trap ground state OH molecules [135] and trapping of ultracold polar alkali-metal molecules with a thin-wire electrostatic trap was demonstrated [140].

By focusing laser beams of light far-detuned from any transition an optical dipole trap is created. The optical dipole traps, that are based on the dynamic Stark effect, are much shallower than MOTs, but the evaporative cooling of atoms in optical dipole trap allows to obtain temperatures much below the Doppler limit of laser cooling and the trapping is independent of the sub-level of the electronic ground state that allows to explore the internal ground state dynamics. Optical dipole trapping is usually the next stage after MOT. Until now, the ultracold molecules have been trapped in dipole traps only when first associated from ultracold atoms [141], but due to the generality of the method most of molecules should be trappable once pre-cooled to a low enough temperature.

Optical lattices

The interference of two counter-propagating laser beams creates standing waves. Each maximum of the field intensity in this periodic structure can be seen as an optical dipole trap that can trap ultracold atoms or molecules. By combing two or three lasers the 2D or 3D optical lattices can be created. The coherence and life-time of atomic or molecular gases trapped in the optical lattices can significantly be increased due to reducing collisional decoherence or possible chemical reactivity [142]. This opens the way for many exciting applications described in Chapter 1.4. Ultracold alkali-metal dimers were both formed and trapped in optical lattices [143, 115, 114, 144, 142].

1.3 Quantum control

For a long time, physicists and chemists have developed and employed various methods to observe quantum systems and processes on the atomic and molecular level. Afterwards, attention has been paid to actively manipulate the atomic and molecular quantum system to explore their dynamics [145, 146]. The first quantum control attempts originated in the idea of using lasers to manipulate chemical reactions, especially, breaking particular selected bonds in molecules [147]. At present, most of quantum control schemes is based on the quantum interference controlled by laser fields [148] and development of new schemes for control of quantum processes is one of the most important research goals.

Coherent control via quantum interference

The importance of the quantum interference in optical control of molecular systems was identified by Brumer and Shapiro [149, 150]. They proposed using two monochromatic laser fields for creating quantum interference between two reaction pathways and controlling the outcome by tuning the phase difference between the two laser fields. This scheme can be used to control the branching ratios of molecular reactions [151] or population transfer between bound states [152]. The interference of two pathways in above described scheme can be generalized to the interference and control of many pathways by using broad-bandwidth shaped pulses.

Pump-dump scheme

The other method to control molecular dynamics was proposed by Tannor, Rice, and Kosloff [153, 154] and uses two successive femtosecond laser pulses with a controllable time delay between

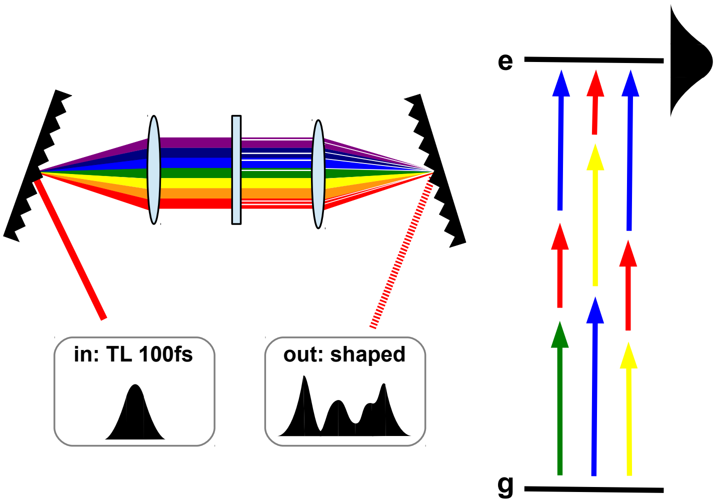

Figure 1.2: Schematic presentation of the pulse shaper (a) and the principle of the coherent control of the three-photon transition in two-level system as a result of the interference of many possible excitations paths (b).

them. The first laser ’pump’ pulse creates a wave packet in the manifold of vibrational levels of the electronically excited state of the molecule. Afterwards, the wave packet evolves freely until the second laser ’dump’ pulse transfers part of the population back to the ground electronic state into the desired reaction channel. By manipulating the delay between the two laser pulses, the location at which the excited wave packet is dumped to the ground electronic state and thus the reaction selectivity can be controlled. More effective control of the molecular dynamics in pump-dump scheme can be achieved by using shaped laser pulses. Another option is the Ramsey interference of optically excited wave packets called the wave-packet interferometry where the two pump pulses excite two wave packets which interference is controlled by tuning the time delay between the laser pulses [155, 156, 157].

STIRAP

Stimulated Raman adiabatic passage, that is very important method used in production of ultracold ground state molecules, was demonstrated by Bergmann and collaborators [158] as a very efficient adiabatic method for population transfer between discrete quantum states in atoms or molecules [159]. In this method the two time-delayed but overlapping pulses are applied to a three-level Λ-type system to achieve complete population transfer without populating the intermediate upper level and avoiding potential losses by radiative decay. This is archived by employing counter-intuitive pulse sequence when the dump/Stokes laser pulse is applied before the pump laser pulse. The control of population transfer between a discret states is archived by tuning the time delay between pulses.

Quantum optimal control theory

The mentioned above methods of quantum control manipulate the evolution of quantum systems by controlling just one parameter: the phase difference or time delay. Rabitz and collaborators [160, 161, 162] suggested that the specifically shaped laser pulses can be suitable to steer the quantum evolution to a desired product channel. Quantum version of optimal control theory (OCT) with a specified control objective and with restrictions imposed by equations of motion and many possible constraints can be employed to design laser pulse shapes best suited for driving system into the desired direction. The optimal control theory approach can be combined with all mentioned control schemes such as the two-pathway quantum interference and pump-dump control.

1.4 Applications of ultracold molecules

Ultracold atoms have found a wide range of current and possible future applications [22, 163, 164]. The ultracold molecules have a much richer internal structure including rotational and vibrational levels and possible permanent electric and magnetic dipole moments. This results in long-range interactions and combined with external electric, magnetic, or electromagnetic fields allows for manipulation and control to a much larger extent as compared to atomic systems [165, 166]. All of these combined together promise a number of exciting applications [16, 15].

Precision measurements and tests of fundamental laws

Reduction of temperature to fractions of Kelvin facilitates high-resolution spectroscopy, quantum measurements and precision tests of fundamental laws of nature. Ultracold atomic gases have resulted in a new generation of high-accuracy atomic clocks [167, 168, 169, 170], quantum sensors [171, 172], the precise measurements of fundamental constants [171, 172], and their possible time-dependent variations [173, 174].

Ultracold molecules with their rich internal structure bring a variety of new possibilities. On one hand, high-resolution spectroscopy of molecules prepared in a single quantum state give a precise information on their rovibrational structure and indirectly on electronic structure including potential energy surfaces for the ground [175] and excited [176, 177] electronic states, transition dipole moments [178], spin-orbit couplings [179], and polarizabilities [180]. On the other hand the precision test of the electron-to-proton mass ratio variation in time with lattice-confined ultracold molecules [181, 182] or nuclear spin-dependent parity violation due to the enhanced sensitivity of rovibrational spectra to nuclear effects [183] were proposed, and the limits on the electric dipole moment of the electron were imposed by using greatly enhanced measurement sensitivity due to very large internal electric fields in polar molecules [184, 185].

Ultracold collisions and controlled chemistry

At ultralow temperatures the collision energy becomes much smaller than the interatomic or intermolecular interactions as well as the perturbations due to external fields. This opens the door to the world of ultracold controlled collisions [186, 187, 165] and controlled chemistry [188, 189]. The atomic and molecular collisional dynamics can be controlled with external electric [190, 191], magnetic [192, 90], and laser fields [193, 194, 195]. The ultracold elastic, inelastic, and chemical reactive collisions can be studied with beam-decelerated molecules or with ultracold gases in traps.

The crossed beams of cold, decelerated molecules have been employed to investigate the quantum-state resolved bimolecular collisions of velocity-controlled OH with NO radicals [196], large effects of electric fields on the atom-molecule collisions at milliKelvin temperatures [197] or the resonances in the Penning ionization reactions in merged beams [198], and can be used to investigate cold chemical reactions in other systems [199].

The creation of ultracold dense gas of the KRb molecules in their rovibrational ground state [91] allowed the study of quantum-state controlled chemical reactions [200], electric-field-controlled dipolar collisions of polar molecules in the quantum regime [201], and controlling the quantum stereodynamics of ultracold bimolecular reactions by confining in quasi-two-dimensional geometry, with the dipoles oriented along the tight confinement direction [202]. At present experimental efforts aim on the realization and controlling the state-to-state ultracold dynamics and state-selected products detection [199].

Bose-Einstein condensation

In 1995 the Bose-Einstein condensate of alkali atoms [203] was produced for the first time by Eric Cornell and Carl Wieman at the University of Colorado at Boulder [11] and by Wolfgang Ketterle at MIT [12]. Thereafter the condensates of the highly magnetic atoms such as chromium [204], erbium [126], and dysprosium [128] as well as the closed-shell strontium [205, 206], calcium [207] and ytterbium [208] atoms were obtained. In 2003 the condensate of weakly bound Feshbach-type molecules was produced by adjusting the interaction strength in an ultracold Fermi gas of atoms [209, 210] but the condensate of the molecules in the rovibrational ground state has remained an elusive goal. At present the efforts to produce it are undertaken, fueled by the promise of exciting applications and a new insight into the importance of the rovibrational and spin structure, and long-range intermolecular dipolar interactions on the properties of molecular BEC.

Many-body physics

Bose-Einstein condensate of bosonic particles is the only one of many quantum phases of matter at ultralow temperatures [163]. Few years after the first observation of BEC, the production of the degenerate atomic Fermi gas has been achieved [211, 212]. This has paved the way towards the observation of the Fermi superfluidity and BEC-BCS crossover in the limit of strong correlations [213, 214, 163].

A new variety of possibilities appears when the ultracold gas is trapped in an optical lattice on one hand or when the long-range dipolar interactions are present on the other hand. Quantum phase transition from a superfluid state to a Mott insulator state in a gas of ultracold lattice-confined bosonic atoms with repulsive interactions was observed [215]. Similar phases in ultracold lattice-confined one- and two-component Fermi gases were also reported [216, 217]. Different quantum phases of dipolar bosons in optical lattices were predicted [218, 219] and strong dipolar effects in a quantum ferrofluid based on the ultracold chromium atoms were investigated [220]. Multi-component quantum gases in spin-dependent hexagonal lattices [221] and quantum phase transition to an unconventional multi-orbital superfluidity in honeycomb lattice [222, 223] were also realized.

Ultracold polar molecules are perfectly suitable for realization of dipolar quantum phases. Additionally, it was shown that even the singlet state polar molecules in an optical lattice can be used to engineer quantum spin models with arbitrary spin by an appropriate dressing of the rotational states with a microwave field [224] and spin crystals in different quantum phases can nonadiabatically be prepared [225].

Quantum simulations

Ultracold trapped gases are highly controllable systems which interactions, structure, and geometry can potentially be controlled over a wide range of parameters [163, 165]. While a simulation of the quantum many-body dynamics for any physical system using classical computer is a challenging problem, the trapped ultracold atoms or molecules can be used to realize the Feynman's dream of building a quantum simulator [226]. The idea of the quantum simulator is based on the assumption that the Hamiltonian and hence the resulting many-body dynamics of the system that cannot be simulated by using classical computers, can be mapped onto another highly controllable many-body system [227, 228].

Recent advances with ultracold atoms in optical latices, including single-atom-resolved fluorescence imaging [229] and single-spin addressing in an atomic Mott insulator [230], allowed for the first quantum simulations using systems at ultralow temperatures. The Bose-Hubbard model and the superfluid-to-Mott insulator transition at the single atom level [231, 232] and the nearest-neighbor correlations of ultracold fermions in an optical lattice [233] were investigated. The antiferromagnetic spin chains [234], magnon bound states and their dynamics [235], short-range quantum magnetism of ultracold fermions [236], artificial graphene with tunable interactions [237], and negative absolute temperature for motional degrees of freedom [238] were simulated. Recently, an optical lattice clock was also used to simulate a quantum many-body spin system [169].

The rotational structure and permanent dipole moments of polar molecules expand the range of their potential applications in quanutm simulations. Ultracold polar molecules with

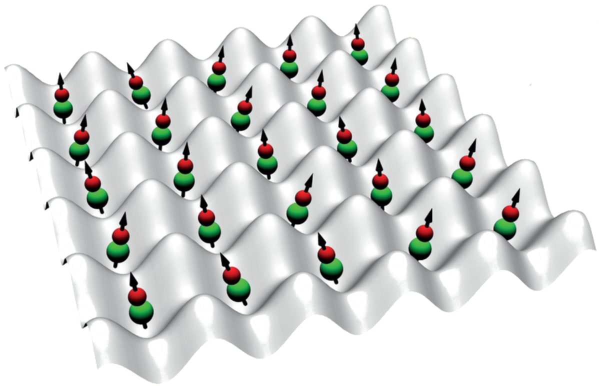

Figure 1.3: Ultracold polar molecules trapped in an optical lattice [227].

spin structure were proposed for simulating lattice-spin models [239], tunable superfluidity and quantum magnetism [240], far-from-equilibrium quantum magnetism [241], topological phases [224], controlled collective spin excitations [242], tunable disorder [243], biexciton interactions [244], and polaron transitions [245]. The production of the high phase-space-density gas of ultracold molecules, the reduction of its dimensionality, and recently the observation of dipolar spin-exchange interactions between lattice-confined polar molecules [246] or magnetic dimers [247], bring us closer and closer to the realization of fully controllable systems of ultracold molecules in optical lattices and thus quantum simulators.

Quantum computations and information processing

Due to the relatively long decoherence time, the ultracold gases in traps can potentially find applications as quantum registers for quantum information processing or even can be used to build universal quantum gates. Qubits can be encoded into hyperfine [248] or Rydberg [249] states of the isolated atoms trapped in an optical lattice [250]. Alkaline-earth-metal atoms were proposed for few-qubit quantum registers [251]. Fast one- and two-qubit quantum gates for neutral atoms can be realized by using controlled collisions [252, 253] and superexchange interactions [254]. Combining ultracold trapped atoms with ions should result in faster quantum computations [255, 256]. Ultracold polar molecules trapped in an optical lattice, with their rotational structure suitable for encoding qubits and dipole moments enabling realization of quantum gates based on the long-range interactions, can potentially be used for quantum computation [257, 258], but actual schemes for robust and universal quantum computation must still be developed.

Chapter 2

Motivation and objectives

2.1 Context and motivation of the proposed research

The developments of methods for the creation, manipulation, and control of photonic, atomic, and ionic quantum system have been awarded Nobel prizes in 1997 [8, 9, 10], 2001 [13, 14], 2005 [17, 18, 19], and 2012 [20, 21]. As it was presented in the Introduction, molecules are much more complex objects as compared to atoms due to their internal structure of vibrational and rotational states and possible permanent electric dipole moments. Therefore, the creation, manipulation, and control of molecular quantum systems and processes are much more challenging. Nevertheless, fueled by the promise of exciting current and possible future applications, more and more efforts are made to produce and investigate ultracold molecular gases.

The present thesis is concerned with theoretical studies of the quantum dynamics and control of ultracold molecules in external fields. Particular attention is paid to the direct methods of formation of ultracold molecules, both employing standard methods to non-standard systems and proposing new schemes of molecular formation. The reported studies involve both the theoretical developments and numerical implementations and applications. Numerical calculations are performed for systems being investigated experimentally or potentially prospective for future experiments.

Photoassociation of closed-shell atoms

Indirect methods of the molecular formation by photo- or magnetoassociation of ultracold atoms are the most successful way of producing ultracold molecules. However, these methods have been applied mostly to ultracold gases of alkali-metal or other open-shell atoms with few exceptions as formation of ultracold Sr_2 [105], Ca_2 [108], and Yb_2 [110] dimers. Until now, except the photoassociation of heteronuclear but homoatomic ${}^{n}\mathrm{Yb}{}^{m}\mathrm{Yb}$ dimers [109], there were no ultracold heteroatomic molecules consisting of closed-shell atoms produced. Molecules containing closed-shell atoms are interesting because of their relatively simple electronic structure of the ground state ideally suited for precision measurements [181, 182, 183] and a rich structure of the excited states correlated with the metastable atomic states. Heteronuclear molecules consisting of the closed-shell atom may also possess a permanent electric dipole moment. The experiment aiming on building molecular clock for precision measurements with ultracold SrYb molecules in an optical lattice is planned in the group of prof. Tanya Zelevinsky at the University of Columbia. For the above reasons we investigated the electronic structure and formation paths of the ultracold SrYb molecules by using photoassociation spectroscopy.

Photoassociation with short laser pulses

Photoassociation forming molecules from ultracold atoms using laser light is a prime candidate for coherent control which utilizes the wave nature of matter in order to steer a process, such as formation of a chemical bond, toward a desired target [146, 259]. At ultralow temperatures, the delicate build-up of constructive and destructive interference between different quantum pathways is not hampered by thermal averaging. The basic tool for coherent control are short laser pulses that can be shaped in their amplitude, phase and polarization. They can drive both adiabatic and non-adiabatic photoassociation dynamics [27].

The efficient formation of ultracold molecules with short picosecond laser pulses in a pump-dump scheme was proposed a few years ago [260, 261] but has not been realized yet due to technical limitations of the picosecond lasers. In contrast, pulse shaping techniques of femtosecond lasers are well developed. Femtosecond photoassociation at ultralow temperatures corresponds to driving a narrow-band transition with a broad-band laser. This can be achieved by employing multi-photon rather than one-photon transitions [262] but the control schemes have to be applied in order to suppress the excitation of atoms. The coherent control of two-photon photoassociation in a simple two-state model of ultracold Ca_2 molecule was proposed [263] but the generality and usefulness of the method for other systems are still an open question. For the above reasons we investigated the multi-photon photoassociation of ultracold atoms with femtosecond pulses shaped by using principles of coherent control or optimal control theory.

The photoassociation is the first out of two steps in the formation of ground-state molecules. The lifetime of photoassocited molecules is finite but usually much longer than the duration of the shaped femto- or picosecond pulse and the timescale of vibrational dynamics. This suggests the use of the stabilization pulse in order to drive the photoassociated wave packet to the deeply bound ground state [264]. Therefore, we investigated the evolution of photoassociated wave packet and its stabilization by using short shaped pulses.

Control of ultracold molecular processes with a non-resonant light

Pulses of a non-resonant laser field have been employed to control the rotational dynamics, alignment and orientation of molecules [265, 266]. Recently, the non-resonant light was also proposed to enhance the photoassociation efficiency by controlling the positions of shape resonances [194]. However, only the compression of the scattering state and photoassociation in a simple two electronic state model were considered. Therefore, we investigated the influence of the non-resonant field on the rovibrational levels of the open-shell excited electronic states and stabilization pathways in the schemes of the formation of ultracold ground-state molecules.

The proposal of the non-resonant field controled photoassociation suggests to harness the non-resonant light to control magnetoassociation. The formation of the $^2\Sigma$ state molecules in mixtures of open-shell and closed-shell atoms is currently a very important and challenging research goal. The Feshbach resonances were theoretically predicted and magnetoassociation of the $^2\Sigma$ state molecules was proposed [130, 131] but the resonance widths are very small and render this process very difficult. Therefore, we investigated the possibility of controlling the magnetoassociation of the $^2\Sigma$ molecules and increasing the resonance widths by applying the non-resonant light.

Ultracold polar molecules with spin structure

The first proposals of the ultracold quantum simulation of spin models [239] or magnetic field controlled chemistry [267] needed polar molecules with spin structure. The simplest molecules with spin structure are those in the electronic states of $^2\Sigma$ and $^3\Sigma$ symmetries. The former ones can consist of closed-shell atom such as strontium or ytterbium and open-shell atom such as rubidium or fluorine, whereas the latter ones can be found in alkali-metal dimers. Until now, ultracold dense gas of $^2\Sigma$ state molecules has not yet been produced albeit the efforts are undertaken to direct laser cool molecules such as SrF [81] and photo- or magnetoassociate molecules such as RbYb [104] and RbSr [268]. The magnetoassociation of $^2\Sigma$ molecules though possible is rendered very difficult due to very small resonance widths [130, 131, 132]. The ultracold dense gases of alkali metal-dimers in $^3\Sigma$ state have already been produced [91] but their application can be affected by potential inelastic collisions and chemical reactions. For the above reasons, in the quest of the molecules with the spin structure, we investigated the possibility of the non-resonant light controlled magnetoassociative formation of $^2\Sigma$ molecules, chemical reactions of $^3\Sigma$ alkali-metal molecules, and the new class of highly magnetic and polar molecules based on the chromium and close-shell atoms.

Hybride system of ultracold atoms and ions

The trapped ions are highly controllable and strongly interacting systems therefore they have found applications in precision measurements, quantum simulations, and quantum computations [136], just to mention the most prominent. Currently, combing trapped ions with ultracold atoms in one experiment is emerging as another important research goal. For example, the dynamics of a single ion immersed in an atomic Bose-Einstein condensate [269] and controlling chemical reactions of a single ion with ultracold atoms [270] have already been investigated. However, the new experimental proposals e.g. aiming at building quantum simulator emulating solid-state physics with a hybrid system of ultracold ions and atoms [271, 272] still request a detailed knowledge of the microscopic ion-atom collisional dynamics. Therefore, we investigated the cold and ultracold interactions and collisions of Yb^+ ion with Li atoms, the system present in the ongoing experiment in the group of prof. Rene Gerritsma at the University of Mainz.

2.2 Objectives of the proposed research

The primary objectives of the presented thesis are the following:

1. To explore the electronic structure of the molecular systems relevant for ongoing experimental and theoretical investigations by means of the state-of-the-art *ab initio* methods. The task includes:

    - calculations of the potential energy curves, permanent and transition electric dipole moments, electric dipole polarizabilities, nonadiabatic and spin-orbit coupling matrix elements for the ground and excited states of the SrYb molecule, LiYb^+ molecular ion, Rb_2 molecule, $^2\Sigma$ molecules, and chromium–closed-shell-atom molecules, as well as the calculations of the minimum energy paths for reactions of alkali-metal dimers in $a^3\Sigma^+$ state to investigate the stability of these molecules.

2. To study the interactions and dynamics of the ultracold SrYb molecule and LiYb^+ molecular ion and their formation by using standard methods of photoassociation. The task includes:

    - calculations of the rovibrational structure and photoassociation rates for the SrYb molecule, and proposal of a scheme for an effective production of the ultracold ground state SrYb molecules.
    - calculations of rates for the elastic and inelastic collisions due to the radiative charge transfer and radiative association between the Yb^+ ion and Li atoms, and of the photoassociation rates. Proposal of schemes for an effective production of the LiYb^+ molecular ions in both singlet and triplet states by using the photoassociation technique.

3. To examine the possibility of an effective production of ultracold molecules by using the short-pulse photoassociation with multi-photon transitions driven by shaped laser pulses. The task includes:

    - development of the theory of multiphoton photoassociation driven by pulses shaped by means of coherent and optimal control theory. Example calculations for three-photon non-resonant photoassociation of the Rb_2 molecule.

- analysis of the time evolution of the photoassociated excited-state wave packet and finding the optimal time delay for the stabilization pulse. Investigation of the efficiency of population transfer in the stabilization step by using transform-limited and linearly chirped laser pulses. Use of the optimal control theory to determine the most efficient stabilization pathways.
- proposal of a new scheme for an effective multi-photon formation of the ultracold ground state Rb_2 molecules where transitions are driven by pulses shaped with the optimal control theory.

4. To investigate the influence of the non-resonant field on the ultracold collisions and rovibrational structure of open-shell molecules and to propose new schemes of controlling the formation of ultracold molecules with a non-resonant light. The task includes:
    - formulation of the theory for a diatomic molecule in a spatially degenerate electronic state interacting with the non-resonant laser field, example calculations for the manifold of $A^1\Sigma_u^+ + b^3\Pi_u$ excited states coupled by spin-orbit coupling in the Rb_2 molecule. Proposal of a new scheme of controlling photoassociative formation of ultracold molecules with the non-resonant light.
    - formulation of the theory for a $^2\Sigma$ molecule in the combined non-resonant and magnetic fields. Investigation of the influence of the non-resonant field on the magnetically tunable Feshbach resonances. Example calculations for the RbYb molecule, and finally proposal of a new scheme of controlling Feshbach resonances and manetoassociative formation of ultracold polar open-shell molecules with the non-resonant light.

The present thesis is organized as follows. In Chapter 3 we present the results of the electronic structure calculations for the SrYb molecule, Rb_2 molecule, LiYb^+ molecular ion, $^2\Sigma$ molecules, chromium–closed-shell-atom molecules, and finally the reactions of the $^3\Sigma$ molecules. In Chapter 4 we employ the results of the electronic structure calculations to investigate the nuclear dynamics and formation of ultracold ground state SrYb molecules and LiYb^+ molecular ions by means of standard continuous wave laser photoassociation. Chapter 5 presents results on the formation of ultracold molecules by short-pulse photoassociation. We investigate the coherent and optimal control of multi-photon photoassociation and subsequent stabilization driven by shaped femtosecond pulses, and the detection scheme of the wave packet photoassociated with a picosecond pulse. In Chapter 6 we investigate the influence of the non-resonant laser field on the molecular rovibrational structure and propose new schemes of controlling the photoassociative and magnetoassociative formation of ultracold molecules with non-resonant light. Chapter 7 concludes and summarizes the main achievements of the thesis. The last part of the thesis contains reprints of six papers published in international scientific journals which describe in details all the obtained results. We will refer to these papers as to Paper I to VI.

Chapter 3

Ab initio electronic structure calculations for ultracold molecules

3.1 Introductory remarks

Ab initio electronic structure calculations play a very important role in physics and chemistry of ultracold atoms and molecules. Any reliable theoretical prediction or experimental proposal is not possible without a credible knowledge of the electronic structure. Before starting any experiment this knowledge can only be gained either from *ab initio* calculations or from earlier conventional spectroscopy measurements which often are not available.

The state-of-the-art methods of modern quantum chemistry describe the atomic and molecular properties at an unprecedented level of accuracy and allow to calculate interaction potentials, transition dipole moments, matrix elements of the spin-orbit and non-adiabatic coupling operators, polarizabilities, or coefficients in the multipole expansion of the interaction at large interatomic or intermolecular distances, and in fact any other derivative property. The electronic structure data can later be employed in dynamical calculations but it is quite often the case that the insight into the physics of the problem gained already from the electronic structure picture allows to understand the essence of the problem.

Solving the Schrödinger equation for many-electron systems is a challenging task. Almost exact solutions can be found only for the smallest molecular systems such as the hydrogen molecule [273] or helium dimer [274] for which the numerically accurate result for the non-relativistic interaction energy in the Born-Oppenheimer approximation can be obtained in the first step, and the adiabatic, non-adiabatic, relativistic, and QED corrections can be included in the second step. The errors of the electronic structure calculations increase with the size of the system and at present the *ab initio* results cannot compete in accuracy with the most accurate spectroscopic measurements for systems larger than lithium [79] or berylium [275] dimers. Nevertheless, accurate spectroscopic predictions can be based on *ab initio* calculations even for such large systems as rubidium [276] or strontium dimers [277, 278].

In the research on utracold atoms and molecules the needed accuracy of the molecular property varies from problem to problem. On one hand, the scattering length that determines the collisional properties of gases at ultralow temperatures cannot be obtained with the input from *ab initio* calculations for any system larger than few-electron atoms because the results of the scattering calculations at low and ultralow temperatures are extremely sensitive to fine details of the interaction potential. On the other hand, the same potentials can be used to determine reliable photoassociation rates, and the permanent electric dipole moments or polarizabilities can be calculated with an accuracy that is sufficient for investigations of the many-body dynamics and trapping.

In this chapter we present the results of the state-of-the-art *ab initio* electronic structure calculations for molecular system relevant for the ongoing experiments on one hand, and used in our scattering or time-dependent simulations of molecular processes in next chapters on the other hand.

3.2 Electronic structure methods

The diversity of the molecular world is responsible for the developments of many methods describing electronic structure of molecules [279]. Depending on the physical characteristics of the system, the type of property to be calculated, and the intended application, a suitable method has to be chosen which is often a challenge.

The system of N_e electrons and N_n nuclei in a stationary state is fully characterized by the wave function $\Psi(\vec{r}_1,..,\vec{r}_{N_e},\vec{R}_1,..,\vec{R}_{N_n})$ that depends on the positions of all electrons $\vec{r}_i$ and all nuclei $\vec{R}_j$, and, in the non-relativistic limit, is the solution of the time-independent Schrödinger equation [280]. Solving the Schrödinger equation even for a few electrons and nuclei without separating their motion is a very challenging problem. Fortunately, the motion of electrons and nuclei can be separated due to a large difference in their masses and the resulting dynamics time scales. In the Born-Oppenheimer approximation, assuming that the nuclear motion is adiabatically followed by the motion of the electron cloud, the total wave function is represented as a product of the electronic Ψ_{el} and nuclear Ψ_{nuc} wave functions

$$\Psi(\vec{r}_1,..,\vec{r}_{N_e},\vec{R}_1,..,\vec{R}_{N_n}) \approx \Psi_{\mathrm{el}}(\vec{r}_1,..,\vec{r}_{N_e};\vec{R}_1,..,\vec{R}_{N_n})\Psi_{\mathrm{nuc}}(\vec{R}_1,..,\vec{R}_{N_n})\,. \tag{3.1}$$

The electronic wave function depends directly on the positions of all electrons and is a solution of the electronic Schrödinger equation with the Hamiltonian with frozen positions of the nuclei as parameters. By solving the Schrödinger equation with the electronic Hamiltonian for all possible positions of nuclei one obtains the potential energy surface for the nuclear motion. The nuclear wave function is the solution of the Schrödinger equation with the Hamiltonian for the nuclear dynamics given by the nuclear kinetic term and the potential energy surface of a given electronic state as the potential term. If electronic states are coupled the total wave function of Eq. (3.1) can be generalized to the sum over many electronic states.

The Born-Oppenheimer approximation divides the description of any molecular process into two steps. In the first step, the electronic Schrödinger equation is solved for all possible positions of the nuclei (present Chapter), and in the second step, the nuclear dynamics is investigated on single or many potential energy surfaces obtained in the first step (Chapters 4, 5, and 6).

Most of the efforts of modern quantum chemistry is devoted to developments of the theoretical and numerical methods for efficiently solving the electronic Schrödinger equation. Well-established scheme starts with defining a set of single-electron basis functions and approximating the total wave function by a single Slater determinant (or a combination of a few Slater determinants if the ground state is dominated by more than one electronic configuration). By invoking the variational principle, one can derive and solve a set of equations that yields the Hartree-Fock mean-field solution for the wave function and energy of the system.

The wave function and the set of one-electron spin-orbitals obtained in the Hartree-Fock method is a convenient starting point for calculations going beyond the mean-field approximation.

Configuration interaction methods

For given set of one-electron basis functions the exact solution of the electronic Schrödinger equation can be written as a combination of all Slater determinants that can be constructed from the one-electron basis

$$|\Psi_{\mathrm{FCI}}\rangle = (1 + \sum_{A,I} C_I^A a_A^\dagger a_I + \sum_{A,B,I,J} C_{IJ}^{AB} a_A^\dagger a_B^\dagger a_I a_J + \dots)|\Psi_0\rangle \,, \tag{3.2}$$

where $|\Psi_0\rangle$ is the Hartree-Fock solution, and $a_i^\dagger$ and a_j are the creation and annihilation operators of the spin-orbitals i and j, respectively. The expansion coefficients C can be obtained from the variational principle or direct diagonalization.

Unfortunately, the length of the expansion of Eq. (3.2), called Full Configuration Interaction (FCI) wave function, depends factorially on the number of electrons and basis functions. This makes FCI calculations infeasible for systems of more than a few electrons. Therefore, the methods selecting the most important terms from expansion (3.2) have been developed.

If the state is dominated by a single electronic configuration it is reasonable to assume that the lowest-order excitations will be the most important. By truncating the expansion (3.2) one can arrive with e.g. the configuration interaction restricted to single and double (CISD) excitations method.

If the state is dominated by more than one electronic configuration (the system is degenerate or quasidegenerate) then the multireference configuration interaction (MRCI) wave function can be generated by including in the wave function all important configurations (instead of single $|\Psi_0\rangle$), as well as all excitations from each configuration up to level of truncation.

Coupled cluster methods

The hierarchy of configuration interaction methods suffers from the lack of the size-consistency and slow convergence towards the FCI limit. The lack of size-consistency can especially affect the interaction energy at large internuclear distances which are very important for ultracold processes. These problems of the CI methods are overcome when the coupled cluster wave function is used [281]

$$|\Psi_{\mathrm{CC}}\rangle = \exp\left(\sum_{A,I} t_I^A a_A^\dagger a_I + \sum_{A,B,I,J} t_{IJ}^{AB} a_A^\dagger a_B^\dagger a_I a_J + \dots\right)|\Psi_0\rangle \,. \tag{3.3}$$

The above nonlinear exponential parametrization of the wave function called exponential Ansatz of the coupled cluster theory is equivalent to the FCI wave function if all excitations are included. By truncating the expansion in the exponent of Eq. (3.3) one can arrive at, e.g., coupled cluster restricted to single and double excitations (CCSD) model. In contrast to truncated CI methods, the truncated CC wave functions contain the contributions from all determinants excited to the level of truncation and all determinants that can be obtained by all possible products of the excitation operators below the truncation. This makes the CC methods size-consistent and usually allows to recover more of the correlation energy than from the CI calculations.

The standard coupled cluster methods work very well only for systems dominated by a single electronic configuration. Nevertheless, there exist multireference generalizations of the CC methods to describe states that are dominated by more than one electronic configuration [282]. On one hand, one can include in the wave function all important reference configurations (instead of a single $|\Psi_0\rangle$) and define the corresponding exponential operators staying in a single Hilbert space. On the other hand, the problem can be redefined in the Fock space when the reference state $|\Psi_0\rangle$ can be the ionic structure with attached or removed electrons that can be correctly described by single electronic configuration and single-determinant method. By starting with such a reference state and by using the electron attachment or electron ionization formalism [283, 284] the systems in degenerate or quasidegenerate states can accurately be described.

Effective core potentials

The Schrödinger equation describes quantum systems in the non-relativistic approximation. When heavy atoms are present in the system the relativistic effects can play an important role. To incorporate fully the relativistic effects, generalization of the Dirac equation for many particles should be used. For example, one can employ the Dirac-Coulomb, Breit-Pauli, or Douglas-Kroll-Hess Hamiltonians. At the same time, the accuracy of the calculations for systems containing heavy atoms with many electrons is limited by either the necessity to use more approximate and less accurate methods or the basis sets being far from completeness.

All the problems mentioned above can partly be solved by using the effective core pseudopotentials to replace the most inner-shell electrons [285]. The use of pseudopotentials allows to reduce the number of electrons, to use larger basis sets to describe the valence electrons, to model the inner-shells electrons density as accurately as in the high quality atomic calculation used to fit them, and finally to include scalar relativistic effects.

3.3 SrYb molecule

In this section we present the results of the electronic structure calculations for the ground and excited states of the SrYb molecule. This work is motivated by the experiment aiming on building molecular clock for precision measurements planned in the group of prof. Tanya Zelevinsky at the University of Columbia. *Ab initio* data will be employed in photoassociation and STIRAP calculations in Chapter 4.2 whereas a detailed description of the results is presented in Paper I.

Computational details

The potential energy curves for the ground and first fifteen (eight singlet and seven triplet) excited states of the SrYb molecule have been obtained by the supermolecule method [286]. For the ground state potential we used the coupled cluster method restricted to single, double, and noniterative triple excitations, CCSD(T) [281]. Calculations on all the excited states employed the linear response theory within the coupled cluster singles and doubles (LRCCSD) framework [287], also known as the equation of motion coupled cluster method (EOM-CCSD) [288]. The CCSD(T) and LRCCSD calculations were performed with the DALTON program [289].

For each electronic state relevant for the photoassociation we have computed the long-range coefficients describing the dispersion and induction interactions from the standard expressions [290]. The long-range dispersion coefficients were computed with the recently introduced explicitly connected representation of the expectation value and polarization propagator within the coupled cluster method [291, 292, 293]. For the singlet and triplet states dissociating into Sr(^1P)+Yb(^1S), and Sr(^3P)+Yb(^1S), respectively, the dispersion coefficients were obtained from the sum-over-state expression with the transition moments and excitation energies computed with the multireference configuration interaction method limited to single and double excitations (MRCI).

The transitions from the ground $X^1\Sigma^+$ state to the $^1\Sigma^+$ and $^1\Pi$ states are electric dipole allowed. In the present calculations the electric transition dipole moments were computed as the first residue of the LRCCSD linear response function with two electric dipole operators [287]. In these calculations we have used the DALTON program [289]. The matrix elements of nonadiabatic angular coupling between low lying excited states of the SrYb molecule have been also calculated with the MRCI method and the MOLPRO code [294].

Strontium and ytterbium are heavy atoms, so the electronic states of the SrYb molecule are strongly mixed by the spin-orbit (SO) interactions. We have evaluated the spin-orbit coupling matrix elements for the lowest dimer states that couple to the states with the projection of

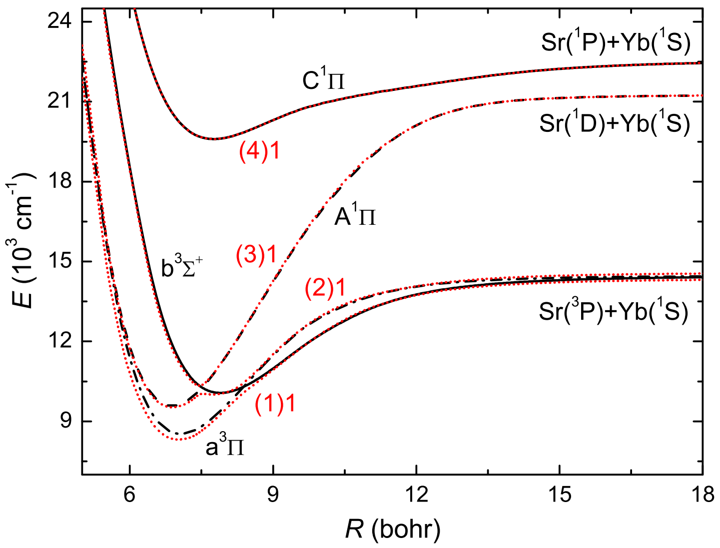

Figure 3.1: The $a^3\Pi$, $b^3\Sigma^+$, $A^1\Pi$ and $C^1\Pi$ potential energy curves (solid and dashed black curves) in Hunds case (a) representation that are coupled by the spin-orbit interaction and the resulting $\Omega = 1$ relativistic states (red dotted curves) in Hund's case (c) representation of the SrYb dimer.

the electronic angular momentum on the internuclear axis Ω equal to $0^{+/-}$, 1, with the spin-orbit coupling operator H_{SO} defined within the Breit-Pauli approximation [295]. The spin-orbit coupling matrix elements have been computed within the MRCI framework with the Molpro code [294]. Diagonalization of the relativistic Hamiltonian gives the spin-orbit coupled potential energy curves for the $0^{+/-}$, 1 and 2 states, respectively. In order to mimic the scalar relativistic effects some electrons were described by pseudopotentials. For Yb we took the ECP28MWB pseudopotential [296], while for Sr the ECP28MDF [297] pseudopotential, both from the Stuttgart library. For the strontium and ytterbium atoms we used *spdfg* quality basis sets [297, 298], augmented with a set of [2*pdfg*] diffuse functions. In addition, this basis set was augmented by the set of bond functions consisting of [3*s*3*p*2*d*1*f*] functions placed in the middle of SrYb dimer bond. The full basis of the dimer was used in the supermolecule calculations and the Boys and Bernardi scheme was used to correct for the basis-set superposition error [286].

Numerical results

The ground state potential of a Van der Waals type with binding energy of 828 cm^{-1} is presented in Fig. 1 of Paper I. The permanent dipole moment of SrYb in the ground electronic state as a function of the interatomic distance R is presented in Fig. 1 of Paper I. Except for short interatomic distances, the dipole moment is very small. This is not very surprising since the two atoms have very similar electronegativities and the charge flow from one atom to the other, after the formation of the weak Van der Waals bond, is very small. The vibrationally averaged dipole moment of SrYb in the ground vibrational state is very small and equal to 0.058 D.

Potential energy curves of the excited singlet and triplet states of SrYb are presented in Fig. 2 of Paper I. The spectroscopic characteristics of all these states are reported in Table I of Paper I and the corresponding long-range coefficients are reported in Table II of Paper I. The long-range potential given by multipole expansion was smoothly connected with the *ab initio* data at distances larger than $R = 15$ bohr. The agreement between the raw *ab initio* data and the asymptotic expansion was of the order of 1% for the ground state and 3 to 4% for the excited states at $R = 15$ bohr. Inspection of Fig. 2 of Paper I reveals that the potential energy curves for the excited states of the SrYb molecule are smooth with well defined minima. The potential energy curves of the (2) and $(3)^3\Sigma^+$ states show an avoided crossing and exhibit a double minimum structure. These double minima on the potential energy curves are due to strong nonadiabatic interactions between these states. Other potential energy curves do not show any unusual features, except for the broad maximum of the potential of the $(4)^1\Sigma^+$ which is most likely due to the interaction with a higher excited state. Except for the shallow double minima of the $(2)^3\Sigma^+$ and $(3)^3\Sigma^+$ states, and shallow Δ states, all other excited states of the SrYb molecule are strongly bound with binding energies D_e ranging from 1790 cm^{-1} for the $(4)^1\Sigma^+$ state up to as much as 11851 cm^{-1} for the $A^1\Pi$ state.

The $a^3\Pi$, $b^3\Sigma^+$, $A^1\Pi$, and $C^1\Pi$ excited states essential for the photoassociative formation of the ground state SrYb molecule proposed in Chapter 4.2 are plotted in Fig. 3.1. The matrix elements of the spin-orbit coupling were calculated for the manifolds of coupled $a^3\Pi$, $b^3\Sigma^+$, $A^1\Pi$ states and presented in Fig. 3 of Paper I. The knowledge of the spin-orbit coupling between $a^3\Pi$, $b^3\Sigma^+$, $A^1\Pi$, and $C^1\Pi$ states allows us to obtain the relativistic $(1)0^-$, $(2)0^-$, $(1)0^+$, (1)1, (2)1,(3)1, (4)1 and (1)2 states by diagonalizing the appropriate relativistic Hamiltonian matrices. The $|\Omega| = 1$ states are also plotted in Fig. 3.1. Note that the crossing of the $b^3\Sigma^+$ and $A^1\Pi$ nonrelativistic states becomes an avoided crossing between the (2)1 and (3)1 states.

3.4 Rb$_2$ molecule

In this part we summarize the results of the high-accuracy electronic structure calculations for the ground and excited states of the rubidium dimer. We have employed the state-of-the-art Fock space coupled cluster method in the double electron attachment formalism which allows to accurately describe a molecular system that cannot be treated with standard single reference methods. The *ab initio* data presented below will be employed in the time-dependent studies of the multi-photon molecular formation in Chapter 5 and Paper III. A detailed description of the results is presented in Paper II.

Computational details

The potential energy curves for the singlet and triplet gerade and ungerade states of the Rb$_2$ molecule corresponding to the seven lowest dissociation limits, $5s+5s$, $5s+5p$, $5s+4d$, $5s+6s$, $5s+6p$, $5p+5p$, and $5s+5d$, have been obtained by a supermolecule method [286]. The calculations employed the recently introduced double electron sttachment intermediate Hamiltonian

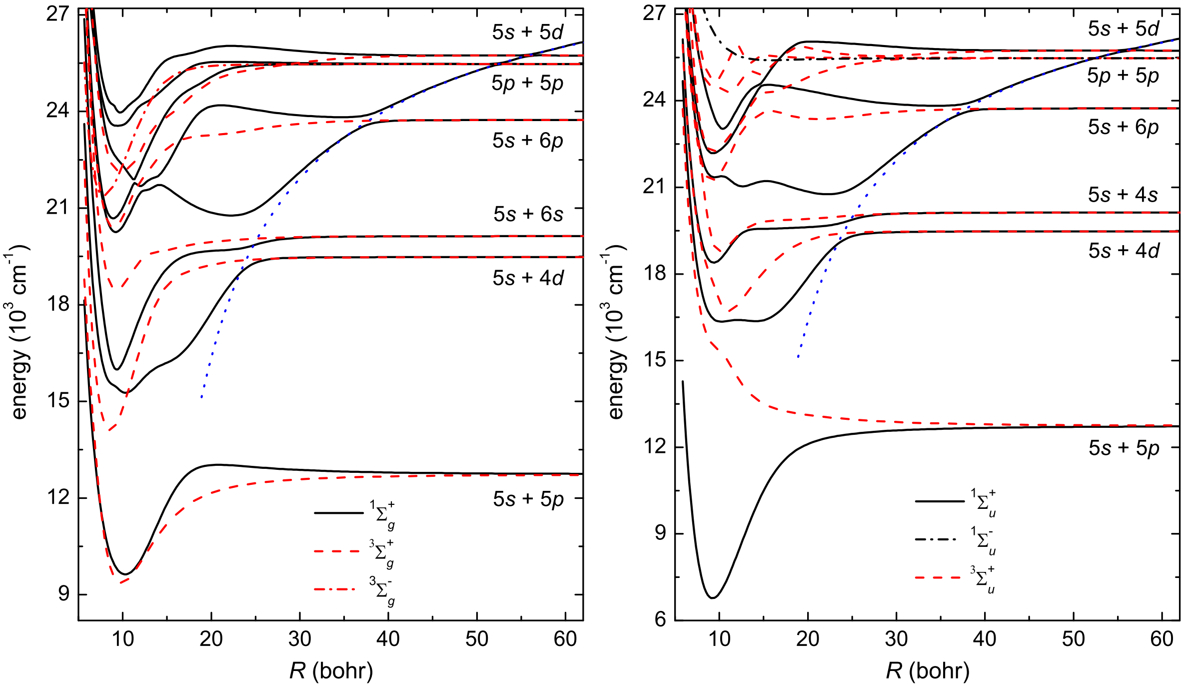

Figure 3.2: Potential energy curves for the $^1\Sigma_g^+$ and $^3\Sigma_g^\pm$ (left panel) and $^1\Sigma_u^\pm$ and $^3\Sigma_u^+$ (right panel) states of the Rb_2 molecule.

Fock space coupled cluster method restricted to single and double excitations (DEA-IH-FS-CCSD) [283, 281, 282]. Starting with the closed-shell reference state for the doubly ionized molecule Rb_2^{2+} that shows the correct dissociation at large interatomic separations R into closed-shell subsystems, Rb^++Rb^+, and using the double electron attachment operators in the Fock space coupled cluster Ansatz makes our method size-consistent at any interatomic separation R and guarantees the correct large-R asymtptotics. The potential energy curves obtained from the *ab initio* calculations were smoothly connected at intermediate interatomic separations with the asymptotic multipole expansion [299]. The C_6 coefficient of the electronic ground state and the C_3 coefficient of the first excited state were fixed at their empirical values [300, 301], while the remaining coefficients were taken from Ref. [302].

Electric transition dipole moments, radial non-adiabatic coupling and spin-orbit coupling matrix elements were obtained by the Multireference Configuration Interaction method (MRCI) restricted to single and double excitations with a large active space. Scalar relativistic effects were included by using the small-core fully relativistic energy-consistent pseudopotential ECP28MDF [303] from the Stuttgart library. Thus, in the present study the Rb_2 molecule was treated as a system of effectively 18 electrons. The $[14s14p7d6f]$ basis set was employed in all calculations. This basis was obtained by decontracting and augmenting the basis set of Ref. [303] by a set of additional functions improving the accuracy of the atomic excitation energies of the rubidium atom with respect to the NIST database [304]. The DEA-IH-FS-CCSD calculations were done with the code based on the Aces II program system [305], while the MRCI calculations were performed with the Molpro code [294].

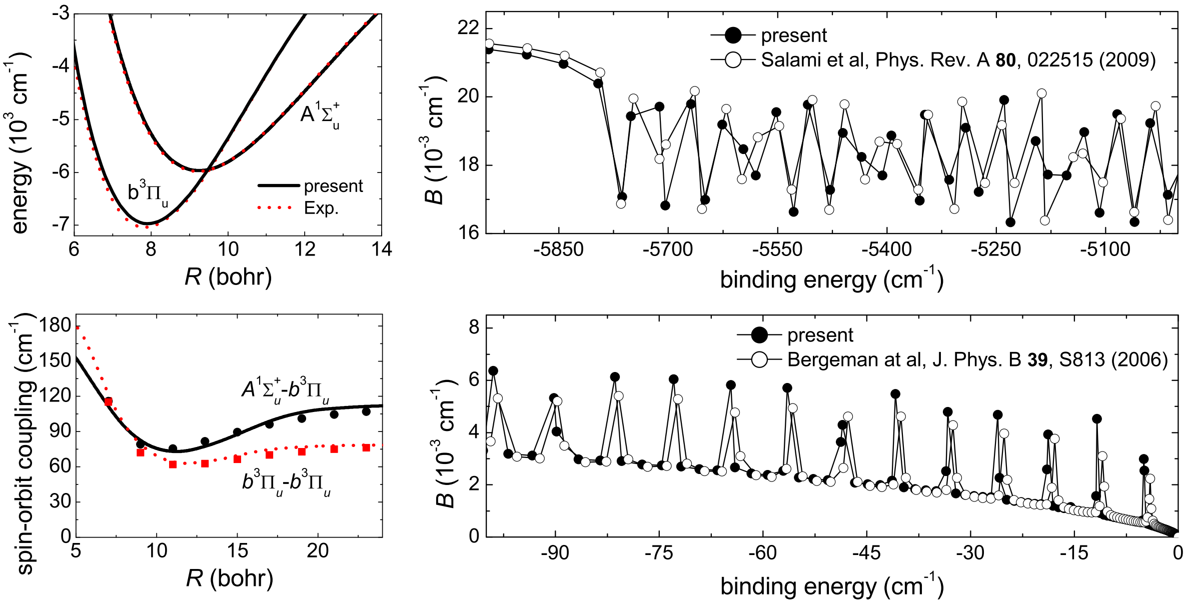

Figure 3.3: Characteristics of the rovibrational levels for the $\Omega = 0_u^+$ component of the coupled $A^1\Sigma_u^+$ and $b^3\Pi_u$ manifold of states in $^{87}Rb_2$: present and empirical potential energy curves [179] (left upper panel), present and empirical spin-orbit coupling [179] (left lower panel), and $j = 1$ rotational constants for strongly bound levels (right upper panel) and close to the dissociation limit (right lower panel).

Numerical results

The computed potential energy curves for the $^1\Sigma_g^+$, $^3\Sigma_g^+$, $^1\Sigma_u^+$, $^3\Sigma_u^+$, $^1\Pi_g$, $^3\Pi_g$, $^1\Pi_u$, $^3\Pi_u$, $^1\Delta_g$, $^3\Delta_g$, $^1\Delta_u$, and $^3\Delta_u$ symmetries are presented in Fig. 1-5 of Paper II. The spectroscopic characteristics of these states are reported in Tables 2-5 of Paper II. Example potential energy curves for sates of Σ symmetry are shown in Fig. 3.2. Inspection of Fig. 1-5 of Paper II reveals that almost all potential energy curves show a smooth behavior with well defined minima. Some higher states display perturbations, mostly in the form of avoided crossings, due to the interaction with other electronic states of the same symmetry that are located nearby. At high energies the density of states becomes so high that the avoided crossings produce some irregularities in the curves.

The agreement of the present potentials with those derived from the experimental data is very good (cf. Fig. 3.3). This is demonstrated in Tables 2-5 of Paper II, where we compare the potential characteristics with the available experimental data and with the most recent calculations [306]. For all the experimentally observed states, the root-mean-square deviation (RMSD) of our calculation is only $75.9\,\text{cm}^{-1}$, i.e., the error is 3.2% on average, better than the most recent calculations by Allouche and Aubert-Frécon [306] with a RMSD of $129\,\text{cm}^{-1}$ corresponding to an average error of 5.5%. It is gratifying to observe that we reproduce low lying and highly excited electronic states equally well. This is in a sharp contrast to Ref. [306] which reproduces the well depth of the $(2)^1\Pi_u$ state only with an error of 12% compared to 3.5% for our calculation.

The importance of the nonadiabatic interactions between electronic states, resulting in the avoided crossings of the corresponding potential energy curves observed in Fig. 1-5 of Paper II, can nicely be explained by analysing the nonadiabatic coupling matrix elements. The nonadiabatic coupling matrix elements are reported in Fig. 6 of Paper II for the singlet and triplet states of Σ_g^+ and Σ_u^+ symmetry (top) and the Π states (bottom). As expected, the nonadiabatic coupling matrix elements are smooth, Lorenzian-type functions, which, in the limit of an inifintely close avoided crossing, become the Dirac δ-function. The height and width of the curve depends on the strength of the interaction. The smaller the width and the larger the peak, the stronger is the interaction between the electronic states, and the corresponding potential energy curves are closer to each other at the avoided crossing.

Rubidium is a heavy atom and the electronic states of the Rb_2 molecule show strong couplings due to the relativistic spin-orbit interaction. Figure 7 of Paper II reports the spin-orbit coupling matrix elements as a function of the interatomic separation. The matrix elements are all represented by smooth curves approaching the atomic limit at large R. The fine splittings of the atomic states are very accurately reproduced by our calculations. For the first excited P state, the theoretical splitting between the 1/2 and 3/2 components is $236.2\,\mathrm{cm}^{-1}$ as compared to $237.6\,\mathrm{cm}^{-1}$ from the experiment. It is also gratifying to observe that our *ab initio* calculations reproduce very well the spin-orbit coupling functions obtained from fitting analytical functions to high-resolution spectroscopic data for the $A^1\Sigma_u^+$ and $b^3\Pi_u$ manifold of states [179], see Fig. 3.3. Figure 3.3 also reports the rotational constants for the deeply bound rovibrational levels and levels at the threshold. Inspection of Fig. 3.3 reveals that theory correctly locates all levels that are not perturbed by the spin-orbit interaction, and the first perturbed level. The overall agreement is very good.

A full characterization of the molecular spectra requires knowledge of the electric transition dipole moments. These were calculated and are presented in Fig. 8 of Paper II for transitions from the $X^1\Sigma_g^+$ ground state (upper panel) and from the $a^3\Sigma_u^+$ lowest triplet state (lower panel). The transition moments do not show a strong dependence on R, except at small interatomic separations, and smoothly tend to their asymptotic atomic value.

The static electric dipole polarizabilities for the $X^1\Sigma_g^+$ electronic ground state, the $a^3\Sigma_u^+$ state, and the relevant excited $A^1\Sigma_u^+$ and $b^3\Pi_u$ states are presented in Fig. 9 of Paper II. They show an overall smooth behavior and also tend smoothly to their asymptotic atomic values. The interaction-induced variation of the polarizability is clearly visible while changing the internuclear distance R. It is significant for excited states, especially for the $A^1\Sigma_u^+$ state for which the isotropic part reaches $8000\,a_0^3$, and the anisotropic part $6000\,a_0^3$. Such large values of the interaction-induced variation of both the isotropic and anisotropic polarizabilities suggest that the influence of the non-resonant laser field on the rovibrational dynamics and transitions between the ground $X^1\Sigma_g^+$ state, and the $A^1\Sigma_u^+$ and $b^3\Pi_u$ states should be significant even at relatively weak field intensities.

3.5 LiYb$^+$ molecular ion

In this section we present the results of the electronic structure calculations for the ground and excited states of the LiYb$^+$ molecular ion. This work is motivated by the ongoing experiment in the group of prof. Rene Gerritsma at the University of Mainz aiming at building quantum simulator emulating solid-state physics with a hybrid system of ultracold ions and atoms [271, 272]. *Ab initio* data will be employed in the scattering and photoassociation calculations discussed in Chapter 4.2.

Computational details

The potential energy curve for the $X^1\Sigma^+$ ground electronic state have been obtained with the coupled cluster method restricted to single, double, and noniterative triple excitations method, CCSD(T) [281]. Curves for the first states in the $^3\Sigma$ and $^3\Pi$ symmetries were obtained with the spin-restricted coupled cluster method restricted to single, double, and noniterative triple excitations method, RCCSD(T) [307]. Calculations on all other excited states employed the linear response theory (equation of motion) within the coupled cluster singles, doubles, and linear triples framework, LRCC3 [308, 309]. The basis set superposition error was eliminated by using the counterpoise correction of Boys and Bernardi [286]. The CCSD(T) and RCCSD(T) calculations were performed with the MOLPRO suite of codes [294], while LRCC3 calculations were done with DALTON program [289].

The lithium atom was described with the augmented core-valence correlation consistent polarized Valence Quadrupole-ζ quality basis sets, aug-cc-pCVQZ. The ytterbium atom was described by the fully relativistic small-core energy consistent pseudopotential, ECPMDF28 [297], and associated basis set $(15s14p12d11f8g)/[8s8p7d7f5g]$. Due to the less efficient numerical code for the LRCC3 method it was not computationally feasible to carry out calculations for excited states correlating all electron included in the model and using the large basis set therefore in these calculations core electrons were frozen and only 12 outer-shells electrons were correlated.

The long-range asymptotics of the interaction between an S-state ion A^+ and an S-state atom B is given by $-\frac{C_4^{\text{ind}}}{R^4}-\frac{C_6^{\text{ind}}}{R^6}-\frac{C_6^{\text{disp}}}{R^6}+\dots$, where the leading long-range induction coefficients $C_4^{\text{ind}}=\frac{1}{2}\alpha_B$ and $C_6^{\text{ind}}=\frac{1}{2}\beta_B$, and dispersion one $C_6^{\text{disp}}=\frac{3}{\pi}\int_0^\infty \alpha_{A^+}(i\omega)\alpha_B(i\omega)d\omega$, where α_B is the static electric dipole polarizability of neutral atom B, β_B is the electric quadrupole polarizability of neutral atom B, and $\alpha_X(i\omega)$ is the dynamic polarizbility of atom X at imaginary frequency.

The dynamic polarizability at imaginary frequency of the Yb atom and the Li ion were obtained by using the explicitly connected representation of the expectation value and polarization propagator within the coupled cluster method [292] and the best approximation XCCSD4 proposed by Korona and collaborators [293]. The dynamic polarizability at imaginary frequency of the Li atom was taken from the work by Derevianko et al. [310] and the dynamic polarizbility of

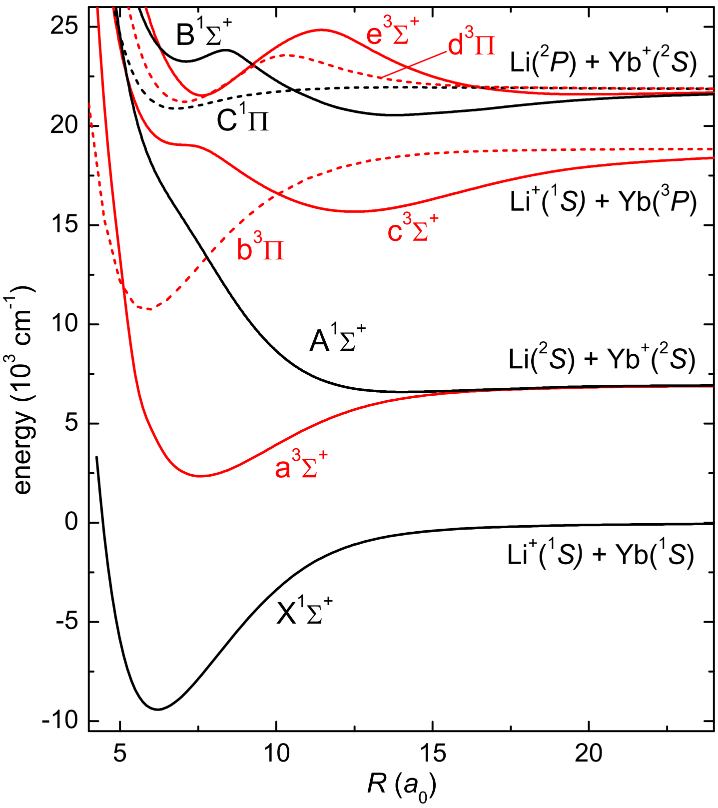

Figure 3.4: Non-relativistic potential energy curves of the (LiYb)$^+$ molecular ion.

Yb ion was obtained as a sum over states using transition moments from the work by Safronova and Safronova [311]. The static quadruple polarizabilities of the Li and Yb atoms were taken from accurate atomic calculations reported in Ref. [312] and Ref. [313], respectively.

Numerical results

The potential energy curves for the ground and excited stats of (LiYb)$^+$ molecular ion are presented in Fig. 3.4 and the spectroscopic characteristics are reported in Table 3.1. The transition electric dipole moments are plotted in Fig. 3.5. The leading long-range coefficients for the dispersion and induction interactions between the Li$^+$ ion and the Yb atom and between the Yb$^+$ ion and the Li atom, all in the ground electronic state, are reported in Table 3.2.

The interaction of the ground-state Li$^+$ ion with the ground-state ytterbium atom results in single $X^1\Sigma^+$ electronic ground state of LiYb$^+$ molecular ion. The interaction between ion and atom is dominated by the induction contribution that results in the large binding energy of 9412 cm^{-1} with the equalibrium distance equal to 6.2 bohr. The interaction of the ground-state Yb$^+$ ion with the ground-state lithium atom, which both are open-shell, results in the two electronic states $a^3\Sigma^+$ and $A^1\Sigma^+$. The triplet state is strongly bound with binding energy equal to 4609 cm^{-1} whereas the singlet potential is weakly bound by only 358 cm^{-1}. The large biding energy of the triplet state as compared to the singlet state can be rationalized by looking at the molecular orbitals picture where the triplet state is stabilized by the admixture of the

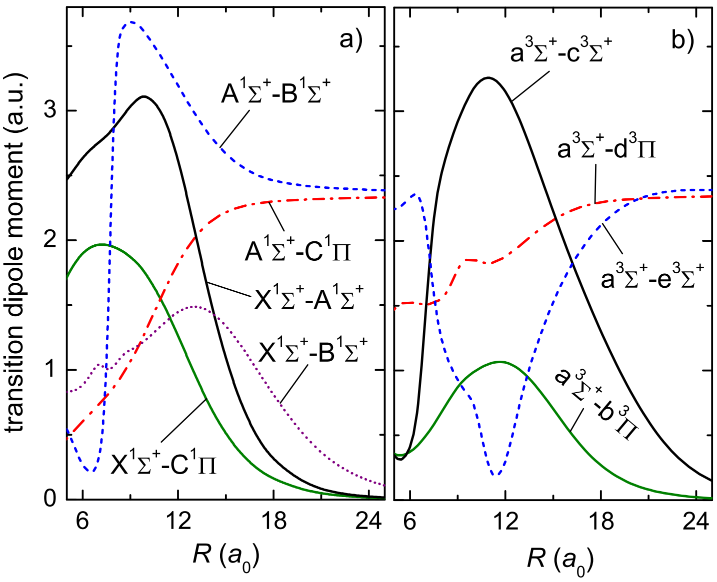

Figure 3.5: Transition electric dipole moments between singlet (a) and triplet (b) states of the (LiYb)$^+$ molecular ion.

Table 3.1: Spectroscopic characteristics: equilibrium bond length R_e, well depth D_e, harmonic constant ω_0, and rotrational constant B_0 (for ^{7}Li^{172}Yb) of the electronic states of the (LiYb)$^+$ molecular ion.

State	R_e (bohr)	D_e (cm^{-1})	ω_0 (cm^{-1})	B_0 (cm^{-1})
		Li$^+$(^1S)+Yb(^1S):		
$X^1\Sigma^+$	6.20	9412	231	0.23
		Li(^1S)+Yb$^+$(^2S):		
$A^1\Sigma^+$	14.04	358	37.1	0.045
$a^3\Sigma^+$	7.59	4609	140	0.16
		Li$^+$(^1S)+Yb(^3P):		
$b^3\Pi$	5.83	8130	232	0.26
$c^3\Sigma^+$	12.46	3177	60.9	0.057
		Li(^2P)+Yb$^+$(^2S):		
$B^1\Sigma^+$	14.02	1332	50.1	0.045
$C^1\Pi$	6.71	1025	138	0.20
$e^3\Pi$	7.05	640	170	0.18
$d^3\Sigma^+$	7.56	426	218	0.16
$d^3\Sigma^+$	19.93	267	24.4	0.022

antibonding orbital correlated with the lowest asymptote.

The experimental proposals consider emerging the ytterbium ion into a gas of ultracold lithium atoms. The electronic states corresponding with their interaction are well separated from all other electronic states. This means that the potential losses due to reactive collisions should be smaller than in case of ultracold collisions of the Ba$^+$ ion with ultracold Rb atoms [314, 270].

Table 3.2: The induction and dispersion coefficients describing the long-range part of the interaction potential between the Li ion and the Yb atom and between the Yb ion and the Li atom, all in the ground electronic state.

System	C_4^{ind} (a.u.)	C_6^{ind} (a.u.)	C_6^{disp} (a.u.)
Li^++Yb	72.0	1280	6.4
Yb^++Li	82.1	711.7	711

3.6 $^2\Sigma$ molecules

In this section we present the results of the electronic structure calculations for the electronic ground state of the $^2\Sigma$ molecules such as RbSr, LiYb, RbYb, and CsYb. This work was motivated by the ongoing experiments in many groups working on the mixtures of open-shell alkali-metal and closed-shell alkali-earth-metal or ytterbium atoms [315, 316, 317, 104, 318, 268]. *Ab initio* data will be employed in the investigation of the control of magnetic Feshbach resonances with non-resonant laser field in Chapter 6.3 and Paper IV.

Computational details

The potential energy curve for the $X^2\Sigma^+$ ground electronic state have been obtained with the spin restricted open-shell coupled cluster method restricted to single, double, and noniterative triple excitations, RCCSD(T) [307]. The scalar relativistic effects were included within small-core energy-consistent pseudopotentials, ECP. The basis set superposition error was eliminated by using the counterpoise correction of Boys and Bernardi [286]. The permanent electric dipole moments and parallel and perpendicular components of static electric dipole polarizabilities were computed with the finite field technique.

The Rb, Sr, and Yb atoms were described with the ECP28MDF pseudopotentials [303, 297, 319] and $[14s14p7d6f]$ [276], $[14s11p6d5f4g]$ [320], $[15s14p12d11f8g]$ [319] basis sets, respectively. The Cs atom was described with the ECP46MDF pseudopotential and $[12s11p6d4f2g]$ basis set [303]. The Li atom was described with the augmented correlation consistent polarized Valence Quadrupole-ζ quality basis sets, aug-cc-pVQZ [321].

All calculations were performed with the MOLPRO package of *ab initio* programs [294].

Numerical results

Potential energy curves, permanent electric dipole moments, averaged and anisotropic static electric dipole polarizabilities of the LiYb, RbSr, RbYb, and CsYb molecules are presented in Fig. 3.6.

The ground state interaction between an alkali-metal atom and a closed-shell atom is of a Van der Waals character with a binding energy ranging from 712 cm^{-1} for CsYb to 1748 cm^{-1} for LiYb, and with the corresponding equilibrium distances between 9.35 bohr and 8.83 bohr for CsYb and LiYb, respectively.

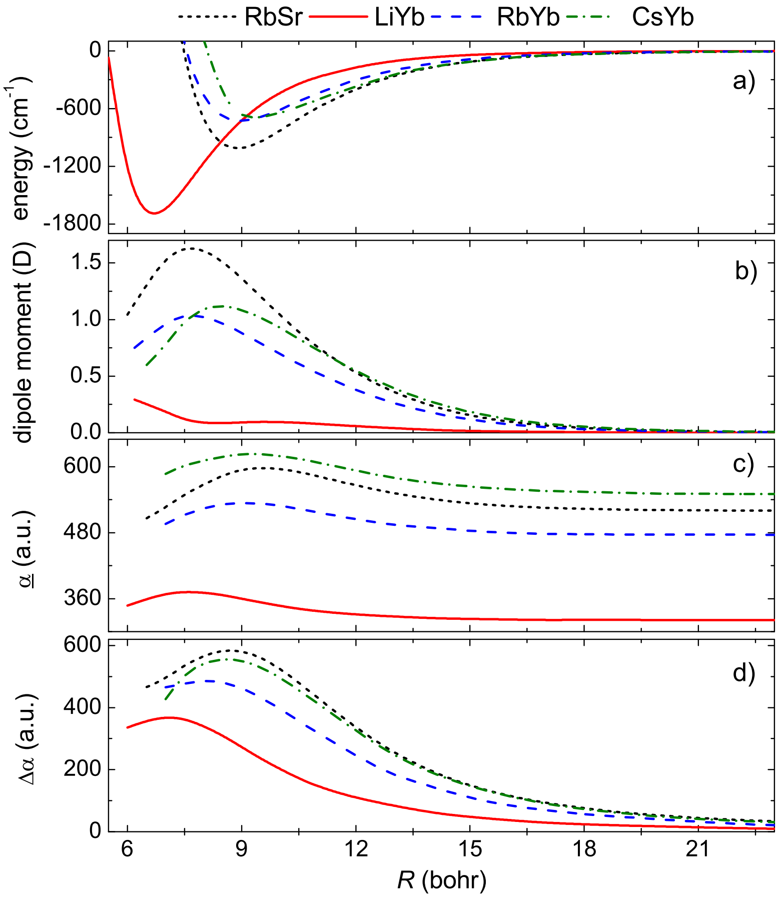

Figure 3.6: Potential energy curves (a), permanent electric dipole moments (b), trace (c) and anisotropy (d) of the static electric dipole polarizabilities of the LiYb, RbSr, RbYb, and CsYb molecules in the $X^2\Sigma^+$ electronic ground state.

The permanent electric dipole moment of the LiYb molecule is very small. Thus, the use of a static electric field to control dynamics of this molecule will not be efficient. The permanent electric dipole moments of other investigate a $^2\Sigma$ molecules take values around 1 Debye for the rovibrational ground state.

The interaction-induced variation of the static electric dipole polarizabilities for all investigated $^2\Sigma$ molecules is clearly visible with the polarizability anisotropy for the rovibrational ground state around 400-600 a.u. that should allow for an easy non-resonant light control.

3.7 Cr–closed-shell-atom molecules

In this section we propose a new class of highly magnetic and polar molecules consisting of the chromium and closed-shell alkali-earth-metal or ytterbium atoms and investigate properties of their electronic ground states. The molecules under investigation possess both large magnetic and electric dipole moments that makes them potentially interesting candidates for the studies of ultracold many-body dynamics in combined external electric and magnetic fields. A detailed description of the results is presented in Paper V.

Computational details

The chromium–closed-shell-atom molecules are open-shell, therefore we have calculated the corresponding potential energy curves in the Born-Oppenheimer approximation with the spin restricted open-shell coupled cluster method restricted to single, double, and noniterative triple excitations, RCCSD(T) [307]. The interaction energies have been obtained with the supermolecule method and the basis set superposition error was corrected [286]. The permanent electric dipole moments and static electric dipole polarizabilities were calculated with the finite field technique.

The scalar relativistic effects in the calculations for the CrBe, CrMg, and CrCa molecules were included by employing the second order Douglas-Kroll-Hess (DKH) Hamiltonian [322], whereas for the CrSr, CrBa, and CrYb molecules the relativistic effects were accounted for by using small-core fully relativistic energy-consistent pseudopotentials (ECP) to replace the inner-shell electrons [285]. We used the pseudopotentials to introduce the relativistic effects for heavier molecules instead of using the Douglas-Kroll-Hess Hamiltonian, because it allowed to use larger basis sets to describe the valence electrons and model the inner-shells electrons density as accurately as in the high quality atomic calculations used to fit the pseudopotentials.

In all calculations for the CrBe, CrMg, and CrCa molecules the augmented correlation consistent polarized valence quintuple-ζ quality basis sets, aug-cc-pV5Z, were used. The Be and Cr atoms were described with the aug-cc-pV5Z-DK basis sets [323], whereas for the Mg and Ca atoms, the cc-pV5Z-DK and cc-pV5Z basis sets [324], respectively, were augmented at first. In all calculations for CrSr, CrBa, and CrYb the pseudopotentials from the Stuttgart library were employed. The Cr atom was described by the ECP10MDF pseudopotential [325] and the $[14s13p10d5f4g3h]$ basis set with coefficients taken from the aug-cc-pVQZ-DK basis [323]. The Sr atom was described with the ECP28MDF pseudopotential [297] and the $[14s11p6d5f4g]$ basis set obtained by augmenting the basis set suggested in Ref. [297]. The Ba atom was described with the ECP46MDF pseudopotential [297] and the $[13s12p6d5f4g]$ basis set obtained by augmenting the basis set suggested in Ref. [297]. The Yb atom was described with the ECP28MDF pseudopotential [319] and the $[15s14p12d11f8g]$ basis set [319]. In all calculations the basis sets were augmented by the set of $[3s3p2d1f1g]$ bond functions [326].

The leading long-range dispersion coefficients C_6 were calculated as the integral over the dynamic polarizabilities of the interacting atoms at imaginary frequencies which for the alkali-earth-metal atoms were taken from the work by Derevianko et al. [310], whereas the dynamic polarizability of the ytterbium atom was obtained by using the explicitly connected representation of the expectation value and polarization propagator within the coupled cluster method [292] and the best approximation XCCSD4 proposed by Korona and collaborators [293]. The dynamic polarizability of the chromium atom was constructed from the sum over states expression. The oscillator strengths and energy levels for the discrete transitions were taken from the NIST Atomic Spectra Database [304], whereas the contribution form the bound-continuum transitions were included as a sum over oscillator strengths to quasi-bound states obtained within

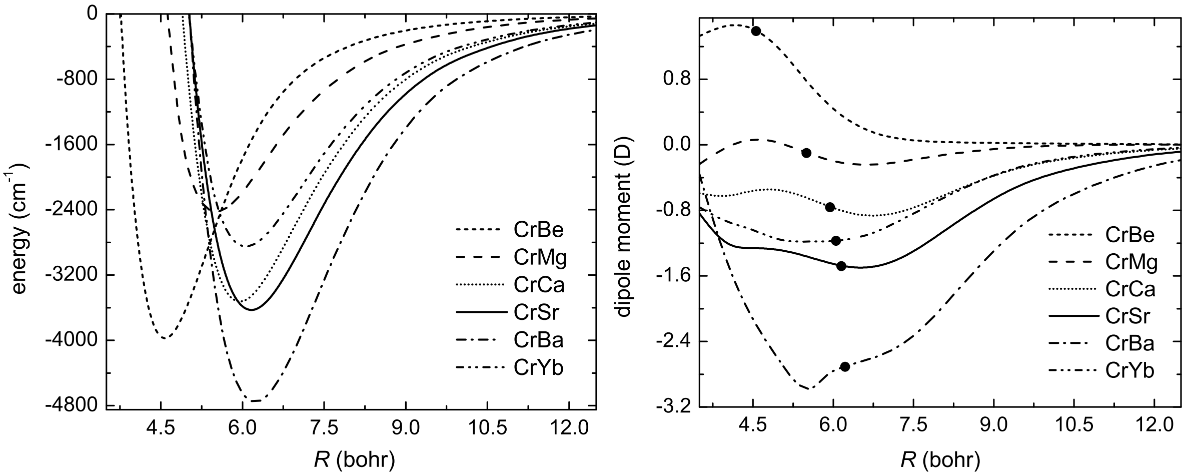

Figure 3.7: Potential energy curves of the $X^7\Sigma^+$ electronic ground state of the CrBe, CrMg, CrCa, CrSr, CrBa, and CrYb molecules (left panel) and permanent electric dipole moments of the $X^7\Sigma^+$ electronic ground state of the same molecules. Points indicate the values for the ground rovibrational level (right panel).

the multireference configuration interaction method.

All calculations were performed with the MOLPRO package of *ab initio* programs [294].

Numerical results

The computed potential energy curves of the $X^7\Sigma^+$ electronic ground state and the permanent electric dipole moments as functions of the interatomic distance for the CrBe, CrMg, CrCa, CrSr, CrBa, and CrYb molecules are presented in Fig. 3.7. The corresponding long-range C_6 coefficients, equilibrium distances, R_e, well depths, D_e, and values of the permanent electric dipole moments for the ground rovibrational level are reported in Table 1 of Paper V. The average polarizability and the polarizability anisotropy of the electronic ground state of the investigated molecules are presented in Fig. 3 of Paper V and the values for the ground rovibrational level are reported in Table 1 of Paper V.

The well depths of the chromium–alkaline-earth-metal-atom and chromium–ytterbium molecules are significantly larger than those of the Van der Waals type homonuclear alkaline-earth-metal-atom [327, 277, 328] or ytterbium molecules [329]. The largest dissociation energy is 4723 cm^{-1} for the CrBa molecule and the smallest one is 2371 cm^{-1} for the CrMg molecule. The equilibrium distances range from 4.56 bohr for the CrBe molecule up to 6.22 bohr for the CrBa molecule. We have found that the CrBa molecule has the largest electric dipole moment in the rovibrational ground state, 2.67 D, only slightly smaller than the CrRb molecule with 2.9 D [330]. However, the CrSr and CrYb molecules have also significant dipole moments, 1.48 D and 1.19 D, respectively. Since the cooling techniques for the Sr and Yb atoms are much better established, the CrSr and CrYb molecules should in first place be considered as candidates for ultracold molecules with large both magnetic and electric dipole moments.

The investigated molecules have both significant magnetic and electric dipole moments. To get a good understanding of their collisional properties at ultralow temperatures and the interplay between the electric dipole-dipole, magnetic dipole-dipole, and long-range dispersion interactions, the characteristic energy and length scales are analyzed in Section III.D of Paper V. The intermolecular magnetic dipole-dipole interaction should affect the properties of an ultracold gas of heavy molecules containing chromium atom to a larger extent than it was observed for the ultracold gas of atomic chromium [cf. Fig. 4 of Paper V] and a competition between the magnetic and electric dipolar interactions should be an interesting problem in ultracold many-body physics.

3.8 $^3\Sigma$ alkali-metal molecules

In the present section we summarize the results of the electronic structure calculations of the potential energy for the binary interactions of polar alkali dimers AB($a^3\Sigma^+$) in the quintet state of the bimolecular complex. The creation of polar alkali dimers in the rovibrational ground state of the $a^3\Sigma^+$ electronic state [91] is currently emerging as an important research goal. Heteronuclear molecules in the $a^3\Sigma^+$ state have both the electric and magnetic dipole moments. However, alkali dimers in the $a^3\Sigma^+$ state may undergo inelastic collisions and chemical reactions necessitating the use of an optical lattice to segregate the molecules and suppress losses [142]. The main goal is to explore the possibility of reaction barriers that would prevent molecules from reaching the short-range interaction region. A detailed description of the results is presented in Paper VI.

Computational details

The potential energy surfaces have been calculated with the spin restricted open-shell coupled cluster method restricted to single, double, and noniterative triple excitations, RCCSD(T) [307]. The Li and Na atoms were described with the augmented core-valence correlation consistent polarized valence triple-ζ atomic basis sets (aug-cc-pCVTZ) and the H atom with the augmented correlation consistent polarized valence quadruple-ζ atomic basis sets (aug-cc-pVQZ) [321]. The relativistic effects in the heavier alkali atoms were accounted for with the fully relativistic small-core energy consistent pseudopotentials ECP28MDF for Rb and ECP46MDF for Cs and the corresponding basis sets $(13s10p5d3f)/[8s7p5d3f]$ and $(12s11p6d4f)/[8s8p6d4f]$ [303]. The basis set superposition error was eliminated by using the counterpoise correction of Boys and Bernardi [286]. All electronic structure calculations were performed with the MOLPRO package of *ab initio* programs [294].

In order to prove the absence of barriers in the reactions

$$\mathrm{A}B(a^3\Sigma^+) + \mathrm{A}B(a^3\Sigma^+) \;\to\; \mathrm{A}_2(a^3\Sigma^+) + \mathrm{B}_2(a^3\Sigma^+) \tag{3.4}$$

$$\mathrm{A}B(a^3\Sigma^+) + \mathrm{A}B(a^3\Sigma^+) \;\to\; \mathrm{A}_2\mathrm{B} + \mathrm{B} \tag{3.5}$$

we calculated the potential energy of the four-atom complex along the minimum energy path of the reaction (3.4). The calculations were performed in two steps. First, the minimum energy path was found by optimizing the geometries of the reaction complexes with the spin restricted open-shell coupled cluster method including single and double excitations (RCCSD), and basis sets as described above but truncated to s, p and d orbitals only. We defined the intermolecular coordinates R_1 and R_2 that specify the separation between the geometric centers of the heteronuclear molecules and the separations between the centers of the homonuclear molecules, respectively. The geometries were optimized at 20 values of R_1 and R_2 between the position of the global minimum and 40 bohr by varying all other degrees of freedom. In the second step, the interaction energies for the optimized geometries were calculated using the more accurate RCCSD(T) method and the full basis sets. For a few points we optimized the geometry with the full basis sets and the RCCSD(T) method and found that using the smaller basis set and the lower level of theory introduces negligible errors in the optimized geometry parameters but significantly underestimates the interaction energy.

We computed the dipole moments for the alkali dimers in the $a^3\Sigma^+$ state using the RCCSD(T) approach with the aug-cc-pCVQZ basis for Na and Li, the aug-cc-pVQZ basis for H, and the small-core fully relativistic pseudopotentials ECPnMDF [303] and large basis sets for K [$11s11p5d3f$], Rb [$14s14p7d6f1g$] and Cs [$12s11p5d3f2g$].

Numerical results

It is known from the previous calculations [331, 332, 333, 334] that the potential energy of alkali trimers is dominated by the non-additive interactions. The same should be expected for the interaction of four alkali atoms. However, unlike in the atom-diatom case, reaction between molecules involves the dissociation of two molecular bonds. The dissociation energy of these bonds may be expected to give rise to reaction barriers. We have found no such barriers, meaning that the reaction (3.4), if energetically allowed, and reaction (3.5) should be very fast at ultralow temperatures. Our calculations show that the non-additive three- and four-body interactions are much stronger than the binding energy of alkali dimers in the $a^3\Sigma^+$ state.

Figure 3.8 presents the results of the calculations for the reactive interactions of the LiNa, LiCs and RbCs molecules. These molecules represent three limiting cases of polar alkali metal dimers from the lightest and most compact molecule to the most polar and the heaviest. The four-body reactions are clearly barrierless and proceed through the formation of a stable reaction complex corresponding to the deep global minimum of the interaction potential surface. The reaction complex has a tetrahedral geometry as shown in Fig. 3.8. The deep minimum of the potential energy is the manifestation of the non-additive forces in a four-body complex (see inset of Fig. 3.8).

While there are no reaction barriers to prevent the reactions (3.4) - (3.5), some of the reaction channels may be energetically closed. The relative energies for the reactants and products for reactions (3.4) and (3.5) are summarized in Tables 1 and 2 of Paper VI. The

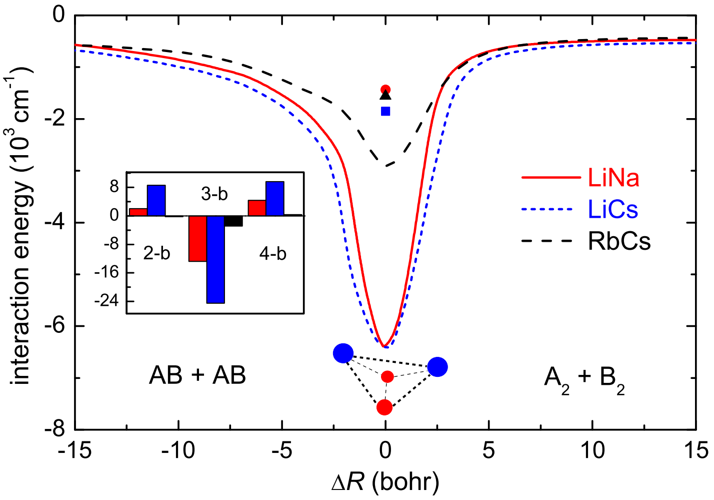

Figure 3.8: The minimum energy path of the adiabatic reaction for the LiCs-LiCs, LiNa-LiNa, and RbCs-RbCs reaction complexes in the quintet spin state from the optimized geometry calculations. $\Delta R = (R_{AB} + R_{AB})/2 - (R_{AA} + R_{BB})/2$, where R_{AB} is the separation between the atoms A and B. The interaction energy equal to zero corresponds with all atoms dissociated. The symbols show the most negative values of the potential energy that can be obtained by adding binding energies of the dimers: ● - Li_2Na_2, ▲ - Rb_2Cs_2, ■ - Li_2Cs_2.The inset shows the decomposition of the interaction energy for the reaction complexes at the minimum energy geometry into 2-, 3-, and 4-body contributions.

reaction (3.4) is endothermic, and thus forbidden at ultralow temperatures, only for KRb. The change of energy in the reaction (3.4) is very small for any combination of alkali dimers. This suggests that the former is bound to form diatomic molecules in the ground vibrational state and the latter can be stimulated by vibrational excitation of the reactants. Given that the reaction (3.4) combines polar species to form non-polar products, the probability of this reaction must be sensitive to external electric fields. Table 2 of Paper VI shows that the reaction (3.5) is exothermic for all combinations of molecules. In combination with the results of Fig. 3.8, this means that all alkali dimers in the $a^3\Sigma^+$ state are chemically reactive at ultralow temperatures and can be used for practical applications only if protected from binary collisions by segregation in an optical lattice [335] or if confined in a quasi-two-dimensional potential with their electric dipoles oriented parallel and perpendicular to the plane of confinement.

The magnitude of the permanent dipole moments is a figure of merit for experiments with molecules in optical lattices therefore we have computed the dipole moments for the alkali-metal dimers in the $a^3\Sigma^+$ state. The results are presented and discussed in Fig. 3 and Table IV of Paper VI.

Chapter 4

Formation of ultracold molecules by cw photoassociation

4.1 Introductory remarks

The one-photon photoassociation with continuous wave laser and magnetoassociation within magnetically tunable Feshbach resonance presented in Chapter 1.2 as well as magnetoassociation with subsequent transfer to deeply bound levels by stimulated Raman adiabatic passage described in Chapter 1.3 are at present the standard methods of formation of molecules at ultralow temperatures. However, the efficiency of the direct cw-laser photoassociation can be small due to small probability of finding the colliding atoms at short internuclear distance. At the same time, the Feshbach resonances with large width convenient for magnetoassociation are present only in the mixtures of open-shell atoms such as alkali-metal atoms. Nevertheless, recently there has been an increased interest in the study of ultracold mixtures of closed-shell atoms such as alkaline-earth-metal and ytterbium atoms and mixtures of open-shell and closed-shell atoms.

The ultracold hybrid system of ultracold atoms and ions attract currently more and more attention emerging as another important research subject with many potential applications in many-body physics and quantum simulations. These interests give rise to the need for the detailed microscopic description of the ultracold ion-atom collisions on the one hand, and creates the possibility of the formation and applications of ultracold molecular ions, a new species in the field of ultracold matter on the other hand.

The new challenges described above and experimental proposals cause that the standard methods of the formation of ultracold molecules have to be revisited while applied to non-standard systems such as ultracold mixtures of closed-shell atoms or hybrid systems of atoms and ions. In this chapter we present results of the investigation of the formation of ultracold ground-state SrYb molecules by cw-laser photoassociation of ultracold strontium and ytterbium atoms and the formation of ultracold LiYb$^+$ molecular ions by both cw-laser photoassociation of cold ytterbium ions emerged into ultracold gas of lithium atoms.

4.2 Formation of ultracold SrYb molecules in an optical lattice by photoassociation spectroscopy

In this section we present the results on the photoassociative formation of SrYb molecules in their electronic ground state using transitions near an intercombination line. The dynamical calculations are based on the *ab initio* electronic structure presented in Chapter 3.3. This work is motivated by the experiment aiming on building molecular clock for precision measurements planed in the group of prof. Tanya Zelevinsky at the University of Columbia. A detailed description of the results is presented in Paper I.

Theoretical model

Photoassociation is considered for a continuous-wave laser that is red-detuned with respect to the intercombination line. This transition is dipole-forbidden. However, the $a^3\Pi$ state correlating to the asymptote of the intercombination line transition, cf. Fig. 4.1, is coupled by spin-orbit interaction to two singlet states, $A^1\Pi$ and $C^1\Pi$, that are connected by a dipole-allowed transition to the ground electronic state, $X^1\Sigma^+$. Thus an effective transition matrix element is created which can be written, to a very good approximation, as

$$d_{SO}(R) = \frac{\langle X^1\Sigma^+|\hat{\mathbf{d}}|C^1\Pi\rangle\langle C^1\Pi|\hat{\mathbf{H}}_{SO}|a^3\Pi\rangle}{E_{a^3\Pi} - E_{C^1\Pi}} + \frac{\langle X^1\Sigma^+|\hat{\mathbf{d}}|A^1\Pi\rangle\langle A^1\Pi|\hat{\mathbf{H}}_{SO}|a^3\Pi\rangle}{E_{a^3\Pi} - E_{A^1\Pi}}\,, \tag{4.1}$$

where $\hat{\mathbf{H}}_{SO}$ is the spin-orbit Hamiltonian in the Breit-Pauli approximation [295]. The long-range part of $d_{SO}(R)$, dominated by the first term in the above expression, is due to the coupling with the $C^1\Pi$ state, ideally suited for photoassociation. The short-range part is due to the coupling with the $A^1\Pi$ state, paving the way towards an efficient stabilization of the photoassociated molecules to the electronic ground state. The $a^3\Pi$ state, in addition to the spin-orbit coupling with the two singlet states, is also coupled to the $b^3\Sigma^+$ state correlating to the same asymptote, Sr(^3P)+Yb(^1S). In the rotating-wave approximation the Hamiltonian describing these couplings yielding the Hund's case (c) $\Omega = 1$ states reads

$$\hat{\mathbf{H}} = \begin{pmatrix} \hat{\mathbf{H}}^{X^1\Sigma^+} & 0 & 0 & \frac{1}{2}d_1(R)E_0 & \frac{1}{2}d_2(R)E_0 \\ 0 & \hat{\mathbf{H}}^{a^3\Pi} & \xi_1(R) & \xi_2(R) & \xi_4(R) \\ 0 & \xi_1(R) & \hat{\mathbf{H}}^{b^3\Sigma^+} & \xi_3(R) & \xi_5(R) \\ \frac{1}{2}d_1(R)E_0 & \xi_2(R) & \xi_3(R) & \hat{\mathbf{H}}^{A^1\Pi} & 0 \\ \frac{1}{2}d_2(R)E_0 & \xi_4(R) & \xi_5(R) & 0 & \hat{\mathbf{H}}^{C^1\Pi} \end{pmatrix}\,, \tag{4.2}$$

where $\hat{\mathbf{H}}^{2S+1|\Lambda|}$ is the Hamiltonian for nuclear motion in the $^{2S+1}|\Lambda|$ electronic state, $\hat{\mathbf{H}}^{2S+1|\Lambda|} = \hat{\mathbf{T}} + V^{2S+1|\Lambda|}(R) + V_{\text{trap}}^{2S+1|\Lambda|}(R) - (1-\delta_{n0})\hbar\omega_L$. The kinetic energy operator is given by $\hat{\mathbf{T}} =$

$\hat{\mathbf{P}}^2/2\mu$ with μ the reduced mass of SrYb. The trapping potential, $V_{\text{trap}}^{2S+1|\Lambda|}(R)$, is relevant only in the electronic ground state for the detunings considered below, even for large trapping frequencies. We approximate it by a harmonic potential which is well justified for atoms cooled down to the lowest trap states and corresponds to the radial confinement in a 3D optical lattice. The parameters of the photoassociation laser are the frequency, ω_L, and the maximum field amplitude, E_0. The electric transition dipole moments are denoted by $d_1(R) = \langle X^1\Sigma^+|\hat{\mathbf{d}}|A^1\Pi\rangle$, $d_2(R) = \langle X^1\Sigma^+|\hat{\mathbf{d}}|C^1\Pi\rangle$, and the matrix elements of the spin-orbit coupling are given by $\xi_i(R)$. The Hamiltonian (4.2) has been represented on a Fourier grid with adaptive step size [336, 337, 338].

Results

The key idea of photoassociation using a continuous-wave laser is to excite a colliding pair of atoms into a bound level of an electronically excited state [339, 23]. For maximum photoassociation efficiency, the detuning of the laser with respect to the atomic asymptote, in our case Sr($^3P_1$)+Yb(^1S), is chosen to coincide with the binding energy of one of the vibrational levels in the electronically excited state. Fig. 5 of Paper I shows two such levels with binding energies $E_b = 5.1\,\text{cm}^{-1}$ (left) and $E_b = 18.9\,\text{cm}^{-1}$ (right). Since four electronically excited states are coupled by the spin-orbit interaction, the vibrational wave functions have components on all four electronically excited states, shown in Fig. 6 (top) of Paper I. The vibrational level with binding energy $E_b = 5.1\,\text{cm}^{-1}$ is predominantly of triplet character, while the vibrational level with binding energy $E_b = 18.9\,\text{cm}^{-1}$ shows a truly mixed character. The fact that multiple classical turning points are clearly visible in the vibrational wavefunction with $E_b = 18.9\,\text{cm}^{-1}$ reflects the resonant nature of the spin-orbit coupling of this level. Such a structure of the vibrational wavefunctions was shown to be ideally suited for efficient stabilization of the photoassociated molecules into deeply bound levels in the ground electronic state [340, 341, 342, 343].

In view of the formation of deeply bound molecules in their electronic ground state, it might be advantageous to choose the larger detuning of $18.9\,\text{cm}^{-1}$ despite the photoassociation probability being smaller by about a factor of 6 compared to a detuning of $5.1\,\text{cm}^{-1}$. This becomes evident by inspecting Fig. 8 of Paper I which displays the bound-to-bound transition matrix elements between the two electronically excited vibrational wavefunctions with $E_b = 5.1\,\text{cm}^{-1}$ and $E_b = 18.9\,\text{cm}^{-1}$ and all bound levels of the $X^1\Sigma^+$ electronic ground state. These transition matrix elements govern the branching ratios for spontaneous decay of the photoassociated molecules. While the excited state vibrational level with $E_b = 5.1\,\text{cm}^{-1}$ has its largest transition dipole matrix elements with the last bound levels of the $X^1\Sigma^+$ ground electronic state that are only weakly bound, a striking difference is observed for the excited state vibrational wavefunction with $E_b = 18.9\,\text{cm}^{-1}$. The strong singlet-triplet mixing of this level, in particular the pronounced peak near the outer classical turning point of the $A^1\Pi$ state, cf. Fig. 5 of Paper I, leads to significantly stronger transition dipole matrix elements with deeply bound levels of the $X^1\Sigma^+$ ground electronic state for $v' = -18$ compared to $v' = -11$, the one with $v'' = 1$ being

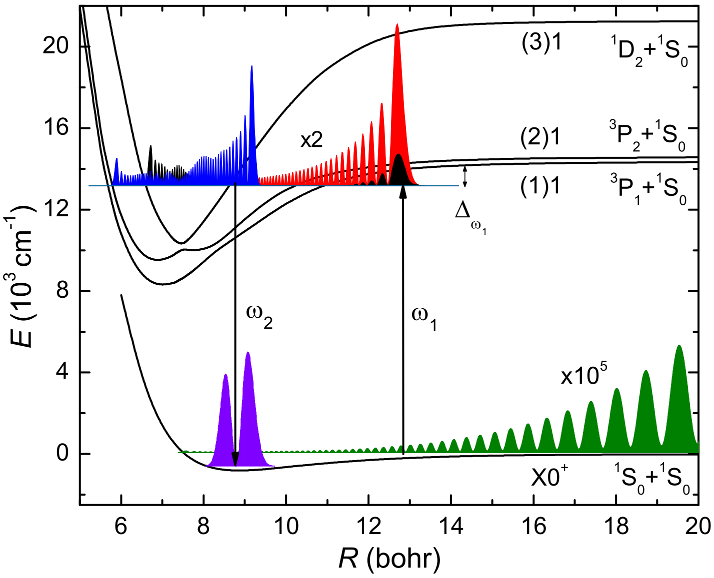

Figure 4.1: Proposed scheme for the formation of ground state SrYb molecules via photoassociation near the intercombination line transition with detuning $\Delta_{\omega_L} = 18.9\,\mathrm{cm}^{-1}$ ($\nu_{\mathrm{trap}} = 100\,\mathrm{kHz}$).

the largest. Of course, the transition dipole matrix elements govern not only the spontaneous decay of the photoassociated molecules but also stabilization via stimulated emission. Due to the comparatively long lifetime of the photoassociated molecules, estimated to be of the order of $15\,\mu$s, stabilization into a selected single vibrational level of the electronic ground state can be achieved by stimulated emission using a second continuous-wave laser. The lifetimes of the excited state vibrational levels vary between 5 μs and 20 μs, cf. Fig. 6 of Paper I.

The exact position and the character of the excited state vibrational level, strongly perturbed such as the one with $E_b = 18.9\,\mathrm{cm}^{-1}$ or more regular such as that with $E_b = 5.1\,\mathrm{cm}^{-1}$ in Fig. 5 of Paper I, can be determined experimentally [341, 344]. A possible spectroscopic signature of the character of the vibrational wavefunctions is the dependence of the rotational constants, $\langle v'|\frac{1}{2\mu R^2}|v'\rangle$, on the binding energy of the corresponding levels. This is shown in Fig. 9 of Paper I for different isotope combinations of strontium and ytterbium. The rotational constants of these levels that are predominantly of triplet character lie on a smooth curve, while those that are mixed deviate from this curve. Spectroscopic determination of the rotational constants thus allows for identifying those excited state levels that show the strongest singlet-triplet mixing [341, 344] and are best suited to the formation of ground state molecules. Spectroscopy is also needed to refine the value for the transition frequency of the stabilization laser.

Combining all results shown above and assuming that the relevant spectroscopic data have been confirmed or adjusted experimentally, we suggest the following scheme for the photoassociation of SrYb molecules followed by stabilization via stimulated emission, see Fig. 4.1:

1. A large trapping frequency of the optical lattice is chosen to optimally compress the pair density of strontium and ytterbium atoms prior to photoassociation.

2. A photoassociation laser with frequency $\omega_1 \approx 690\,\mathrm{nm}$, red-detuned from the intercombination line transition and resonant with an electronically excited vibrational level, v', of strongly mixed singlet-tripled character, is applied for a few μs. The duration of the photoassociation laser (roughly $5\,\mu$s is an upper bound) is a compromise between saturating photoassociation and avoiding spontaneous emission losses (lifetime of about $15\,\mu$s) while the laser is on.

3. As the photoassociation laser is switched off, the stabilization laser is switched on. Due to the strong bound-to-bound transition matrix elements, saturation of the transition is expected already for shorter pulses ($\leq 1\,\mu$s). The frequency of the stabilization laser, $\omega_2 \approx 655\,\mathrm{nm}$, is chosen to be resonant with the transition from the electronically excited level, v', to the first excited vibrational level of the $X^1\Sigma^+$ electronic ground state, $v'' = 1$.

4. Before repeating steps 2 and 3, both photoassociation and stabilization lasers remain turned off for a hold period in which the $X^1\Sigma^+(v'' = 1)$ molecules decay to the vibronic ground state, $X^1\Sigma^+(v'' = 0)$. This ensures that the molecules created in the electronic ground state by the first sequence of the photoassociation and stabilization steps are not re-excited in a following sequence. The formed molecules can then be accumulated in $X^1\Sigma^+(v'' = 0)$.

Step 4 needs to involve a dissipative element in order to ensure the unidirectionality of the molecule formation scheme [345]. Dissipation can be provided by infrared spontaneous emission due to the permanent dipole moment of the heteronuclear dimers. However, its time scale is estimated to be of the order of 5 s, much too slow to be efficient for accumulation of the ground state molecules. A second possibility is due to collisional decay.

In order to overcome the problem of unidirectionality that occurs in repeating the photoassociation and stabilization steps many times, the whole ensemble of atom pairs in the trap can be addressed within a single stimulated Raman adiabatic passage (STIRAP) [159] for the photoassociation (pump) and stabilization (Stokes) pulses [346, 347] or within a single sequence of phase-locked STIRAP pulse pairs [346]. The feasibility of STIRAP formation of the ground state molecules depends on isolating the initial state sufficiently from the scattering continuum. In a series of ground-breaking experiments, STIRAP transfer to the ground state was therefore preceded by Feshbach-associating the molecules [348, 349, 91, 121]. An alternative way to isolate the initial state for STIRAP from the scattering continuum is given by strong confinement in a deep optical lattice. In a strong optical lattice the thermal spread can be made much smaller than the vibrational frequency of the trap. Hence a deep optical lattice with trapping frequency of the order of a hundred kHz (and corresponding temperatures $T \ll 5\,\mu$K) should be sufficient to enable STIRAP-formation of ground state molecules. In order to be adiabatic with respect to the vibrational motion in the trap with periods of the order of about $1\,\mu$s, the duration of the photoassociation pulse needs to be rather long, at least of the order of $10\,\mu$s. The challenge might be to maintain phase coherence between the photoassociation pulse and the stabilization pulse over such time scales. For a train of phase-locked STIRAP-pulse pairs [346], the requirement of durations of the order of 10 μs or larger applies to the length of the sequence of pulse pairs. The minimum Rabi frequencies to enforce adiabatic following are $\Omega = 159\,\text{kHz}$ for a 10 μs-pulse or $\Omega = 15.9\,\text{kHz}$ for a 100 μs-pulse. As a further prerequisite, all or at least most atom pairs should reside in the lowest trap state, $v_{\text{trap}} = 0$. Then steps 2-4 above might be replaced, provided the trapping frequency is sufficiently large, by

2.′ a single STIRAP-sweep [159] forming ground state molecules with μs-pulses where the stabilization laser, tuned on resonance with the $v' \to v'' = 0$ transition ($\omega_2 \approx 654\,\text{nm}$), precedes the photoassociation laser, tuned on resonance with the $v_{\text{trap}} = 0 \to v'$ transition ($\omega_2 \approx 690\,\text{nm}$);

2.″ or, a train of short, phase-locked STIRAP pulse pairs with correctly adjusted pulse amplitudes [346].

4.3 Formation of ultracold LiYb$^+$ molecular ions by photoassociation

In this section we present the results on collisions of the ultracold Yb$^+$ ion with Li atoms and the formation of ultracold LiYb$^+$ molecular ions by photoassociation. The dynamical calculations are based on the *ab initio* electronic structure presented in Chapter 3.5. This work is motivated by the ongoing experiment in the group of prof. Rene Gerritsma at the University of Mainz aiming on building quantum simulator emulating solid-state physics with a hybrid system of ultracold ions and atoms [271, 272].

Theoretical model

The most general Hamiltonian describing collisions of the Yb$^+$ ions with the Li atoms reads

$$\hat{H} = \frac{\hbar^2}{2\mu}\left(-\frac{1}{r}\frac{d^2}{dr^2}r + \frac{\hat{L}}{r^2}\right) + \sum_{S,M_S} |S, M_S\rangle V_S(r) \langle S, M_S| + \hat{H}_{\text{Yb}^+} + \hat{H}_{\text{Li}}\,, \tag{4.3}$$

where r is the internuclear distance, $\hat{L}$ is the rotational angular momentum operator, μ the reduced mass, and $V_S(R)$ is the the potential energy curve for the state with total electronic spin S. The atomic Hamiltonian including Zeeman and hyperfine interactions is given by

$$\hat{H}_j = \zeta_j \hat{i}_j \cdot \hat{s}_j + \left(g_e \mu_B \hat{s}_{j,z} + g_j \mu_N \hat{i}_{j,z}\right) B \tag{4.4}$$

with $\hat{s}_j$ and $\hat{i}_j$ the electron and nuclear spin operators, $g_{e/j}$ the electron and nuclear g factors, and $\mu_{B/N}$ the Bohr and nuclear magnetons. ζ_j denotes the hyperfine coupling constant.

The bound rovibrational levels are calculated by the diagonalization of the nuclear Hamiltonian represented on a Fourier grid with adaptive step size [336, 337, 338]. The wave functions for scattering states are constructed in an uncoupled basis set. The coupled channels equations are solved using a renormalized Numerov propagator [350] with step-size doubling and about

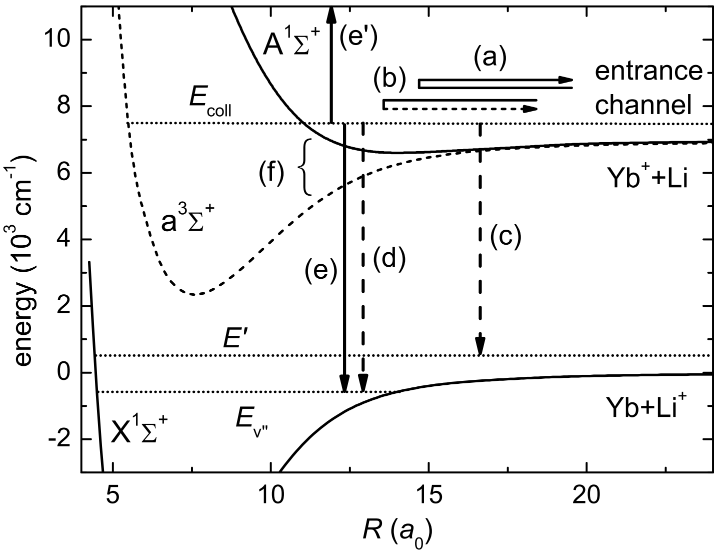

Figure 4.2: The scheme showing all possible processes in the system of Yb$^+$ ion colliding with the Li atom: elastic scattering (a), inelastic (spin-changing) scattering (b), radiative charge transfer (c), radiative association (d), photoassociation to ground (e) or excited (e') states, and magnetic Feshbach resonances and possible magnetoassociation (f).

100 step points per de Broglie wave length. The wave function ratio, given by $R_i = \Psi_{i+1}/\Psi_i$ at the ith grid step, is propagated to large interatomic separations, transformed to the diagonal basis, and the K and S matrices are extracted by imposing long-range scattering boundary conditions in terms of Bessel functions.

The rate constant for the elastic collisions in the ith channel is given by the diagonal elements of the S matrix

$$K^i_{el}(E) = \frac{\pi\hbar}{\mu k}\sum_{J=0}^{\infty}(2J+1)\left|1-S^J_i(E)\right|^2 , \tag{4.5}$$

where $k=\sqrt{2\mu E/\hbar}$ with E collision energy and J is total angular momentum.

The $A^1\Sigma^+$ electronic state is coupled by the interaction-induced transition electric dipole moment with the ground $X^1\Sigma^+$ electronic state. This coupling is responsible for the potential inelastic losses due to the spontaneous radiative charge transfer (CT) or radiative association (RA) and can be used for the laser-field-induced photoassociation (PA) to the singlet state. The $a^3\Sigma^+$ state is coupled by the interaction-induced transition electric dipole moment with the excited $b^3\Pi$ and $c^3\Sigma^+$ states. These couplings can be used for the laser-field-induced photoassociation (PA) to the triplet states.

Radiative processes are governed by the Einstein coefficients for the spontaneous emission. The Einstein coefficients for the transitions between two bound rovibrational states $v'J'$ and $v''J''$, scattering state of energy E' and bound state $v'J'$, and two scattering states of energies

E' and E'' are given by

$$\begin{aligned}
A_{v'J',v''J''} =& \frac{4\alpha^3}{3e^4\hbar^2} H_{J'}(E_{v'J'} - E_{v''J''})^3 \Big| \langle \Psi_{v'J'} | d(R) | \Psi_{v''J''} \rangle \Big|^2 , \\
A_{E'J',v''J''} =& \frac{4\alpha^3}{3e^4\hbar^2} H_{J'}(E' - E_{v''J''})^3 \Big| \langle \Psi_{E'J'} | d(R) | \Psi_{v''J''} \rangle \Big|^2 , \\
A_{E'J',E''J''} =& \frac{4\alpha^3}{3e^4\hbar^2} H_{J'}(E' - E'')^3 \Big| \langle \Psi_{E'J'} | d(R) | \Psi_{E''J''} \rangle \Big|^2 ,
\end{aligned} \tag{4.6}$$

respectively, where the primed and double primed quantities pertain to the excited and ground state potentials, respectively, $d(R)$ is the transition moment from the ground to the excited electronic state, α is the fine structure constant, e is the electron charge, and the Höhn-London factor $H_{J'}$ is equal to $(J'+1)/(2J'+1)$ for the P branch ($J' = J'' - 1$), and to $J'/(2J'+1)$ for the R branch ($J' = J'' + 1$).

Neglecting the hyperfine structure the radiative charge transfer can be described by the following Fermi golden type expression for rate constant [351, 352, 353]

$$K_{\mathrm{CT}}(E) = \frac{4\pi^2\hbar^2}{\mu k} \sum_{J=0}^{\infty} (2J+1) \sum_{J'=J\pm 1} \int_0^{\infty} A_{EJ,E'J'} \mathrm{d}\varepsilon \,, \tag{4.7}$$

where $\varepsilon = E' - E''$. Respectively the rate constant for the radiative association is given by

$$K_{\mathrm{RA}}(E) = \frac{4\pi^2\hbar^2}{\mu k} \sum_{J=0}^{\infty} (2J+1) \sum_{J'=J\pm 1} \sum_{v'} A_{EJ,v'J'} \,. \tag{4.8}$$

The total rate constant for the radiative losses is the sum of Eqs. (4.7) and (4.8)

$$K_R(E) = K_{\mathrm{CR}}(E) + K_{\mathrm{RA}}(E) \,. \tag{4.9}$$

By applying a laser field, the stimulated radiative association (photoassociation) is possible. The rate constant for the photoassociation reads [354, 355]

$$K_{\mathrm{PA}}(\omega, E) = \frac{\pi\hbar}{\mu k} \sum_J (2J+1) \sum_{v'J'} |S_{v'J'}(E, J, \omega)|^2, \tag{4.10}$$

with

$$|S_{v'J'}(E, J, \omega)|^2 = \frac{\gamma^s_{v'J'}(E, J)\gamma^d_{v'J'}}{(E - \Delta_{v'J'}(\omega))^2 + \frac{1}{4}[\gamma^s_{v'}(E, J) + \gamma^d_{v'J'}]^2} \,, \tag{4.11}$$

where $\gamma^s_{v'J'}(E, J)$ is the stimulated emission rate, $\gamma^d_{v'}(E, J)$ the rate for the spontaneous decay, both in units of $\hbar$, $\Delta_{v'J'}(\omega)$ is the detuning relative to the position of the bound rovibrational level $v'J'$, i.e., $\Delta_{v'J'} = E_{v'J'} - \hbar\omega$, where $E_{v'J'}$ is the binding energy of the level $v'J'$.

The spontaneous emission rates $\gamma^d_{v'J'}$ are obtained from the Einstein coefficients $A_{v'J',vJ}$,

$$\gamma^d_{v'J'} = \sum_{vJ} A_{v'J',vJ} \,. \tag{4.12}$$

At low laser intensity, I, the stimulated emission rate is given by Fermi's golden rule expression

$$\gamma^s_{v'J'}(E, J) = 4\pi^2 \frac{I}{c} (2J'+1) H_{J'} |\langle \Psi_{EJ} | d(R) | \Psi_{v'J'} \rangle|^2 \,. \tag{4.13}$$

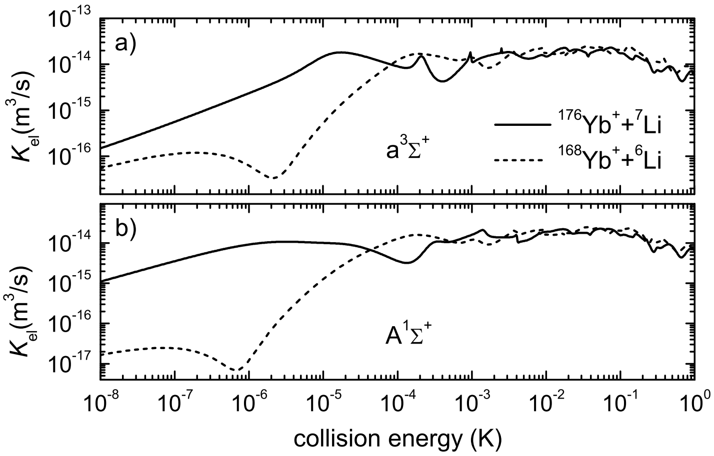

Figure 4.3: Rates for the elastic scattering of the Yb$^+$ ion with the Li atom in the $a^3\Sigma^+$ (a) and $A^1\Sigma^+$ (b) electronic states.

Equations (4.7), (4.8) and (4.10) give rate constants for a single scattering energy E. In practice, we have an ensemble of thermally populated states and the rate constants at a temperature T can by obtained by thermal averaging

$$K(T) = \frac{2}{\sqrt{\pi}(k_B T)^{3/2}} \int_0^\infty K(E)\sqrt{E}\mathrm{e}^{-E/k_B T} dE\,. \tag{4.14}$$

Results

Ab initio electronic structure calculations do not provide enough accurate interaction energy potentials to predict the scattering lengths therefore we calculate scattering proprties for a few isotopic mixtures. Note that the low energy s-wave scattering length for the present $A^1\Sigma^+$ ($a^3\Sigma^+$) potential is -328 a_0 (-572 a_0) for ^{6}Li^{168}Yb and 2491 a_0 (888 a_0) for ^{7}Li^{176}Yb.

For collision energies larger than 10 μK when more than s partial wave contributes to the scattering process, the total rate of elastic collisions is similar for all isotopic mixtures and is of the order of 10^{-14} m^3/s, cf. Fig. 4.3. The possibility of the realization of experimental proposals for e.g. simulating solid states physics with hybrid systems of cold ions and atoms will depend on the ratio of the rates for elastic to all inelastic or reactive collisions. The sympathetic cooling will be possible if this ratio is larger than 100.

Figure 4.4 presents the rate constants for the radiative losses in the collision of the Yb$^+$ ion with the Li atom in the $A^1\Sigma^+$ electronic state. The rates depend strongly on the presence of the resonances in the entrance channel. The radiative association is the main source of the radiative losses and its rate constant is one order of magnitude larger than the rate for the radiative charge transfer. At the same time the rates for the radiative losses are relatively small and 100-1000 times smaller than the rates for elastic scattering. The radiative losses presented in Fig. 4.4 will be reduced by next few orders of magnitude when the collisional dynamics of the Yb$^+$ ion and the Li atom is restricted to the high-spin triplet $a^3\Sigma^+$ state by applying external

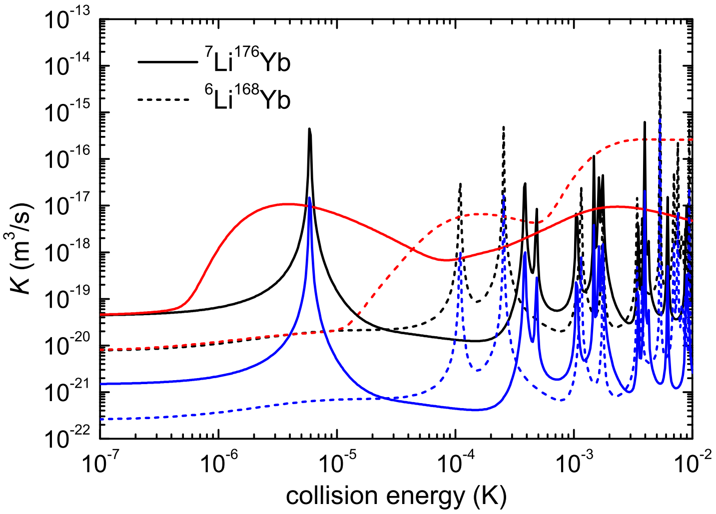

Figure 4.4: Rates for the radiative losses i.e. radiative association and radiative charge transfer due to electric dipole transitions between $A^1\Sigma^+$ and $X^1\Sigma^+$ states in the collision of Yb$^+$ ion with Li atom. The red envelops are the thermally averaged rates and blue lines are the free to free radiative charge transfer contribution.

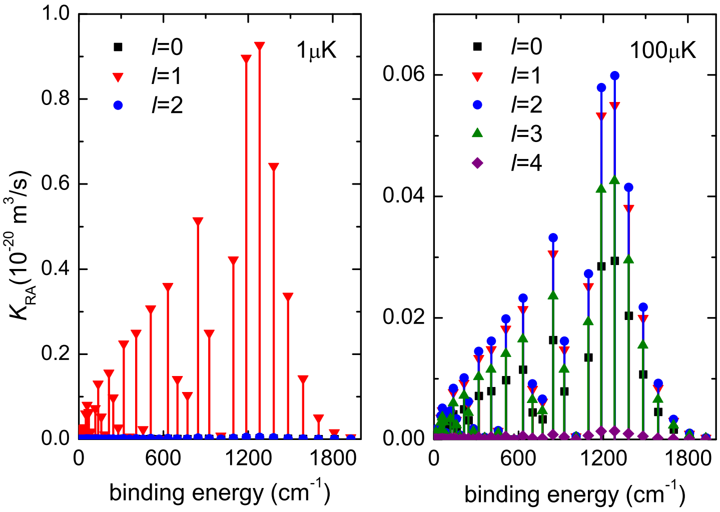

Figure 4.5: Rates for the radiative association of colliding Yb$^+$ ion and Li atom in $A^1\Sigma^+$ state vs binding energy of the final vibrational level of the $X^1\Sigma^+$ ground electronic state for collision energy 1 μK (left panel) and 100 μK (right panel).

magnetic field. Because there is no radiative loss channel for the triplet $a^3\Sigma^+$ state the only radiative losses for collisions in magnetic field originate from the admixture of the singlet $A^1\Sigma^+$ state. For the maximally spin-stretched electronic state the admixture of the singlet $A^1\Sigma^+$ state is given by spin-orbit coupling with higher excited states which is rather small. For these reasons, the radiative losses should not be a problem for any experiment employing the Yb$^+$ ions emerged into ultracold Li atoms especially if the external magnetic field is applied.

Figure 4.5 presents the rates for the association of the colling Yb$^+$ ion and Li atom into

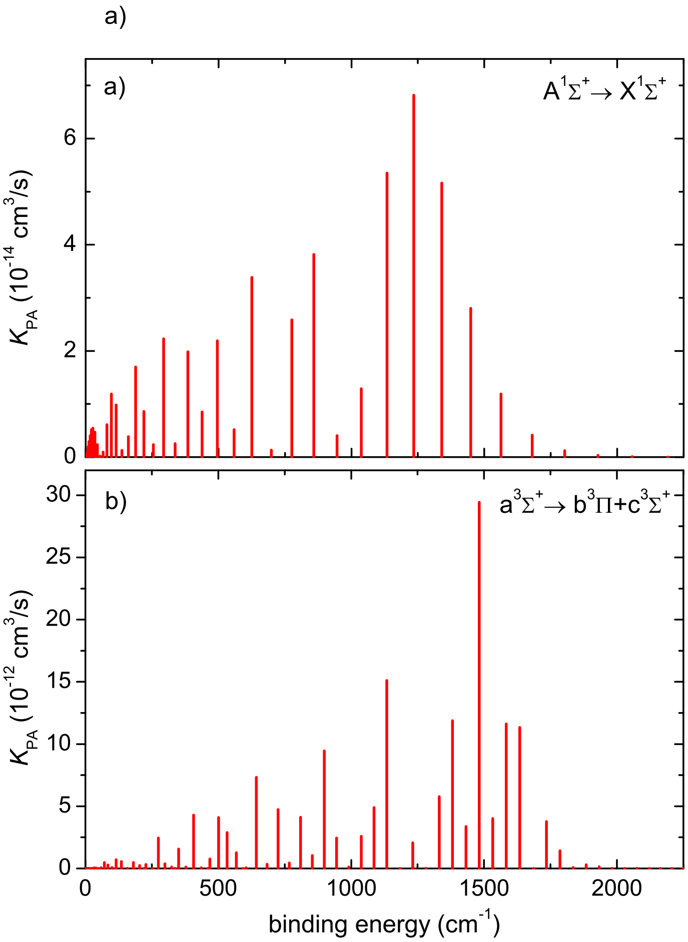

Figure 4.6: Rates for the photoassociation of the Yb$^+$ ion colliding with the Li atom in the $A^1\Sigma^+$ state into rovibrational levels of the $X^1\Sigma^+$ state (upper panel) and in the $a^3\Sigma^+$ state into rovibrational levels of the $c^1\Sigma^+$ and $b^3\Pi$ states (lower panel) for a laser intensity $I = 1\,\mathrm{W/cm^2}$ and temperature of $10\,\mu$K.

different rovibrational levels of the ^{7}Li^{176}Yb$^+$ molecular ion at temperatures $1\,\mu$K and $100\,\mu$K. Spectra for other isotopes have very similar shapes but the amplitudes of the rates varies with the presence of resonances in the entrance channel. Interestingly, the largest partial rates for the formation of molecular ion are for the relatively strongly bound vibrational levels with binding energy of about $1200\,\mathrm{cm}^{-1}$. The spontaneous radiative association thus can be used to produced the LiYb$^+$ molecular ions.

The other way to produce the LiYb$^+$ molecular ions is to apply a laser field to drive photoassociation. If the colliding Yb$^+$ ion and Li atom interact via the $A^1\Sigma^+$ electronic state then the photoassociation to the $X^1\Sigma^+$ state is possible with wavelength $\leq 1438\,\mathrm{nm}$. If they are in the $a^3\Sigma^+$ state then the photoassociation into the manifold of $b^3\Pi$ and $c^3\Sigma^+$ states is possible with wavelength $\geq 906\,\mathrm{nm}$. The photoassociation spectra are presented in Fig. 4.6(a) and Fig. 4.6(b) for the singlet and triplet spin symmetries, respectively. In both cases the relatively strongly bound rovibrational levels can be populated, with binding energy of $1200\,\mathrm{cm}^{-1}$ and

7000 cm^{-1} for singlet and triplet symmetries, respectively.

Combining all the results presented above, the inelastic losses due to the radiative charge transfer and radiative association should not be a problem for the realization of experimental proposals employing hybride ion-atom systems based on the Yb$^+$ ion emerged into a gas of the Li atoms. Additionally, because the radiative association dominates the radiative inelastic processes, it can be employed for the formation of the ultracold LiYb$^+$ molecular ions. By applying laser field the LiYb$^+$ molecular ions can be formed by photoassociation both in the singlet and triplet electronic states. It would be interesting to measure the photoassociation spectrum by using a single ion trapped in Paul's trap in the series of the photoassociation and dissociation experiments provided that the scheme of the detection of a single molecular ion in the trap is developed. Such a detection scheme can be based on the change of the trapping frequency due to the change of the ion mass and the discrimination of the rovibrational levels can employ the modification of the trapped-ion spectrum induced by the differences in the Stark shifts of different rovibrational levels.

Chapter 5

Formation of ultracold molecules by short-pulse photoassociation

5.1 Introductory remarks

Photoassociation i.e. formation of molecules from ultracold atoms by using laser light [23], is a prime candidate for coherent control which utilizes the wave nature of matter in order to steer a process, such as formation of a chemical bond, toward a desired target [259, 146]. At very low temperatures, the delicate build-up of constructive and destructive interference between different quantum pathways is not hampered by thermal averaging. The basic tool for coherent control are short laser pulses that can be shaped in their amplitude, phase and polarization. They can drive both adiabatic and non-adiabatic photoassociation dynamics.

A particular feature of photoassociation at very low temperatures is the excitation of an atom pair at fairly large interatomic separations [23]. This results from a compromise between the atom pair density in the electronic ground state, highest at large interatomic separations, and population of excited state bound levels with reasonable binding energies, that increase with decreasing interatomic separations. Therefore, the free-to-bound transition matrix elements are largest for photoassociation at separations of $50\,\mathrm{a}_0$ to $150\,\mathrm{a}_0$ with the corresponding detunings of less than $20\,\mathrm{cm}^{-1}$. Although these matrix elements are optimally chosen, they are several orders of magnitude smaller than those for the excitation of atoms. This poses a problem for photoassociation with short laser pulses which inherently have a large bandwidth. As soon as the wings of the pulse spectrum overlap with the atomic resonance, atoms instead of bound levels are excited [260], and subsequent spontaneous emission depletes the trapped sample [356, 357]. In the photoassociation experiments with broadband femtosecond laser pulses, the pulse spectrum needs to be cut to suppress excitation of the atomic resonance [358, 359, 360, 361].

Femtosecond photoassociation at very low temperatures corresponds to driving a narrow-band transition with a broad-band laser. This can be achieved by employing multi-photon rather than one-photon transitions [262]. The high peak powers of femtosecond laser pulses easily allow for driving multi-photon transitions, and multi-photon control schemes have been demonstrated for both weak [262, 362] and strong laser pulses [363, 364, 365]. In the weak-field regime, perturbation theory shows that optical interference of two or more photons can be used to completely suppress absorption [262, 362]. For intermediate intensities, higher order perturbation theory can be employed to obtain rational pulse shapes that allow to control the absorption [366, 367, 368, 369, 370]. In the strong-field regime, dynamic Stark shifts drive the transition out of the resonance. This can be countered by a linear chirp of the pulse which compensates the phase accumulated due to the Stark shift. Aditionally adjusting the amplitude of the pulse to guarantee a π or 2π pulse controls the absorption [363, 364, 365]. These control schemes can be applied to femtosecond photoassociation in order to suppress the excitation of atoms [263]. Multi-photon transitions can also be utile for femtosecond photoassociation at high temperature [327, 371, 372]. There, the main advantage derives from the larger flexibility in transition energies, obtained when combining two or more photons, and the new selection rules. The disadvantage of high temperatures is the low initial coherence, or quantum purity, of the thermal ensemble of atoms.

Besides the possibility of driving a narrow-band transition, multi-photon femtosecond photoassociation also allows for accessing highly excited electronic states that may have significant ion-pair character. Such states are expected to be well suited for the formation of stable molecules in their electronic ground state due to the peculiar shapes of the potential energy curves obtained when an ion-pair state crosses covalent ones [373, 374].

These effects become most significant for heavy atoms with strong spin-orbit interaction. The coupling of two (or more) electronic states leads to strong mixing of the rovibrational levels provided the coupling becomes resonant [375]. The wave functions of such strongly mixed levels display peaks at all the four classical turning points. This leads to large transition matrix elements for both photoassociation and subsequent stabilization steps to the electronic ground state [340]. For homonuclear diatomics, usually several neighbouring vibrational levels are affected by the resonant coupling [341, 344], making them particularly suitable for short pulse photoassociation and stabilization since a laser pulse addresses a wave packet, not just a single level. In the case of heteronuclear molecules, the resonantly perturbed levels are typically isolated within the vibrational spectrum. However, the peaks at the inner turning points are so large that stabilization into deeply bound levels of the ground state well [342, 343] all the way down to $v'' = 0$ for SrYb [320] becomes feasible in a single step. Furthermore strong spin-orbit interaction allows for singlet-triplet conversion [103, 376].

In this chapter we present results of the investigation of the multi-photon photoassociation of ultracold atoms driven by femtosecond pulses shaped by using the optimal control theory, analysis of the time evolution of photoassociated wave packet, and finally optimization of population transfer in the stabilization step by using shaped femtosecond pulses.

5.2 Optimal control of the femtosecond three-photon photoassociation of ultracold atoms

In this section we present the results on the multi-photon photoassociation driven by shaped femtosecond laser pulses. The optimal control theory is employed to find these pulses. Example calculations are presented for the three-photon phtotoassociation of ultracold Rb$_2$ molecules. The dynamical calculations are based on the *ab initio* electronic structure data presented in Chapter 3.4 and Paper II.

Theoretical model

Hamiltonian

We consider a pair of ^{87}Rb atoms, held at the temperature of 100 μK, typical for magneto-optical traps, colliding in the lowest triplet $a^3\Sigma_u^+$ state. A photoassociation laser pulse drives a three-photon transition, in the vicinity of the $^2S(5s)+^2P_{1/2}(6p)$ asymptote, creating a molecular wave packet in the manifold of the $(5)^1\Sigma_g^+$, $(6)^1\Sigma_g^+$, $(7)^1\Sigma_g^+$, $(3)^3\Pi_g$, and $(4)^3\Pi_g$ electronically excited states that partially have an ion-pair character. The states in this manifold are coupled by the spin-orbit interaction and radial non-adiabatic coupling matrix elements. In our calcuations, only the $(5)^1\Sigma_g^+$, $(6)^1\Sigma_g^+$, and $(3)^3\Pi_g$ components of the photoassociated wave packet turned out to be significant. Specifically, the population of the $(7)^1\Sigma_g^+$ and $(4)^3\Pi_g$ states at instant of time turned out to be smaller by a factor 100 or more than the population of the $(5)^1\Sigma_g^+$, $(6)^1\Sigma_g^+$, and $(3)^3\Pi_g$ states. Neglecting the $(7)^1\Sigma_g^+$ and $(4)^3\Pi_g$ states, the Hamiltonian describing the three-photon photoassociation in the three-photon rotating wave approximation reads

$$\hat{\mathbf{H}}_{\text{pump}}(t) = \begin{pmatrix} \hat{\mathbf{H}}^{a^3\Sigma_u^+}(R) & 0 & \frac{1}{8}|\epsilon(t)|^3 \mathrm{e}^{-i3\phi(t)}\chi^{(3)}(\omega_L,R) & 0 \\ 0 & \hat{\mathbf{H}}^{(5)^1\Sigma_g^+}(R) & \xi_3(R) & A(R) \\ \frac{1}{8}|\epsilon(t)|^3 \mathrm{e}^{i3\phi(t)}\chi^{(3)}(\omega_L,R) & \xi_3(R) & \hat{\mathbf{H}}^{(3)^3\Pi_g}(R) - \xi_4(R) & \xi_5(R) \\ 0 & A(R) & \xi_5(R) & \hat{\mathbf{H}}^{(6)^1\Sigma_g^+}(R) \end{pmatrix}, \tag{5.1}$$

where $\hat{\mathbf{H}}^{(n)^{2S+1}|\Lambda|_{g/u}}$ denotes the Hamiltonian for the nuclear motion in the $(n)^{2S+1}|\Lambda|_{g/u}$ electronic state,

$$\hat{\mathbf{H}}^{(n)^{2S+1}|\Lambda|_{g/u}} = \hat{\mathbf{T}} + V^{(n)^{2S+1}|\Lambda|_{g/u}}(R) - \frac{1}{4}\alpha^{\text{eff}}_{(n)^{2s+1}|\Lambda|_{g/u}}(\omega_L,R)|\epsilon(t)|^2 + \Delta_{\omega_L}, \tag{5.2}$$

with the kinetic energy operator given by $\hat{\mathbf{T}}$ and $V^{(n)^{2S+1}|\Lambda|_{g/u}}(R)$ the potential energy curve. $\xi_i(R)$ and $A(R)$ denote the spin-orbit coupling and radial non-adiabatic coupling matrix elements, respectively, $\epsilon(t)$ is the envelope and $\phi(t)$ is the temporal phase of the laser field of the form $\frac{1}{2}|\epsilon(t)|\left(e^{i\phi(t)}e^{-i\omega_L t} + e^{-i\phi(t)}e^{i\omega_L t}\right)$. The dynamic Stark shift, $-\frac{1}{4}\alpha^{\text{eff}}_{(n)^{2s+1}|\Lambda|_{g/u}}(\omega_L,R)|\epsilon(t)|^2$, arises from the interaction of the $(n)^{2s+1}|\Lambda|_{g/u}$ state with the intermediate off-resonant states

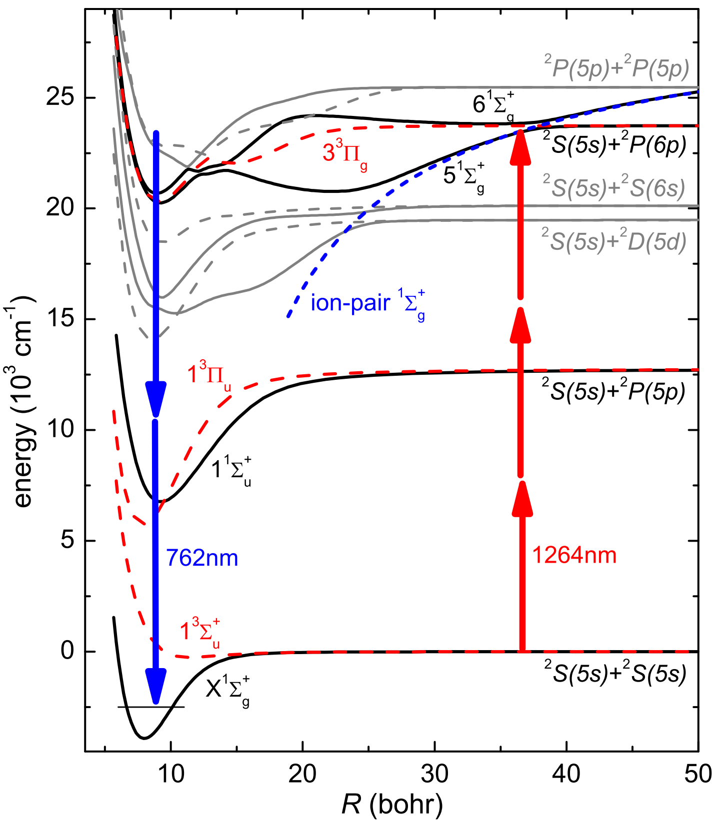

Figure 5.1: Proposed scheme for the multi-photon photoassociation and subsequent stabilization producing ultracold Rb$_2$ molecules in their electronic ground state.

and is given by the effective dynamic electric dipole polarizability,

$$\alpha^{\mathrm{eff}}_{(n)^{2s+1}|\Lambda|_{g/u}}(\omega_L,R)=\frac{1}{3}\sum_{i=x,y,z}\left(\sum_{n'}\frac{2\omega_{n,n'}\left|\langle(n)^{2s+1}|\Lambda|_{g/u}|d_i|(n')^{2s+1}|\Lambda'|_{u/g}\rangle\right|^2}{\omega^2_{n',n}-\omega^2_L}\right)\tag{5.3}$$

where the term in parenthesis is the iith component of the polarizability tensor constructed of the transition dipole moments, $\langle(n)^{2s+1}|\Lambda|_{g/u}|d_i|(n')^{2s+1}|\Lambda'|_{u/g}\rangle$, and excitation energies, $\omega_{n,n'}$, between the $(n)^{2s+1}|\Lambda|_{g/u}$ and $(n')^{2s+1}|\Lambda|_{u/g}$ states. $\chi^{(3)}(\omega_L,R)$ in the Hamiltonian (5.1) is the three-photon transition moment between the $a^3\Sigma_u^+$ and $(3)^3\Pi_u$ states and is given by

$$\chi^{(3)}(\omega_L,R)=\sum_{i,j,k=x,y,z}A_{ijk}\left(\sum_{n,n'}\frac{\langle a^3\Sigma_u^+|d_i|(n)^3|\Lambda|_g\rangle\langle(n)^3|\Lambda|_g|d_j|(n')^3|\Lambda|_u\rangle\langle(n')^3|\Lambda|_u|d_k|(3)^3\Pi_g\rangle}{(\omega_{n,a}-\omega_L)(\omega_{n',a}-2\omega_L)}\right)\tag{5.4}$$

where the term in parenthesis is the ijkth component of the three-photon electric dipole transition tensor and the numerical coefficients A_{ijk} results from the spatial averaging for linearly polarized laser field.

The potential energy curve for the initial $a^3\Sigma_u^+$ state was taken from the experimental fit of Ref. [175] to reproduce correctly the scattering length and the potential energy curves and spin-orbit coupling matrix elements for the excited electronic states in the Hamiltonian (5.1) were taken from the state-of-the-art *ab initio* calculations presented in Chapter 3.4 and Paper

II. The three-photon electric dipole transition moment, Eq. (5.4), and dynamic electric dipole polarizabilities, Eq. (5.3), were calculated as sum-over-states using the potential energy curves and transition electric dipole moments from Chapter 3.4 and Paper II.

The Hamiltonian (5.1) is represented on a Fourier grid with an adaptive step size [336, 337, 338] using $N = 2048$ grid points and the $R_{max} = 2 \cdot 10^4\, a_0$. The time-dependent Schrödinger equation for the pump Hamiltonian is solved by the Chebyshev propagator [377].

Optimal control theory

The control problem is defined by the minimization of the functional

$$J = J_T + \int_0^T g[\epsilon(t)]dt\,, \tag{5.5}$$

where the first term denotes the final-time T objective and the second one denotes the intermediate-time costs. The final-time target can be specified in terms of some desired unitary operator $\hat{\mathbf{O}}$, for example,

$$J_T = 1 - \left|\left\langle \Psi_{in} \left| \hat{\mathbf{U}}^\dagger(T,0;\epsilon)\hat{\mathbf{O}}\hat{\mathbf{U}}(T,0;\epsilon) \right| \Psi_{in} \right\rangle\right|\,, \tag{5.6}$$

where $\hat{\mathbf{U}}(T,0;\epsilon)$ denotes the time evolution operator from the initial time $t = 0$ to the final time T under the action of the field ϵ and $|\Psi_{in}\rangle$ is the initial state of the system.

The intermediate time cost, $g[\epsilon(t)]$, restricts the change of the integrated pulse energy

$$g[\epsilon(t)] = \frac{\lambda_0}{S(t)} \left|\epsilon(t) - \epsilon^{\text{ref}}(t)\right|^2\,, \tag{5.7}$$

where $\epsilon^{\text{ref}}(t)$ denotes some reference field (e.g. field form the previous iteration), the shape function $S(t)$ enforces a smooth switch on and off of the field (e.g. $S(t) = \sin^2(\pi t/T)$) and λ_0 is a weight. Note that the laser field is complex since we employ the rotating-wave approximation. A non-zero phase indicates a relative phase with respect to the laser pulse peak center, or, in the spectral domain, with respect to the phase of the central laser frequency.

The objective, Eq. (5.6), for the photoassociation must suppress atomic excitation and maximize the formation of molecules. This goal can be achieved by choosing the operator $\hat{\mathbf{O}}$ in Eq. (5.6) e.g. as the projection operator onto the desired set of vibrational levels in the manifold of the excited electronic states

$$\hat{\mathbf{O}}_v = \sum_{v'=v'_{min}}^{v'_{max}} |\Psi_{v'}\rangle\langle\Psi_{v'}|\,, \tag{5.8}$$

where the sum goes over levels desired to construct the wave packet. At the same time the target for the atomic system suppressing atomic excitation must be employed.

The other choice of the operator $\hat{\mathbf{O}}$ in Eq. (5.6) can be the R-dependent operator rewarding excitation to the short-range molecular part and punishing excitation to the long-range scattering part. Such an operator can be of the form

$$\hat{\mathbf{O}}_R = \tanh\left(\frac{R_0 - R}{\gamma_R}\right)\,, \tag{5.9}$$

where R_0 separates the molecular and atomic parts and γ_R defines the sharpness of the step. The function of Eq. (5.9) can be modified to distinguish the strength of the reward for molecular excitation and penalty for atomic excitation e.q. by multiplying negative part of $O_R(R)$ by Γ.

Using the linear variant of Krotov's method [378, 379], with the functional given by Eqs. (5.5)-(5.7), the update equation for the complex laser field, $\epsilon(t) = |\epsilon(t)|\mathrm{e}^{i\phi(t)}$, at the iteration step $i+1$ can be derived,

$$\begin{aligned}\epsilon^{(i+1)}_{Re/Im}(t) =& \epsilon^{(i)}_{Re/Im}(t) \\ &+ \frac{S(t)}{\lambda}\mathfrak{Im}\left\{ \left\langle \chi^{(i)}(t) \middle| \chi^{(i)}(t) \right\rangle \left\langle \chi^{(i)}(t) \middle| \frac{\partial \hat{\mathbf{H}}}{\partial \epsilon_{Re/Im}}\bigg|_{\epsilon^{(i+1)}_{Re},\epsilon^{(i+1)}_{Im},\phi^{(i+1)}} \middle| \phi^{(i+1)}(t) \right\rangle \right\},\end{aligned} \tag{5.10}$$

where the initial state forward propagated under the new field,

$$\left|\phi^{(i+1)}(t)\right\rangle = \hat{\mathbf{U}}(t,0,\epsilon^{(i+1)})\left|\Psi_{in}\right\rangle \tag{5.11}$$

and the adjoint states backward propagated under the old field,

$$\left|\chi^{(i)}(t)\right\rangle = \hat{\mathbf{U}}(t,T,\epsilon^{(i)})\hat{\mathbf{O}}\hat{\mathbf{U}}(T,0,\epsilon^{(i)})\left|\Psi_{in}\right\rangle . \tag{5.12}$$

New field enters Eq. (5.10) not only on the left side, but also on the right side in the derivative of the Hamiltonian. Therefore Eq. (5.10) should be solved iteratively, but in the first approach one can assume

$$\frac{\partial \hat{\mathbf{H}}}{\partial \epsilon_{Re/Im}}\bigg|_{\epsilon^{(i+1)}_{Re},\epsilon^{(i+1)}_{Im}} \approx \frac{\partial \hat{\mathbf{H}}}{\partial \epsilon_{Re/Im}}\bigg|_{\epsilon^{(i)}_{Re},\epsilon^{(i)}_{Im}}, \tag{5.13}$$

which is valid approximation for a small change of the field.

Optimization approaches

The Hamiltonian for multiphoton processes, Eq. (5.1), and its derivative in Eq. (5.10) are non-linear in the field and this can affect the convergence rate and the results. For the three-photon transition the update of the field, Eq. (5.10), is proportional to the square of the field,

$$\epsilon^{(i+1)}(t) - \epsilon^{(i)}(t) \sim \epsilon^{(i)}(t)^2 , \tag{5.14}$$

thus for a small amplitude of the field the change of the field will be very small and the shape of the optimized pulse will be restricted to the shape of the initial guess pulse. This problem can be solved in several ways.

On one hand, one can make coupling terms in the Hamiltonian (5.1) linear in the field by using the following substitution

$$\epsilon(t)^3 = |\epsilon(t)|^3 e^{i3\phi(t)} = \tilde{\epsilon}(t) , \tag{5.15}$$

that results in the field-independent coupling in the derivative in Eq. (5.10), but at the same time the diagonal term is not a monotonic function of the new field that can lead to numerical instabilities. Additionally, the transformation (5.15) may introduce artificial features in the pulse spectrum.

On the other hand, one can use time-dependent weight $\lambda(t)$ in Eq. (5.7) that cancels the strong dependence of the update, Eq. (5.10), on the field amplitude,

$$\lambda(t) = \lambda_0 \left| \frac{\epsilon^{ref}(t)}{\epsilon^{ref}_{max}} \right|^2 . \tag{5.16}$$

Pulse optimization with such a weight treats field at each time step on an equal footing.

In summary, the optimization algorithm described in the present section gives flexibility in following points:

- the non-linear dependence of the Hamiltonian with respect to the field and update equation can be balanced by substitution, Eq. (5.15), or time-dependent λ, Eq. (5.16),
- the operator $\hat{\mathbf{O}}$ in the final time cost, Eq. (5.6) can be $\hat{\mathbf{O}}_R$, Eq. (5.9), or $\hat{\mathbf{O}}_v$, Eq. (5.8),
- the shape and integrated energy of the initial guess pulse can be chosen in many ways.

The final result of optimization can depend on the chosen approach.

Results

To characterize the optimization results quantitatively we define the population of the initial scattering wave function that can be photoassociated into a molecular wave packet, $P^E_{\mathrm{SR}}(R_0) = \int_0^{R_0} |\Psi_E(R)|^2 dR$, where $\Psi_E(R)$ is the $a^3\Sigma_u^+$ state scattering wave function with the energy E and R_0 is the internuclear distance, that separates the short-range wave function, that can be photoassociated and the long-range one that is of purely atomic nature. The selectivity in exciting molecular compared to atomic states is being measured by $\eta = \frac{P^{\mathrm{bound}}_{\mathrm{ex}}}{P_{\mathrm{ex}}}$, where $P^{\mathrm{bound}}_{\mathrm{ex}}$ is the population of the molecular part of the photoassociated wave packet and P_{ex} is the total population. We measure the efficiency of the photoassociation as a ratio of the population of the photoassociated molecular wave packet in the manifold of excited states, to the population of the initial scattering state which can be depleted, $\zeta = \frac{P^{\mathrm{bound}}_{\mathrm{ex}}}{P^E_{\mathrm{SR}}}$.

The functional (5.5) with the operator given by Eq. (5.9) allows to suppress completely the atomic excitation leaving molecular excitation unaffected or slightly enhanced. This procedure results in a selectivity of the molecular excitation $\eta \gtrsim 99.99\,\%$ out of total excitation. Figure 5.2 shows the monotonic convergence of the selectivity η with the number of iteration steps for an example of TL 100 fs pulse optimized over 1 ps. The probability of exciting atoms is suppressed by a factor of 10^7 whereas molecule formation is suppressed by a factor of 1.5, which results in the monotonic increase of the selectivity η from 0.01% for the TL pulse to 99.99% for the optimized pulse. We have found that a similar suppression of the atomic excitation can be found for all guess pulses. By increasing the penalty on the scattering part in Eq. (5.9), the arbitrarily large suppression of the atomic transition can be achieved for all pulse durations between 1 and 10 ps.

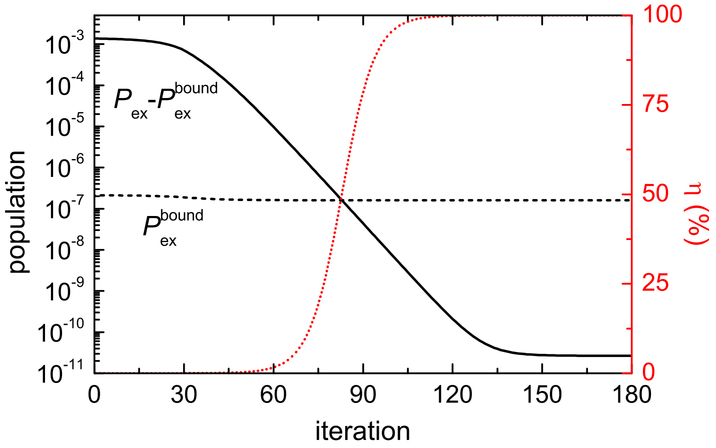

Figure 5.2: The population excited to the molecular short range part P_{ex}^{bound} and to the atomic long range part $P_{ex} - P_{ex}^{bound}$ (left axis) and the selectivity η (right axis) vs the number of iteration steps for TL 100 fs pulse optimized over 1 ps.

Effective formation of the molecules using a multiphoton transition with shaped pulses needs not only large selectivity η but also large efficiency ζ. Efficient excitation of the short range part of the scattering state is more challenging than suppressing atomic excitations.

We have found that the results of the optimization strongly depend on the shape of the initial guess pulse. Therefore, we have examined the following guess pulses optimized over the period of time between 1 ps and 10 ps: TL 100 fs pulses, train of TL 100 fs pulses, linearly chirped TL 100 fs pulses, TL 1-4 ps pulses detuned from atomic transition, and chirped 1-4 ps pulses detuned from atomic transition.

The common feature of the results with all guess pulses is that the amount of molecules photoassociated with an optimized pulse depends strongly on the amount of molecules photoassociated with an unshaped pulse. Once the atomic transition is strongly suppressed ($\eta \sim 1$) the optimization algorithm reaches the local minimum and further optimization does not results in any enhancement of the molecule formation probability. Therefore, the guess pulse exciting as many molecules as possible should always be chosen.

One solution that allows to avoid fast trapping in the local minimum during the optimization is to decrease the penalty for the atomic excitation in the operator $O_R(R)$, optimize the pulse to increase the efficiency ζ, and then restore the penalty on the atomic transition to suppress it and to increase the selectivity η.

None of the investigated guess pulses allows to excite a significant fraction of the population of the molecules i.e. to obtain a large efficiency ζ. It is in a sharp contrast to one-photon photoassociation [261, 260] where the picosecond pulse detuned from the atomic transition can create a wave packet exciting a significant part of the initial scattering state and leaving a large "hole" in the ground-state wave function. The limiting factor is the Stark shift which plays a more important role in the many-photon transitions [263] compared to the one-photon ones. Especially, in the case of the three-photon transition, for which the three-photon coupling is

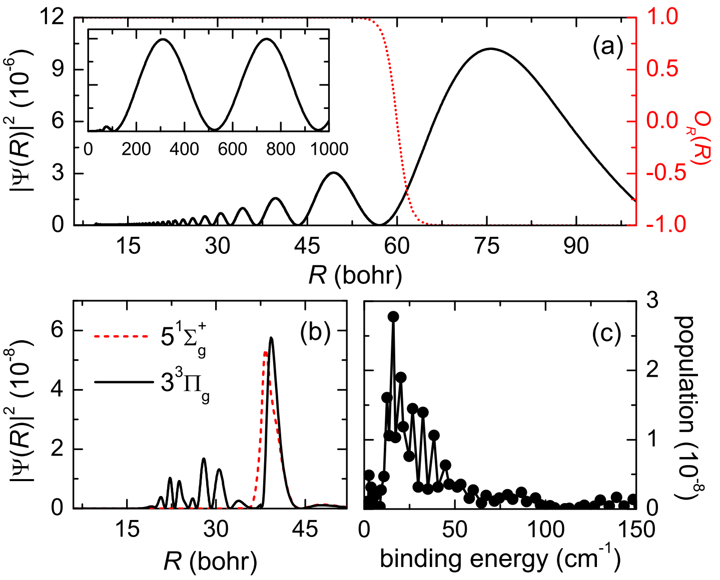

Figure 5.3: Upper panel: The wave function of the initial scattering state with energy 100 μK. Bottom panel: Final excited-state wave packet after applying TL 100fs pulse optimized over 1 ps and its decomposition onto vibrational levels.

cubic in field ($\sim \epsilon^3(t)$) whereas the Stark shift depends quadratically on it ($\sim \epsilon^2(t)$), the Stark shift efficiently shifts the transition out of the resonance.

Numerical simulations confirm predictions based on Eq. (5.14). When the standard approach with the couplings cubic in field in the Hamiltonian and with the time-independent weight λ is employed for the optimization of the three-photon transition, then the shape of the optimized pulse depends strongly on the shape of the initial guess pulse. Especially the time of the pulse, when the amplitude of the initial guess pulse is small, is not used. Both substitution given by Eq. (5.15) and the use of the time-dependent weight (5.16) remove the strong dependence of the update equation on the local amplitude of the field and resulting convergence, selectivity, efficiency and fields $\tilde{\epsilon}(t)$ and $\epsilon(t)$ are similar.

Figure 5.3(b) presents the wave packet created with TL 100 fs pulse optimized over 1 ps. For as short pulse durations as 1-2 ps, the creation of the wave packet is governed mainly by the projection of the ground-state scattering state onto the vibrational levels of the excited states (Franck-Condon factors) and by the fact that the excitation to the most weakly bound vibrational levels is suppressed similarly to the atomic transition. The resulting wave packet has the maximum located around 40 bohr and binding energy of about 20 cm^{-1}, Fig. 5.3(c). The inspection of the initial scattering wave function, Fig. 5.3(a), reveals that there is a large wave function amplitude between 60 bohr and 110 bohr that is of molecular character and could potentially be photoassociated similarly to the one-photon photoassociation case [261, 260]. Unfortunately, we have found that regardless of the chosen parameter R_0 in the operator $O_R(R)$, Eq. (5.9), it is not feasible to create excited wave packet with amplitude at a distance larger than 60 bohr. The reason is that the transition to the very weakly bound vibrational levels

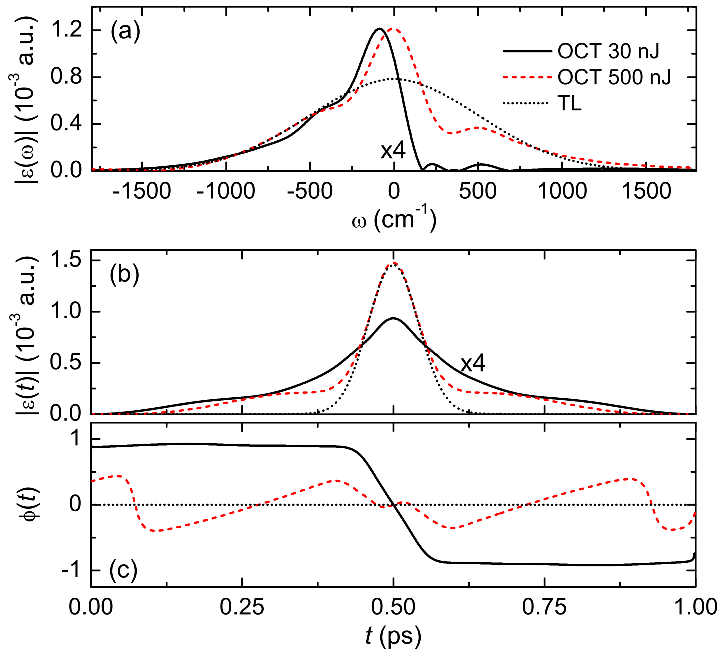

Figure 5.4: Temporal envelope (a), phase (b), and spectrum (c) of the TL 100 fs pulses optimized over 1 ps for two integrated energies in weak and strong fields regimes. $\lambda(t) = |\epsilon(t)|^2/\epsilon^2_{max}$.

cannot be distinguished from the atomic transition by broadband pulse shaped to suppress atomic excitation, especially when the differential Stark shift that can discriminate atomic and molecular transitions takes the asymptotic atomic value at distances larger than 50 bohr.

The TL 100 fs pulse optimized over 1 ps allows to achieve an efficiency ζ of the order of a few percent, when $R_0 = 50$ bohr. When the duration of the optimized pulse is longer then the vibrational dynamics on the excited state potentials plays a role and a larger photoassociation efficiency ζ is feasible.

For all guess pulses we have found that if the initial guess pulse is at least π or more energetic pulse then the optimization leads to $n2\pi$ pulse solution for the atomic transition. Once the initial pulse is closer to the $n2\pi$-pulse the convergence is faster. For the weak guess pulse the optimization removes the part of the spectrum driving atomic transition, cf. Fig.5.4.

The initial state of ultracold atom for photoassociation is the thermally populated continuum of scattering states. We have found that a pulse optimized for one initial scattering energy and partial wave works also for all other collision energies within the thermal ensemble and for the lowest partial waves. Figure 5.5 shows the performance of the TL 100 fs pulse optimized over 1 ps for initial state of energy 100 μK and angular momentum $l = 0$ applied to initial states of other energy and higher partial waves. The selectivity η for the large range of the collision energies is almost constant and larger than 99.99 %, cf. Fig. 5.5(a). When the same pulse is applied to initial states with higher rotational angular momentum the selectivity over 99.99 % persists for $j = 1$ and for higher partial waves the selectivity decreases to $\sim$ 98 %, Fig. 5.5(b). Similar behavior is observed for all optimized pulses. When the optimization of the pulse is not converged, i.e. $\eta <$ 99 %, the performance of the pulse optimized for one state is much worse

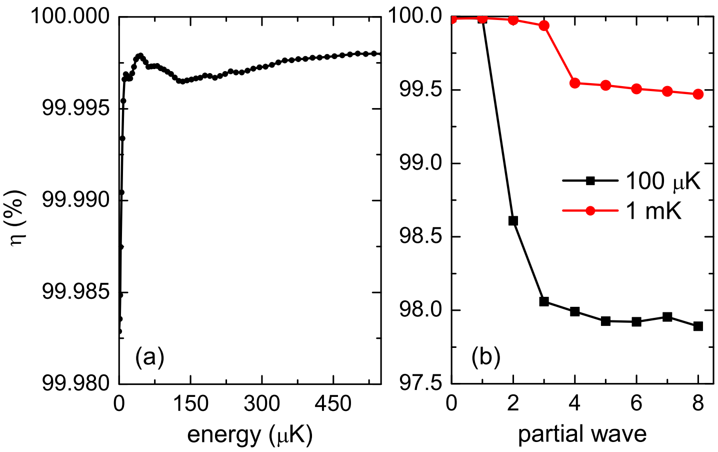

Figure 5.5: The performance of the TL 100 fs pulse optimized over 1 ps for one discreet initial state ($E_{col} = 100\,\mu$K, $j = 0$, $\eta = 99.99\,\%$) applied to states of the other collision energy (left panel) and of the higher partial waves but the same collision energy (right panel).

with states of other energy and angular momentum.

5.3 Optimized two-photon stabilization employing potentials with ion-pair character and strong spin-orbit coupling

In this section we analyze the evolution of the wave packet formed in the three-photon photoassociation presented in the previous Chapter 5.2. Next, the excited state wave packet is transferred to the ground electronic state by a second laser pulse, driving a resonant two-photon transition. We discuss the efficiency of the population transfer using transform-limited and linearly chirped laser pulses. Finally, we employ the optimal control theory to determine the most efficient stabilization pathways. The dynamical calculations are based on the *ab initio* electronic structure presented in chapter 3.4 and Paper II. A detailed description is presented in Paper III.

Theoretical model

Hamiltonian

We consider a pair of ^{85}Rb atoms, held at the temperature of 100 μK, typical for magneto-optical traps, colliding in the lowest $a^3\Sigma_u^+$ triplet state. The formation of molecules by photoassociation and stabilization of the excited state molecules to the eletronic ground $X^1\Sigma_g^+$ state are treated separately. First, a photoassociation laser pulse drives a three-photon transition, red detuned with respect to the $^2S(5s) + {}^2P_{1/2}(6p)$ asymptote, creating a molecular wave packet in the manifold of the $(5)^1\Sigma_g^+$, $(6)^1\Sigma_g^+$, and $(3)^3\Pi_g$ electronically excited states as was described in Chapter 5.2.

In the second step, the initial wave packet created by the three-photon photoassociation, is deexcited to the $X^1\Sigma_g^+$ ground electronic state via a resonant two-photon electric dipole transition. The intermediate states for the two-photon transition are the $A^1\Sigma_u^+$ and $b^3\Pi_u$ states, correlating to the ${}^2S(5s) + {}^2P(5p)$ asymptote, that are also strongly coupled by the spin-orbit interaction. Electric dipole transitions are allowed between all components of the initial wave packet and the intermediate states, whereas the $X^1\Sigma_g^+$ ground electronic state is only connected to the $A^1\Sigma_u^+$ state by the strong electric dipole transition. The Hamiltonian describing the stabilization of the photoassociated wave packet to the electronic ground state via a resonant two-photon transition reads

$$\hat{\mathbf{H}}_{\text{dump}}(t) = \begin{pmatrix} \hat{\mathbf{H}}^{X^1\Sigma_g^+}(R) & \epsilon^*(t)d_1(R) & 0 & 0 & 0 & 0 \\ \epsilon(t)d_1(R) & \hat{\mathbf{H}}^{A^1\Sigma_u^+}(R) & \xi_1(R) & \epsilon^*(t)d_2(R) & 0 & \epsilon^*(t)d_4(R) \\ 0 & \xi_1(R) & \hat{\mathbf{H}}^{b^3\Pi_u}(R) - \xi_2(R) & 0 & \epsilon^*(t)d_3(R) & 0 \\ 0 & \epsilon(t)d_2(R) & 0 & \hat{\mathbf{H}}^{(5)^1\Sigma_g^+}(R) & \xi_3(R) & A(R) \\ 0 & 0 & \epsilon(t)d_3(R) & \xi_3(R) & \hat{\mathbf{H}}^{(3)^3\Pi_g}(R) - \xi_4(R) & \xi_5(R) \\ 0 & \epsilon(t)d_4(R) & 0 & A(R) & \xi_5(R) & \hat{\mathbf{H}}^{(6)^1\Sigma_g^+}(R) \end{pmatrix}, \tag{5.17}$$

in a one-photon rotating wave approximation. The Hamiltonian for field-free nuclear motion in the ${}^{2S+1}|\Lambda|_{g/u}$ electronic state, $\hat{\mathbf{H}}^{{}^{2S+1}|\Lambda|_{g/u}}$, is now given by

$$\hat{\mathbf{H}}^{{}^{2S+1}|\Lambda|_{g/u}} = \hat{\mathbf{T}} + V^{{}^{2S+1}|\Lambda|_{g/u}}(R) + \Delta_{\omega_L}^{np} \tag{5.18}$$

with the detunings $\Delta_{\omega_L}^{5p} = \omega_{{}^2P(5p)} - \omega_L$ and $\Delta_{\omega_L}^{6p} = \omega_{{}^2P(6p)} - 2\omega_L$ for the states dissociating into the ${}^2S(5s) + {}^2P(5p)$ and ${}^2S(5s) + {}^2P(6p)$ asymptotes, respectively. $d_i(R)$ are the electric transition dipole moments and $\xi_i(R)$ are the spin-orbit coupling matrix elements.

The Hamiltonian Eq. (5.17) is represented on a Fourier grid with an adaptive step size [336, 337, 338] and the time-dependent Schrödinger equation for the dump Hamiltonian is solved by the Chebyshev propagator [377].

Optimal control theory

Optimal control theory (OCT) can be used to calculate the shape of laser pulses that efficiently drive a desired transition. We will employ it here to determine the most efficient stabilization between an initial molecular wave packet and deeply bound levels in the ground electronic state. In principle, this problem is completely controllable such that perfect population transfer can be realized. However, contraints such as limited pulse duration, spectral bandwidth and pulse intensity will compromise the stabilization process, reducing the transfer efficiency.

The control problem was described in the previous Chapter 5.2 and is defined by minimization of the functional J, Eq. (5.5). The final-time target, J_T, can be chosen to maximize a single state-to-state transition by choosing the projection onto a single state $\hat{\mathbf{O}}_{v'} = |\Psi_{v'}\rangle\langle\Psi_{v'}|$ or the transition into a manifold of final states with projection operator given by Eq. (5.8). For a single state-to-state transition from an initial state $|\Psi_{in}\rangle$ to the target state, here a vibrational level of the electronic ground state, v'', the final-time functional can be written as

$$J_T^{ss} = 1 - |\langle\Psi_{v''}|\hat{\mathbf{U}}(T,0;\epsilon)|\Psi_{in}\rangle|^2 . \tag{5.19}$$

$\hat{\mathbf{U}}(T,0;\epsilon)|\Psi_{in}\rangle$ represents the formal solution of the time-dependent Schrödinger equation where $\hat{\mathbf{U}}(T,0;\epsilon)$ is the time evolution operator, and J_T^{ss} corresponds to the overlap of the initial state, propagated to the final time T under the action of the laser field $\epsilon(t)$, with the target state. Optimizing a transition into a manifold of states is expressed by the functional

$$J_T^{sm} = 1 - \sum_{v''=v''_{min}}^{v''_{max}} |\langle\Psi_{v''}|\hat{\mathbf{U}}(T,0;\epsilon)|\Psi_{in}\rangle|^2 , \tag{5.20}$$

where any vibrational level of the electronic ground state with the quantum number between v''_{min} and v''_{max} can be populated at the final time. Once the optimum is reached, both functionals, J_T^{ss} and J_T^{sm}, take the value zero. The intermediate time cost, $g[\epsilon(t)]$, was chosen as given by Eq. (5.7) and restricts the change of the integrated pulse energy.

Using the linear variant of Krotov's method [378, 379], the update equation with the operator $\hat{\mathbf{O}}_v$ for the laser field at the iteration step $k+1$ can be derived,

$$\begin{aligned}\epsilon^{(k+1)}_{Re/Im}(t) =& \epsilon^{(k)}_{Re/Im}(t) - \frac{S(t)}{2\lambda} Im \Bigg\{ \sum_{v''=v''_{min}}^{v''_{max}} \left\langle \Psi_{in} \left| \hat{\mathbf{U}}^\dagger \left(T,0;\epsilon^{(k)}\right) \right| \Psi_{v''} \right\rangle \\ & \left\langle \Psi_{v''} \left| \hat{\mathbf{U}}^\dagger \left(t,T;\epsilon^{(k)}\right) \frac{\partial \hat{\mathbf{H}}_{dump}}{\partial \epsilon_{Re/Im}} \right|_{\epsilon^{(k+1)}_{Re/Im}} \hat{\mathbf{U}}\left(t,0;\epsilon^{(k+1)}\right) \right| \Psi_{in} \right\rangle \Bigg\},\end{aligned} \tag{5.21}$$

where $\hat{\mathbf{U}}(t,0;\epsilon^{(k+1)})|\Psi_{in}\rangle$ is the initial state forward propagated to the time t under the action of the new field, $\epsilon^{(k+1)}$, and $\hat{\mathbf{U}}(t,T;\epsilon^{(k)})|\Psi_{v''}\rangle$ denotes the target state(s) backward propagated to time t under the action of the old field, $\epsilon^{(k)}$. The derivative of the Hamiltonian with respect to the field yields a matrix having as its elements all the transition dipole moments d_i, cf. Eq. (5.17). Optimization of the functionals J_T^{ss} or J_T^{sm} requires repeated forward and backward propagations of the initial and target states.

Results

Evolution of phtotoassociated wave packet

The initial wave packet for the stabilization step is created by the photoassociation pulse as desribed in Chapter 5.2. For the simplicity we assume a transform-limited (TL) Gaussian pulse which excites the wave packet very similar to optimally shaped pulse over a short period of time. The intensity of the laser pulse is chosen to be in the perturbative weak-field regime, where the composition of the photoassociated wave packet reflects the bandwidth of the laser pulse combined with the vibrationally averaged three-photon electric dipole transition moments between the initial scattering state and the excited state vibrational levels below ${}^2S(5s) + {}^2P_{1/2}(6p)$ dissociation limit. A pulse duration of 4 ps full width at half maximum (FWHM) is considered, corresponding to a spectral bandwidth of 3.7 cm^{-1}. The pulse is red detuned by 12 cm^{-1} from the ${}^2S(5s) \longrightarrow {}^2P_{1/2}(6p)$ atomic three-photon transition.

The initial wave packet for the stabilization step is plotted in Fig. 4 of Paper III and discussed extensively in Section III of Paper III. Note that the photoassociated wave packet shows truly mixed character with about 65% of its norm residing in the $(3)^3\Pi_g$ triplet component and 35% in the $(5)^1\Sigma_g^+$ singlet component.

The initial wavepacket propagates toward shorter interatomic separations under the influence of the excited state potentials. At large interatomic separations, the potential energy curve of the $(5)^1\Sigma_g^+$ state displays a strong $-1/R$ ion-pair character. The singlet-triplet oscillations are analyzed in Fig. 5(a) of Paper III displaying the singlet and triplet components of the wave packet evolving after the photoassociation pulse in the manifold of electronically excited states. The population of the $(3)^3\Pi_g$ triplet component oscillates around 60%, whereas the population of the $(6)^1\Sigma_g^+$ component, that was absent just after photoassociation, reaches a maximum of 27% at $t = 12.7$ ps after the peak of photoassociating pulse. A second maximum of the $(6)^1\Sigma_g^+$ component is observed after a period of 20.1 ps and a third one after another 36.2 ps. The times at which the $(6)^1\Sigma_g^+$ component reaches maximal values can be interpreted as moments when the wave packet arrives at its shortest distance and is reflected from the innermost repulsive short range wall. This observation is confirmed by calculating the average bond length of the wave packet, shown in Fig. 5(b) of Paper III, which allows to estimate the revival time of the present wave packet to be between 20 ps and 30 ps.

The knowledge of the revival time of the wave packet is useful for the interpretation of the projections of the time-dependent wave packet, $|\langle \Psi_{in}(t)|v''\rangle|^2$, onto the vibrational levels v'' of the $X^1\Sigma_g^+$ ground electronic state, shown in Fig. 5(c) of Paper III for all ground state levels with binding energies up to 1000 cm^{-1}. These projections are largest when the wave packet is localized at its inner turning point. The time at which the projections show maxima correspond to optimal time delays between photoassociation and stabilization pulse. The transition probability does not only depend on the overlap of initial and final wave function, but also on the dipole moments and the topology of the intermediate state surfaces and their coupling [cf. Fig. 5(d) of Paper III]. Based on the time-dependence of the projection and the stabilization probability analyzed in Fig. 5 of Paper III , we choose $t_0 = 13.3$ ps for the time delay, taken between the peak of the photoassociating pulse and the center of all pulses used in the following subsections.

Two-photon stabilization with transform-limited and linearly chirped pulses

In order to understand the role of the basic pulse parameters such as intensity and spectral width and to investigate dynamical effects we first study transform-limited (TL) and linearly chirped stabilization pulses. In the weak-field regime and for the TL pulses, the probability of the resonant two-photon transition is obtained by perturbation theory. It is determined by the effective two-photon transition moment given by Eq. (12) of Paper III.

The two-photon transition moments are shown in Fig. 6(a) of Paper III for all vibrational levels v'' of the $X^1\Sigma_g^+$ ground electronic state. The large peak around a binding energy of $2650\,\mathrm{cm}^{-1}$ indicates that stabilization of the excited state wave packet to levels with binding energies in this range is the most efficient. The peak maximum in Fig. 6(a) of Paper III corresponds to a transition to the vibrational level $v'' = 23$, with a binding energy $E_{v''}$=$2651\,\mathrm{cm}^{-1}$.

The two-photon transition probability can be predicted from the effective two-photon transition moment only in the weak-field regime when the dynamic Stark shifts and other time-dependent effects do not play any role. The dependence of the two-photon transition probability on the pulse intensity and detuning $\Delta\omega_L = 2\omega_L - \omega_{^2P_{1/2}(6p)}$ is illustrated in Fig. 6(b) of Paper III. The pulse duration is kept fixed at 100 fs FWHM. For weak and intermediate pulse intensities, with the integrated pulse energy corresponding to 8.3 nJ and 25.4 nJ, the final $X^1\Sigma_g^+$ ground state population as a function of the pulse detuning reflects the shape of the effective two-photon transition moment, Fig. 6(a) of Paper III. On the other hand, the final $X^1\Sigma_g^+$ population decreases for the detuning corresponding to the maximum of the two-photon transition moment and increases for smaller detunings when the integrated pulse energy is increased. This observation is rationalized in terms of the strong dynamic Stark shift by analyzing the vibrational distribution of the final $X^1\Sigma_g^+$ state population in Fig. 6(c) of Paper III for a detuning, $\Delta\omega_L$=$2650\,\mathrm{cm}^{-1}$, corresponding to the maximum of the two-photon transition moment. When increasing the integrated pulse energy from 25.4 nJ to 2 μJ, i.e., from the intermediate to the strong field regime, two peaks are observed in the vibrational distribution rather than a single Gaussian around the binding energy of $v'' = 23$, reflecting the bandwidth of the pulse. In the strong field regime, one peak of the vibrational distribution is still located around the binding energy of the resonant level, while the second one is shifted by $800\,\mathrm{cm}^{-1}$ to smaller binding energies. This is due to the positive differential Stark shift caused by the coupling to the intermediate states, which indeed increases the energy separation between ground and excited states by about $800\,\mathrm{cm}^{-1}$. Figure. 6(c) of Paper III compares the final state vibrational distribution for two different detunings of the stabilization pulse, $\Delta\omega_L = 2650\,\mathrm{cm}^{-1}$ corresponding to the peak of the two-photon transition probability for weak and intermediate fields (black dotted and red solid curves in Fig. 6(b) of Paper III) and $\Delta\omega_L = 1240\,\mathrm{cm}^{-1}$ corresponding to the peak of the two-photon transition probability for strong fields (black dot-dashed curve in Fig. 6(b) of Paper III). Inspection of the vibrational distributions in Fig. 6(c) of Paper III reveals that for $\Delta\omega_L = 1240\,\mathrm{cm}^{-1}$ and 2 μJ integrated pulse energy, a peak at binding energies larger than the detuning appears. Also, this peak is caused by the differential Stark shift which this time is negative, decreasing the energy separation between ground and excited states by about $600\,\mathrm{cm}^{-1}$. In the weak and intermediate field regime, almost no population is transferred for $\Delta\omega_L = 1240\,\mathrm{cm}^{-1}$ (red empty circles in Fig. 6(c) of Paper III), confirming a strong field effect.

The total population that is transferred by a TL pulse, with 100 fs FWHM and a detuning in the range of $2500\,\mathrm{cm}^{-1}$ to $2600\,\mathrm{cm}^{-1}$, from the initial wave packet to the $X^1\Sigma_g^+$ ground electronic state amounts to up to 1.7% in the weak and intermediate field regime. For strong fields, up to 2.9% of the population can be transferred for detunings between $1000\,\mathrm{cm}^{-1}$ and $1500\,\mathrm{cm}^{-1}$ and pulse energies above $1\,\mu$J. The subsequent analysis is restricted to pulses with detunings between $2500\,\mathrm{cm}^{-1}$ and $2650\,\mathrm{cm}^{-1}$ corresponding to the maximum of the effective two-photon transition moment where the smallest pulse intensities should be required.

The dynamic Stark shift is detrimental to efficient population transfer by the stabilization pulse. One option to increase the integrated pulse power while keeping the maximum field intensity, and thus the dynamic Stark shift, small is to consider a train of short TL pulses. A second option is given by chirping the pulse. The efficiency of the two-photon population transfer to the electronic ground with the first option, a train of 100 fs TL pulses delayed relative to each other by 200 fs and with a sinusoidal envelope, is analyzed in Fig. 7 of Paper III. While increasing the pulse energy of a 100 fs pulse does not improve the population transfer to the electronic ground state beyond 1.7%, a train of pulses yields up to about 6% for pulse energies that are still in the nJ range. Using a train of pulses instead of a single pulse with the same bandwidth, one can produce 3.5 times more ground state molecules.

From the coherent control of atomic transitions using strong fields, it is known that the influence of the dynamic Stark shift can be compensated by chirping the pulse [363, 364]. We investigate in Fig. 8(a) of Paper III showing the final ground state population vs. chirp rate for increasing pulse energy whether this approach also works for molecular transitions. We use a positive chirp to correct the influence of the dynamic Stark shift since the differential Stark shift for stabilization to vibrational levels with binding energies close to $2650\,\mathrm{cm}^{-1}$ is positive. Chirping a weak-field pulse (black dot-dashed curve) deteriorates the population transfer. When more energetic pulses are used, chirping increases the final $X^1\Sigma_g^+$ state population from 1.5% for unchirped pulses to almost 9% for the best chirped pulses. In total we find that chirping the pulse improves the stabilization process and enhances the amount of ground state population by a factor of about six. Figure 8(a) of Paper III showing the final state vibrational distribution confirms that the same mechanism as in the atomic case is at work [363, 364]: When increasing the pulse energy from 25.4 nJ to 300 nJ without chirping the pulse, a second peak shifted by $500\,\mathrm{cm}^{-1}$ appears. The energies of the levels of this second peak correspond exactly to the detuning corrected by the Stark shift.

Two-photon stabilization with optimally shaped pulses

We employ the optimization algorithm described above to find those laser pulses that stabilize the initial wave packet most efficiently to the $X^1\Sigma_g^+$ electronic state. The final $X^1\Sigma_g^+$ state population, shown in Fig. 5.6(a), converges smoothly to the maximal value that can be obtained with a given pulse duration, displayed in Fig. 5.6(b). The maximum stabilization probability

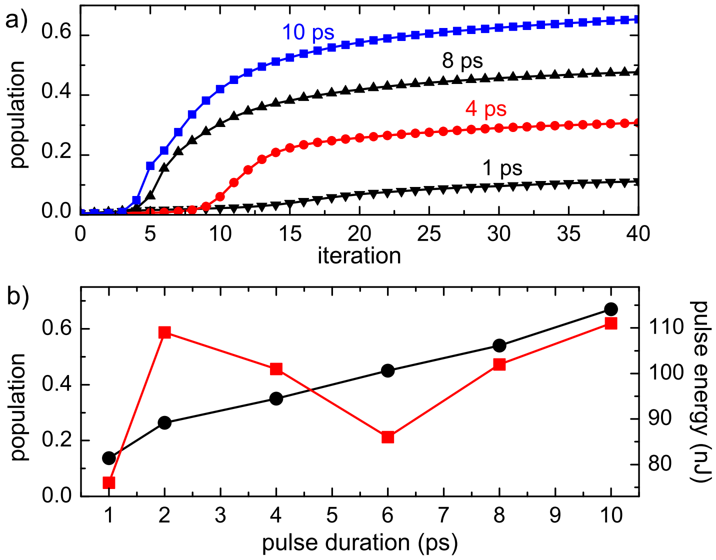

Figure 5.6: (a) Final $X^1\Sigma_g^+$ state population after optimized pulses of different pulse duration vs number of iteration steps. (b) Final $X^1\Sigma_g^+$ state population (left scale, black circles) and corresponding pulse energy (right scale, red squares) vs pulse duration. The values were collected after 50 iterations, starting with the same weak-field guess pulse ($E = 10\,$nJ) and using the same weight, $\lambda = 400$, in all optimizations.

for a pulse duration of 1 ps is 14%. Increasing the pulse duration, the stabilization probability reaches 26% for 2 ps pulse and 67% for 10 ps pulses. This is significantly more efficient than any existing proposal for short-pulse photoassociation [261, 260]. The integrated pulse energies of the optimized pulses vary between 80 nJ and 150 nJ. This is two to three times smaller than the integrated pulse energies for the trains of pulses and the linearly chirped pulses. The guess pulse for the optimizations shown in Fig. 5.6 is a TL pulse with a pulse duration of 100 fs and integrated pulse energy of 10 nJ. For all the results presented here, the state-to-manifold-of-states functional, Eq. (5.20), was employed. The results obtained by using the state-to-state functional, Eq. (5.19), do not differ significantly. In particular, the same bounds on the maximum stabilization efficiencies are observed. The integrated energy of the optimal pulses presented in Fig. 5.6(b) does not depend strongly on the optimal pulse duration. The slightly oscillatory behavior of the integrated pulse energy as a function of pulse duration is observed irrespective of the shape and energy of the guess pulse and the weight λ.

The fact that the maximum population transfer to the $X^1\Sigma_g^+$ state is clearly less than 100% is due to the pulses being too short to drive the complete wave packet to the ground state [264]. When the pulse duration is much shorter than the time scale of the vibrational motion and spin-orbit oscillations, then only that part of the wave packet that shows a favorable overlap with the target state during the optimization window is transferred. For example, the pulse with 1 ps duration essentially reflects the overlap of the initial wave packet. By increasing the pulse duration, cf. Fig. 5.6(b), the stabilization efficiency increases monotonically. A stabilization probability of 100% is expected once the pulse duration is longer than the revival time of the

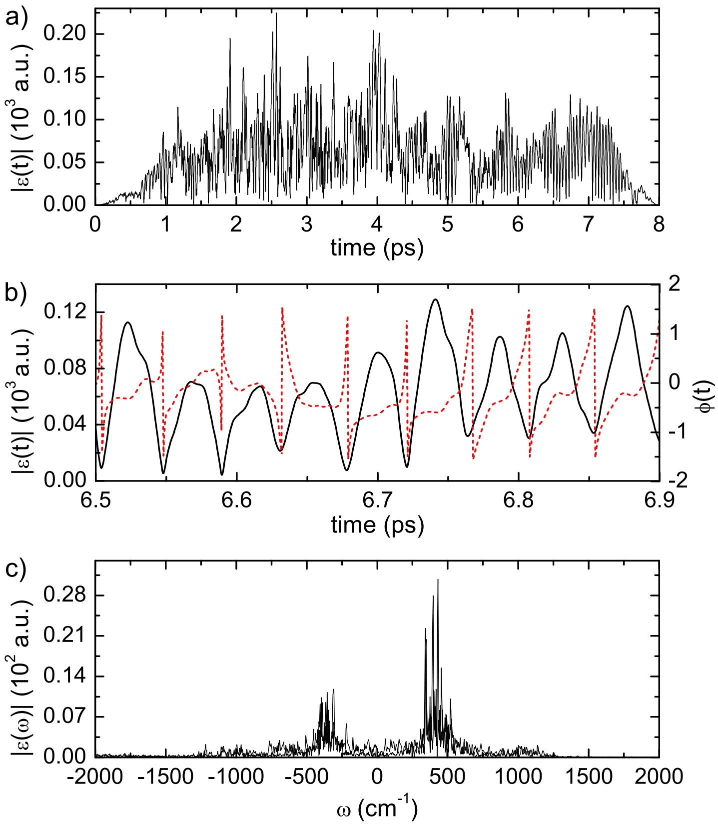

Figure 5.7: Temporal envelope (a) and spectrum (c) of an optimized pulse. (b) Envelope (left scale, solid black line) and temporal phase (right scale, red dashed line) of the optimized pulse in a short time interval.

wave packet, estimated above to be between 20 ps and 30 ps. In fact, optimizations with pulse durations of 20 ps and 30 ps yield stabilization efficiencies of 93% and 99%, respectively, with pulse energies below 150 nJ. However, we restrict our analysis to pulse durations up to 10 ps since stretching a TL 100 fs pulse by more than a factor of 100 due to the pulse shaping is not realistic.

Analyzing the time evolution of the population on each of the electronic states during an optimized pulse of 10 ps pulse duration, the molecules are found to first accumulate in the intermediate $A^1\Sigma_u^+$ and $b^3\Pi_u$ states before being dumped to the $X^1\Sigma_g^+$ electronic ground state. The example of an optimized pulse with pulse duration of 8 ps is presented in Fig. 5.7. Inspection of the optimized pulse during a short interval of 400 fs, Fig. 5.7(b), reveals that each peak of the pulse amplitude is correlated to a change of the temporal phase by π. The spectrum, Fig. 5.7(c), displays two pronounced peaks with maxima at $\pm 400\,\mathrm{cm}^{-1}$ with respect to the central laser frequency. The disappearence of the central frequency during the optimization and appearance of two slightly detuned frequencies is somewhat surprising since the central frequency was chosen to maximize the effective two-photon transition moment. There are two possibilities to rationalize this result of the optimization: Either the detuning shifted by the additional $400\,\mathrm{cm}^{-1}$ is better and should be chosen for the guess pulse, or the absorption of two photons with different energies is more optimal than that of two identical photons. The latter explains the observed optimal spectrum: Analysis of the electric transition dipole moment between the initial wave packet and the intermediate vibrational levels, $\langle \Psi_{in} | \hat{\mathbf{d}}_{\mathbf{e}} | v' \rangle$, reveals that it takes its maximal value for levels v' that are detuned from the frequency corresponding to the maximum of the effective two-photon transition moment by $460\,\mathrm{cm}^{-1}$. The electric transition dipole moment between the intermediate and the ground state vibrational level, $\langle v' | \hat{\mathbf{d}}_{\mathbf{e}} | v'' \rangle$, attains its maximum for a transition frequency that is smaller than the laser frequency corresponding to the maximum of the effective two-photon transition moment by $250\,\mathrm{cm}^{-1}$. Note that the transition moments for absorption of the first photon, $\langle \Psi_{in} | \hat{\mathbf{d}}_{\mathbf{e}} | v' \rangle$, are about 7 times smaller than those for absorption of the second photon, $\langle v' | \hat{\mathbf{d}}_{\mathbf{e}} | v'' \rangle$. The effective two-photon transition moment is obtained as a compromise of the two one-photon transition moments. Allowing for two photons of different energy in the calculation of the effective two-photon transition moment, we still find a peak for a ground state binding energy of $2650\,\mathrm{cm}^{-1}$, which is at best 40% higher when energies of photons are detuned by $\pm 390\,\mathrm{cm}^{-1}$. It corresponds to the transition frequency from the initial wave packet to the intermediate state being $390\,\mathrm{cm}^{-1}$ larger and that between the intermediate state and the ground electronic state being $390\,\mathrm{cm}^{-1}$ smaller than the frequency for a transition with two identical photons. Equipped with this information, we can construct a guess pulse that is the sum of two TL pulses with their central frequencies separated by $780\,\mathrm{cm}^{-1}$. In this case, half of the integrated guess pulse energy is sufficient to reach the same initial stabilization probability, reflecting the stronger effective two-photon transition moment but the bound for the stabilization efficiency, Fig. 5.6, remains in place.

Chapter 6

Non-resonant light control

6.1 Introductory remarks

Full quantum control of molecular processes, especially of bimolecular reactions, is an ultimate and still elusive goal of the ultracold community. On one hand, the molecular dynamics can be driven by shaped short laser pulses on the time scale of rotational and vibrational motion as presented in Chapter 5. On the other hand, the static electric, magnetic, or laser fields can be used to modify the molecular structure and collisional processes. At ultralow temperatures, the collisional process can be characterized by a single parameter, the scattering length. It has been shown that the scattering length can be controlled with a dc electric field [190, 191, 380], nearly resonant light [116], non-resonant light [194], optically induced Feshbach resonances [381], or optically controled molecular dark states [193].

A non-resonant laser light, i.e. a laser light far detuned from any transition, was recently proposed to enhance the photoassociation efficiency by controlling the positions of shape resonances [194]. However, there is no much knowledge about the influence of the strong non-resonant field on the structure of excited rovibrational levels and stabilization pathways in the schemes of formation of ultracold ground-state molecules. At the same time strong pulses of non-resonant light are used for alignment and orientation of molecules [266, 382, 383], controlling rotational dynamics [265, 384, 385], and even controlling the photochemical processes [386]. That makes non-resonant light a promising and potentially universal knob to control the quantum molecular processes [387].

Inspired by the proposal for controlling photoassociation with non-resonant light, one can ask a question how to use the non-resonant light to control magnetoassociation. At present one of the most challenging and required goals is the formation of ultracold polar molecules with spin structure e.g. from the mixtures of open-shell and closed-shell atoms. Somewhat unexpectedly, Feshbach resonances have been predicted for diatomics with a $^2\Sigma$ ground electronic state such as RbSr and LiYb [130, 131]. The resonances are caused by a modification of the alkali atom's hyperfine structure due to the presence of the other atom [130] or by creating a hyperfine coupling due to the alkali atom polarizing the nuclear spin density of fermionic Yb [131]. However, the width of these resonances does not exceed a few milli-Gauss. This renders their use in magnetoassociation very difficult, if not impossible.

In this chapter, first we investigate the influence of the non-resonant laser field on the rovibrational dynamics and electric dipole transitions in the open-shell molecules, and next we propose the new scheme of engineering the position and width of magnetic Feshbach resonances in polar open-shell molecules with non-resonant light.

6.2 Influence of a non-resonant light on the rovibrational structure

In this section we formulate the theory for a diatomic molecule in a spatially degenerate electronic state interacting with a non-resonant laser field and investigate its rovibrational structure in the presence of the field. When a molecule is exposed to strong non-resonant light, its rovibrational levels get hybridised. We study the spectroscopic signatures of this effect for transitions between the $X^1\Sigma_g^+$ electronic ground state and the coupled by spin-orbit interaction $A^1\Sigma_u^+$ and $b^3\Sigma_u$ excited state manifold. We find that for non-resonant field strengths of the order $10^9\,\mathrm{W/cm^2}$, the spin-orbit interaction and coupling to the non-resonant field become comparable. The non-resonant field can then be used to control the singlet-triplet character of a rovibrational level. A detailed description of the results is presented in Paper II.

Theoretical model

We consider the interaction of a homonuclear diatomic molecule with an electric field with the direction taken along the Z axis of the space-fixed coordinate system, $\vec{\mathcal{E}} = (0, 0, \mathcal{E})$. To the second order, the Hamiltonian for the interaction of the molecule with the electric field in the space-fixed frame can be written as,

$$H_{\mathrm{int}} = -\frac{1}{2}\alpha_{ZZ}^{\mathrm{SF}}\mathcal{E}^2\,, \tag{6.1}$$

where $\alpha_{ZZ}^{\mathrm{SF}}$ denote the appropriate component of the electric dipole polarizability in the space-fixed frame. To evaluate the matrix elements of the Hamiltonian in the electronic and rovibrational basis, we rewrite $\alpha_{ZZ}^{\mathrm{SF}}$ in terms of space-fixed irreducible tensor components $\alpha_m^{(l),\mathrm{SF}}$ [299]. For the irreducible tensor components, the transformation from the space-fixed to the body-fixed coordinate system is given simply by the rotation matrices $D_{m,k}^{(l)\star}(\widehat{R})$ [cf. Eq. (3) in Paper II]. For simplicity, we omit the superscripts SF/BF in the rest of the section as from now we will use only the body-fixed quantities.

For any diatomic molecule, the non-zero irreducible components of the dipole polarizability are $\alpha_0^{(0)}$ and $\alpha_0^{(2)}$. In addition, for a diatomic molecule in a Π electronic state, the $\alpha_{-2}^{(2)}$ and $\alpha_2^{(2)}$ terms do not vanish. They should be viewed as off-diagonal polarizability tensor components connecting two degenerate electronic states, $|\Pi_1\rangle$ and $|\Pi_{-1}\rangle$, with opposite projection of the total electronic orbital angular momentum on the molecular axis. See, for instance, Eq. (16) of Ref. [388].

The non-vanishing body-fixed polarizability components are most conveniently expressed in terms of the Cartesian tensor elements α_{ii}, $i = x, y, z$. Then $\alpha_0^{(0)}$ is related to the trace of the polarizability, $\alpha_0^{(0)} = -\frac{1}{\sqrt{3}}\left(\alpha_{xx}+\alpha_{yy}+\alpha_{zz}\right)$, $\alpha_0^{(2)}$ to the anisotropy of the polarizability, $\alpha_0^{(2)} = \frac{1}{\sqrt{6}}\left(2\alpha_{zz}-\alpha_{xx}-\alpha_{yy}\right)$ and, for a molecule in a Π electronic state, $\alpha_{-2}^{(2)}$ and $\alpha_2^{(2)}$ reflect the difference between two perpendicular components, $\alpha_2^{(2)} = \alpha_{-2}^{(2)} = \alpha_{yy}-\alpha_{xx}$.

As presented in detail in Section 2 of Paper II one arrives at the following Hamiltonian for the interaction of the homonuclear diatomic molecule with the static electric field,

$$H_{\rm int} = -\frac{\mathcal{E}^2}{2}\left[-\frac{1}{\sqrt{3}}\alpha_0^{(0)} + \sqrt{\frac{2}{3}}\alpha_0^{(2)}P_2^0(\cos\theta) + \frac{1}{6}\alpha_2^{(2)}P_2^2(\cos\theta) + 4\alpha_{-2}^{(2)}P_2^{-2}(\cos\theta)\right]. \tag{6.2}$$

The above Hamiltonian is valid for any isolated electronic state of a diatomic homonuclear molecule. Albeit, the last two terms in this equation are relevant only for molecules in a Π electronic state. Let us stress here that although this form of the Hamiltonian seems a bit elaborate at first glance, it simplifies the evaluation of the matrix elements in the symmetry-adapted basis set, and it also avoids any ambiguities when employing the Cartesian polarizability components for degenerate electronic states. Equation (6.2) also assumes the frequency of the non-resonant field to be far from any resonance which allows for using the static polarizability and the two-photon rotating-wave approximation.

We construct the Hamiltonian for the nuclear motion in Hund's case (a) coupling scheme with the primitive basis functions $|n,\Lambda\rangle|S,\Sigma\rangle|J,\Omega,M\rangle$ that are products of the electronic $|n,\Lambda\rangle$, electron spin $|S,\Sigma\rangle$ and rotational $|J,\Omega,M\rangle$ functions. Here, j is the total angular momentum quantum number, S is the total electronic spin quantum number, Λ and Σ are the projections of the total electronic orbital and total electronic spin angular momenta onto the molecular axis, and M is the projection of the total angular momentum onto the Z space-fixed axis. n labels the nonrelativistic dissociation limit of the molecular state. We also define the projection of the total, electronic orbital plus spin, angular momentum onto the molecular axis, $\Omega = \Lambda + \Sigma$. For the coupled $A^1\Sigma_u^+$ and $b^3\Pi_u$ manifold, we consider the rovibrational levels of the e spectroscopic symmetry and odd parity. For simplicity, any hyperfine structure effects are neglected here. The properly symmetry-adapted Hund's case (a) wavefunctions read,

$$\begin{aligned}
|A^1\Sigma_{0_u^+}, J, M, e\rangle &= |A,0\rangle|0,0\rangle|J,0,M\rangle\,,\\
|b^3\Pi_{0_u^+}, J, M, e\rangle &= \frac{1}{\sqrt{2}}\left[|b,1\rangle|1,-1\rangle|J,0,M\rangle - |b,-1\rangle|1,1\rangle|J,0,M\rangle\right]\,,\\
|b^3\Pi_{2_u}, J, M, e\rangle &= \frac{1}{\sqrt{2}}\left[|b,1\rangle|1,1\rangle|J,2,M\rangle - |b,-1\rangle|1,-1\rangle|J,-2,M\rangle\right]\,.
\end{aligned} \tag{6.3}$$

The first two states have a projection of the total angular momentum onto the molecular axis $|\Omega| = 0$, while the third one has $|\Omega| = 2$. In the field-free case, the state with $|\Omega| = 2$ is decoupled from the states with $|\Omega| = 0$, and it is not accessible from the ground electronic state in the one-photon dipolar transitions considered here. Consequently, the field-free model Hamiltonian H_0 describing the nuclear motion in the manifol of the coupled $A^1\Sigma_u^+$ and $b^3\Pi_u$ states can be represented by following 2×2 matrix,

$$H_0 = \begin{pmatrix} T_R + \frac{\vec{j}^2}{2\mu R^2} + V^{A^1\Sigma_u^+}(R) & \xi_1(R) \\ \xi_1(R) & T_R + \frac{\vec{j}^2}{2\mu R^2} + V^{b^3\Pi_u}(R) - \xi_2(R) \end{pmatrix}, \tag{6.4}$$

where $T = T_R + \frac{\vec{j}^2}{2\mu R^2}$ is the sum of the vibrational and rotational kinetic energy operators with $\vec{j} = \vec{J} - \vec{L} - \vec{S}$ being the mechanical angular momentum of the molecule and $V^k(R)$, $k = A^1\Sigma_u^+$, $b^3\Pi_u$, denotes the respective potential energy curves in the Born-Oppenheimer approximation. $\xi_1(R) = \langle A^1\Sigma_u^+ | H_{\text{SO}} | b^3\Pi_u \rangle_{|\Omega|=0}$ and $\xi_2(R) = \langle b^3\Pi_u | H_{\text{SO}} | b^3\Pi_u \rangle_{|\Omega|=0}$ are the spin-orbit coupling matrix elements, and only the electronic states with $|\Omega| = 0$ are included. Our model does not account for Coriolis-type angular couplings, i.e., the couplings of the $\Omega = 0$ states with $\Omega = 1$ states because their effect on the rovibrational dynamics is negligible compared to the spin-orbit couplings, the error of the electronic structure data and the influence of the weak non-resonant field.

When the electric field is switched on, the $\Lambda = 1$ and $\Lambda = -1$ components of the $b^3\Pi_u$ state are coupled. The coupling results form the off-diagonal polarizability tensor components in the Hamiltonian of Eq. (6.2). Therefore, not only the interaction H_{int} from Eq. (6.2) has to be added to the Hamiltonian H_0 for the $A^1\Sigma_u^+$ and $b^3\Pi_u$ states with $|\Omega| = 0$, but also the matrix (6.4) has to be extended so as to include the $|\Omega| = 2$ component originating from the $b^3\Pi_u$ state since it has the Λ projections exactly opposite to those found in the state with $|\Omega| = 0$ while all other quantum numbers are the same. Hence, in the presence of the electric field the rovibrational levels of the $A^1\Sigma_u^+$ and $b^3\Pi_u$ manifold are obtained by diagonalizing the Hamiltonian represented by the following 3×3 matrix,

$$H = \begin{pmatrix} T + W^{A^1\Sigma_u^+}(R,\theta) & \xi_1(R) & 0 \\ \xi_1(R) & T + W^{b^3\Pi_u}(R,\theta) - \xi_2(R) & W_{0/2}(R,\theta) \\ 0 & W_{0/2}(R,\theta) & T + W^{b^3\Pi_u}(R,\theta) + \xi_2(R) \end{pmatrix}. \tag{6.5}$$

The diagonal elements of the interaction potentials incorporating the interaction with non-resonant field are given by,

$$W^k(R,\theta) = V^k(R) + H^k_{\text{int}}, \tag{6.6}$$

where $k = A^1\Sigma_u^+$ or $b^3\Pi_u$ and H^k_{int} is given by Eq. (6.2) for the electronic state labeled by k. The off-diagonal term due to the non-resonant field, $W_{0/2}(R,\theta)$, couples the $|\Omega| = 0_u^+$ and $|\Omega| = 2_u$ components resulting from the $b^3\Pi_u$ state. It is proportional to the off-diagonal polarizability of the molecule in the $b^3\Pi$ state,

$$W_{0/2}(R,\theta) = -\frac{1}{12}\mathcal{E}^2 \alpha_2^{(2),b^3\Pi_u}(R) P_2^2(\cos\theta). \tag{6.7}$$

Analogously to Eqs. (6.5) and (6.6), the Hamiltonian for the molecule in its electronic ground state interacting with a non-resonant field is simply given by $T + W^{X^1\Sigma_g^+}(R,\theta)$.

The rovibrational levels of $X^1\Sigma_g^+$ ground and $A^1\Sigma_u^+$ and $b^3\Pi_u$ excited state manifold in the field are computed by diagonalizing the full two-dimensional Hamiltonian Eq. (6.5) represented on a mapped Fourier grid, employing about $N_R = 512$ radial grid points complemented by a basis set expansion in terms of Legendre polynomials for the angular part, taking advantage of the magnetic quantum number m being conserved. We find that $j_{max} = 19$ is sufficient to obtain converged results for $I \leq 2 \times 10^9\,\mathrm{W/cm^2}$.

Results

Bound rovibrational levels are strongly affected by a non-resonant field [194]. We demonstrate in this section that not only the levels are shifted in energy and their rotational motion is strongly hybridized, but also, for levels in the coupled $A^1\Sigma_u^+$ and $b^3\Pi_u$ excited state manifold, the singlet-triplet composition can be changed. Note that the non-resonant field mixes different rotational and possibly also vibrational states, and in the presence of the field, v, j, v', j' are not good quantum numbers anymore. However, for simplicity, we do not distinguish between the field-free quantum numbers v, j, v', j' and the corresponding field-dressed labels $\tilde{v}, \tilde{j}$, $\tilde{v}', \tilde{j}'$ [194]. The carbon dioxide laser with wavelength of about $10\,\mu$m is assumed to be used as a source of a non-resonant field. For this wavelength, the static electric dipole polarizability is good approximation for the dynamic one with a few percent error both for the ground and excited $A + b$ states.

Comparing three different intensities, Fig. 6.1 illustrates the effect of the non-resonant field on the transition dipole matrix elements for transitions between the $X^1\Sigma_g^+$ ground state and the $A^1\Sigma_u^+$ and $b^3\Pi_u$ excited states. The transition dipole matrix elements are calculated as rovibrational average of transition dipole moment for given field-dressed rovibrational levels, i.e., $\sum_{k=A^1\Sigma_u^+, b^3\Pi_u} \left\langle \varphi^k_{v',j'} \middle| d_z(k \leftarrow X)(R) \cos\theta \middle| \varphi^{X^1\Sigma_g^+}_{v,j} \right\rangle$, and shown for the $X^1\Sigma_g^+$ state ground level in Fig. 6.1(a) and a vibrationally highly excited level in Fig. 6.1(b). These levels could be studied using molecules in a molecular beam (a) or produced by photoassociation (b) [389]. Inspection of Fig. 6.1 reveals that the transitions get shifted as expected, due to the decrease of all eigenenergies in the non-resonant field [194]. Moreoever, the transition strengths are strongly modified. This modification is analyzed in more detail in Fig. 12 of Paper II for the strongest transition from the $X^1\Sigma_g^+$ state ground level indicated by an arrow in Fig. 6.1(a). For the largest intensity shown in Fig. 6.1, $I = 2 \cdot 10^9\,\mathrm{W/cm^2}$, the transition matrix elements for the strongest lines are clearly larger than in the field-free case. This is rationalized by an alignment of the field-dressed levels in the ground and excited electronic states, with $\langle \cos^2\theta \rangle \gtrsim 0.73$ for $I = 2 \cdot 10^9\,\mathrm{W/cm^2}$. Correspondingly, the field-dressed wavefunctions are localized in the angular regions θ close to 0 and π. As a consequence, the field-dressed transition strengths are larger than the field-free ones due to the angular dependence of the matrix elements on $\cos\theta$ [390].

Figure 13 of Paper II illustrates the effect of a non-resonant field on the transition dipole moments for a weakly bound level in the excited $A^1\Sigma_u^+$ and $b^3\Pi_u$ state manifold. This level is particularly well-suited for the photoassociative production of Rb_2 molecules [389], and the

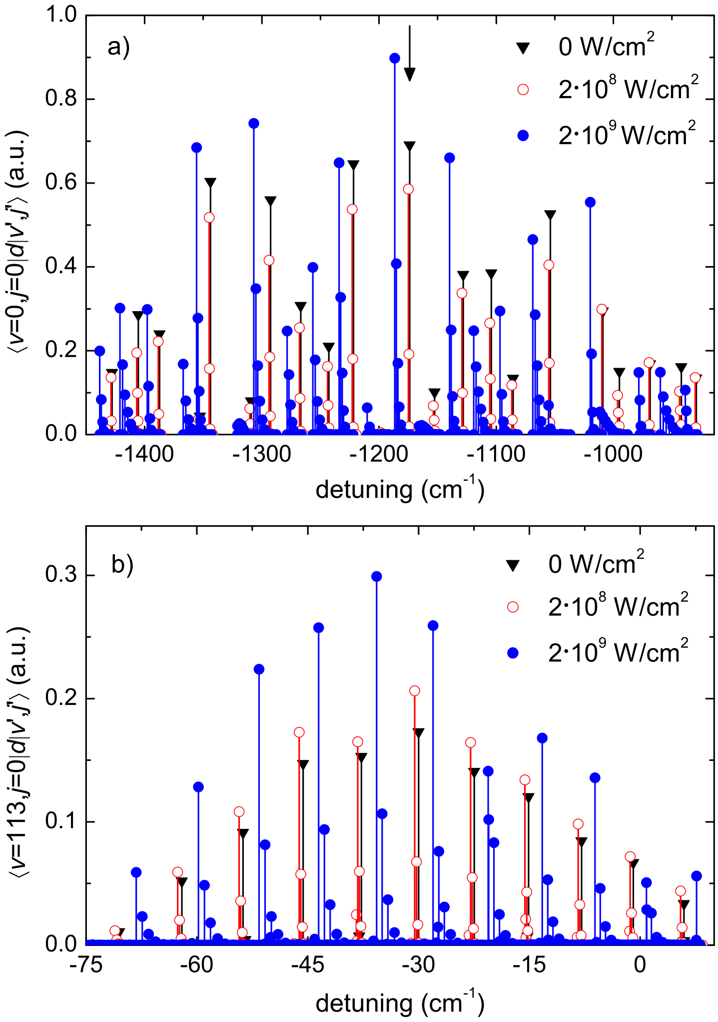

Figure 6.1: Transition dipole matrix elements between the ground rovibrational level $v = 0, j = 0$ (a) and the highly excited level $v = 113, j = 0$ (b) of the $X^1\Sigma_g^+$ ground electronic state and rovibrational levels of the $A^1\Sigma_u^+$ and $b^3\Pi_u$ manifold for three intensities of the non-resonant field in $^{87}\mathrm{Rb}_2$. The binding energy of the field-free $X^1\Sigma_g^+$ $v = 113, j = 0$ level is $E_b = 8.3\,\mathrm{cm}^{-1}$. The detuning is computed as $E_{v',J'} - E_{v,J} - (E_{^2P_{1/2}} - E_{^2S})$, with $E_{^2P_{1/2}}$, $E_{^2S}$ the field-free energies of the atomic levels.

analysis of Fig. 13 of Paper II is motivated by a recent proposal for enhancing photoassociation rates using a non-resonant field [194]. The non-resonant field will affect the spontaneous decay of the photoassociated molecules which is governed by the matrix elements shown in Fig. 13 of Paper II. A weak non-resonant field splits the two lines originating from the $j' = 1$ level into several ones, similar to Fig.12(c) of Paper II. The transition strength for $j = 0$ is almost not affected by the weak field. This behavior is similar to what has been observed for transitions between weakly bound levels of the strontium dimer [194]. For a strong non-resonant field, the binding energies are shifted and the overall behavior is similar to Ref. [194]. This implies that a non-resonant field may enhance the photoassociation rate without compromising an efficient stabilization into bound ground state levels by spontaneous emission as it was observed in Ref. [389].

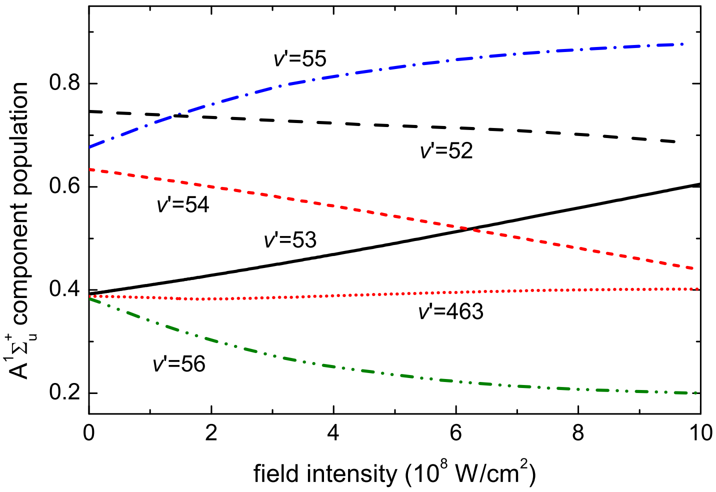

Figure 6.2: Singlet component of the coupled excited state rovibrational levels vs non-resonant field intensity with v' the field-free vibrational quantum number. Data shown for $j = 1$ (the behavior for other j is very similar).

Finally, Fig. 6.2 analyzes the interplay of the spin-orbit coupling and the interaction with the non-resonant field for several of the rovibrational levels of the $A^1\Sigma_u^+$ and $b^3\Pi_u$ manifold. Surprisingly, the levels from the middle of the well, $v' = 52, \ldots, 56$, show a remarkable dependence of the singlet-triplet decomposition on the non-resonant field intensity. On the other hand, the singlet-triplet character of weakly bound levels of the $A^1\Sigma_u^+$ and $b^3\Pi_u$ manifold, shown here for the representative $v' = 463$, is hardly affected. This behavior can be understood by inspection of the R-dependence of the polarizability components and the spin-orbit coupling matrix elements, cf. Fig. 7 and 9 of Paper II. Weakly bound levels have most of their amplitude at internuclear separations larger than $R = 20\,\mathrm{a}_0$. The spin-orbit coupling is strong at large internuclear separations and smaller at intermediate separations, while the opposite is true for the polarizability components. A large dependence of the singlet-triplet character on the non-resonant field intensity is expected when the interaction energy with the field and the spin-orbit coupling become comparable. Due to the R-dependence of the polarizability, for weakly bound levels this requires field intensities in excess of $10^{10}\,\mathrm{W/cm}^2$. On the other hand, the more deeply bound levels, $v' = 52, \ldots, 56$, have their outer turning point near $R = 12\,a_0$ where the polarizability is large and the spin-orbit coupling is small. Therefore, intensities of the order of $10^9\,\mathrm{W/cm}^2$ yield an interaction energy with the field that is comparable to the spin-orbit coupling. For example, for $10^9\,\mathrm{W/cm}^2$, the Stark shift of the levels amounts to about $15\,\mathrm{cm}^{-1}$. Their vibrational spacing, of the order of $20\,\mathrm{cm}^{-1}$, is also comparable. The interaction with the non-resonant field will then affect the singlet-triplet character of a rovibrational wavefunction, provided the R-dependence of polarizabilities differs for singlet and triplet states. This is indeed the case, cf. Fig. 9 of Paper II, explaining the changes in the singlet-triplet decomposition observed in Fig. 6.2.

6.3 Non-resonant light control of magnetic Feshbach resonances

In the present section we show that the non-resonant light, which universally couples to the polarizability anisotropy of a molecule, induces Feshbach resonances and modifies their positions and widths in the mixtures of open-shell/closed-shell atoms. This is due to the non-resonant light changing the background scattering length and altering the differential magnetic susceptibility. Our proposal opens the way for producing ultracold molecules with sizeable electric and magnetic dipole moments and thus for many-body quantum simulations with such particles. A detailed description is presented in Paper IV.

Theoretical model

Magnetoassociation can employ an adiabatic ramp of the magnetic field across the resonance or a time-dependent magnetic or radio-frequency (rf) field that drives a transition from a scattering state to a molecular level [111]. These two routes imply different requirements on the characteristics of the resonance. In both cases, a broad FR is needed. Adiabatic passage additionally requires a large product of the width, Δ, and background scattering length, a_{bg}. This is seen in the atom-molecule conversion efficiency, given by the Landau-Zener formula $1 - \exp\left[-\eta n \frac{\hbar}{\mu}\left|\frac{a_{bg}\Delta}{\dot{B}}\right|\right]$ with n the atomic number density, $\dot{B}$ the magnetic field ramp speed, μ the reduced mass and η a dimensionless prefactor [391]. Using the Fermi's Golden Rule, the resonance width Δ can be estimated from the expression

$$\Delta \sim \frac{|\langle v|H|k\rangle|^2}{a_{bg}\delta\chi}\,, \tag{6.8}$$

in terms of the coupling $\langle v|H|k\rangle$ between the molecular level $|v\rangle$ and scattering states $|k\rangle$, the background scattering length a_{bg}, and the differential magnetic susceptibility, $\delta\chi$ [132]. The latter is simply the difference in slope of the bound and continuum energies as a function of the magnetic field at resonance. When the background scattering length a_{bg} is larger than the mean scattering length $\bar{a}$ ($\bar{a} \approx 0.48(2\mu C_6/\hbar)^{1/4}$ with C_6 the dispersion coefficient), the coupling $|\langle v|H|k\rangle|$ becomes proportional to a_{bg}. The width is then determined by the background scattering length and differential magnetic susceptibility, $\Delta \sim a_{bg}/\delta\chi$ [132]. The key point of our proposal is that both $\delta\chi$ and a_{bg} can be tuned by applying a non-resonant field. This leads to significant changes in the resonance width Δ and the adiabaticity parameter $|a_{bg}\Delta|$.

The Hamiltonian describing the relative nuclear motion of an open-shell ${}^2S$ atom, a, and a closed-shell ${}^1S$ atom, b, reads

$$\hat{H} = \frac{\hbar^2}{2\mu}\left(-\frac{1}{r}\frac{d^2}{dr^2}r + \frac{\hat{L}^2}{r^2}\right) + \hat{H}_a + \hat{H}_b + V(r,\theta)\,, \tag{6.9}$$

where r is the interatomic separation, $\hat{L}$ the rotational angular momentum operator, and θ the angle between the molecular axis and the space-fixed Z-axis. The atomic Hamiltonian including Zeeman and hyperfine interactions is given by

$$\hat{H}_j = \zeta_j \hat{i}_j \cdot \hat{s}_j + \left(g_e\mu_B\hat{s}_{j,z} + g_j\mu_N\hat{i}_{j,z}\right)B\,, \tag{6.10}$$

with $\hat{s}_j$ and $\hat{i}_j$ the electron and nuclear spin operators, $g_{e/j}$ the electron and nuclear g factors, and $\mu_{B/N}$ the Bohr and nuclear magnetons. ζ_j denotes the hyperfine coupling constant. For a fermionic closed-shell ${}^1S$ atom, Eq. (6.10) reduces to the nuclear Zeeman term, whereas for a bosonic one it is zero. The interatomic interaction reads

$$V(r,\theta) = V_{X^2\Sigma^+}(r) + \Delta\zeta_a(r)\hat{i}_a \cdot \hat{s}_a - \frac{I}{2\epsilon_0 c}\left(\alpha_\perp(r) + \Delta\alpha(r)\cos^2\theta\right)$$

for both the magnetic and non-resonant laser fields parallel to the space-fixed Z-axis. $V_{X^2\Sigma^+}(r)$ is the potential energy curve for the $X^2\Sigma^+$ ground electronic state, and $\Delta\zeta_a(r)$ the interaction-induced variation of the hyperfine coupling constant [130, 131]. The molecular static polarizability with perpendicular component $\alpha_\perp(r)$ and anisotropy $\Delta\alpha(r)$ couples to non-resonant light of intensity I, linearly polarized along the space-fixed Z-axis. We omit spin-rotation coupling terms as well as the coupling resulting from a non-zero nuclear spin of a fermionic closed-shell atom since they are significantly smaller than $\Delta\zeta_a(r)$.

We focus on RbYb for which spectroscopic and *ab initio* data for the interaction potential are available [392]. The r-dependent isotropic and anisotropic polarizabilities were calculated in chapter 3.6. The interaction-induced variation of the hyperfine coupling, $\Delta\zeta_a(r)$, is taken from Ref. [132]. The total scattering wave function is constructed in an uncoupled basis set, $|i_a, m_{i,a}\rangle|s_a, m_{s,a}\rangle|L, m_L\rangle$ with m_j the projection of the angular momentum j on the space-fixed Z axis, assuming the projection of the total angular momentum of rubidium $m_f = m_{i,a} + m_{s,a}$ to be conserved. The coupled channels equations are solved using the renormalized Numerov propagator [350]. The scattering lengths and elastic cross sections are obtained from the S matrix for the entrance channel, $a = (1 - S_{11})/(1 + S_{11})/(ik)$ and $\sigma_{el} = \pi|1 - S_{11}|/k^2$, with $k = \sqrt{2\mu E}/\hbar$ and E the collision energy, assumed to be 100 nK. The resonance width Δ is determined by fitting the scattering length to $a(B) = a_{bg}(1 - \Delta/(B - B_{res}))$ [24, 111].

Results

Non-resonant light modifies the energies of rovibrational levels and scattering states alike [393, 394, 194, 276]. The latter implies control of scattering properties such as the cross sections. This is illustrated by Fig. 1 of Paper IV which displays a series of maxima and minima of the elastic cross section as a function of non-resonant field intensity. New Feshbach resonances are created by the non-resonant light shifting bound levels. This happens when a bound level crosses the atomic threshold of a different hyperfine level as indicated by the dots in Fig. 6.3(a). New resonances, higher than s-wave, may also be induced by mixing partial waves or by spin-rotation coupling between higher partial waves. The non-resonant field dependence of the background scattering length observed in Fig. 1 of Paper IV and the creation of new Feshbach resonance due to the non-resonant light shown in Fig. 6.3 together with Eq. (6.8) suggest three mechanisms to increase the width of Feshbach resonances: (i) $\delta\chi \to 0$, (ii) $|a_{bg}| \to \infty$, and (iii) $|a_{bg}| \to 0$. In case (i), $|a_{bg}\Delta|$ becomes large unless it coincides with case (iii), and large $|a_{bg}\Delta|$ is guaranteed in case (ii). Then both adiabatic ramping across the resonance and rf association

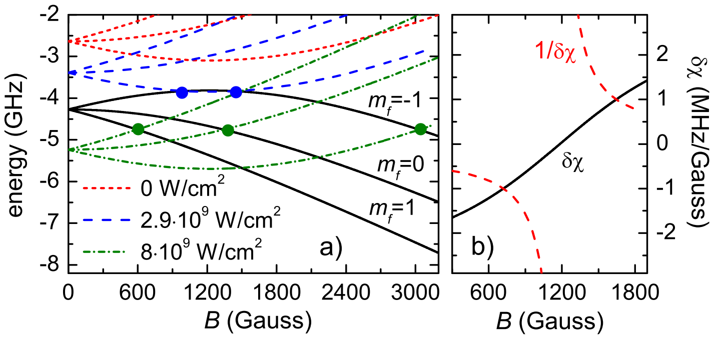

Figure 6.3: Creating new FR with non-resonant light: (a) Atomic thresholds (solid black lines) start to cross molecular levels (dashed lines) as the non-resonant light shifts the level positions (^{87}Rb^{176}Yb with $|m_f| \leq i_a - 1/2$). The dots indicate the position of the new FR. (b) The level shifts are accompanied by a variation of the differential magnetic susceptibility $\delta\chi$ vs magnetic field ($m_f = -1$, $I = 0$).

are possible. In contrast, $|a_{bg}\Delta|$ will always stay small in the case (iii), preventing adiabatic passage. Since adiabatic ramping is the most popular technique for magnetoassociation, we focus on the cases (i) and (ii) here and will report on case (iii) elsewhere [395].

We find that the case (i) yields the largest widths. This is illustrated in Fig. 6.4(a) for ^{87}Rb^{176}Yb: A pair of resonances is created when the molecular level crosses an atomic threshold close to the maximum of its magnetic field dependence, cf. blue dots in Fig. 6.3(a). The resonances come with a very large width Δ, of the order of a few Gauss, cf. the left peak in Fig. 6.4(a), and are separated by several Gauss (by 6 G for example for $\Delta \approx 3$ G). The large width is rationalized by the broad pole of $1/\delta\chi$ shown in Fig. 6.3(b) which enters Eq. (6.8). Not only the width Δ but also the adiabaticity parameter $|a_{bg}\Delta|$ is found to be large, of the order of 10 a_0·G, whereas the background scattering length remains comparatively small, of the order of 10 a_0. A second peak of the width Δ, of the order of 10 G, is observed in Fig. 6.4(a), at $I = 2.88 \cdot 10^9$ W/cm^2. It is caused by a_{bg} going to zero, which can be inferred from the corresponding minimum of the blue dashed curve in Fig. 1 of Paper IV. The joint occurrence of $\delta\chi \to 0$ and $a_{bg} \to 0$ is a coincidence. As can be seen in Fig. 6.4(a) and (b), such a coincidence leads to particularly broad resonances for a range of non-resonant field intensities which at the same time are separated by several hundreds Gauss. However, due to $a_{bg} \to 0$, the adiabaticity parameter $|a_{bg}\Delta|$ remains small. The adiabaticity parameter is guaranteed to be large in case (ii) when the non-resonant field is used to tune the background scattering length to very large values. This is illustrated in Fig. 6.4c) and d). The maximum width Δ which is not limited in theory will depend on the stability of the non-resonant field intensity in practice. For example, an increase by 10^3 requires intensity stabiliziation of the order 10^{-3} to 10^{-4}. The actual value of Δ that can be obtained also depends on the field-free width. But even for very narrow resonances, with the field-free Δ below 1 mG, the engineered width easily reaches 100 mG, as demonstrated by Fig. 6.4c).

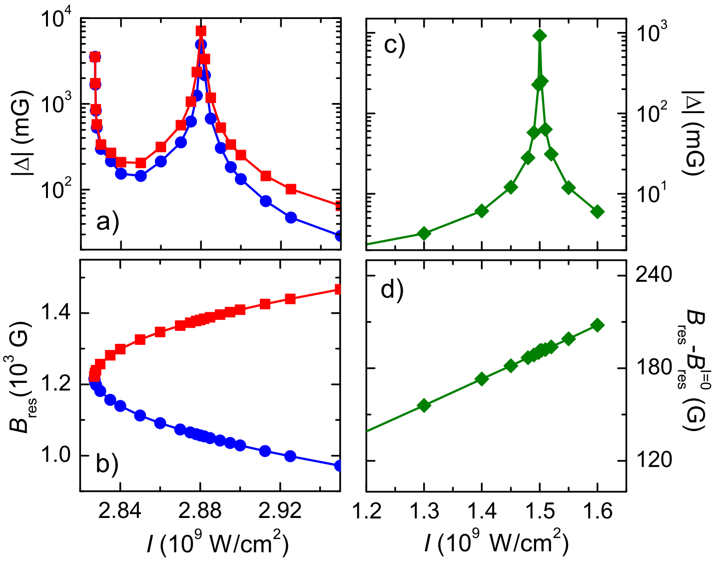

Figure 6.4: Controlling the width of a FR by modifying $\delta\chi$ (a),(b): Resonance width Δ and resonance position B_{res} vs non-resonant light intensity for ^{87}Rb^{176}Yb and the pair of resonances indicated by blue dots in Fig. 6.3 ($m_f = -1$, $B_{res} = 1219\,$G). Controlling the width of a FR by tuning a_{bg} to large values (c,d): Resonance width Δ and change in resonance position $B_{res} - B_{res}^{I=0}$ vs non-resonant light intensity for ^{87}Rb^{172}Yb ($m_f = 1$, $B_{res}^{I=0} = 1592\,$G).

We find non-resonant light intensities of the order of 10^9 W/cm^2 to be sufficient to create FRs for all isotopologues of RbYb. The smallest intensity is required for diatomics with a molecular level just above the atomic threshold since the non-resonant field always lowers the energy in the electronic ground state [276]. For example, a pair of broad resonances as shown in Fig. 6.4(a),(b) is also observed for ^{85}Rb^{170}Yb (with $\Delta > 0.5\,$G at $I = 1.29 \cdot 10^9\,$W/cm^2). When only the rubidium isotope is exchanged, the dependence on the non-resonant light intensity remains essentially unchanged compared to Fig. 6.4(a),(b). Of course, different hyperfine levels may come into play, e.g., $m_f = -2$ or $m_f = -1$, which imply different magnetic fields ($B_{res} = 722\,$G and $B_{res} = 361\,$G, respectively, for ^{85}Rb^{176}Yb). The left peak of Δ in Fig. 6.4(a) and the associated increase in $|a_{bg}\Delta|$ is found for all RbYb isotopologues. The right peak corresponds to a coincidence of case (i) with case (iii) and is specific to ^{87}Rb^{176}Yb. Case (i) may coincide also with case (ii). This happens for ^{87}Rb^{174}Yb, yielding an adiabaticity parameter $|a_{bg}\Delta|$ of the order of 100 $a_0 \cdot$G. Case (ii), i.e., large a_{bg}, is most easily realized for molecules with a large and negative field-free background scattering length a_s. For ^{87}Rb^{172}Yb shown in Fig. 6.4c,d) for example $a_s = -131\,a_0$ [396]. Another good candidate for case (ii) is ^{87}Rb^{173}Yb (with $a_s = -431\,a_0$ [396]).

The three mechanisms are generally applicable due to the universal coupling to non-resonant light. Notably, we find the characteristics of controlling the resonance width by tuning the background scattering length as shown in Fig. 6.4c,d) to be common to all $^2\Sigma$ molecules. When considering closed-shell/open-shell mixtures other than RbYb, different strengths of both magnetic field and non-resonant light might, however, be required. For example, LiYb has a smaller reduced mass than RbYb and Li a smaller polarizability than Rb which implies a larger non-resonant field intensity. The magnetic field strength for which a molecular level crosses the atomic threshold close to the maximum of its magnetic field dependence, relevant for case (i), is determined by the hyperfine splitting [132]. It is thus smaller for mixtures involving Li, Na or K and larger for those involving Cs instead of Rb. Prospects are best for RbSr and CsYb [395] for which the interaction induced variation of the hyperfine structure and the polarizabilities are largest. Together with the tunability of the field-free background scattering length by choice of the Yb isotope, this makes CsYb in particular another very promising candidate.

Our proposal for non-resonant light controlled magnetoassociation requires intensities of the order of $10^9\,\mathrm{W/cm}^2$ and magnetic fields of the order of 1000 G. These requirements are within current experimental capabilities. Intensities of the order $10^9\,\mathrm{W/cm}^2$ can be achieved using intracavity beams with spot sizes of about $10\,\mu$m and powers of the order of 1 kW. Such spot sizes could be desirable for creating an additional trap. Larger spot sizes, up to $100\,\mu$m, are possible when using an optical buildup cavity [397, 398]. The required intensity can be stabilized at a level of 0.001, but even 10^{-4} should be reachable with refined feedback techniques. Magnetic fields can be stabilized at the level 10^{-5}-10^{-6} [399] such that magnetic field stability is not a concern for the resonance widths and separations discussed here. Losses due to photon scattering can be kept minimal by choosing light, such as that of a CO_2 laser, that is far off resonance with any molecular transition. Estimating the heating rates for $I = 10^9\,\mathrm{W/cm}^2$ in terms of the atomic photon scattering rates [400], we find the largest heating rate, that of the alkali atom, to be only of the order of 1 nK/s for a wavelength of $10\,\mu$m.

Chapter 7

Summary and conclusions

The present thesis concerned theoretical studies of the quantum dynamics and control of ultracold molecules in external fields. The new schemes of the formation and quantum control have been proposed and investigated and pave the way towards the ultimate goal of the full quantum control over molecular processes.

The state-of-the-art *ab initio* methods have been applied to investigate the electronic structure of molecular systems important for the ongoing or planned experimental and theoretical research at ultralow temperatures. Next, the electronic structure data have been employed in both time-dependent and time-independent studies of molecular dynamics in the number of projects on the structure, formation, control, and collisions of ultracold atoms and molecules.

The main achievements of the thesis may be summarized as follows:

1. The electronic structure of the SrYb molecule has been investigated for the first time and employed to investigate the possibility of forming deeply bound ultracold SrYb molecules in an optical lattice in a photoassociation experiment using continuous-wave lasers, the first reported in the literature investigation of the formation of a polar ultracold molecule from two closed-shell atoms. Photoassociation near the intercombination line transition of atomic strontium into the vibrational levels of the strongly spin-orbit mixed $b^3\Sigma^+$, $a^3\Pi$, $A^1\Pi$, and $C^1\Pi$ states with subsequent efficient stabilization into the $v''=1$ vibrational level of the electronic ground state is proposed. Ground state SrYb molecules can be accumulated by making use of collisional decay from $v''=1$ to $v'''=0$. Alternatively, photoassociation and stabilization to $v''=0$ can proceed via stimulated Raman adiabatic passage provided that the trapping frequency of the optical lattice is large enough and phase coherence between the pulses can be maintained over at least tens of microseconds.

2. The electronic structure of the Rb_2 molecule has been investigated by employing the double electron attachment intermediate Hamiltonian Fock space coupled cluster method restricted to single and double excitations for all electronic states up to and including the

$5s + 5d$ dissociation limit at about 26,000 cm^{-1}. The calculation was the first reported in literature use of this recently developed method to generate highly accurate interatomic interaction potentials. In order to correctly predict the spectroscopic behaviour of Rb_2, the electric transition dipole moments, non-adiabatic coupling and spin-orbit coupling matrix elements, and static dipole polarisabilities have also been calculated with the multireference configuration interaction method.

3. The optimal control theory has been applied to ultracold multi-photon photoassociation. An optimization functional that suppresses atomic excitation and maximizes the formation of molecules has been derived and tested. The optimal control theory has been employed to maximize the efficiency of the non-resonant three-photon photoassociation of ultracold rubidium atoms when the initial state is the thermally populated continuum of scattering states in a magneto-optical trap. Using a linear variant of Krotov's method, we find that at ultralow temperatures a pulse optimized for one initial scattering energy works also for all other collision energies within the thermal ensemble and for the lowest partial waves. Our study is the first application of the optimal control theory properly treating the initial thermal ensemble of the scattering states in photoassociation and our results open the way to the coherent control of binary reactions.

4. Next we investigated the evolution of wave packet created in thee-photon photoassociation and employed a second laser pulse to drive a resonant two-photon transition transferring the excited-state wave packet to the ground electronic state. After analyzing the transition matrix elements governing the stabilization step, we discussed the efficiency of the population transfer by using the transform-limited and linearly chirped laser pulses. Finally, we employed the optimal control theory to determine the most efficient stabilization pathways. We found that the stabilization efficiency can be increased by one and two orders of magnitude when using linearly chirped and optimally shaped laser pulses, respectively.

5. The electronic structure of the $(\mathrm{LiYb})^+$ molecular ion has been investigated for the first time and the results of *ab initio* calculations have been employed in the scattering calculations. The prospects for the sympathetic cooling of the Yb^+ ion emerged into ultracold gas of Li atoms have been investigated. The rates for the elastic and inelastic due to the radiative charge transfer and radiative association collisions have been calculated. The photoassociation spectra for the one-photon formation of the singlet state molecular ion and for the two-photon formation of the triplet state molecular ion have been evaluated and single molecule photoassociation spectroscopy is proposed. Consequences of the present results for building a quantum simulator emulating solid-state physics with a hybrid system of ultracold Yb ions and Li atoms have been analyzed.

6. The influence of the non-resonant laser light on the rovibrational structure of open-

shell molecules has been investigated. The spectroscopic signatures of this effect in Rb_2 molecule for transitions between the $X^1\Sigma_g^+$ electronic ground state and the $A^1\Sigma_u^+$ and $b^3\Pi_u$ excited state manifold has been studied. The latter is characterized by strong perturbations due to the spin-orbit interaction. For non-resonant field strengths of the order $10^9\,\mathrm{W/cm}^2$, the spin-orbit interaction and coupling to the non-resonant field become comparable. The non-resonant field can then be used to control the singlet-triplet character of a rovibrational level.

7. The non-resonant laser light was proposed to be used to engineer the Feshbach resonances in their position and width in polar paramagnetic ground-state molecules. Magnetically tunable Feshbach resonances in such molecules are too narrow to allow for magnetoassociation starting from trapped, ultracold atoms. For non-resonant field intensities of the order of $10^9\,\mathrm{W/cm}^2$, we have found the width to be increased by three orders of magnitude, reaching a few Gauss. This opens the way for producing ultracold molecules with sizeable electric and magnetic dipole moments and thus for many-body quantum simulations with such particles.

8. A new class of highly magnetic and polar molecules consisting of chromium and closed-shell alkali-metal atoms has been proposed and investigated. These molecules are examples of species possessing large both magnetic and electric dipole moments making them potentially interesting candidates for ultracold many-body physics studies. Especially, the competition between the magnetic and electric dipolar interactions and the control with external electric and magnetic fields can be realized and investigated with these molecules .

9. The interactions of polar alkali-metal dimers in the quintet spin state have been investigated and the formation of deeply bound reaction complexes was demonstrated. The reaction complexes can decompose adiabatically into homonuclear alkali-metal dimers (for all molecules except KRb) and into alkali-metal trimers (for all molecules) with no barriers for these chemical reactions. This means that all alkali-metal dimers in the $a^3\Sigma^+$ state are chemically unstable at ultracold temperatures, and the use of an optical lattice to segregate the molecules and suppress the losses may be necessary. The unique features of the chemical reactions of ultracold alkali-metal dimers in the $a^3\Sigma^+$ electronic state that can be control with external electric fields have been discussed.

Six papers (Appendices A-F), published in international scientific journals, constitute the core of the thesis and contain a detailed account of the obtained results.

All programs written as a part of the graduate research have been included in the library of programs for the simulation of time-dependent quantum molecular dynamics QDYN developed in the group of professor Christiane Koch at the University of Kassel in Germany.

Bibliography

[1] S. Wróblewski and K. Olszewski. Ueber die Verflssigung des Sauerstoffs, Stickstoffs und Kohlenoxyds. *Annalen der Physik*, 256:243, 1883.

[2] H. K. Onnes. Further experiments with liquid helium. C. On the change of electric resistance of pure metals at very low temperatures etc. IV. The resistance of pure mercury at helium temperatures. In *KNAW, Proceedings*, volume 13, page 1910, 1911.

[3] P. Kapitza. Viscosity of liquid helium below the λ-point. *Nature*, 141:74, 1938.

[4] J. Allen and A. Misener. Flow of liquid helium II. *Nature*, 141:75, 1938.

[5] S. N. Bose. Plancks Gesetz und Lichtquantenhypothese. *Z. Phys.*, 26:178, 1924.

[6] A. Einstein. *Sitzber. Kgl. Preuss. Akad. Wiss.*, page 261, 1924.

[7] A. Einstein. Quantentheorie des einatomigen idealen Gases. *Sitzber. Kgl. Preuss. Akad. Wiss.*, page 3, 1925.

[8] S. Chu. Nobel lecture: The manipulation of neutral particles. *Rev. Mod. Phys.*, 70:685, 1998.

[9] C. N. Cohen-Tannoudji. Nobel lecture: Manipulating atoms with photons. *Rev. Mod. Phys.*, 70:707, 1998.

[10] W. D. Phillips. Nobel lecture: Laser cooling and trapping of neutral atoms. *Rev. Mod. Phys.*, 70:721, 1998.

[11] M. H. Anderson, J. R. Ensher, M. R. Matthews, C. E. Wieman, and E. A. Cornell. Observation of Bose-Einstein condensation in a dilute atomic vapor. *Science*, 269:198, 1995.

[12] K. B. Davis, M. O. Mewes, M. R. Andrews, N. J. van Druten, D. S. Durfee, D. M. Kurn, and W. Ketterle. Bose-Einstein condensation in a gas of sodium atoms. *Phys. Rev. Lett.*, 75:3969, 1995.

[13] E. A. Cornell and C. E. Wieman. Nobel lecture: Bose-Einstein condensation in a dilute gas, the first 70 years and some recent experiments. *Rev. Mod. Phys.*, 74:875, 2002.

[14] W. Ketterle. Nobel lecture: When atoms behave as waves: Bose-Einstein condensation and the atom laser. *Rev. Mod. Phys.*, 74:1131, 2002.

[15] R. Krems, B. Friedrich, and W. C. Stwalley, editors. *Cold Molecules: Theory, Experiment, Applications.* CRC Press, 2009.

[16] L. D. Carr, D. DeMille, R. V. Krems, and J. Ye. Cold and ultracold molecules: science, technology and applications. *New J. Phys.*, 11:055049, 2009.

[17] T. W. Hänsch. Nobel lecture: Passion for precision. *Rev. Mod. Phys.*, 78:1297, 2006.

[18] R. J. Glauber. Nobel lecture: One hundred years of light quanta. *Rev. Mod. Phys.*, 78:1267, 2006.

[19] J. L. Hall. Nobel lecture: Defining and measuring optical frequencies. *Rev. Mod. Phys.*, 78:1279, 2006.

[20] D. J. Wineland. Nobel lecture: Superposition, entanglement, and raising Schrödinger's cat. *Rev. Mod. Phys.*, 85:1103, 2013.

[21] S. Haroche. Nobel lecture: Controlling photons in a box and exploring the quantum to classical boundary. *Rev. Mod. Phys.*, 85:1083, 2013.

[22] J. Weiner, V. S. Bagnato, S. Zilio, and P. S. Julienne. Experiments and theory in cold and ultracold collisions. *Rev. Mod. Phys.*, 71:1, 1999.

[23] K. M. Jones, E. Tiesinga, P. D. Lett, and P. S. Julienne. Ultracold photoassociation spectroscopy: Long-range molecules and atomic scattering. *Rev. Mod. Phys.*, 78:483, 2006.

[24] T. Köhler, K. Góral, and P. S. Julienne. Production of cold molecules via magnetically tunable Feshbach resonances. *Rev. Mod. Phys.*, 78:1311, 2006.

[25] O. Dulieu and C. Gabbanini. The formation and interactions of cold and ultracold molecules: new challenges for interdisciplinary physics. *Rep. Prog. Phys.*, 72:086401, 2009.

[26] J. Ulmanis, J. Deiglmayr, M. Repp, R. Wester, and M. Weidemüller. Ultracold molecules formed by photoassociation: Heteronuclear dimers, inelastic collisions, and interactions with ultrashort laser pulses. *Chem. Rev.*, 112:4890, 2012.

[27] C. P. Koch and M. Shapiro. Coherent control of ultracold photoassociation. *Chem. Rev.*, 112:4928, 2012.

[28] M. D. Morse. Supersonic beam sources. *Experimental methods in the physical sciences*, 29:21, 1996.

[29] H. L. Bethlem and G. Meijer. Production and application of translationally cold molecules. *Int. Rev. Phys. Chem.*, 22:73, 2003.

[30] S. D. Hogan, M. Motsch, and F. Merkt. Deceleration of supersonic beams using inhomogeneous electric and magnetic fields. *Phys. Chem. Chem. Phys.*, 13:18705, 2011.

[31] N. R. Hutzler, H.-I. Lu, and J. M. Doyle. The buffer gas beam: An intense, cold, and slow source for atoms and molecules. *Chem. Rev.*, 112:4803, 2012.

[32] S. Y. T. van de Meerakker, H. L. Bethlem, N. Vanhaecke, and G. Meijer. Manipulation and control of molecular beams. *Chem. Rev.*, 112:4828, 2012.

[33] W. Gerlach and O. Stern. Der experimentelle Nachweis der Richtungsquantelung im Magnetfeld. *Z. Physik*, 9:349, 1922.

[34] E. Wrede. ber die Ablenkung von Molekularstrahlen elektrischer Dipolmolekle im inhomogenen elektrischen Feld. *Z. Physik*, 44:261, 1927.

[35] W. L. Fite and S. Datz. Chemical research with molecular beams. *Annu. Rev. Phys. Chem.*, 14:61, 1963.

[36] J. M. Hayes. Analytical spectroscopy in supersonic expansions. *Chem. Rev.*, 87:745, 1987.

[37] P. Casavecchia. Chemical reaction dynamics with molecular beams. *Rep. Prog. Phys.*, 63:355, 2000.

[38] J. M. Hutson. Intermolecular forces from the spectroscopy of van der waals molecules. *Annu. Rev. Phys. Chem.*, 41:123, 1990.

[39] H. L. Bethlem, G. Berden, and G. Meijer. Decelerating neutral dipolar molecules. *Phys. Rev. Lett.*, 83:1558, 1999.

[40] E. Narevicius and M. G. Raizen. Toward cold chemistry with magnetically decelerated supersonic beams. *Chem. Rev.*, 112:4879, 2012.

[41] H. Odashima, S. Merz, K. Enomoto, M. Schnell, and G. Meijer. Microwave lens for polar molecules. *Phys. Rev. Lett.*, 104:253001, 2010.

[42] S. A. Schulz, H. L. Bethlem, J. van Veldhoven, J. Küpper, H. Conrad, and G. Meijer. Microstructured switchable mirror for polar molecules. *Phys. Rev. Lett.*, 93:020406, 2004.

[43] H. L. Bethlem, G. Berden, F. M. Crompvoets, R. T. Jongma, A. J. Van Roij, and G. Meijer. Electrostatic trapping of ammonia molecules. *Nature*, 406:491, 2000.

[44] S. Y. T. van de Meerakker, P. H. M. Smeets, N. Vanhaecke, R. T. Jongma, and G. Meijer. Deceleration and electrostatic trapping of OH radicals. *Phys. Rev. Lett.*, 94:023004, 2005.

[45] F. M. Crompvoets, H. L. Bethlem, R. T. Jongma, and G. Meijer. A prototype storage ring for neutral molecules. *Nature*, 411:174, 2001.

[46] C. E. Heiner, H. L. Bethlem, and G. Meijer. A synchrotron for neutral molecules. *Chem. Phys. Lett.*, 473:1, 2009.

[47] P. C. Zieger, S. Y. T. van de Meerakker, C. E. Heiner, H. L. Bethlem, A. J. A. van Roij, and G. Meijer. Multiple packets of neutral molecules revolving for over a mile. *Phys. Rev. Lett.*, 105:173001, 2010.

[48] J. R. Bochinski, E. R. Hudson, H. J. Lewandowski, G. Meijer, and J. Ye. Phase space manipulation of cold free radical OH molecules. *Phys. Rev. Lett.*, 91:243001, 2003.

[49] M. R. Tarbutt, H. L. Bethlem, J. J. Hudson, V. L. Ryabov, V. A. Ryzhov, B. E. Sauer, G. Meijer, and E. A. Hinds. Slowing heavy, ground-state molecules using an alternating gradient decelerator. *Phys. Rev. Lett.*, 92:173002, 2004.

[50] S. Y. T. van de Meerakker, I. Labazan, S. Hoekstra, J. Kpper, and G. Meijer. Production and deceleration of a pulsed beam of metastable NH($a^1\Delta$) radicals. *J. Phys. B*, 39:S1077, 2006.

[51] E. R. Hudson, C. Ticknor, B. C. Sawyer, C. A. Taatjes, H. J. Lewandowski, J. R. Bochinski, J. L. Bohn, and J. Ye. Production of cold formaldehyde molecules for study and control of chemical reaction dynamics with hydroxyl radicals. *Phys. Rev. A*, 73:063404, 2006.

[52] S. K. Tokunaga, J. M. Dyne, E. A. Hinds, and M. R. Tarbutt. Stark deceleration of lithium hydride molecules. *New J. Phys.*, 11:055038, 2009.

[53] N. Vanhaecke, U. Meier, M. Andrist, B. H. Meier, and F. Merkt. Multistage Zeeman deceleration of hydrogen atoms. *Phys. Rev. A*, 75:031402, 2007.

[54] S. D. Hogan, D. Sprecher, M. Andrist, N. Vanhaecke, and F. Merkt. Zeeman deceleration of H and D. *Phys. Rev. A*, 76:023412, 2007.

[55] E. Narevicius, A. Libson, C. G. Parthey, I. Chavez, J. Narevicius, U. Even, and M. G. Raizen. Stopping supersonic oxygen with a series of pulsed electromagnetic coils: A molecular coilgun. *Phys. Rev. A*, 77:051401, 2008.

[56] A. Wiederkehr, H. Schmutz, M. Motsch, and F. Merkt. Velocity-tunable slow beams of cold O_2 in a single spin-rovibronic state with full angular-momentum orientation by multistage Zeeman deceleration. *Mol. Phys.*, 110:1807, 2012.

[57] S. D. Hogan, A. W. Wiederkehr, H. Schmutz, and F. Merkt. Magnetic trapping of hydrogen after multistage Zeeman deceleration. *Phys. Rev. Lett.*, 101:143001, 2008.

[58] S. Chervenkov, X. Wu, J. Bayerl, A. Rohlfes, T. Gantner, M. Zeppenfeld, and G. Rempe. Continuous centrifuge decelerator for polar molecules. *Phys. Rev. Lett.*, 112:013001, 2014.

[59] J. M. Doyle, B. Friedrich, J. Kim, and D. Patterson. Buffer-gas loading of atoms and molecules into a magnetic trap. *Phys. Rev. A*, 52:R2515, 1995.

[60] J. Kim, B. Friedrich, D. P. Katz, D. Patterson, J. D. Weinstein, R. DeCarvalho, and J. M. Doyle. Buffer-gas loading and magnetic trapping of atomic europium. *Phys. Rev. Lett.*, 78:3665, 1997.

[61] S. E. Maxwell, N. Brahms, R. deCarvalho, D. R. Glenn, J. S. Helton, S. V. Nguyen, D. Patterson, J. Petricka, D. DeMille, and J. M. Doyle. High-flux beam source for cold, slow atoms or molecules. *Phys. Rev. Lett.*, 95:173201, 2005.

[62] J. D. Weinstein, R. deCarvalho, J. Kim, D. Patterson, B. Friedrich, and J. M. Doyle. Magnetic trapping of atomic chromium. *Phys. Rev. A*, 57:R3173, 1998.

[63] N. Brahms, B. Newman, C. Johnson, T. Greytak, D. Kleppner, and J. Doyle. Magnetic trapping of silver and copper, and anomalous spin relaxation in the Ag-He system. *Phys. Rev. Lett.*, 101:103002, 2008.

[64] T. V. Tscherbul, J. Kłos, A. Dalgarno, B. Zygelman, Z. Pavlovic, M. T. Hummon, H.-I. Lu, E. Tsikata, and J. M. Doyle. Collisional properties of cold spin-polarized nitrogen gas: Theory, experiment, and prospects as a sympathetic coolant for trapped atoms and molecules. *Phys. Rev. A*, 82:042718, 2010.

[65] J. D. Weinstein, T. Guillet, B. Friedrich, and J. M. Doyle. Magnetic trapping of calcium monohydride molecules at millikelvin temperatures. *Nature*, 395:148, 1998.

[66] D. Egorov, W. Campbell, B. Friedrich, S. Maxwell, E. Tsikata, L. van Buuren, and J. Doyle. Buffer-gas cooling of NH via the beam loaded buffer-gas method. *Eur. Phys. J. D*, 31:307, 2004.

[67] K. Maussang, D. Egorov, J. S. Helton, S. V. Nguyen, and J. M. Doyle. Zeeman relaxation of CaF in low-temperature collisions with helium. *Phys. Rev. Lett.*, 94:123002, 2005.

[68] M. Stoll, J. M. Bakker, T. C. Steimle, G. Meijer, and A. Peters. Cryogenic buffer-gas loading and magnetic trapping of CrH and MnH molecules. *Phys. Rev. A*, 78:032707, 2008.

[69] S. C. Doret, C. B. Connolly, W. Ketterle, and J. M. Doyle. Buffer-gas cooled Bose-Einstein condensate. *Phys. Rev. Lett.*, 103:103005, 2009.

[70] C. J. Myatt, E. A. Burt, R. W. Ghrist, E. A. Cornell, and C. E. Wieman. Production of two overlapping Bose-Einstein condensates by sympathetic cooling. *Phys. Rev. Lett.*, 78:586, 1997.

[71] S. K. Tokunaga, W. Skomorowski, P. S. Zuchowski, R. Moszynski, J. M. Hutson, E. A. Hinds, and M. R. Tarbutt. Prospects for sympathetic cooling of molecules in electrostatic, ac and microwave traps. *Eur. Phys. J. D*, 65:141, 2011.

[72] P. Soldán, M. T. Cvitaš, J. M. Hutson, P. Honvault, and J.-M. Launay. Quantum dynamics of ultracold Na+Na_2 collisions. *Phys. Rev. Lett.*, 89:153201, 2002.

[73] M. T. Cvitaš, P. Soldán, J. M. Hutson, P. Honvault, and J.-M. Launay. Ultracold Li+Li_2 collisions: Bosonic and fermionic cases. *Phys. Rev. Lett.*, 94:033201, 2005.

[74] M. T. Cvitaš, P. Soldán, J. M. Hutson, P. Honvault, and J.-M. Launay. Ultracold collisions involving heteronuclear alkali metal dimers. *Phys. Rev. Lett.*, 94:200402, 2005.

[75] P. Soldán and J. M. Hutson. Interaction of NH molecules with rubidium atoms: Implications for sympathetic cooling and the formation of extremely polar molecules. *Phys. Rev. Lett.*, 92:163202, 2004.

[76] M. Lara, J. L. Bohn, D. Potter, P. Soldán, and J. M. Hutson. Ultracold Rb-OH collisions and prospects for sympathetic cooling. *Phys. Rev. Lett.*, 97:183201, 2006.

[77] A. O. G. Wallis and J. M. Hutson. Production of ultracold NH molecules by sympathetic cooling with Mg. *Phys. Rev. Lett.*, 103:183201, 2009.

[78] P. S. Żuchowski and J. M. Hutson. Low-energy collisions of NH_3 and ND_3 with ultracold Rb atoms. *Phys. Rev. A*, 79:062708, 2009.

[79] W. Skomorowski, F. Pawlowski, T. Korona, R. Moszynski, P. S. Zuchowski, and J. M. Hutson. Interaction between LiH molecule and Li atom from state-of-the-art electronic structure calculations. *J. Chem. Phys.*, 134:114109, 2011.

[80] M. L. González-Martinez and J. M. Hutson. Ultracold hydrogen atoms: A versatile coolant to produce ultracold molecules. *Phys. Rev. Lett.*, 111:203004, 2013.

[81] E. Shuman, J. Barry, and D. DeMille. Laser cooling of a diatomic molecule. *Nature*, 467:820, 2010.

[82] M. T. Hummon, M. Yeo, B. K. Stuhl, A. L. Collopy, Y. Xia, and J. Ye. 2D magneto-optical trapping of diatomic molecules. *Phys. Rev. Lett.*, 110:143001, 2013.

[83] I. Manai, R. Horchani, H. Lignier, P. Pillet, D. Comparat, A. Fioretti, and M. Allegrini. Rovibrational cooling of molecules by optical pumping. *Phys. Rev. Lett.*, 109:183001, 2012.

[84] J. F. Barry, E. S. Shuman, E. B. Norrgard, and D. DeMille. Laser radiation pressure slowing of a molecular beam. *Phys. Rev. Lett.*, 108:103002, 2012.

[85] M. Zeppenfeld, M. Motsch, P. W. H. Pinkse, and G. Rempe. Optoelectrical cooling of polar molecules. *Phys. Rev. A*, 80:041401, 2009.

[86] M. Zeppenfeld, B. G. Englert, R. Glöckner, A. Prehn, M. Mielenz, C. Sommer, L. D. van Buuren, M. Motsch, and G. Rempe. Sisyphus cooling of electrically trapped polyatomic molecules. *Nature*, 491:570, 2012.

[87] N. Masuhara, J. M. Doyle, J. C. Sandberg, D. Kleppner, T. J. Greytak, H. F. Hess, and G. P. Kochanski. Evaporative cooling of spin-polarized atomic hydrogen. *Phys. Rev. Lett.*, 61:935, 1988.

[88] W. Petrich, M. H. Anderson, J. R. Ensher, and E. A. Cornell. Stable, tightly confining magnetic trap for evaporative cooling of neutral atoms. *Phys. Rev. Lett.*, 74:3352, 1995.

[89] B. K. Stuhl, M. T. Hummon, M. Yeo, G. Quéméner, J. L. Bohn, and J. Ye. Evaporative cooling of the dipolar hydroxyl radical. *Nature*, 492:396, 2012.

[90] L. M. C. Janssen, A. van der Avoird, and G. C. Groenenboom. Quantum reactive scattering of ultracold NH radicals in a magnetic trap. *Phys. Rev. Lett.*, 110:063201, 2013.

[91] K. K. Ni, S. Ospelkaus, M. H. G. de Miranda, A. Pe'er, B. Neyenhuis, J. J. Zirbel, S. Kotochigova, P. S. Julienne, D. S. Jin, and J. Ye. A high phase-space-density gas of polar molecules. *Science*, 322:231, 2008.

[92] J. Deiglmayr, A. Grochola, M. Repp, K. Mörtlbauer, C. Glück, J. Lange, O. Dulieu, R. Wester, and M. Weidemüller. Formation of ultracold polar molecules in the rovibrational ground state. *Phys. Rev. Lett.*, 101:133004, 2008.

[93] H. R. Thorsheim, J. Weiner, and P. S. Julienne. Laser-induced photoassociation of ultracold sodium atoms. *Phys. Rev. Lett.*, 58:2420, 1987.

[94] P. D. Lett, K. Helmerson, W. D. Phillips, L. P. Ratliff, S. L. Rolston, and M. E. Wagshul. Spectroscopy of Na_2 by photoassociation of laser-cooled Na. *Phys. Rev. Lett.*, 71:2200, 1993.

[95] Y. B. Band and P. S. Julienne. Ultracold-molecule production by laser-cooled atom photoassociation. *Phys. Rev. A*, 51:R4317, 1995.

[96] A. Fioretti, D. Comparat, A. Crubellier, O. Dulieu, F. Masnou-Seeuws, and P. Pillet. Formation of cold Cs_2 molecules through photoassociation. *Phys. Rev. Lett.*, 80:4402, 1998.

[97] E. R. I. Abraham, W. I. McAlexander, C. A. Sackett, and R. G. Hulet. Spectroscopic determination of the s-wave scattering length of lithium. *Phys. Rev. Lett.*, 74:1315, 1995.

[98] H. Wang, P. L. Gould, and W. C. Stwalley. Fine-structure predissociation of ultracold photoassociated $^{39}K_2$ molecules observed by fragmentation spectroscopy. *Phys. Rev. Lett.*, 80:476, 1998.

[99] J. D. Miller, R. A. Cline, and D. J. Heinzen. Photoassociation spectrum of ultracold Rb atoms. *Phys. Rev. Lett.*, 71:2204, 1993.

[100] A. Ridinger, S. Chaudhuri, T. Salez, D. R. Fernandes, N. Bouloufa, O. Dulieu, C. Salomon, and F. Chevy. Photoassociative creation of ultracold heteronuclear $^6Li^{40}K^*$ molecules. *Europhys. Lett.*, 96:33001, 2011.

[101] J. P. Shaffer, W. Chalupczak, and N. P. Bigelow. Photoassociative ionization of heteronuclear molecules in a novel two-species magneto-optical trap. *Phys. Rev. Lett.*, 82:1124, 1999.

[102] M. W. Mancini, G. D. Telles, A. R. L. Caires, V. S. Bagnato, and L. G. Marcassa. Observation of ultracold ground-state heteronuclear molecules. *Phys. Rev. Lett.*, 92:133203, 2004.

[103] J. M. Sage, S. Sainis, T. Bergeman, and D. DeMille. Optical production of ultracold polar molecules. *Phys. Rev. Lett.*, 94:203001, 2005.

[104] N. Nemitz, F. Baumer, F. Münchow, S. Tassy, and A. Görlitz. Production of heteronuclear molecules in an electronically excited state by photoassociation in a mixture of ultracold Yb and Rb. *Phys. Rev. A*, 79:061403, 2009.

[105] T. Zelevinsky, M. M. Boyd, A. D. Ludlow, T. Ido, J. Ye, R. Ciuryło, P. Naidon, and P. S. Julienne. Narrow line photoassociation in an optical lattice. *Phys. Rev. Lett.*, 96:203201, 2006.

[106] G. Reinaudi, C. B. Osborn, M. McDonald, S. Kotochigova, and T. Zelevinsky. Optical production of stable ultracold $^{88}Sr_2$ molecules. *Phys. Rev. Lett.*, 109:115303, 2012.

[107] S. Stellmer, B. Pasquiou, R. Grimm, and F. Schreck. Creation of ultracold Sr_2 molecules in the electronic ground state. *Phys. Rev. Lett.*, 109:115302, 2012.

[108] M. Kahmann, E. Tiemann, O. Appel, U. Sterr, and F. Riehle. Photoassociation spectroscopy of ^{40}Ca measured with kilohertz accuracy near the $^3P_1 + ^1S_0$ asymptote and its Zeeman effect. *Phys. Rev. A*, 89:023413, 2014.

[109] M. Borkowski, R. Ciuryło, P. S. Julienne, R. Yamazaki, H. Hara, K. Enomoto, S. Taie, S. Sugawa, Y. Takasu, and Y. Takahashi. Photoassociative production of ultracold heteronuclear ytterbium molecules. *Phys. Rev. A*, 84:030702, 2011.

[110] S. Kato, R. Yamazaki, K. Shibata, R. Yamamoto, H. Yamada, and Y. Takahashi. Observation of long-lived van der Waals molecules in an optical lattice. *Phys. Rev. A*, 86:043411, 2012.

[111] C. Chin, R. Grimm, P. S. Julienne, and E. Tiesinga. Feshbach resonances in ultracold gases. *Rev. Mod. Phys.*, 82:1225, 2010.

[112] H. Feshbach. A unified theory of nuclear reactions. ii. *Ann. Phys.*, 19:287, 1962.

[113] J. Herbig, T. Kraemer, M. Mark, T. Weber, C. Chin, H.-C. Ngerl, and R. Grimm. Preparation of a pure molecular quantum gas. *Science*, 301:1510, 2003.

[114] C. Ospelkaus, S. Ospelkaus, L. Humbert, P. Ernst, K. Sengstock, and K. Bongs. Ultracold heteronuclear molecules in a 3D optical lattice. *Phys. Rev. Lett.*, 97:120402, 2006.

[115] F. Lang, K. Winkler, C. Strauss, R. Grimm, and J. H. Denschlag. Ultracold triplet molecules in the rovibrational ground state. *Phys. Rev. Lett.*, 101:133005, 2008.

[116] P. O. Fedichev, Y. Kagan, G. V. Shlyapnikov, and J. T. M. Walraven. Influence of nearly resonant light on the scattering length in low-temperature atomic gases. *Phys. Rev. Lett.*, 77:2913, 1996.

[117] K. Enomoto, K. Kasa, M. Kitagawa, and Y. Takahashi. Optical Feshbach resonance using the intercombination transition. *Phys. Rev. Lett.*, 101:203201, 2008.

[118] M. Yan, B. J. DeSalvo, B. Ramachandhran, H. Pu, and T. C. Killian. Controlling condensate collapse and expansion with an optical Feshbach resonance. *Phys. Rev. Lett.*, 110:123201, 2013.

[119] S. Inouye, M. Andrews, J. Stenger, H.-J. Miesner, D. Stamper-Kurn, and W. Ketterle. Observation of Feshbach resonances in a Bose-Einstein condensate. *Nature*, 392:151, 1998.

[120] P. Courteille, R. S. Freeland, D. J. Heinzen, F. A. van Abeelen, and B. J. Verhaar. Observation of a Feshbach resonance in cold atom scattering. *Phys. Rev. Lett.*, 81:69, 1998.

[121] J. G. Danzl, E. Haller, M. Gustavsson, M. J. Mark, R. Hart, N. Bouloufa, O. Dulieu, H. Ritsch, and H.-C. Ngerl. Quantum gas of deeply bound ground state molecules. *Science*, 321:1062, 2008.

[122] S. Inouye, J. Goldwin, M. L. Olsen, C. Ticknor, J. L. Bohn, and D. S. Jin. Observation of heteronuclear Feshbach resonances in a mixture of bosons and fermions. *Phys. Rev. Lett.*, 93:183201, 2004.

[123] E. Wille, F. M. Spiegelhalder, G. Kerner, D. Naik, A. Trenkwalder, G. Hendl, F. Schreck, R. Grimm, T. G. Tiecke, J. T. M. Walraven, S. J. J. M. F. Kokkelmans, E. Tiesinga, and P. S. Julienne. Exploring an ultracold fermi-fermi mixture: Interspecies Feshbach resonances and scattering properties of ^{6}Li and ^{40}K. *Phys. Rev. Lett.*, 100:053201, 2008.

[124] C.-H. Wu, J. W. Park, P. Ahmadi, S. Will, and M. W. Zwierlein. Ultracold fermionic Feshbach molecules of ^{23}Na^{40}K. *Phys. Rev. Lett.*, 109:085301, 2012.

[125] J. Werner, A. Griesmaier, S. Hensler, J. Stuhler, T. Pfau, A. Simoni, and E. Tiesinga. Observation of Feshbach resonances in an ultracold gas of ^{52}Cr. *Phys. Rev. Lett.*, 94:183201, 2005.

[126] K. Aikawa, A. Frisch, M. Mark, S. Baier, A. Rietzler, R. Grimm, and F. Ferlaino. Bose-Einstein condensation of erbium. *Phys. Rev. Lett.*, 108:210401, 2012.

[127] A. Frisch, M. Mark, K. Aikawa, F. Ferlaino, J. L. Bohn, C. Makrides, A. Petrov, and S. Kotochigova. Quantum chaos in ultracold collisions of erbium. *Nature*, 507:475, 2014.

[128] M. Lu, N. Q. Burdick, S. H. Youn, and B. L. Lev. Strongly dipolar Bose-Einstein condensate of dysprosium. *Phys. Rev. Lett.*, 107:190401, 2011.

[129] A. Petrov, E. Tiesinga, and S. Kotochigova. Anisotropy-induced Feshbach resonances in a quantum dipolar gas of highly magnetic atoms. *Phys. Rev. Lett.*, 109:103002, 2012.

[130] P. S. Żuchowski, J. Aldegunde, and J. M. Hutson. Ultracold RbSr molecules can be formed by magnetoassociation. *Phys. Rev. Lett.*, 105:153201, 2010.

[131] D. A. Brue and J. M. Hutson. Magnetically tunable Feshbach resonances in ultracold Li-Yb mixtures. *Phys. Rev. Lett.*, 108:043201, 2012.

[132] D. A. Brue and J. M. Hutson. Prospects of forming ultracold molecules in $^2\Sigma$ states by magnetoassociation of alkali-metal atoms with Yb. *Phys. Rev. A*, 87:052709, 2013.

[133] A. L. Migdall, J. V. Prodan, W. D. Phillips, T. H. Bergeman, and H. J. Metcalf. First observation of magnetically trapped neutral atoms. *Phys. Rev. Lett.*, 54:2596, 1985.

[134] W. C. Campbell, E. Tsikata, H.-I. Lu, L. D. van Buuren, and J. M. Doyle. Magnetic trapping and Zeeman relaxation of NH. *Phys. Rev. Lett.*, 98:213001, 2007.

[135] B. C. Sawyer, B. L. Lev, E. R. Hudson, B. K. Stuhl, M. Lara, J. L. Bohn, and J. Ye. Magneto-electrostatic trapping of ground state OH molecules. *Phys. Rev. Lett.*, 98:253002, 2007.

[136] K. Singer, U. Poschinger, M. Murphy, P. Ivanov, F. Ziesel, T. Calarco, and F. Schmidt-Kaler. Trapped ions as quantum bits: Essential numerical tools. *Rev. Mod. Phys.*, 82:2609, 2010.

[137] W. H. Wing. Electrostatic trapping of neutral atomic particles. *Phys. Rev. Lett.*, 45:631, 1980.

[138] H. L. Bethlem, J. v. Veldhoven, M. Schnell, and G. Meijer. Trapping polar molecules in an ac trap. *Phys. Rev. A*, 74:063403, 2006.

[139] J. van Veldhoven, H. L. Bethlem, and G. Meijer. ac electric trap for ground-state molecules. *Phys. Rev. Lett.*, 94:083001, 2005.

[140] J. Kleinert, C. Haimberger, P. J. Zabawa, and N. P. Bigelow. Trapping of ultracold polar molecules with a thin-wire electrostatic trap. *Phys. Rev. Lett.*, 99:143002, 2007.

[141] J. J. Zirbel, K.-K. Ni, S. Ospelkaus, T. L. Nicholson, M. L. Olsen, P. S. Julienne, C. E. Wieman, J. Ye, and D. S. Jin. Heteronuclear molecules in an optical dipole trap. *Phys. Rev. A*, 78:013416, 2008.

[142] A. Chotia, B. Neyenhuis, S. A. Moses, B. Yan, J. P. Covey, M. Foss-Feig, A. M. Rey, D. S. Jin, and J. Ye. Long-lived dipolar molecules and Feshbach molecules in a 3D optical lattice. *Phys. Rev. Lett.*, 108:080405, 2012.

[143] G. Thalhammer, K. Winkler, F. Lang, S. Schmid, R. Grimm, and J. H. Denschlag. Long-lived feshbach molecules in a three-dimensional optical lattice. *Phys. Rev. Lett.*, 96:050402, 2006.

[144] J. G. Danzl, M. J. Mark, E. Haller, M. Gustavsson, R. Hart, J. Aldegunde, J. M. Hutson, and H.-C. Nägerl. An ultracold high-density sample of rovibronic ground-state molecules in an optical lattice. *Nature Phys.*, 6:265, 2010.

[145] C. Brif, R. Chakrabarti, and H. Rabitz. Control of quantum phenomena: past, present and future. *New J. Phys.*, 12:075008, 2010.

[146] P. Brumer and M. Shapiro. *Principles and Applications of the Quantum Control of Molecular Processes.* Wiley, 2003.

[147] A. H. Zewail. Laser selective chemistry-is it possible? *Phys. Today*, 30:23, 1980.

[148] P. Brumer and M. Shapiro. Laser control of molecular processes. *Annu. Rev. Phys. Chem.*, 43:257, 1992.

[149] P. Brumer and M. Shapiro. Control of unimolecular reactions using coherent light. *Chem. Phys. Lett.*, 126:541, 1986.

[150] M. Shapiro, J. W. Hepburn, and P. Brumer. Simplified laser control of unimolecular reactions: Simultaneous (ω_1, ω_3) excitation. *Chem. Phys. Lett.*, 149:451, 1988.

[151] B. Sheehy, B. Walker, and L. F. DiMauro. Phase control in the two-color photodissociation of HD^+. *Phys. Rev. Lett.*, 74:4799, 1995.

[152] C. Chen, Y.-Y. Yin, and D. S. Elliott. Interference between optical transitions. *Phys. Rev. Lett.*, 64:507, 1990.

[153] D. J. Tannor and S. A. Rice. Control of selectivity of chemical reaction via control of wave packet evolution. *J. Chem. Phys.*, 83:5013, 1985.

[154] D. J. Tannor, R. Kosloff, and S. A. Rice. Coherent pulse sequence induced control of selectivity of reactions: Exact quantum mechanical calculations. *J. Chem. Phys.*, 85:5805, 1986.

[155] M. M. Salour and C. Cohen-Tannoudji. Observation of Ramsey's interference fringes in the profile of doppler-free two-photon resonances. *Phys. Rev. Lett.*, 38:757, 1977.

[156] R. Teets, J. Eckstein, and T. W. Hänsch. Coherent two-photon excitation by multiple light pulses. *Phys. Rev. Lett.*, 38:760, 1977.

[157] K. Ohmori. Wave-packet and coherent control dynamics. *Annu. Rev. Phys. Chem.*, 60:487, 2009.

[158] U. Gaubatz, P. Rudecki, M. Becker, S. Schiemann, M. Külz, and K. Bergmann. Population switching between vibrational levels in molecular beams. *Chem. Phys. Lett.*, 149:463, 1988.

[159] K. Bergmann, H. Theuer, and B. W. Shore. Coherent population transfer among quantum states of atoms and molecules. *Rev. Mod. Phys.*, 70:1003, 1998.

[160] W. S. Warren, H. Rabitz, and M. Dahleh. Coherent control of quantum dynamics: The dream is alive. *Science*, 259:1581, 1993.

[161] H. A. Rabitz, M. M. Hsieh, and C. M. Rosenthal. Quantum optimally controlled transition landscapes. *Science*, 303:1998, 2004.

[162] H. Rabitz, R. de Vivie-Riedle, M. Motzkus, and K. Kompa. Whither the future of controlling quantum phenomena? *Science*, 288:824, 2000.

[163] I. Bloch, J. Dalibard, and W. Zwerger. Many-body physics with ultracold gases. *Rev. Mod. Phys.*, 80:885, 2008.

[164] M. Weidemüller and C. Zimmermann, editors. *Cold Atoms and Molecules*. Wiley, 2009.

[165] G. Quemener and P. S. Julienne. Ultracold molecules under control! *Chem. Rev.*, 112:4949, 2012.

[166] M. Lemeshko, R. V. Krems, J. M. Doyle, and S. Kais. Manipulation of molecules with electromagnetic fields. *Mol. Phys.*, 111:1648, 2013.

[167] A. D. Ludlow, T. Zelevinsky, G. K. Campbell, S. Blatt, M. M. Boyd, M. H. G. de Miranda, M. J. Martin, J. W. Thomsen, S. M. Foreman, J. Ye, T. M. Fortier, J. E. Stalnaker, S. A. Diddams, Y. Le Coq, Z. W. Barber, N. Poli, N. D. Lemke, K. M. Beck, and C. W. Oates. Sr lattice clock at 10^{16} fractional uncertainty by remote optical evaluation with a ca clock. *Science*, 319:1805, 2008.

[168] T. Rosenband, D. B. Hume, P. O. Schmidt, C. W. Chou, A. Brusch, L. Lorini, W. H. Oskay, R. E. Drullinger, T. M. Fortier, J. E. Stalnaker, S. A. Diddams, W. C. Swann, N. R. Newbury, W. M. Itano, D. J. Wineland, and J. C. Bergquist. Frequency ratio of Al^+ and Hg^+ single-ion optical clocks - metrology at the 17th decimal place. *Science*, 319:1808, 2008.

[169] M. J. Martin, M. Bishof, M. D. Swallows, X. Zhang, C. Benko, J. von Stecher, A. V. Gorshkov, A. M. Rey, and J. Ye. A quantum many-body spin system in an optical lattice clock. *Science*, 341:632, 2013.

[170] B. Bloom, T. Nicholson, J. Williams, S. Campbell, M. Bishof, X. Zhang, W. Zhang, S. Bromley, and J. Ye. An optical lattice clock with accuracy and stability at the 10^{-18} level. *Nature*, 2014.

[171] A. Peters, K. Y. Chung, and S. Chu. Measurement of gravitational acceleration by dropping atoms. *Nature*, 400:849, 1999.

[172] M. Cadoret, E. de Mirandes, P. Cladé, S. Guellati-Khélifa, C. Schwob, F. m. c. Nez, L. Julien, and F. m. c. Biraben. Combination of bloch oscillations with a Ramsey-Borde interferometer: New determination of the fine structure constant. *Phys. Rev. Lett.*, 101:230801, 2008.

[173] M. Fischer, N. Kolachevsky, M. Zimmermann, R. Holzwarth, T. Udem, T. W. Hänsch, M. Abgrall, J. Grünert, I. Maksimovic, S. Bize, H. Marion, F. P. D. Santos, P. Lemonde, G. Santarelli, P. Laurent, A. Clairon, C. Salomon, M. Haas, U. D. Jentschura, and C. H. Keitel. New limits on the drift of fundamental constants from laboratory measurements. *Phys. Rev. Lett.*, 92:230802, 2004.

[174] E. Peik, B. Lipphardt, H. Schnatz, T. Schneider, C. Tamm, and S. G. Karshenboim. Limit on the present temporal variation of the fine structure constant. *Phys. Rev. Lett.*, 93:170801, 2004.

[175] C. Strauss, T. Takekoshi, F. Lang, K. Winkler, R. Grimm, J. Hecker Denschlag, and E. Tiemann. Hyperfine, rotational, and vibrational structure of the $a^3\Sigma_u^+$ state of ^{87}Rb$_2$. *Phys. Rev. A*, 82:052514, 2010.

[176] M. Semczuk, X. Li, W. Gunton, M. Haw, N. S. Dattani, J. Witz, A. K. Mills, D. J. Jones, and K. W. Madison. High-resolution photoassociation spectroscopy of the ^{6}Li$_2$ in $1^3\Sigma_g^+$ state. *Phys. Rev. A*, 87:052505, 2013.

[177] W. Gunton, M. Semczuk, N. S. Dattani, and K. W. Madison. High-resolution photoassociation spectroscopy of the ^{6}Li$_2$ in $A^1\Sigma_u^+$ state. *Phys. Rev. A*, 88:062510, 2013.

[178] E. Ahmed, A. Hansson, P. Qi, T. Kirova, A. Lazoudis, S. Kotochigova, A. M. Lyyra, L. Li, J. Qi, and S. Magnier. Measurement of the electronic transition dipole moment by Autler-Townes splitting: Comparison of three- and four-level excitation schemes for the Na$_2$ $A^1\Sigma_u^+ - X^1\Sigma_g^+$ system. *J. Chem. Phys.*, 124, 2006.

[179] H. Salami, T. Bergeman, B. Beser, J. Bai, E. H. Ahmed, S. Kotochigova, A. M. Lyyra, J. Huennekens, C. Lisdat, A. V. Stolyarov, O. Dulieu, P. Crozet, and A. J. Ross. Spectroscopic observations, spin-orbit functions, and coupled-channel deperturbation analysis of data on the $A^1\Sigma_u^+$ and $b^3\Pi_u$ states of Rb$_2$. *Phys. Rev. A*, 80:022515, 2009.

[180] B. Neyenhuis, B. Yan, S. A. Moses, J. P. Covey, A. Chotia, A. Petrov, S. Kotochigova, J. Ye, and D. S. Jin. Anisotropic polarizability of ultracold polar ^{40}K^{87}Rb molecules. *Phys. Rev. Lett.*, 109:230403, 2012.

[181] T. Zelevinsky, S. Kotochigova, and J. Ye. Precision test of mass-ratio variations with lattice-confined ultracold molecules. *Phys. Rev. Lett.*, 100:043201, 2008.

[182] D. DeMille, S. Sainis, J. Sage, T. Bergeman, S. Kotochigova, and E. Tiesinga. Enhanced sensitivity to variation of m_e/m_p in molecular spectra. *Phys. Rev. Lett.*, 100:043202, 2008.

[183] D. DeMille, S. B. Cahn, D. Murphree, D. A. Rahmlow, and M. G. Kozlov. Using molecules to measure nuclear spin-dependent parity violation. *Phys. Rev. Lett.*, 100:023003, 2008.

[184] J. J. Hudson, D. M. Kara, I. J. Smallman, B. E. Sauer, M. R. Tarbutt, and E. A. Hinds. Improved measurement of the shape of the electron. *Nature*, 473:493, 2011.

[185] T. A. Collaboration, J. Baron, W. C. Campbell, D. DeMille, J. M. Doyle, G. Gabrielse, Y. V. Gurevich, P. W. Hess, N. R. Hutzler, E. Kirilov, I. Kozyryev, B. R. OLeary, C. D. Panda, M. F. Parsons, E. S. Petrik, B. Spaun, A. C. Vutha, and A. D. West. Order of magnitude smaller limit on the electric dipole moment of the electron. *Science*, 343:269, 2014.

[186] J. Doyle, B. Friedrich, R. Krems, and F. Masnou-Seeuws. Quo vadis, cold molecules? *Eur. Phys. J. D*, 31:149, 2004.

[187] R. V. Krems. Molecules near absolute zero and external field control of atomic and molecular dynamics. *Int. Rev. Phys. Chem.*, 24:99, 2005.

[188] R. V. Krems. Cold controlled chemistry. *Phys. Chem. Chem. Phys.*, 10:4079, 2008.

[189] M. T. Bell and T. P. Softley. Ultracold molecules and ultracold chemistry. *Molecular Physics*, 107:99, 2009.

[190] R. V. Krems. Controlling collisions of ultracold atoms with dc electric fields. *Phys. Rev. Lett.*, 96:123202, 2006.

[191] Z. Li and R. V. Krems. Electric-field-induced Feshbach resonances in ultracold alkali-metal mixtures. *Phys. Rev. A*, 75:032709, 2007.

[192] L. M. C. Janssen, P. S. Żuchowski, A. van der Avoird, G. C. Groenenboom, and J. M. Hutson. Cold and ultracold NH-NH collisions in magnetic fields. *Phys. Rev. A*, 83:022713, 2011.

[193] H. Wu and J. E. Thomas. Optical control of Feshbach resonances in Fermi gases using molecular dark states. *Phys. Rev. Lett.*, 108:010401, 2012.

[194] R. González-Férez and C. P. Koch. Enhancing photoassociation rates by nonresonant-light control of shape resonances. *Phys. Rev. A*, 86:063420, 2012.

[195] M. Tomza, R. González-Férez, C. P. Koch, and R. Moszynski. Controlling magnetic Feshbach resonances in polar open-shell molecules with nonresonant light. *Phys. Rev. Lett.*, 112:113201, 2014.

[196] M. Kirste, X. Wang, H. C. Schewe, G. Meijer, K. Liu, A. van der Avoird, L. M. C. Janssen, K. B. Gubbels, G. C. Groenenboom, and S. Y. T. van de Meerakker. Quantum-state resolved bimolecular collisions of velocity-controlled OH with NO radicals. *Science*, 338:1060, 2012.

[197] L. P. Parazzoli, N. J. Fitch, P. S. Żuchowski, J. M. Hutson, and H. J. Lewandowski. Large effects of electric fields on atom-molecule collisions at millikelvin temperatures. *Phys. Rev. Lett.*, 106:193201, 2011.

[198] A. B. Henson, S. Gersten, Y. Shagam, J. Narevicius, and E. Narevicius. Observation of resonances in penning ionization reactions at sub-kelvin temperatures in merged beams. *Science*, 338:234, 2012.

[199] D. J. Nesbitt. Toward state-to-state dynamics in ultracold collisions: Lessons from high-resolution spectroscopy of weakly bound molecular complexes. *Chem. Rev.*, 112:5062, 2012.

[200] S. Ospelkaus, K.-K. Ni, D. Wang, M. De Miranda, B. Neyenhuis, G. Quéméner, P. Julienne, J. Bohn, D. Jin, and J. Ye. Quantum-state controlled chemical reactions of ultracold potassium-rubidium molecules. *Science*, 327:853, 2010.

[201] K.-K. Ni, S. Ospelkaus, D. Wang, G. Quéméner, B. Neyenhuis, M. De Miranda, J. Bohn, J. Ye, and D. Jin. Dipolar collisions of polar molecules in the quantum regime. *Nature*, 464:1324, 2010.

[202] M. De Miranda, A. Chotia, B. Neyenhuis, D. Wang, G. Quéméner, S. Ospelkaus, J. Bohn, J. Ye, and D. Jin. Controlling the quantum stereodynamics of ultracold bimolecular reactions. *Nature Phys.*, 7:502, 2011.

[203] A. J. Leggett. Bose-Einstein condensation in the alkali gases: Some fundamental concepts. *Rev. Mod. Phys.*, 73:307, 2001.

[204] A. Griesmaier, J. Werner, S. Hensler, J. Stuhler, and T. Pfau. Bose-Einstein condensation of chromium. *Phys. Rev. Lett.*, 94:160401, 2005.

[205] S. Stellmer, M. K. Tey, B. Huang, R. Grimm, and F. Schreck. Bose-Einstein condensation of strontium. *Phys. Rev. Lett.*, 103:200401, 2009.

[206] Y. N. M. de Escobar, P. G. Mickelson, M. Yan, B. J. DeSalvo, S. B. Nagel, and T. C. Killian. Bose-Einstein condensation of ^{84}Sr. *Phys. Rev. Lett.*, 103:200402, 2009.

[207] S. Kraft, F. Vogt, O. Appel, F. Riehle, and U. Sterr. Bose-Einstein condensation of alkaline earth atoms: ^{40}Ca. *Phys. Rev. Lett.*, 103:130401, 2009.

[208] Y. Takasu, K. Maki, K. Komori, T. Takano, K. Honda, M. Kumakura, T. Yabuzaki, and Y. Takahashi. Spin-singlet Bose-Einstein condensation of two-electron atoms. *Phys. Rev. Lett.*, 91:040404, 2003.

[209] M. Greiner, C. A. Regal, and D. S. Jin. Emergence of a molecular Bose-Einstein condensate from a Fermi gas. *Nature*, 426:537, 2003.

[210] S. Jochim, M. Bartenstein, A. Altmeyer, G. Hendl, S. Riedl, C. Chin, J. Hecker Denschlag, and R. Grimm. Bose-Einstein condensation of molecules. *Science*, 302:2101, 2003.

[211] B. DeMarco and D. S. Jin. Onset of Fermi degeneracy in a trapped atomic gas. *Science*, 285:1703, 1999.

[212] A. G. Truscott, K. E. Strecker, W. I. McAlexander, G. B. Partridge, and R. G. Hulet. Observation of Fermi pressure in a gas of trapped atoms. *Science*, 291:2570, 2001.

[213] M. Greiner, C. A. Regal, and D. S. Jin. Probing the excitation spectrum of a Fermi gas in the BCS-BEC crossover regime. *Phys. Rev. Lett.*, 94:070403, 2005.

[214] S. Giorgini, L. P. Pitaevskii, and S. Stringari. Theory of ultracold atomic Fermi gases. *Rev. Mod. Phys.*, 80:1215, 2008.

[215] M. Greiner, O. Mandel, T. Esslinger, T. W. Hänsch, and I. Bloch. Quantum phase transition from a superfluid to a Mott insulator in a gas of ultracold atoms. *Nature*, 415:39, 2002.

[216] U. Schneider, L. Hackermller, S. Will, T. Best, I. Bloch, T. A. Costi, R. W. Helmes, D. Rasch, and A. Rosch. Metallic and insulating phases of repulsively interacting fermions in a 3D optical lattice. *Science*, 322:1520, 2008.

[217] R. Jördens, N. Strohmaier, K. Günter, H. Moritz, and T. Esslinger. A Mott insulator of fermionic atoms in an optical lattice. *Nature*, 455:204, 2008.

[218] K. Góral, L. Santos, and M. Lewenstein. Quantum phases of dipolar bosons in optical lattices. *Phys. Rev. Lett.*, 88:170406, 2002.

[219] S. Yi, T. Li, and C. P. Sun. Novel quantum phases of dipolar bose gases in optical lattices. *Phys. Rev. Lett.*, 98:260405, 2007.

[220] T. Lahaye, T. Koch, B. Fröhlich, M. Fattori, J. Metz, A. Griesmaier, S. Giovanazzi, and T. Pfau. Strong dipolar effects in a quantum ferrofluid. *Nature*, 448:672, 2007.

[221] P. Soltan-Panahi, J. Struck, P. Hauke, A. Bick, W. Plenkers, G. Meineke, C. Becker, P. Windpassinger, M. Lewenstein, and K. Sengstock. Multi-component quantum gases in spin-dependent hexagonal lattices. *Nature Phys.*, 7:434, 2011.

[222] P. Soltan-Panahi, D.-S. Luhmann, J. Struck, P. Windpassinger, and K. Sengstock. Quantum phase transition to unconventional multi-orbital superfluidity in optical lattices. *Nature Phys.*, 8:71, 2011.

[223] L. Tarruell, D. Greif, T. Uehlinger, G. Jotzu, and T. Esslinger. Creating, moving and merging Dirac points with a Fermi gas in a tunable honeycomb lattice. *Nature*, 483:302, 2012.

[224] S. R. Manmana, E. M. Stoudenmire, K. R. A. Hazzard, A. M. Rey, and A. V. Gorshkov. Topological phases in ultracold polar-molecule quantum magnets. *Phys. Rev. B*, 87:081106, 2013.

[225] M. Lemeshko, R. V. Krems, and H. Weimer. Nonadiabatic preparation of spin crystals with ultracold polar molecules. *Phys. Rev. Lett.*, 109:035301, 2012.

[226] R. P. Feynman. Simulating physics with computers. *Int. J. Theor. Phys.*, 21:467, 1982.

[227] I. Bloch, J. Dalibard, and S. Nascimbène. Quantum simulations with ultracold quantum gases. *Nature Phys.*, 8:267, 2012.

[228] J. I. Cirac and P. Zoller. Goals and opportunities in quantum simulation. *Nature Phys.*, 8:264, 2012.

[229] C. Weitenberg, M. Endres, J. F. Sherson, M. Cheneau, P. Schauss, T. Fukuhara, I. Bloch, and S. Kuhr. Single-spin addressing in an atomic Mott insulator. *Nature*, 471:319, 2011.

[230] J. F. Sherson, C. Weitenberg, M. Endres, M. Cheneau, I. Bloch, and S. Kuhr. Single-atom-resolved fluorescence imaging of an atomic Mott insulator. *Nature*, 467:68, 2010.

[231] W. S. Bakr, J. I. Gillen, A. Peng, S. Fölling, and M. Greiner. A quantum gas microscope for detecting single atoms in a hubbard-regime optical lattice. *Nature*, 462:74, 2009.

[232] W. S. Bakr, A. Peng, M. E. Tai, R. Ma, J. Simon, J. I. Gillen, S. Foelling, L. Pollet, and M. Greiner. Probing the superfluid–to–Mott insulator transition at the single-atom level. *Science*, 329:547, 2010.

[233] D. Greif, L. Tarruell, T. Uehlinger, R. Jördens, and T. Esslinger. Probing nearest-neighbor correlations of ultracold fermions in an optical lattice. *Phys. Rev. Lett.*, 106:145302, 2011.

[234] J. Simon, W. S. Bakr, R. Ma, M. E. Tai, P. M. Preiss, and M. Greiner. Quantum simulation of antiferromagnetic spin chains in an optical lattice. *Nature*, 472:307, 2011.

[235] T. Fukuhara, P. Schauss, M. Endres, S. Hild, M. Cheneau, I. Bloch, and C. Gross. Microscopic observation of magnon bound states and their dynamics. *Nature*, 502:76, 2013.

[236] D. Greif, T. Uehlinger, G. Jotzu, L. Tarruell, and T. Esslinger. Short-range quantum magnetism of ultracold fermions in an optical lattice. *Science*, 340:1307, 2013.

[237] T. Uehlinger, G. Jotzu, M. Messer, D. Greif, W. Hofstetter, U. Bissbort, and T. Esslinger. Artificial graphene with tunable interactions. *Phys. Rev. Lett.*, 111:185307, 2013.

[238] S. Braun, J. P. Ronzheimer, M. Schreiber, S. S. Hodgman, T. Rom, I. Bloch, and U. Schneider. Negative absolute temperature for motional degrees of freedom. *Science*, 339:52, 2013.

[239] A. Micheli, G. K. Brennen, and P. Zoller. A toolbox for lattice-spin models with polar molecules. *Nature Phys.*, 2:341, 2006.

[240] A. V. Gorshkov, S. R. Manmana, G. Chen, J. Ye, E. Demler, M. D. Lukin, and A. M. Rey. Tunable superfluidity and quantum magnetism with ultracold polar molecules. *Phys. Rev. Lett.*, 107:115301, 2011.

[241] K. R. A. Hazzard, S. R. Manmana, M. Foss-Feig, and A. M. Rey. Far-from-equilibrium quantum magnetism with ultracold polar molecules. *Phys. Rev. Lett.*, 110:075301, 2013.

[242] J. Perez-Rios, F. Herrera, and R. V. Krems. External field control of collective spin excitations in an optical lattice of $^2\Sigma$ molecules. *New. J. Phys.*, 12, 2010.

[243] F. Herrera and R. V. Krems. Tunable Holstein model with cold polar molecules. *Phys. Rev. A*, 84:051401, 2011.

[244] P. Xiang, M. Litinskaya, and R. V. Krems. Tunable exciton interactions in optical lattices with polar molecules. *Phys. Rev. A*, 85:061401, 2012.

[245] F. Herrera, K. W. Madison, R. V. Krems, and M. Berciu. Investigating polaron transitions with polar molecules. *Phys. Rev. Lett.*, 110:223002, 2013.

[246] B. Yan, S. A. Moses, B. Gadway, J. P. Covey, K. R. Hazzard, A. M. Rey, D. S. Jin, and J. Ye. Observation of dipolar spin-exchange interactions with lattice-confined polar molecules. *Nature*, 501:521, 2013.

[247] A. de Paz, A. Sharma, A. Chotia, E. Maréchal, J. H. Huckans, P. Pedri, L. Santos, O. Gorceix, L. Vernac, and B. Laburthe-Tolra. Nonequilibrium quantum magnetism in a dipolar lattice gas. *Phys. Rev. Lett.*, 111:185305, 2013.

[248] S. Chaudhury, S. Merkel, T. Herr, A. Silberfarb, I. H. Deutsch, and P. S. Jessen. Quantum control of the hyperfine spin of a Cs atom ensemble. *Phys. Rev. Lett.*, 99:163002, 2007.

[249] J. Ahn, T. C. Weinacht, and P. H. Bucksbaum. Information storage and retrieval through quantum phase. *Science*, 287:463, 2000.

[250] G. K. Brennen, C. M. Caves, P. S. Jessen, and I. H. Deutsch. Quantum logic gates in optical lattices. *Phys. Rev. Lett.*, 82:1060, 1999.

[251] A. V. Gorshkov, A. M. Rey, A. J. Daley, M. M. Boyd, J. Ye, P. Zoller, and M. D. Lukin. Alkaline-earth-metal atoms as few-qubit quantum registers. *Phys. Rev. Lett.*, 102:110503, 2009.

[252] D. Jaksch, J. I. Cirac, P. Zoller, S. L. Rolston, R. Côté, and M. D. Lukin. Fast quantum gates for neutral atoms. *Phys. Rev. Lett.*, 85:2208, 2000.

[253] D. Jaksch, H.-J. Briegel, J. I. Cirac, C. W. Gardiner, and P. Zoller. Entanglement of atoms via cold controlled collisions. *Phys. Rev. Lett.*, 82:1975, 1999.

[254] S. Trotzky, P. Cheinet, S. Flling, M. Feld, U. Schnorrberger, A. M. Rey, A. Polkovnikov, E. A. Demler, M. D. Lukin, and I. Bloch. Time-resolved observation and control of superexchange interactions with ultracold atoms in optical lattices. *Science*, 319:295, 2008.

[255] J. I. Cirac and P. Zoller. Quantum computations with cold trapped ions. *Phys. Rev. Lett.*, 74:4091, 1995.

[256] H. Doerk, Z. Idziaszek, and T. Calarco. Atom-ion quantum gate. *Phys. Rev. A*, 81:012708, 2010.

[257] D. DeMille. Quantum computation with trapped polar molecules. *Phys. Rev. Lett.*, 88:067901, 2002.

[258] S. F. Yelin, K. Kirby, and R. Côté. Schemes for robust quantum computation with polar molecules. *Phys. Rev. A*, 74:050301, 2006.

[259] S. A. Rice and M. Zhao. *Optical control of molecular dynamics.* John Wiley & Sons, 2000.

[260] C. P. Koch, R. Kosloff, and F. Masnou-Seeuws. Short-pulse photoassociation in rubidium below the D_1 line. *Phys. Rev. A*, 73:043409, 2006.

[261] C. P. Koch, E. Luc-Koenig, and F. Masnou-Seeuws. Making ultracold molecules in a two-color pump-dump photoassociation scheme using chirped pulses. *Phys. Rev. A*, 73:033408, 2006.

[262] D. Meshulach and Y. Silberberg. Coherent quantum control of two-photon transitions by a femtosecond laser pulse. *Nature*, 396:239, 1998.

[263] C. P. Koch, M. Ndong, and R. Kosloff. Two-photon coherent control of femtosecond photoassociation. *Farad. Discuss.*, 142:389, 2009.

[264] C. P. Koch, J. P. Palao, R. Kosloff, and F. Masnou-Seeuws. Stabilization of ultracold molecules using optimal control theory. *Phys. Rev. A*, 70:013402, 2004.

[265] T. Seideman. Revival structure of aligned rotational wave packets. *Phys. Rev. Lett.*, 83:4971, 1999.

[266] H. Stapelfeldt and T. Seideman. Aligning molecules with strong laser pulses. *Rev. Mod. Phys.*, 75:543, 2003.

[267] T. V. Tscherbul, Y. V. Suleimanov, V. Aquilanti, and R. V. Krems. Magnetic field modification of ultracold molecule-molecule collisions. *New J. Phys.*, 11:055021, 2009.

[268] B. Pasquiou, A. Bayerle, S. M. Tzanova, S. Stellmer, J. Szczepkowski, M. Parigger, R. Grimm, and F. Schreck. Quantum degenerate mixtures of strontium and rubidium atoms. *Phys. Rev. A*, 88:023601, 2013.

[269] C. Zipkes, S. Palzer, C. Sias, and M. Köhl. A trapped single ion inside a Bose–Einstein condensate. *Nature*, 464:388, 2010.

[270] L. Ratschbacher, C. Zipkes, C. Sias, and M. Kohl. Controlling chemical reactions of a single particle. *Nature Phys.*, 8:649, 2012.

[271] R. Gerritsma, A. Negretti, H. Doerk, Z. Idziaszek, T. Calarco, and F. Schmidt-Kaler. Bosonic Josephson junction controlled by a single trapped ion. *Phys. Rev. Lett.*, 109:080402, 2012.

[272] U. Bissbort, D. Cocks, A. Negretti, Z. Idziaszek, T. Calarco, F. Schmidt-Kaler, W. Hofstetter, and R. Gerritsma. Emulating solid-state physics with a hybrid system of ultracold ions and atoms. *Phys. Rev. Lett.*, 111:080501, 2013.

[273] K. Piszczatowski, G. Łach, M. Przybytek, J. Komasa, K. Pachucki, and B. Jeziorski. Theoretical determination of the dissociation energy of molecular hydrogen. *J. Chem. Theory Comput.*, 5:3039, 2009.

[274] M. Przybytek, W. Cencek, J. Komasa, G. Łach, B. Jeziorski, and K. Szalewicz. Relativistic and quantum electrodynamics effects in the helium pair potential. *Phys. Rev. Lett.*, 104:183003, 2010.

[275] K. Patkowski, V. Spirko, and K. Szalewicz. On the Elusive Twelfth Vibrational State of Beryllium Dimer. *Science*, 326:1382, 2009.

[276] M. Tomza, W. Skomorowski, M. Musial, R. Gonzalez Ferez, C. Koch, and R. Moszynski. Interatomic potentials, electric properties, and spectroscopy of the ground and excited states of the Rb_2 molecule: Ab initio calculations and effect of a non-resonant field. *Mol. Phys.*, 111:1781, 2013.

[277] W. Skomorowski, F. Pawlowski, C. P. Koch, and R. Moszynski. Rovibrational dynamics of the strontium molecule in the $A^1\Sigma_u^+$, $c^3\Pi_u$, and $a^3\Sigma_u^+$ manifold from state-of-the-art ab initio calculations. *J. Chem. Phys.*, 136:194306, 2012.

[278] B. H. McGuyer, C. B. Osborn, M. McDonald, G. Reinaudi, W. Skomorowski, R. Moszynski, and T. Zelevinsky. Nonadiabatic effects in ultracold molecules via anomalous linear and quadratic zeeman shifts. *Phys. Rev. Lett.*, 111:243003, 2013.

[279] T. Helgaker, S. Coriani, P. Jrgensen, K. Kristensen, J. Olsen, and K. Ruud. Recent advances in wave function-based methods of molecular-property calculations. *Chem. Rev.*, 112:543, 2012.

[280] T. Helgaker, P. Jorgensen, and J. Olsen, editors. *Molecular Electronic-Structure Theory.* Wiley, 2000.

[281] R. J. Bartlett and M. Musial. Coupled-cluster theory in quantum chemistry. *Rev. Mod. Phys.*, 79:291, 2007.

[282] D. I. Lyakh, M. Musial, V. F. Lotrich, and R. J. Bartlett. Multireference Nature of Chemistry: The Coupled-Cluster View. *Chem. Rev.*, 112:182, 2012.

[283] M. Musiał. Multireference Fock space coupled cluster method in the effective and intermediate Hamiltonian formulation for the (2,0) sector. *J. Chem. Phys.*, 136, 2012.

[284] M. Musiał, A. Perera, and R. J. Bartlett. Multireference coupled-cluster theory: The easy way. *J. Chem. Phys.*, 134(11), 2011.

[285] M. Dolg and X. Cao. Relativistic pseudopotentials: Their development and scope of applications. *Chem. Rev.*, 112:403, 2012.

[286] S. Boys and F. Bernardi. Calculation of small molecular interactions by differences of separate total energies - some procedures with reduced errors. *Mol. Phys.*, 19:553, 1970.

[287] H. Koch and P. Jorgensen. Coupled cluster response functions. *J. Chem. Phys.*, 93:3333, 1990.

[288] H. Sekino and R. J. Bartlett. A linear response, coupled-cluster theory for excitation energy. *Int. J. Quantum Chem. Symp.*, 18:255, 1984.

[289] T. Helgaker, H. J. A. Jensen, P. Jorgensen, J. Olsen, K. Ruud, H. Agren, A. A. Auer, K. L. Bak, V. Bakken, O. Christiansen, and et al. Dalton, *a*n ab initio electronic structure program, release 2.0, 2005.

[290] B. Jeziorski, R. Moszynski, and K. Szalewicz. Perturbation-theory approach to intermolecular potential-energy surfaces of van-der-waals complexes. *Chem. Rev.*, 94:1887, 1994.

[291] B. Jeziorski and R. Moszynski. Explicitly connected expansion for the average value of an observable in the coupled-cluster theory. *Int. J. Quantum Chem.*, 48:161, 1993.

[292] R. Moszynski, P. Zuchowski, and B. Jeziorski. Time-independent coupled-cluster theory of the polarization propagator. *Collect. Czech. Chem. Commun.*, 70:1109, 2005.

[293] T. Korona, M. Przybytek, and B. Jeziorski. Time-independent coupled cluster theory of the polarization propagator. Implementation and application of the singles and doubles model to dynamic polarizabilities and van der Waals constants. *Mol. Phys.*, 104:2303, 2006.

[294] H.-J. Werner, P. J. Knowles, F. R. M. R. Lindh, M. Schütz, P. Celani, T. Korona, G. Rauhut, R. D. Amos, A. Bernhardsson, A. Berning, D. L. Cooper, M. J. O. Deegan, A. J. Dobbyn, E. G. F. Eckert, C. Hampel, G. Hetzer, A. W. Lloyd, S. J. McNicholas, W. Meyer, M. E. Mura, A. Nicklass, P. Palmieri, R. Pitzer, U. Schumann, H. Stoll, A. J. Stone, R. Tarroni, T. Thorsteinsson, M. Wang, and A. Wolf. *MOLPRO, version 2012.1, a package of ab initio programs*, 2012. See http://www.molpro.net.

[295] H. A. Bethe and E. E. Salpeter. *Quantum Mechanics of One- and Two-Electron Atoms.* Academic Press, New York, 1957.

[296] M. Kaupp, P. v. R. Schleyer, H. Stoll, and H. Preuss. Pseudopotential approaches to Ca, Sr, and Ba hydrides. why are some alkaline earth MX_2 compounds bent? *J. Chem. Phys.*, 94:1360, 1991.

[297] I. S. Lim, H. Stoll, and P. Schwerdtfeger. Relativistic small-core energy-consistent pseudopotentials for the alkaline-earth elements from Ca to Ra. *J. Chem. Phys.*, 124:034107, 2006.

[298] X. Cao and M. Dolg. Valence basis sets for relativistic energy-consistent small-core lanthanide pseudopotentials. *J. Chem. Phys.*, 115:7348, 2001.

[299] T. G. A. Heijmen, R. Moszynski, P. E. S. Wormer, and A. van der Avoird. Symmetry-adapted perturbation theory applied to interaction-induced properties of collisional complexes. *Mol. Phys.*, 89:81, 1996.

[300] A. Marte, T. Volz, J. Schuster, S. Dürr, G. Rempe, E. G. M. van Kempen, and B. J. Verhaar. Feshbach resonances in rubidium 87: Precision measurement and analysis. *Phys. Rev. Lett.*, 89:283202, 2002.

[301] R. F. Gutterres, C. Amiot, A. Fioretti, C. Gabbanini, M. Mazzoni, and O. Dulieu. Determination of the ^{87}Rb $5p$ state dipole matrix element and radiative lifetime from the photoassociation spectroscopy of the Rb_2 $0_g^-(P_{3/2})$ long-range state. *Phys. Rev. A*, 66:024502, 2002.

[302] M. Marinescu and A. Dalgarno. Dispersion forces and long-range electronic transition dipole moments of alkali-metal dimer excited states. *Phy. Rev. A*, 52:311, 1995.

[303] I. S. Lim, P. Schwerdtfeger, B. Metz, and H. Stoll. All-electron and relativistic pseudopotential studies for the group 1 element polarizabilities from K to element 119. *J. Chem. Phys.*, 122:104103, 2005.

[304] NIST Atomic Spectra Database http://physics.nist.gov/PhysRefData/ASD.

[305] J. F. Stanton, J. Gauss, S. A. Perera, J. D. Watts, A. Yau, M. Nooijen, N. Oliphant, P. Szalay, W. Lauderdale, S. Gwaltney, S. Beck, A. Balkov, D. Bernholdt, K. Baeck, P. Rozyczko, H. Sekino, C. Huber, J. Pittner, W. Cencek, D. Taylor, , and R. Bartlett. ACES II is a program product of the Quantum Theory Project, University of Florida.

[306] A.-R. Allouche and M. Aubert-Frecon. Transition dipole moments between the low-lying $\Omega_{g,u}^{(+/-)}$ states of the Rb_2 and Cs_2 molecules. *J. Chem. Phys.*, 136:114302, 2012.

[307] P. J. Knowles, C. Hampel, and H.-J. Werner. Coupled cluster theory for high spin, open shell reference wave functions. *J. Chem. Phys.*, 99:5219, 1993.

[308] O. Christiansen, H. Koch, and P. Jorgensen. Response functions in the CC3 iterative triple excitation model. *J. Chem. Phys.*, 103:7429, 1995.

[309] H. Koch, O. Christiansen, P. Jorgensen, A. M. S. de Meras, and T. Helgaker. The CC3 model: An iterative coupled cluster approach including connected triples. *J. Chem. Phys.*, 106:1808, 1997.

[310] A. Derevianko, S. G. Porsev, and J. F. Babb. Electric dipole polarizabilities at imaginary frequencies for hydrogen,the alkali-metal, alkaline-earth, and noble gas atoms. *At. Data Nucl. Data Tables*, 96:323, 2010.

[311] U. I. Safronova and M. S. Safronova. Third-order relativistic many-body calculations of energies, transition rates, hyperfine constants, and blackbody radiation shift in $^{171}Yb^+$. *Phys. Rev. A*, 79:022512, 2009.

[312] C. Chen and Z.-W. Wang. Quadrupole and octupole polarizabilities for the ground states of lithiumlike systems from z = 3 to 20. *J. Chem. Phys.*, 121:4171, 2004.

[313] S. G. Porsev, M. S. Safronova, A. Derevianko, and C. W. Clark. Long-range interaction coefficients for ytterbium dimers. *Phys. Rev. A*, 89:012711, 2014.

[314] M. Krych, W. Skomorowski, F. Pawłowski, R. Moszynski, and Z. Idziaszek. Sympathetic cooling of the Ba^+ ion by collisions with ultracold Rb atoms: Theoretical prospects. *Phys. Rev. A*, 83:032723, 2011.

[315] H. Hara, Y. Takasu, Y. Yamaoka, J. M. Doyle, and Y. Takahashi. Quantum degenerate mixtures of alkali and alkaline-earth-like atoms. *Phys. Rev. Lett.*, 106:205304, 2011.

[316] V. V. Ivanov, A. Khramov, A. H. Hansen, W. H. Dowd, F. Münchow, A. O. Jamison, and S. Gupta. Sympathetic cooling in an optically trapped mixture of alkali and spin-singlet atoms. *Phys. Rev. Lett.*, 106:153201, 2011.

[317] F. Baumer, F. Münchow, A. Görlitz, S. E. Maxwell, P. S. Julienne, and E. Tiesinga. Spatial separation in a thermal mixture of ultracold ^{174}Yb and ^{87}Rb atoms. *Phys. Rev. A*, 83:040702, 2011.

[318] S. L. Cornish. unpublished.

[319] Y. Wang and M. Dolg. Pseudopotential study of the ground and excited states of Yb_2. *Theor. Chem. Acc.*, 100:124, 1998.

[320] M. Tomza, F. Pawlowski, M. Jeziorska, C. P. Koch, and R. Moszynski. Formation of ultracold sryb molecules in an optical lattice by photoassociation spectroscopy: theoretical prospects. *Phys. Chem. Chem. Phys.*, 13:18893, 2011.

[321] J. Thom H. Dunning. Gaussian basis sets for use in correlated molecular calculations. I. the atoms boron through neon and hydrogen. *J. Chem. Phys.*, 90:1007, 1989.

[322] M. Reiher. Douglas-Kroll-Hess Theory: a relativistic electrons-only theory for chemistry. *Theor. Chem. Acc.*, 116:241, 2006.

[323] N. B. Balabanov and K. A. Peterson. Systematically convergent basis sets for transition metals. I. All-electron correlation consistent basis sets for the 3d elements Sc–Zn. *J. Chem. Phys.*, 123:064107, 2005.

[324] J. Koput and K. Peterson. Ab initio potential energy surface and vibrational-rotational energy levels of $X^2\Sigma^+$ CaOH. *J. Phys. Chem. A*, 106:9595, 2002.

[325] M. Dolg, U. Wedig, H. Stoll, and H. Preuss. Energy-adjusted ab initio pseudopotentials for the first row transition elements. *J. Chem. Phys.*, 86:866, 1987.

[326] F.-M. Tao and Y.-K. Pan. Möller-Plesset perturbation investigation of the He_2 potential and the role of midbond basis functions. *J. Chem. Phys.*, 97:4989, 1992.

[327] L. Rybak, S. Amaran, L. Levin, M. Tomza, R. Moszynski, R. Kosloff, C. P. Koch, and Z. Amitay. Generating molecular rovibrational coherence by two-photon femtosecond photoassociation of thermally hot atoms. *Phys. Rev. Lett.*, 107:273001, 2011.

[328] B. Bussery-Honvault, J.-M. Launay, and R. Moszynski. Cold collisions of ground-state calcium atoms in a laser field: A theoretical study. *Phys. Rev. A*, 68:032718, 2003.

[329] A. A. Buchachenko, G. Chalasinski, and M. M. Szczesniak. Interactions of lanthanide atoms: Comparative ab initio study of YbHe, Yb_2 and TmHe, TmYb potentials. *Eur. Phys. J. D*, 45:147, 2007.

[330] Z. Pavlović, H. R. Sadeghpour, R. Côté, and B. O. Roos. CrRb: A molecule with large magnetic and electric dipole moments. *Phys. Rev. A*, 81:052706, 2010.

[331] J. Higgins, T. Hollebeek, J. Reho, T.-S. Ho, K. K. Lehmann, H. Rabitz, G. Scoles, and M. Gutowski. On the importance of exchange effects in three-body interactions: The lowest quartet state of Na_3. *J. Chem. Phys.*, 112:5751, 2000.

[332] P. Soldán, M. T. Cvitaš, and J. M. Hutson. Three-body nonadditive forces between spin-polarized alkali-metal atoms. *Phys. Rev. A*, 67:054702, 2003.

[333] P. Soldán. Lowest quartet states of Li_2A (A = Na, K, Rb, Cs). *Phys. Rev. A*, 77:054501, 2008.

[334] P. Soldán. Lowest quartet states of heteronuclear alkali-metal trimers. *Phys. Rev. A*, 82:034701, 2010.

[335] I. Bloch. Ultracold quantum gases in optical lattices. *Nature Phys.*, 1:23, 2005.

[336] V. Kokoouline, O. Dulieu, R. Kosloff, and F. Masnou-Seeuws. Mapped fourier methods for long-range molecules: Application to perturbations in the $Rb_2(0_u^+)$ photoassociation spectrum. *J. Chem. Phys.*, 110:9865, 1999.

[337] K. Willner, O. Dulieu, and F. Masnou-Seeuws. Mapped grid methods for long-range molecules and cold collisions. *J. Chem. Phys.*, 120:548, 2004.

[338] S. Kallush and R. Kosloff. Improved methods for mapped grids: Applied to highly excited vibrational states of diatomic molecules. *Chem. Phys. Lett.*, 433:221, 2006.

[339] F. Masnou-Seeuws and P. Pillet. Formation of ultracold molecules ($T \leq 200\mu K$) via photoassociation in a gas of laser-cooled atoms. *Adv. Atom. Mol. Opt. Phys.*, 47:53, 2001.

[340] C. M. Dion, C. Drag, O. Dulieu, B. Laburthe Tolra, F. Masnou-Seeuws, and P. Pillet. Resonant Coupling in the Formation of Ultracold Ground State Molecules via Photoassociation. *Phys. Rev. Lett.*, 86:2253, 2001.

[341] H. K. Pechkis, D. Wang, Y. Huang, E. E. Eyler, P. L. Gould, W. C. Stwalley, and C. P. Koch. Enhancement of the formation of ultracold $^{85}\mathrm{Rb}_2$ molecules due to resonant coupling. *Phys. Rev. A*, 76:022504, 2007.

[342] S. Ghosal, R. J. Doyle, C. P. Koch, and J. M. Hutson. Stimulating the production of deeply bound RbCs molecules with laser pulses: the role of spinorbit coupling in forming ultracold molecules. *New J. Phys.*, 11(5):055011, 2009.

[343] B. E. Londoño, J. E. Mahecha, E. Luc-Koenig, and A. Crubellier. Resonant coupling effects on the photoassociation of ultracold Rb and Cs atoms. *Phys. Rev. A*, 80:032511, 2009.

[344] A. Fioretti, O. Dulieu, and C. Gabbanini. Experimental evidence for an isotopic effect in the formation of ultracold ground-state rubidium dimers. *J. Phys. B*, 40:3283, 2007.

[345] C. P. Koch and R. Moszynski. Engineering an all-optical route to ultracold molecules in their vibronic ground state. *Phys. Rev. A*, 78:043417, 2008.

[346] E. A. Shapiro, M. Shapiro, A. Pe'er, and J. Ye. Photoassociation adiabatic passage of ultracold Rb atoms to form ultracold Rb_2 molecules. *Phys. Rev. A*, 75:013405, 2007.

[347] E. Kuznetsova, P. Pellegrini, R. Côté, M. D. Lukin, and S. F. Yelin. Formation of deeply bound molecules via chainwise adiabatic passage. *Phys. Rev. A*, 78:021402, 2008.

[348] F. Lang, K. Winkler, C. Strauss, R. Grimm, and J. H. Denschlag. Ultracold triplet molecules in the rovibrational ground state. *Phys. Rev. Lett.*, 101:133005, 2008.

[349] S. Ospelkaus, A. Pe'er, K.-K. Ni, J. J. Zirbel, B. Neyenhuis, S. Kotochigova, P. S. Julienne, J. Ye, and D. S. Jin. Efficient state transfer in an ultracold dense gas of heteronuclear molecules. *Nature Phys.*, 4:622, 2008.

[350] B. R. Johnson. The renormalized Numerov method applied to calculating bound states of the coupled-channel Schroedinger equation. *J. Chem. Phys.*, 69:4678, 1978.

[351] B. Zygelman and A. Dalgarno. Radiative quenching of He($^2S_1$) induced by collisions with ground-state helium atoms. *Phys. Rev. A*, 38:1877, 1988.

[352] P. S. Julienne. Theory of rare gas-group VI 1S-1D collision-induced transitions. *J. Chem. Phys.*, 68:32, 1978.

[353] J. Tellinghuisen and P. S. Julienne. A simple sum rule for total radiative decay rates: Comparison of quantal and classical methods for diatomics. *J. Chem. Phys.*, 81:5779, 1984.

[354] K. Sando and A. Dalgarno. The absorption of radiation near 600 Å by helium. *Mol. Phys.*, 20:103, 1971.

[355] R. Napolitano, J. Weiner, C. J. Williams, and P. S. Julienne. Line shapes of high resolution photoassociation spectra of optically cooled atoms. *Phys. Rev. Lett.*, 73:1352, 1994.

[356] W. Salzmann, U. Poschinger, R. Wester, M. Weidemüller, A. Merli, S. M. Weber, F. Sauer, M. Plewicki, F. Weise, A. Mirabal Esparza, L. Wöste, and A. Lindinger. Coherent control with shaped femtosecond laser pulses applied to ultracold molecules. *Phys. Rev. A*, 73:023414, 2006.

[357] B. L. Brown, A. J. Dicks, and I. A. Walmsley. Coherent control of ultracold molecule dynamics in a magneto-optical trap using chirped femtosecond laser pulses. *Phys. Rev. Lett.*, 96:173002, 2006.

[358] W. Salzmann, T. Mullins, J. Eng, M. Albert, R. Wester, M. Weidemüller, A. Merli, S. M. Weber, F. Sauer, M. Plewicki, F. Weise, L. Wöste, and A. Lindinger. Coherent transients in the femtosecond photoassociation of ultracold molecules. *Phys. Rev. Lett.*, 100:233003, 2008.

[359] T. Mullins, W. Salzmann, S. Götz, M. Albert, J. Eng, R. Wester, M. Weidemüller, F. Weise, A. Merli, S. M. Weber, F. Sauer, L. Wöste, and A. Lindinger. Photoassociation and coherent transient dynamics in the interaction of ultracold rubidium atoms with shaped femtosecond pulses. i. experiment. *Phys. Rev. A*, 80:063416, 2009.

[360] A. Merli, F. Eimer, F. Weise, A. Lindinger, W. Salzmann, T. Mullins, S. Götz, R. Wester, M. Weidemüller, R. Ağanoğlu, and C. P. Koch. Photoassociation and coherent transient dynamics in the interaction of ultracold rubidium atoms with shaped femtosecond pulses. ii. theory. *Phys. Rev. A*, 80:063417, 2009.

[361] D. J. McCabe, D. G. England, H. E. L. Martay, M. E. Friedman, J. Petrovic, E. Dimova, B. Chatel, and I. A. Walmsley. Pump-probe study of the formation of rubidium molecules by ultrafast photoassociation of ultracold atoms. *Phys. Rev. A*, 80:033404, 2009.

[362] D. Meshulach and Y. Silberberg. Coherent quantum control of multiphoton transitions by shaped ultrashort optical pulses. *Phys. Rev. A*, 60:1287, 1999.

[363] C. Trallero-Herrero, D. Cardoza, T. C. Weinacht, and J. L. Cohen. Coherent control of strong field multiphoton absorption in the presence of dynamic Stark shifts. *Phys. Rev. A*, 71:013423, 2005.

[364] C. Trallero-Herrero, J. L. Cohen, and T. Weinacht. Strong-field atomic phase matching. *Phys. Rev. Lett.*, 96:063603, 2006.

[365] C. Trallero-Herrero and T. C. Weinacht. Transition from weak- to strong-field coherent control. *Phys. Rev. A*, 75:063401, 2007.

[366] A. Gandman, L. Chuntonov, L. Rybak, and Z. Amitay. Coherent phase control of resonance-mediated (2 + 1) three-photon absorption. *Phys. Rev. A*, 75:031401, 2007.

[367] A. Gandman, L. Chuntonov, L. Rybak, and Z. Amitay. Pulse-bandwidth dependence of coherent phase control of resonance-mediated (2 + 1) three-photon absorption. *Phys. Rev. A*, 76:053419, 2007.

[368] L. Chuntonov, L. Rybak, A. Gandman, and Z. Amitay. Enhancement of intermediate-field two-photon absorption by rationally shaped femtosecond pulses. *Phys. Rev. A*, 77:021403, 2008.

[369] L. Chuntonov, L. Rybak, A. Gandman, and Z. Amitay. Frequency-domain coherent control of femtosecond two-photon absorption: intermediate-field versus weak-field regime. *J. Phys. B*, 41:035504, 2008.

[370] Z. Amitay, A. Gandman, L. Chuntonov, and L. Rybak. Multichannel selective femtosecond coherent control based on symmetry properties. *Phys. Rev. Lett.*, 100:193002, 2008.

[371] L. Rybak, Z. Amitay, S. Amaran, R. Kosloff, M. Tomza, R. Moszynski, and C. P. Koch. Femtosecond coherent control of thermal photoassociation of magnesium atoms. *Farad. Discuss.*, 153:383–394, 2011.

[372] S. Amaran, R. Kosloff, M. Tomza, W. Skomorowski, F. Pawowski, R. Moszynski, L. Rybak, L. Levin, Z. Amitay, J. M. Berglund, D. M. Reich, and C. P. Koch. Femtosecond two-photon photoassociation of hot magnesium atoms: A quantum dynamical study using thermal random phase wavefunctions. *J. Chem. Phys.*, 139, 2013.

[373] T. Ban, H. Skenderović, R. Beuc, I. K. Bronić, S. Rousseau, A. Allouche, M. Aubert-Frécon, and G. Pichler. Pure long-range ion-pair Cs_2 molecules. *Chem. Phys. Lett.*, 345:423, 2001.

[374] T. Ban, R. Beuc, H. Skenderovi, and G. Pichler. Rubidium pure long-range ion-pair molecules. *Europhys. Lett.*, 66:485, 2004.

[375] C. Amiot, O. Dulieu, and J. Vergès. Resolution of the Apparent Disorder of the Rb_2 $A^1\Sigma_u^1$ (0_u^+) and $b^3\Pi_u$ (0_u^+) Spectra: A Case of Fully Coupled Electronic States. *Phys. Rev. Lett.*, 83:2316, 1999.

[376] M. Ndong and C. P. Koch. Vibrational stabilization of ultracold KRb molecules. A comparative study. *Phys. Rev. A*, 82:043437, 2010.

[377] R. Kosloff. Propagation methods for quantum molecular-dynamics. *Annu. Rev. Phys. Chem.*, 45:145, 1994.

[378] S. E. Sklarz and D. J. Tannor. Loading a Bose-Einstein condensate onto an optical lattice: An application of optimal control theory to the nonlinear schrödinger equation. *Phys. Rev. A*, 66:053619, 2002.

[379] D. M. Reich, M. Ndong, and C. P. Koch. Monotonically convergent optimization in quantum control using Krotov's method. *J. Chem. Phys.*, 136:104103, 2012.

[380] B. Marcelis, B. Verhaar, and S. Kokkelmans. Total control over ultracold interactions via electric and magnetic fields. *Phys. Rev. Lett.*, 100:153201, 2008.

[381] M. Theis, G. Thalhammer, K. Winkler, M. Hellwig, G. Ruff, R. Grimm, and J. H. Denschlag. Tuning the scattering length with an optically induced Feshbach resonance. *Phys. Rev. Lett.*, 93:123001, 2004.

[382] L. Holmegaard, J. H. Nielsen, I. Nevo, H. Stapelfeldt, F. Filsinger, J. Küpper, and G. Meijer. Laser-induced alignment and orientation of quantum-state-selected large molecules. *Phys. Rev. Lett.*, 102:023001, 2009.

[383] O. Ghafur, A. Rouzée, A. Gijsbertsen, W. K. Siu, S. Stolte, and M. J. Vrakking. Impulsive orientation and alignment of quantum-state-selected no molecules. *Nature Phys.*, 5:289, 2009.

[384] S. S. Viftrup, V. Kumarappan, S. Trippel, H. Stapelfeldt, E. Hamilton, and T. Seideman. Holding and spinning molecules in space. *Phys. Rev. Lett.*, 99:143602, 2007.

[385] J. H. Nielsen, H. Stapelfeldt, J. Küpper, B. Friedrich, J. J. Omiste, and R. González-Férez. Making the best of mixed-field orientation of polar molecules: A recipe for achieving adiabatic dynamics in an electrostatic field combined with laser pulses. *Phys. Rev. Lett.*, 108:193001, 2012.

[386] B. J. Sussman, D. Townsend, M. Y. Ivanov, and A. Stolow. Dynamic Stark control of photochemical processes. *Science*, 314:278, 2006.

[387] D. Townsend, B. J. Sussman, and A. Stolow. A Stark future for quantum control. *J. Phys. Chem. A*, 115:357, 2011.

[388] W. Skomorowski and R. Moszynski. Long-range interactions between an atom in its ground S state and an open-shell linear molecule. *J. Chem. Phys.*, 134:124117, 2011.

[389] H. K. Pechkis, D. Wang, Y. Huang, E. E. Eyler, P. L. Gould, W. C. Stwalley, and C. P. Koch. Enhancement of the formation of ultracold $^{85}\mathrm{Rb}_2$ molecules due to resonant coupling. *Phys. Rev. A*, 76:022504, 2007.

[390] M. Mayle, R. González-Férez, and P. Schmelcher. Controlling molecular orientation through radiative rotational transitions in strong static electric fields. *Phys. Rev. A*, 75:013421, 2007.

[391] E. Hodby, S. T. Thompson, C. A. Regal, M. Greiner, A. C. Wilson, D. S. Jin, E. A. Cornell, and C. E. Wieman. Production efficiency of ultra-cold Feshbach molecules in bosonic and fermionic systems. *Phys. Rev. Lett.*, 94:120402, 2005.

[392] M. Borkowski, P. S. Żuchowski, R. Ciuryło, P. S. Julienne, D. Kedziera, L. Mentel, P. Tecmer, F. Münchow, C. Bruni, and A. Görlitz. Scattering lengths in isotopologues of the RbYb system. *Phys. Rev. A*, 88:052708, 2013.

[393] M. Lemeshko and B. Friedrich. Probing weakly bound molecules with nonresonant light. *Phys. Rev. Lett.*, 103:053003, 2009.

[394] M. Lemeshko and B. Friedrich. Fine-tuning molecular energy levels by nonresonant laser pulses. *J. Phys. Chem. A*, 114:9848, 2010.

[395] M. Tomza, R. González-Férez, C. P. Koch, and R. Moszynski. in preparation.

[396] F. Münchow. *Data-Driven Batch Scheduling.* PhD thesis, Universität Düsseldorf, 2012.

[397] D. C. Yost, A. Cingöz, T. K. Allison, A. Ruehl, M. E. Fermann, I. Hartl, and J. Ye. Power optimization of XUV frequency combs for spectroscopy applications. *Opt. Express*, 19:23483, 2011.

[398] A. Cingöz, D. C. Yost, T. K. Allison, A. Ruehl, M. E. Fermann, I. Hart, and J. Ye. Direct frequency comb spectroscopy in the extreme ultraviolet. *Nature*, 482:68, 2012.

[399] G. Zürn, T. Lompe, A. N. Wenz, S. Jochim, P. S. Julienne, and J. M. Hutson. Precise characterization of ^{6}Li Feshbach resonances using trap-sideband-resolved rf spectroscopy of weakly bound molecules. *Phys. Rev. Lett.*, 110:135301, 2013.

[400] R. Grimm, M. Weidemüller, and Y. B. Ovchinnikov. Optical dipole traps for neutral atoms. *Adv. At. Mol. Opt. Phys.*, 42:95, 2000.

Appendices

Appendix A

Paper I

"Formation of ultracold SrYb molecules in an optical lattice by photoassociation spectroscopy: theoretical prospects"

Michał Tomza, Filip Pawłowski, Małgorzata Jeziorska,
Christiane P. Koch, Robert Moszynski

Physical Chemistry Chemical Physics, **13**, 18893 (2011).

PCCP

View Online / Journal Homepage / Table of Contents for this issue
Dynamic Article Links

Cite this: *Phys. Chem. Chem. Phys.*, 2011, **13**, 18893–18904

www.rsc.org/pccp

PAPER

Formation of ultracold SrYb molecules in an optical lattice by photoassociation spectroscopy: theoretical prospects

Michał Tomza,[a] Filip Pawłowski,[ab] Małgorzata Jeziorska,[a] Christiane P. Koch[c] and Robert Moszynski*[a]

Received 15th April 2011, Accepted 29th July 2011
DOI: 10.1039/c1cp21196j

State-of-the-art *ab initio* techniques have been applied to compute the potential energy curves for the SrYb molecule in the Born–Oppenheimer approximation for the electronic ground state and the first fifteen excited singlet and triplet states. All the excited state potential energy curves were computed using the equation of motion approach within the coupled-cluster singles and doubles framework and large basis-sets, while the ground state potential was computed using the coupled cluster method with single, double, and noniterative triple excitations. The leading long-range coefficients describing the dispersion interactions at large interatomic distances are also reported. The electric transition dipole moments have been obtained as the first residue of the polarization propagator computed with the linear response coupled-cluster method restricted to single and double excitations. Spin–orbit coupling matrix elements have been evaluated using the multireference configuration interaction method restricted to single and double excitations with a large active space. The electronic structure data were employed to investigate the possibility of forming deeply bound ultracold SrYb molecules in an optical lattice in a photoassociation experiment using continuous-wave lasers. Photoassociation near the intercombination line transition of atomic strontium into the vibrational levels of the strongly spin–orbit mixed $b^3\Sigma^+$, $a^3\Pi$, $A^1\Pi$, and $C^1\Pi$ states with subsequent efficient stabilization into the $v'' = 1$ vibrational level of the electronic ground state is proposed. Ground state SrYb molecules can be accumulated by making use of collisional decay from $v'' = 1$ to $v'' = 0$. Alternatively, photoassociation and stabilization to $v'' = 0$ can proceed *via* stimulated Raman adiabatic passage provided that the trapping frequency of the optical lattice is large enough and phase coherence between the pulses can be maintained over at least tens of microseconds.

1 Introduction

Molecules cooled to temperatures below $T = 10^{-3}$ K allow for tackling questions touching upon the very fundamentals of quantum mechanics. They are also promising candidates in novel applications, ranging from ultracold chemistry and precision measurements to quantum computing. Cold and ultracold molecules are thus opening up new and exciting areas of research in chemistry and physics. Due to their permanent electric dipole moment, polar molecules are particularly interesting objects of study: dipole–dipole interactions are long range and can precisely be controlled with external electric fields. This turns the experimental parameters field strength and orientation into the knobs that control the quantum dynamics of these molecules. Hence, it is not surprising that a major objective for present day experiments on cold molecules is to achieve quantum degeneracy for polar molecules. Two approaches to this problem are being used—indirect methods, in which molecules are formed from pre-cooled atomic gases,[1–8] and direct methods, in which molecules are cooled from molecular beam temperatures, typically starting at tens of Kelvins.[9–13]

Direct cooling techniques, based on buffer gas cooling[9] or Stark deceleration,[10] produce cold molecules with a temperature well below 1 K. However, a second-stage cooling process is required to reach temperatures below 10^{-3} K. The second-stage technique which has long been thought to be the most promising is sympathetic cooling where cold molecules are introduced into an ultracold atomic gas and equilibrate with it. Sympathetic cooling has successfully been used to achieve Fermi degeneracy in ^{6}Li[14] and Bose–Einstein condensation in ^{41}K[15] and to obtain ultracold ions.[16–19] For molecular systems,

---

[a] *Faculty of Chemistry, University of Warsaw, Pasteura 1, 02-093 Warsaw, Poland. E-mail: robert.moszynski@tiger.chem.uw.edu.pl*
[b] *Physics Institute, Kazimierz Wielki University, pl. Weyssenhoffa 11, 85-072 Bydgoszcz, Poland*
[c] *Theoretische Physik, Universität Kassel, Heinrich-Plett-Str. 40, 34132 Kassel, Germany*

however, sympathetic cooling has not yet been attempted, and there are many challenges to overcome. In fact, calculations of the scattering cross sections for the collisions of molecules with ultracold coolant atoms suggest that sympathetic cooling may not be so very much efficient in many cases.[20–22]

Alternatively, indirect methods first cool atoms to ultralow temperatures and then employ photoassociation[4] or magnetoassociation[5] to create molecules, reaching translational temperatures of the order of a few μK or nK. In particularly fortuitous cases, photoassociation may directly produce molecules in their vibrational ground state.[7] Typically, however, the molecules are created in extremely weakly bound levels, and follow-up stabilization to the ground state is necessary. For molecules built of alkali metal atoms, this has been achieved using stimulated emission pumping[23] or alternatively, employing coherent control techniques such as Stimulated Raman Adiabatic Passage (STIRAP)[6,24–26] and vibrational cooling of molecules with amplitude-shaped broadband laser light.[27]

Closed-shell atoms such as alkali earth metals are more challenging to cool and trap than open-shell atoms such as the alkalis. Closed-shell atoms do not have a magnetic moment in their ground state that enables magnetic trapping. Moreover, for alkaline earth metals the short lifetime of the first excited ^{1}P state implies rather high Doppler temperatures, making dual-stage cooling a necessity where the second stage operates near an intercombination line. Despite these obstacles, cooling of calcium, strontium, and ytterbium atoms to micro-Kelvin temperatures has been achieved, and Bose–Einstein condensates of ^{40}Ca,[28] ^{84}Sr,[29,30] ^{86}Sr,[31] ^{88}Sr,[32] ^{170}Yb,[33] and ^{174}Yb[34] have been obtained.

In contrast to alkali metal dimers,[5] the magnetoassociation of two closed-shell atoms is not feasible experimentally even if the nuclear spin is non-zero. The zero-field splittings and couplings between the atomic threshold and molecular states provided by the largest non-zero terms in the fine structure and hyperfine structure Hamiltonian for the electronic ground state, *i.e.*, the scalar and tensor interactions between the nuclear magnetic dipole moments,[35] are simply too small.[5] On the other hand, the closed-shell structure of the alkali earth metal and ytterbium atoms leads to very simple molecular potentials with low radiative losses and weak coupling to the environment. This opens new areas of possible applications, such as manipulation of the scattering properties with low-loss optical Feshbach resonances,[36] high-resolution photoassociation spectroscopy at the intercombination line,[37,38] precision measurements to test for a time variation of the proton-to-electron mass ratio,[39] quantum computation with trapped polar molecules,[40] and ultracold chemistry.[41]

To the best of our knowledge, production of ultracold heteronuclear diatomic molecules built of closed-shell atoms has not yet been achieved experimentally. Also such processes have not yet been considered theoretically. Here we fill this gap and report a theoretical study of the photoassociative formation of heteronuclear diatomic molecules from two closed-shell atoms on the example of the SrYb molecule. Although the SrYb molecule may seem very exotic, especially for chemists, strontium and ytterbium atoms are promising candidates for producing molecules since they have both successfully been cooled and trapped. Moreover, both Sr and Yb have many stable isotopes. Such a diversity of stable isotopes is key to controlling the collisional properties of bosonic molecules with no magnetic moments and hyperfine structure. For example, one can effectively tune the interatomic interactions by choosing the most suitable isotope to achieve scattering lengths appropriate for evaporative cooling. Last but not least, we consider photoassociative formation of SrYb molecules since there are ongoing experiments[42] aiming at producing cold SrYb molecules in an optical lattice.

The plan of our paper is as follows. Section 2 describes the theoretical methods used in the *ab initio* calculations and discusses the electronic structure of SrYb in terms of the ground and excited-state potentials, transition moments, spin–orbit and nonadiabatic angular couplings. Section 3 analyzes the vibrational structure of the SrYb molecule as a prerequisite to determine an efficient route for photoassociation followed by stabilization into the vibronic ground state. It also discusses prospects of producing cold SrYb molecules by photoassociation near the intercombination line of strontium, and subsequent spontaneous or stimulated emission. Section 4 summarizes our findings.

2 Electronic structure of SrYb

In the present study we adopt the computational scheme successfully applied before to the ground and excited states of the calcium dimer[43–47] and to the (BaRb)$^+$ molecular ion.[19] The potential energy curves for the ground and excited states of the SrYb molecule have been obtained by a supermolecule method,

$$V^{2S+1|\Lambda|}(R) = E^{\mathrm{SM}}_{\mathrm{AB}} - E^{\mathrm{SM}}_{\mathrm{A}} - E^{\mathrm{SM}}_{\mathrm{B}}, \qquad (1)$$

where $E^{\mathrm{SM}}_{\mathrm{AB}}$ denotes the energy of the dimer computed using the supermolecule method SM, and $E^{\mathrm{SM}}_{\mathrm{X}}$, X = A or B, is the energy of the atom X. For the ground state potential we used the coupled cluster method restricted to single, double, and noniterative triple excitations, CCSD(T). Calculations on all the excited states employed the linear response theory within the coupled-cluster singles and doubles (LRCCSD) framework,[48] also known as the equation of motion coupled-cluster method (EOM-CCSD).[49] We refer the reader to the recent review article by Bartlett and Musiał for a detailed discussion of these *ab initio* methods.[50] The CCSD(T) and LRCCSD calculations were performed with the DALTON program.[51] Note that the methods used in our calculations are strictly size-consistent, so they ensure a proper dissociation of the electronic states, and a proper long-range asymptotics of the corresponding potential energy curves. This is especially important when dealing with collisions at ultralow temperatures, where the accuracy of the potential in the long range is crucial. The interaction potential $V^{2S+1|\Lambda|}(R)$ given by eqn (1) has a well defined asymptotics given by the multipole expansion,[52]

$$V^{2S+1|\Lambda|}(R) \approx \sum_{n=3}^{\infty} \frac{C_{2n}}{R^{2n}}, \qquad (2)$$

where C_{2n} are the long-range coefficients related to the atomic properties. In the case of the SrYb molecule the asymptotic expansion starts with the R^{-6} terms describing the dispersion interactions, but for the excited states terms describing the induction quadrupole-induced dipole contributions are also present.

For each electronic state we have computed the long-range coefficients describing the dispersion and induction interactions from the standard expressions (see, *e.g.* ref. 52 and 53) that can be derived from the multipole expansion of the interatomic interaction operator. The long-range dispersion coefficients were computed with the recently introduced explicitly connected representation of the expectation value and polarization propagator within the coupled cluster method,[54,55] and the best approximation XCCSD4 proposed by Korona and collaborators.[56] For the singlet and triplet states dissociating into Sr(^{1}P) + Yb(^{1}S), and Sr(^{3}P) + Yb(^{1}S), respectively, the dispersion coefficients were obtained from the sum-over-state expression with the transition moments and excitation energies computed with the multireference configuration interaction method limited to single and double excitations (MRCI).

The transitions from the ground X$^1\Sigma^+$ state to the $^1\Sigma^+$ and $^1\Pi$ states are electric dipole allowed. The transition dipole moments for the electric, d_i, transitions were computed from the following expression:[57]

$$d_i = \langle \mathrm{X}^1\Sigma^+ |\hat{\mathbf{d}}|(n)^1|\Lambda|\rangle, \tag{3}$$

where $\hat{\mathbf{d}}$ denotes the dipole moment operator. Note that in eqn (3) $i = x$ or y corresponds to transitions to $^1\Pi$ states, while $i = z$ corresponds to transitions to $^1\Sigma^+$ states. In the present calculations the electric transition dipole moments were computed as the first residue of the LRCCSD linear response function with two electric, r, operators.[48] In these calculations we have used the DALTON program.[51] We have evaluated the dependence of the transition dipole moments with the internuclear distance for the same set of distances as the excited state potential energy curves.

The electronic states of the low lying excited states of the SrYb molecule are coupled by nonadiabatic couplings. Therefore, in this work we have computed the most important angular coupling matrix elements,

$$A(R) = \langle (n)^{2S+1}|\Lambda||L_+|\ (n')^{2S+1}|\Lambda'|\rangle. \tag{4}$$

In the above expression L_+ denotes the raising electronic angular momentum operator. Note that the electronic angular momentum operator couples states with Λ differing by one. Nonadiabatic couplings were obtained with the MRCI method and the MOLPRO code.[58] We have evaluated the dependence of the nonadiabatic coupling matrix elements with the internuclear distance for the same set of distances as the excited state potential energy curves.

Strontium and ytterbium are heavy atoms, so the electronic states of the SrYb molecule are strongly mixed by the spin–orbit (SO) interactions. Therefore, in any analysis of the formation of the SrYb molecules the SO coupling and its dependence on the internuclear distance R must be taken into account. We have evaluated the spin–orbit coupling matrix elements for the lowest dimer states that couple to the $0^{+/-}$, 1, and 2 states of SrYb, with the spin–orbit coupling operator H_{SO} defined within the Breit–Pauli approximation.[59] The spin–orbit coupling matrix elements have been computed within the MRCI framework with the MOLPRO code.[58] Diagonalization of the relativistic Hamiltonian gives the spin–orbit coupled potential energy curves for the $0^{+/-}$, 1 and 2 states, respectively. Note that all potentials in the Hamiltonian matrices were taken from CCSD(T) and LRCCSD calculations. Only the diagonal and nondiagonal spin–orbit coupling matrix elements were obtained with the MRCI method. Once the eigenvectors of these matrices are available, one can easily get the electric dipole transition moments and the nonadiabatic coupling matrix elements between the relativistic states. In order to mimic the scalar relativistic effects some electrons were described by pseudopotentials. For Yb we took the ECP28MWB pseudopotential,[60] while for Sr the ECP28MDF[61] pseudopotential, both from the Stuttgart library. For the strontium and ytterbium atoms we used spdfg quality basis sets,[61,62] augmented with a set of [2pdfg] diffuse functions. In addition, this basis set was augmented by the set of bond functions consisting of [3s3p2d1f] functions placed in the middle of the SrYb dimer bond. The full basis of the dimer was used in the supermolecule calculations and the Boys and Bernardi scheme was used to correct for the basis-set superposition error.[63]

Calculations were done for the ground state and first fifteen (eight singlet and seven triplet) excited states of SrYb. The singlet states correspond to the Sr(^{1}D) + Yb(^{1}S), Sr(^{1}P) + Yb(^{1}S), Sr(^{1}S) + Yb(4f^{13}5d6s^2), and Sr(^{1}S) + Yb(^{1}P) dissociations, while triplet states to Sr(^{3}P) + Yb(^{1}S), Sr(^{1}S) + Yb(^{3}P), and Sr(^{3}D) + Yb(^{1}S). The potential energies were calculated for twenty interatomic distances R ranging from 5 to 50 bohr for each potential curve. The ground state potential is presented in Fig. 1, while the potential energy curves for the excited states are plotted in Fig. 2. The spectroscopic characteristics of all these states are reported in Table 1. The separated atoms energy for each state was set equal to the experimental value. Numerical values of the potentials are available from the authors on request.

Before continuing the discussion of the potentials let us note that the atomic excitation energies obtained from the

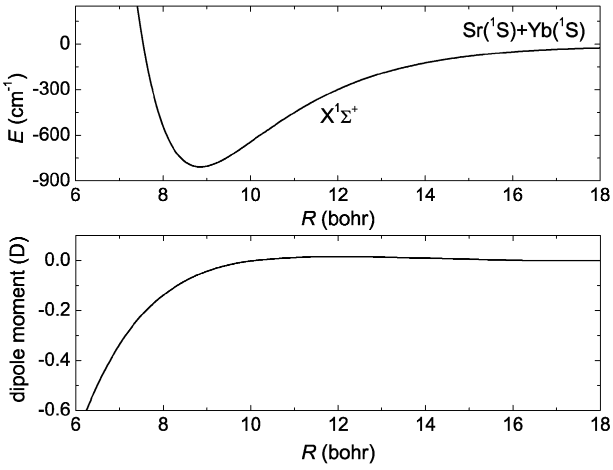

Fig. 1 Potential energy curve (upper panel) and permanent dipole moment (lower panel) of the X$^1\Sigma^+$ electronic ground state of the SrYb molecule.

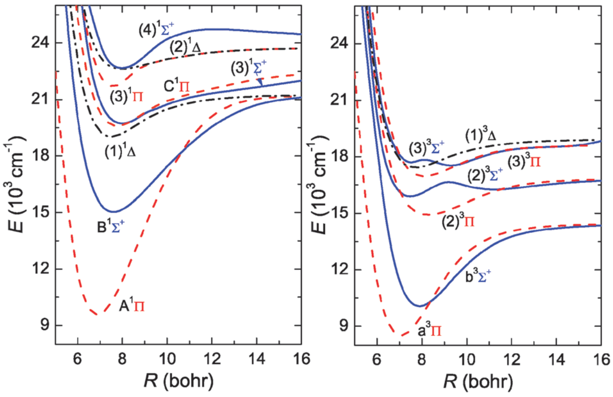

Fig. 2 Potential energy curves of singlet (left) and triplet (right) excited states of a SrYb dimer.

Table 1 Spectroscopic characteristics (equilibrium distance, well depth, harmonic constant) of the non-relativistic electronic states of the ^{88}Sr^{174}Yb dimer

State	R_e/bohr	D_e/cm^{-1}	ω_e/cm^{-1}	Dissociation
X$^1\Sigma^+$	8.78	828	32.8	Sr(^{1}S) + Yb(^{1}S)
A$^1\Pi$	6.84	11 851	94.8	Sr(^{1}D) + Yb(^{1}S)
B$^1\Sigma^+$	7.54	5201	63.5	Sr(^{1}D) + Yb(^{1}S)
(1)$^1\Delta$	7.42	1202	62.5	Sr(^{1}D) + Yb(^{1}S)
(3)$^1\Sigma^+$	7.91	2963	48.5	Sr(^{1}P) + Yb(^{1}S)
(2)$^1\Pi$	7.70	3112	61.6	Sr(^{1}P) + Yb(^{1}S)
(4)$^1\Sigma^+$	7.84	1790	58.6	Sr(^{1}P) + Yb($\frac{7}{2},\frac{3}{2}$)
(3)$^1\Pi$	7.53	2153	72.5	Sr(^{1}P) + Yb($\frac{7}{2},\frac{3}{2}$)
(2)$^1\Delta$	7.89	1175	40.2	Sr(^{1}P) + Yb($\frac{7}{2},\frac{3}{2}$)
a$^3\Pi$	7.02	6078	84.7	Sr(^{3}P) + Yb(^{1}S)
b$^3\Sigma^+$	7.84	4493	71.3	Sr(^{3}P) + Yb(^{1}S)
(2)$^3\Sigma^+$	7.39	1024	61.7	Sr(^{1}S) + Yb(^{3}P)
2nd min	11.02	622	21.0	
(2)$^3\Pi$	8.23	1947	42.4	Sr(^{1}S) + Yb(^{3}P)
(3)$^3\Sigma^+$	7.45	982	92.7	Sr(^{3}D) + Yb(^{1}S)
2nd min	9.33	1077	47.8	
(3)$^3\Pi$	8.04	1678	47.9	Sr(^{3}D) + Yb(^{1}S)
(1)$^3\Delta$	7.65	1422	50.8	Sr(^{3}D) + Yb(^{1}S)

CCSD calculations are accurate. Our predicted position of the nonrelativistic ^{3}P state of strontium is 14 463 cm^{-1}, to be compared with the experimental value of 14 705 cm^{-1}[64] deduced from the positions of the states in the P multiplet and the Landé rule. A similar accuracy is observed for the ^{3}D state, 18 998 cm^{-1} *vs.* 18 426 cm^{-1}. For the ^{1}D and ^{1}P states of Sr we obtain less than 5% difference with the experimental values listed by NIST.[64] Similarly good results are also obtained for the ytterbium atom. Only the ordering of the Yb ^{1}P and ^{3}D states is not reproduced correctly, but the energy difference for these states is small. Table 2 lists a comparison of the computed and experimental atomic excitation energies. We would like to stress that we computed the interaction energies according to eqn (1) using the full basis of the dimer for both the molecule and the atoms to correct the results for the basis-set superposition error, and then added the experimental atomic excitation energies. The Gaussian basis sets used in the present calculations with diffuse exponents and bond functions were optimized to get the correct description of the long-range induction and dispersion interactions, and not the atomic correlation energies. Finally we note that the lifetimes of the ^{3}P$_1$ and ^{1}P$_1$ states of Sr are accurately reproduced. For the ^{1}P$_1$ state we obtained 4.92 ns to be compared with the experimental value of 5.22(3) ns.[65] For the ^{3}P$_1$ the theoretical and experimental numbers are 22 μs and 20 μs,[38] respectively. Such a good agreement between theory and experiment for the atoms gives us confidence that the molecular results will be of similar accuracy, *i.e.* a few percent off from the exact results.

Table 2 Non-relativistic atomic excitation energies (cm^{-1})

Strontium			Ytterbium		
State	Present	Exp.[64]	State	Present	Exp.[64]
^{3}P	14 463	14 705	^{3}P	17 635	18 903
^{3}D	18 998	18 426	^{3}D	25 783	24 801
^{1}D	21 224	20 150	^{1}P	24 249	25 068
^{1}P	22 636	21 698	^{1}D	28 202	27 678

The ground X$^1\Sigma^+$ state potential energy curve is presented in Fig. 1. It follows from the naive molecular orbital theory that the SrYb molecule in the ground state should be considered as a van der Waals molecule since the molecular configuration has an equal number of bonding and antibonding electrons. No regular chemical bond is expected, except for a weak dispersion attraction and exchange-repulsion. Indeed, the ground state potential is weakly bound with the binding energy of 828 cm^{-1}. For $J = 0$ it supports $N_\nu = 62$ vibrational levels for the lightest isotope pair and up to $N_\nu = 64$ for the heaviest isotopes. The changes of the number of bound rovibrational levels and of the position of the last vibrational level for different isotopes result in changes in the sign and value of the scattering length. This should allow to choose isotopes most suitable for cooling and manipulation. The equilibrium distance, well depth, and harmonic frequency of the X$^1\Sigma^+$ state are reported in Table 1. The permanent dipole moment of SrYb in the ground electronic state as a function of the interatomic distance R is presented in Fig. 1. Except for short interatomic distances, the dipole moment is very small. This is not very surprising since the two atoms have very similar electronegativities and the charge flow from one atom to the other, after the formation of the weak van der Waals bond, is very small. In fact, similarly as the bonding of the ground state, the dipole moment of SrYb should be considered as a dispersion dipole.[66] At large interatomic distances it vanishes as R^{-6}.[67,68] The vibrationally averaged dipole moment of SrYb in the ground vibrational state is very small and equal to 0.058 D.

Potential energy curves of the excited singlet and triplet states of SrYb are presented in Fig. 2, and the corresponding long-range coefficients are reported in Table 3. The long-range

Table 3 Long-range dispersion coefficients (in a.u.) for ground and relevant excited states of the SrYb dimer

State	C_6	C_8
X$^1\Sigma^+$	2688	294 748
A$^1\Pi$	3771	502 070
a$^3\Pi$	1265	509 068
b$^3\Sigma^+$	6754	317 656

potential computed according to eqn (2) was used at distances larger than $R = 15$ bohr. A proper damping function describing the charge overlap and damping effects[52,69] was used to match the *ab initio* and the asymptotic results. The agreement between the raw *ab initio* data and the asymptotic expansion (2) with the damping effects neglected was of the order of 1% for the ground state and 3 to 4% for the excited states at $R = 15$ bohr. Inspection of Fig. 2 reveals that the potential energy curves for the excited states of the SrYb molecule are smooth with well defined minima. The potential energy curves of the (2) and (3)$^3\Sigma^+$ states show an avoided crossing and exhibit a double minimum structure. These double minima on the potential energy curves are due to strong nonadiabatic interactions between these states. Other potential energy curves do not show any unusual features, except for the broad maximum of the potential of the (4)$^1\Sigma^+$ which is most likely due to the interaction with a higher excited state not reported in the present work. Except for the shallow double minima of the (2)$^3\Sigma^+$ and (3)$^3\Sigma^+$ states, and shallow Δ states, all other excited states of the SrYb molecule are strongly bound with binding energies D_e ranging from approximately 1790 cm^{-1} for the (4)$^1\Sigma^+$ state up to as much as 11 851 cm^{-1} for the A$^1\Pi$ state.

Let us compare the potential energy curves of the heteronuclear SrYb molecule to those of the homonuclear Sr_2 dimer.[70] In general, molecular orbitals constructed from the linear combinations of the Sr(5p) + Yb(6p) or Sr(4d) + Yb(5d) atomic orbitals are expected to have less bonding or antibonding character than the molecular orbitals constructed from the Sr(5p) + Sr(5p) or Sr(4d) + Sr(4d) atomic orbitals, because large atomic orbital energy differences make combination of these orbitals less effective. This explains why many potential energy curves of the SrYb dimer are less attractive than the corresponding potential energy curves of the Sr_2 dimer. The strongly attractive character of the potential energy curves for the first $^3\Sigma^+$ and the first $^3\Pi$ states converging in the long range to Sr(^{3}P) + Yb(^{1}S) asymptote could be a result of the stabilizing effect of the Yb(5d) orbitals for the lowest unoccupied orbitals of σ and π symmetry (these molecular orbitals are combinations of the Yb(6p) and Sr(5p) orbitals, but also of the appropriate Yb(5d) orbitals, closer in energy to Sr(5p)). Potential energy curves for the second $^1\Sigma^+$ and second $^1\Pi$ states converging to Sr(^{1}P) + Yb(^{1}S) are less attractive than the potential energy curves for the triplet states, similarly as for the corresponding states of the Sr_2 dimer. As for the Sr_2 dimer, potential energy curves for the $^1\Sigma^+$ and $^1\Pi$ states converging to the Sr(^{1}D) + Yb(^{1}S) asymptote have a much more attractive character than the triplet states converging to the Sr(^{3}D) + Yb(^{1}S) asymptote.

The a$^3\Pi$, b$^3\Sigma^+$, A$^1\Pi$ and C$^1\Pi$ excited states essential for the photoassociative formation of the ground state SrYb molecule proposed in the next section are plotted in Fig. 4. The matrix elements of the spin–orbit coupling were calculated for the manifolds of coupled a$^3\Pi$, b$^3\Sigma^+$, A$^1\Pi$ states, *cf.* Fig. 3. The knowledge of the spin–orbit coupling between a$^3\Pi$, b$^3\Sigma^+$, A$^1\Pi$ and C$^1\Pi$ states allows us to obtain the relativistic (1)0$^-$, (2)0$^-$, (1)0$^+$, (1)1, (2)1, (3)1, (4)1 and (1)2 states by diagonalizing the appropriate relativistic Hamiltonian matrices. The $\Omega = 1$ states are also plotted in Fig. 4. Note that the crossing of the b$^3\Sigma^+$ and A$^1\Pi$ nonrelativistic states becomes an avoided crossing between the (2)1 and (3)1 states.

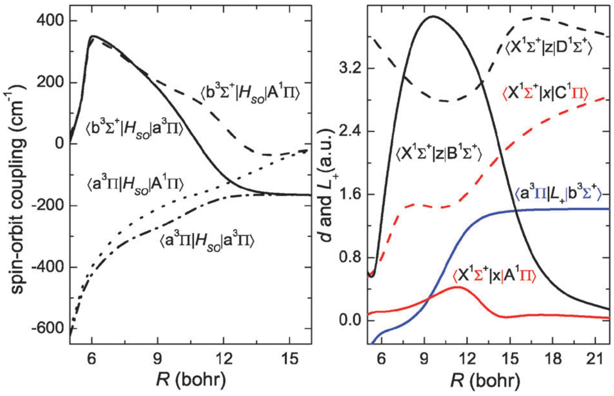

Fig. 3 Left: matrix elements of the spin–orbit interaction for the a$^3\Pi$, b$^3\Sigma^+$, and A$^1\Pi$ electronically excited states of SrYb. Right: matrix elements of the electric transition dipole moment from the X$^1\Sigma^+$ ground electronic state to A$^1\Pi$ state (solid red curve) and to the C$^1\Pi$ state (dashed red curve), and matrix elements of the nonadiabatic angular coupling between the a$^3\Pi$ and b$^3\Sigma^+$ states of SrYb (solid blue curve).

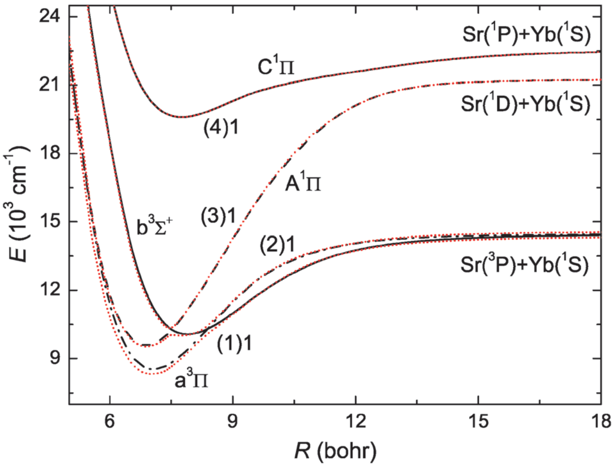

Fig. 4 The a$^3\Pi$, b$^3\Sigma^+$, A$^1\Pi$ and C$^1\Pi$ potential energy curves (solid and dashed black curves) in Hund's case (a) representation that are coupled by the spin–orbit interaction and the resulting $\Omega = 1$ relativistic states (red dotted curves) in Hund's case (c) representation of the SrYb dimer.

Having all the results briefly presented above we are ready to discuss the photoassociation process of cold Sr and Yb atoms, and look for the prospects of producing ultracold SrYb molecules. To conclude this section we would like to emphasize that almost all *ab initio* results were obtained with the most advanced size-consistent methods of quantum chemistry: CCSD(T) and LRCCSD. In all calculations all electrons, except for those described by the pseudopotentials, were correlated (42 for ytterbium and 10 for strontium). Only the SO coupling matrix elements and the nonadiabatic matrix elements were obtained with the MRCI method which is not size consistent. Fortunately enough, all of the couplings are important in the region of the curve crossings or at large distances, so the effect of the size-inconsistency of MRCI on our results should not be dramatic.

3 Photoassociation and formation of ground state molecules

Photoassociation is considered for a continuous-wave laser that is red-detuned with respect to the intercombination line. This transition is dipole-forbidden. However, the $a^3\Pi$ state correlating to the asymptote of the intercombination line transition, *cf.* Fig. 4, is coupled by spin–orbit interaction to two singlet states, $A^1\Pi$ and $C^1\Pi$, that are connected by a dipole-allowed transition to the ground electronic state, $X^1\Sigma^+$. Thus an effective transition matrix element is created which can be written, to a very good approximation, as

$$d_{\mathrm{SO}}(R) = \frac{\langle X^1\Sigma^+|\hat{\mathbf{d}}|C^1\Pi\rangle\langle C^1\Pi|\hat{\mathbf{H}}_{\mathrm{SO}}|a^3\Pi\rangle}{E_{a^3\Pi}-E_{C^1\Pi}} + \frac{\langle X^1\Sigma^+|\hat{\mathbf{d}}|A^1\Pi\rangle\langle A^1\Pi|\hat{\mathbf{H}}_{\mathrm{SO}}|a^3\Pi\rangle}{E_{a^3\Pi}-E_{A^1\Pi}}, \tag{5}$$

where $\hat{\mathbf{H}}_{\mathrm{SO}}$ is the spin–orbit Hamiltonian in the Breit–Pauli approximation.[59] The long-range part of $d_{\mathrm{SO}}(R)$, dominated by the first term in the above expression, is due to the coupling with the $C^1\Pi$ state, ideally suited for photoassociation. The short-range part is due to the coupling with the $A^1\Pi$ state, paving the way toward efficient stabilization of the photoassociated molecules to the electronic ground state. The $a^3\Pi$ state, in addition to the spin–orbit coupling with the two singlet states, is also coupled to the $b^3\Sigma^+$ state correlating to the same asymptote, $\mathrm{Sr}(^3P) + \mathrm{Yb}(^1S)$. The Hamiltonian describing these couplings yielding Hund's case (c) $\Omega = 1$ states reads in the rotating-wave approximation

$$\hat{\mathbf{H}} = \begin{pmatrix} \hat{\mathbf{H}}^{X^1\Sigma^+} & 0 & 0 & \frac{1}{2}d_1(R)E_0 & \frac{1}{2}d_2(R)E_0 \\ 0 & \hat{\mathbf{H}}^{a^3\Pi} & \xi_1(R) & \xi_2(R) & \xi_4(R) \\ 0 & \xi_1(R) & \hat{\mathbf{H}}^{b^3\Sigma^+} & \xi_3(R) & \xi_5(R) \\ \frac{1}{2}d_1(R)E_0 & \xi_2(R) & \xi_3(R) & \hat{\mathbf{H}}^{A^1\Pi} & 0 \\ \frac{1}{2}d_2(R)E_0 & \xi_4(R) & \xi_5(R) & 0 & \hat{\mathbf{H}}^{C^1\Pi} \end{pmatrix}, \tag{6}$$

where $\hat{\mathbf{H}}^{2S+1|\Lambda|}$ is the Hamiltonian for nuclear motion in the $^{2S+1}|\Lambda|$ electronic state, $\hat{\mathbf{H}}^{2S+1|\Lambda|} = \hat{\mathbf{T}} + V^{2S+1|\Lambda|}(R) + V^{2S+1|\Lambda|}_{\mathrm{trap}}(R) - (1-\delta_{n0})\hbar\omega_{\mathrm{L}}$. The kinetic energy operator is given by $\hat{\mathbf{T}} = \hat{\mathbf{P}}^2/2\mu$ with μ the reduced mass of SrYb. The trapping potential, $V^{2S+1|\Lambda|}_{\mathrm{trap}}(R)$, is relevant only in the electronic ground state for the detunings considered below, even for large trapping frequencies. We approximate it by a harmonic potential which is well justified for atoms cooled down to the lowest trap states and corresponds to radial confinement in a 3D optical lattice. The parameters of the photoassociation laser are the frequency, ω_{L}, and the maximum field amplitude, E_0. The electric transition dipole moments are denoted by $d_1(R) = \langle X^1\Sigma^+|\hat{\mathbf{d}}|A^1\Pi\rangle$, $d_2(R) = \langle X^1\Sigma^+|\hat{\mathbf{d}}|C^1\Pi\rangle$, and the matrix elements of the spin–orbit coupling are given by

$$\xi_1(R) = \langle a^3\Pi(\Sigma = 0, \Lambda = \pm1)|\,\hat{\mathbf{H}}_{\mathrm{SO}}\,|b^3\Sigma^+(\Sigma = \pm1, \Lambda = 0)\rangle,$$

$$\xi_2(R) = \langle a^3\Pi(\Sigma = 0, \Lambda = \pm1)|\,\hat{\mathbf{H}}_{\mathrm{SO}}\,|A^1\Pi(\Sigma = 0, \Lambda = \pm1)\rangle,$$

$$\xi_3(R) = \langle b^3\Sigma^+(\Sigma = \pm1, \Lambda = 0)|\,\hat{\mathbf{H}}_{\mathrm{SO}}\,|A^1\Pi(\Sigma = 0, \Lambda = \pm1)\rangle,$$

$$\xi_4(R) = \langle a^3\Pi(\Sigma = 0, \Lambda = \pm1)|\,\hat{\mathbf{H}}_{\mathrm{SO}}\,|C^1\Pi(\Sigma = 0, \Lambda = \pm1)\rangle,$$

$$\xi_5(R) = \langle b^3\Sigma^+(\Sigma = \pm1, \Lambda = 0)|\,\hat{\mathbf{H}}_{\mathrm{SO}}\,|C^1\Pi(\Sigma = 0, \Lambda = \pm1)\rangle,$$

Σ and Λ denote the quantum numbers for the projections of electronic spin and orbital angular momenta, $\hat{\mathbf{S}}$ and $\hat{\mathbf{L}}$, onto the internuclear axis. Note that the specific shape of the $C^1\Pi$ potential energy curve as well as the R-dependence of its spin–orbit coupling and transition dipole matrix elements are not important, since the $C^1\Pi$ state provides the effective dipole coupling only at long range. We have therefore approximated the R-dependence of the couplings with the $C^1\Pi$ state by their constant asymptotic values in the calculations presented below. The Hamiltonian (6) has been represented on a Fourier grid with an adaptive step size[71–73] (using $N = 1685$ grid points and grid mapping parameters $\beta = 0.22$, $E_{\mathrm{min}} = 7 \times 10^{-9}$ hartree).

The key idea of photoassociation using a continuous-wave laser is to excite a colliding pair of atoms into a bound level of an electronically excited state.[4,74] For maximum photoassociation efficiency, the detuning of the laser with respect to the atomic asymptote, $\mathrm{Sr}(^3P_1) + \mathrm{Yb}(^1S)$ in our case, is chosen to coincide with the binding energy of one of the vibrational levels in the electronically excited state. Fig. 5 shows two such levels with binding energies $E_{\mathrm{b}} = 5.1\ \mathrm{cm}^{-1}$ (left) and $E_{\mathrm{b}} = 18.9\ \mathrm{cm}^{-1}$ (right). Since four electronically excited states are coupled by the spin–orbit interaction, the vibrational wavefunctions have components on all four electronically excited states, shown in Fig. 6(top). Note that the norm of the $C^1\Pi$-component of these two vibrational wavefunctions is smaller than 10^{-3}. Nevertheless, this is enough, similar to the photoassociation of the strontium dimers near an intercombination line,[38] to provide the transition dipole for the free-to-bound (or quasi-bound-to-bound, due to the trapping potential) excitation. The vibrational level with binding energy $E_{\mathrm{b}} = 5.1\ \mathrm{cm}^{-1}$ is predominantly of triplet character (with 56% of its norm residing on the $a^3\Pi$ state, 32% on the $b^3\Sigma^+$ state and just 11% on the $A^1\Pi$ state), while the vibrational level with binding energy $E_{\mathrm{b}} = 18.9\ \mathrm{cm}^{-1}$ shows a truly mixed character (55% triplet *vs.* 45% singlet). The fact that multiple

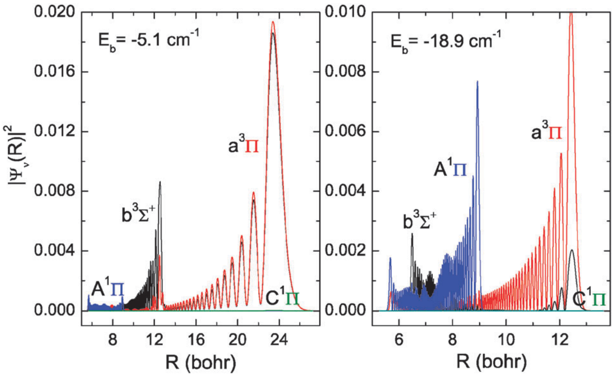

Fig. 5 Vibrational wave functions of the coupled $a^3\Pi$, $b^3\Sigma^+$, $A^1\Pi$, and $C^1\Pi$ electronic states of a SrYb molecule for two binding energies corresponding to vibrational quantum numbers $\nu' = -11$ (left) and $\nu' = -18$ (right) below the dissociation threshold.

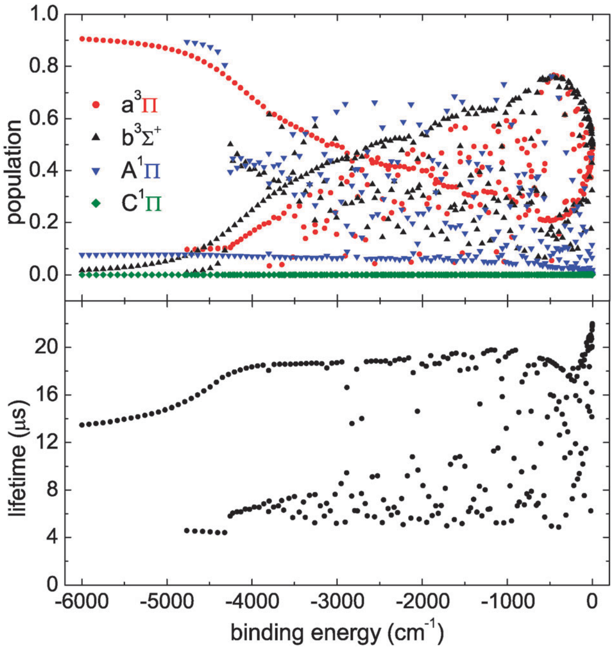

Fig. 6 Top panel: population of the $a^3\Pi$, $b^3\Sigma^+$, $A^1\Pi$ and $C^1\Pi$ components of the vibrational levels *vs.* binding energy. Bottom panel: lifetime of the vibrational levels as a function of binding energy.

classical turning points are clearly visible in the vibrational wavefunction with $E_b = 18.9\ \text{cm}^{-1}$ reflects the resonant nature of the spin–orbit coupling of this level: the coinciding energy of the levels in the coupled vibrational ladders leads to a resonant beating between the different components of the coupled wavefunctions.[75] Such a structure of the vibrational wavefunctions was shown to be ideally suited for efficient stabilization of the photoassociated molecules into deeply bound levels in the ground electronic state.[76–79]

The Condon radius for photoassociation coincides with the classical outer turning point, *i.e.*, roughly speaking with the outermost peak of the vibrational wavefunctions as shown in Fig. 5. Since the pair density of the atoms colliding in their electronic ground state decreases with decreasing interatomic distance, photoassociation is more efficient for small detuning. This is reflected by the larger values of the black compared to the red curve in Fig. 7 which shows the free-to-bound (quasi-bound-to-bound) transition matrix elements for the two vibrational wavefunctions depicted in Fig. 5 as a function of the trapping frequency of the optical lattice. The second observation to be drawn from Fig. 7 is the almost linear scaling of the transition matrix elements, and hence the photoassociation probability, with the trap frequency. That is, enhancing the trap frequency from 50 kHz, which has been employed for photoassociation of Sr_2,[38] to 500 kHz, which is within current experimental feasibility, will increase the number of photoassociated molecules by a half an order of magnitude. This confinement effect is easily understood in terms of the larger compression of the quasi-bound atom pairs in a tighter optical trap.

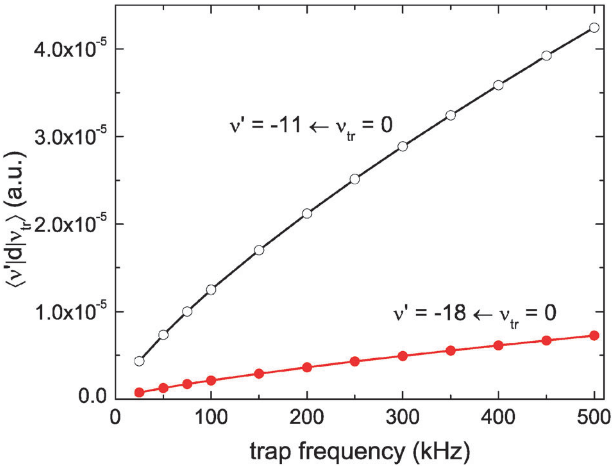

Fig. 7 Vibrationally averaged free-to-bound (or quasi-bound-to-bound) electric transition dipole moments between the lowest trap state of a pair of Sr and Yb atoms colliding in the $X^1\Sigma^+$ ground electronic state in a harmonic trap and two bound levels, *cf.* Fig. 5, of electronically excited SrYb dimers as a function of the trap frequency.

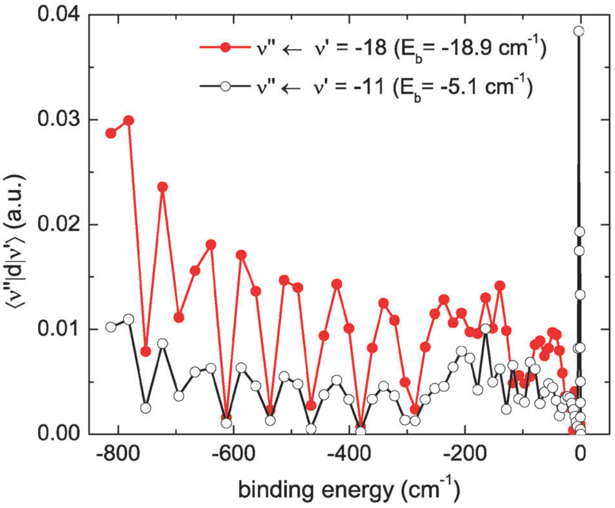

Fig. 8 Vibrationally averaged bound-to-bound electric transition dipole moments between the vibrational levels of the coupled electronically excited states that are shown in Fig. 5 and all vibrational levels of the $X^1\Sigma^+$ ground electronic state.

In view of the formation of deeply bound molecules in their electronic ground state, it might be advantageous to choose the larger detuning of $18.9\ \text{cm}^{-1}$ despite the photoassociation probability being smaller by about a factor of 5.9 compared to a detuning of $5.1\ \text{cm}^{-1}$ for all trap frequencies. This becomes evident by inspecting Fig. 8 which displays the bound-to-bound transition matrix elements between the two electronically excited vibrational wavefunctions with $E_b = 5.1\ \text{cm}^{-1}$ and $E_b = 18.9\ \text{cm}^{-1}$ and all bound levels of the $X^1\Sigma^+$ electronic ground state. These transition matrix elements govern the branching ratios for spontaneous decay of the photoassociated molecules. Note that for $v' = -11$ and $v' = -18$, the electronically excited molecules will decay into bound levels of the electronic ground state with a probability of about 24%. This decay to a large extent into bound levels is a hallmark of photoassociation near an intercombination line.[38] It is in contrast to photoassociation using a dipole-allowed transition where the probability for dissociative decay is often several orders of magnitude larger than that for stabilization into bound ground state levels.[74] While the excited state vibrational level with $E_b = 5.1\ \mathrm{cm}^{-1}$ has its largest transition dipole matrix elements with the last bound levels of the $X^1\Sigma^+$ ground electronic state that are only weakly bound, a striking difference is observed for the excited state vibrational wavefunction with $E_b = 18.9\ \mathrm{cm}^{-1}$. The strong singlet–triplet mixing of this level, in particular the pronounced peak near the outer classical turning point of the $A^1\Pi$ state, *cf.* Fig. 5, leads to significantly stronger transition dipole matrix elements with deeply bound levels of the $X^1\Sigma^+$ ground electronic state for $\nu' = -18$ compared to $\nu' = -11$, the one with $\nu'' = 1$ being the largest. Of course, the transition dipole matrix elements govern not only the spontaneous decay of the photoassociated molecules but also stabilization *via* stimulated emission. Due to the comparatively long lifetime of photoassociated molecules, estimated to be of the order of 15 μs, stabilization into a selected single vibrational level of the electronic ground state can be achieved by stimulated emission using a second continuous-wave laser. The lifetimes of the excited state vibrational levels vary between 5 μs and 20 μs, *cf.* Fig. 6.† The lower limit is roughly constant as a function of binding energy while the upper limit reflects the mixing between the $a^3\Pi$ and $b^3\Sigma^+$ states. It smoothly increases from 14 μs up to 20 μs for binding energies of about 4000 cm^{-1}. The specific value of the lifetime of each level reflects its $A^1\Pi$ state character, *cf.* Fig. 6.

Before outlining how a prospective experiment forming SrYb molecules in their vibronic ground state based on our results could proceed, it is natural to ask whether the accuracy of the calculations is sufficient for such a prediction. In particular, how sensitively do our results for the binding energies and structure of the vibrational levels as well as for the transition matrix elements depend on the accuracy of the electronic structure calculations? The binding energies depend mostly on the quality of the potential energy curves, where the error is estimated to be a few percent, and to some extent, for the spin–orbit coupled excited states, on the accuracy of the spin–orbit interaction matrix elements (error of a few percent). Nevertheless, the uncertainty of our potential energy curves is smaller than the range of reduced masses, as illustrated in Fig. 9. Therefore photoassociation with subsequent stabilization to a low-lying vibrational level should work for all isotope pairs since levels with strong perturbations due to the spin–orbit interaction are always present in the relevant range of binding energies, respectively, detunings, *cf.* Fig. 9.

In fact, the exact position and the character of the excited state vibrational level, strongly perturbed such as the one with $E_b = 18.9\ \mathrm{cm}^{-1}$ or more regular such as that with $E_b = 5.1\ \mathrm{cm}^{-1}$ in Fig. 5, can be determined experimentally.[77,80] A possible spectroscopic signature of the character of the vibrational wavefunctions is the dependence of the rotational constants, $\langle v'|\frac{1}{2\mu\hat{\mathbf{R}}^2}|v'\rangle$, on the binding energy of the corresponding levels. This is shown in Fig. 9 for different isotope combinations of strontium and ytterbium. The rotational constants of those

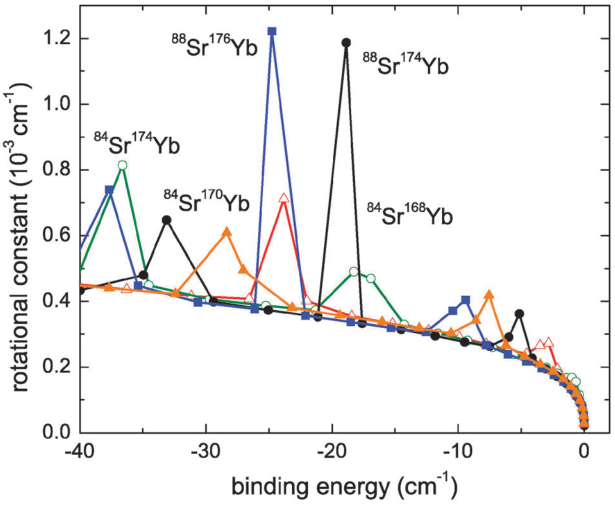

Fig. 9 Rotational constants of the vibrational levels of the coupled $a^3\Pi$, $b^3\Sigma^+$, $A^1\Pi$, and $C^1\Pi$ electronically excited states of the SrYb molecule for different isotope pairs. The isotope $^{88}\mathrm{Sr}^{174}\mathrm{Yb}$ was employed in the calculations shown in Fig. 5–8 and 10.

levels that are predominantly of triplet character lie on a smooth curve, while those that are mixed deviate from this curve. This behavior is easily rationalized as follows: without the coupling due to spin–orbit interaction, the rotational constants of the $a^3\Pi$, $b^3\Sigma^+$ and $A^1\Pi$ states would each lie on a smooth curve with a shape similar to the baseline of Fig. 9. The strongly mixed levels 'belong' to all three curves at the same time. Correspondingly, the value of their rotational constant lies somewhere in between the smooth curves of the regular levels. The lower peaks at small binding energies in Fig. 9 indicate mixing mostly between the $a^3\Pi$ and $b^3\Sigma^+$ states, while the higher peaks at larger binding energies reflect a strong singlet–triplet mixing. Spectroscopic determination of the rotational constants thus allows for identifying those excited state levels that show the strongest singlet–triplet mixing[77,80] and are best suited to the formation of ground state molecules. Spectroscopy is also needed to refine the value for the transition frequency of the stabilization laser. The binding energies of the deeply bound vibrational levels of the $X^1\Sigma^+$ ground electronic state come with an error of 5%, *i.e.*, ±50 cm^{-1}, resulting from the accuracy of the electronic structure calculations. This error defines the window for the spectroscopic search.

Note that our model, eqn (6), does not account for angular couplings, *i.e.*, the couplings of the $\Omega = 1$ states with $\Omega = 0^\pm$ and $\Omega = 2$. When including these non-adiabatic angular couplings, we found the components of the vibrational wavefunctions on the newly coupled surfaces to account for less than 0.001% of the population. The changes in the binding energy of the vibrational levels turned out to be less than $10^{-6}\ \mathrm{cm}^{-1}$, well within the error of the electronic structure calculations. This negligible effect of the angular (Coriolis-type) couplings for SrYb is not surprising due to its large reduced mass whose inverse enters all coupling matrix elements.

Combining all results shown above and assuming that the relevant spectroscopic data have been confirmed or adjusted experimentally, we suggest the following scheme for

---

† We assume no inhomogeneous broadening to be induced by the optical lattice which can be achieved by operating the lattice at the magic wavelength.

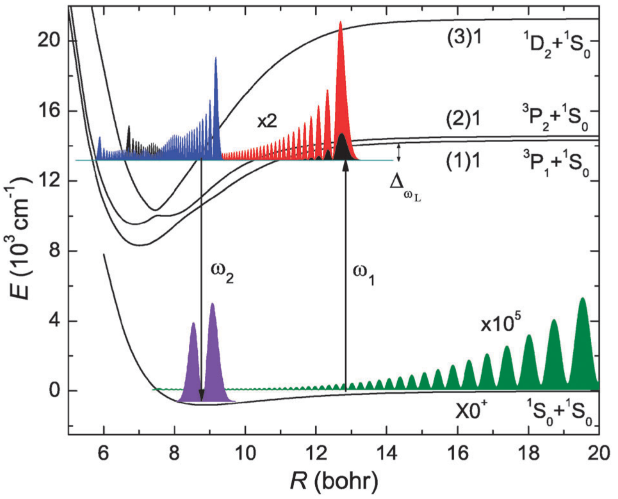

Fig. 10 Proposed scheme for the formation of ground state SrYb molecules *via* photoassociation near the intercombination line transition with detuning $\Delta_{\omega_L} = 18.9$ cm^{-1} ($\nu_{trap} = 100$ kHz).

photoassociation of SrYb dimers followed by stabilization *via* stimulated emission (see Fig. 10):

1. A large trapping frequency of the optical lattice is chosen to optimally compress the pair density of strontium and ytterbium atoms prior to photoassociation.

2. A photoassociation laser with frequency $\omega_1 \approx 690$ nm, red-detuned from the intercombination line transition and resonant with an electronically excited vibrational level, ν', of strongly mixed singlet–triplet character, is applied for a few μs. The duration of the photoassociation laser (about 5 μs roughly is an upper bound) is a compromise between saturating photoassociation and avoiding spontaneous emission losses (lifetime of about 15 μs) while the laser is on.

3. As the photoassociation laser is switched off, the stabilization laser is switched on. Due to the strong bound-to-bound transition matrix elements, saturation of the transition is expected already for shorter pulses (≤ 1 μs). The frequency of the stabilization laser, $\omega_2 \approx 655$ nm, is chosen to be resonant with the transition from the electronically excited level, ν', to the first excited vibrational level of the $X^1\Sigma^+$ electronic ground state, $\nu'' = 1$.

4. Before repeating steps 2 and 3, both photoassociation and stabilization lasers remain turned off for a hold period in which the $X^1\Sigma^+$ ($\nu'' = 1$) molecules decay to the vibronic ground state, $X^1\Sigma^+$ ($\nu'' = 0$). This ensures that the molecules created in the electronic ground state by the first sequence of the photoassociation and stabilization steps are not re-excited in a following sequence. The formed molecules can then be accumulated in $X^1\Sigma^+$ ($\nu'' = 0$).

Note that this scheme does not require phase coherence between the two pulses. Step 4 needs to involve a dissipative element in order to ensure the unidirectionality of the molecule formation scheme.[47] Dissipation can be provided by infrared spontaneous emission due to the permanent dipole moment of the heteronuclear dimers. However, this timescale is estimated to be of the order of 5 s, much too slow to be efficient for accumulation of ground state molecules. A second possibility is due to collisional decay. For the decay to occur within 1 ms, a density of 10^{13} cm^{-3} is required. Note that the density was 3×10^{12} cm^{-3} in the experiment photoassociating Sr_2 in an optical lattice with trapping frequency of 50 kHz.[38] Increasing the trap frequency will further increase the density such that hold times in the sub-ms regime are within the experimental reach.

One might wonder whether the comparatively long hold times can be avoided by using Stimulated Raman Adiabatic Passage (STIRAP)[81] for the photoassociation (pump) and stabilization (Stokes) pulses.[82,83] In order to overcome the problem of unidirectionality that occurs in repeating the photoassociation and stabilization steps many times, the whole ensemble of atom pairs in the trap needs to be addressed within a single STIRAP sweep[83] or within a single sequence of phase-locked STIRAP pulse pairs.[82] Note that the Stokes/stabilization pulse should be tuned to the $\nu' \rightarrow \nu'' = 0$ transition in this case. The feasibility of STIRAP-formation of ground state molecules depends on isolating the initial state sufficiently from the scattering continuum. A possibility to achieve this which was discussed theoretically consists in utilizing the presence of a Feshbach resonance.[83,84] If no resonance is present, *i.e.*, in an unstructured scattering continuum, STIRAP fails. In a series of ground-breaking experiments, STIRAP transfer to the ground state was therefore preceded by Feshbach-associating the molecules.[6,24–26] An alternative way to isolate the initial state for STIRAP from the scattering continuum that does not rely on Feshbach resonances (which are absent for the even isotope species of Sr and Yb) is given by strong confinement in a deep optical lattice. In a strong optical lattice the thermal spread can be made much smaller than the vibrational frequency of the trap. An estimate of the required trap frequency is given in terms of the binding energy of the Feshbach molecules that were STIRAP-transferred to the vibronic ground state. It was for example about 230 kHz for KRb molecules.[6,25] Hence a deep optical lattice with trapping frequency of the order of a hundred kHz (and corresponding temperatures $T \ll 5$ μK) should be sufficient to enable STIRAP-formation of ground state molecules. In order to be adiabatic with respect to the vibrational motion in the trap with periods of the order of about 1 μs, the duration of the photoassociation pulse needs to be rather long, at least of the order of 10 μs. The challenge might be to maintain phase coherence between the photoassociation pulse and the stabilization pulse over such timescales. For a train of phase-locked STIRAP-pulse pairs,[82] the requirement of durations of the order of 10 μs or larger applies to the length of the sequence of pulse pairs. The minimum Rabi frequencies to enforce adiabatic following are $\Omega = 159$ kHz for a 10 μs-pulse or $\Omega = 15.9$ kHz for a 100 μs-pulse. As a further prerequisite, all or at least most atom pairs should reside in the lowest trap state, $\nu_{trap} = 0$. Then steps 2–4 above might be replaced, provided the trapping frequency is sufficiently large, by

2′. a single STIRAP-sweep[81] forming ground state molecules with μs-pulses where the stabilization laser, tuned on resonance with the $\nu' \rightarrow \nu'' = 0$ transition ($\omega_2 \approx 654$ nm), precedes the photoassociation laser, tuned on resonance with the $\nu_{trap} = 0 \rightarrow \nu'$ transition ($\omega_2 \approx 690$ nm);

2″. or, a train of short, phase-locked STIRAP pulse pairs with correctly adjusted pulse amplitudes.[82]

To convert the Rabi frequencies to field amplitudes, note that the transition matrix elements are 5×10^{-6} for the pump pulse (assuming a trap frequency of 300 kHz) and 3×10^{-2} for the Stokes pulse. Phase coherence needs to be maintained throughout the single STIRAP-sweep or sequence of STIRAP pulse pairs.

4 Summary

Based on a first principles study, we predict the photoassociative formation of SrYb molecules in their electronic ground state using transitions near an intercombination line. The potential energy curves, non-adiabatic angular coupling and spin–orbit interaction matrix elements as well as electric dipole transition matrix elements of the SrYb molecule were calculated with state-of-the-art *ab initio* methods, using the coupled cluster and multireference configuration interaction frameworks. Assuming that the accuracy of the calculations for the SrYb molecule is about the same as for the isolated Sr and Yb atoms at the same level of the theory, we estimate the accuracy of the electronic structure data to 5%. However, the crucial point for the proposed photoassociation scheme is the existence and position of the intersection of the potential energy curves corresponding to $b^3\Sigma$ and $A^1\Pi$ states. By contrast to the binding energies of the vibrational levels, the position of this intersection does not depend very much on the overall quality of the computed potential energy curves. The correct structure of the crossings between the potential curves of the $a^3\Pi$, $b^3\Sigma$ and $A^1\Pi$ states is reproduced using even relatively crude computational methods of quantum chemistry which do not account for dynamic correlations such as the multiconfiguration self-consistent field (MCSCF) method employed here.

The spin–orbit coupled $a^3\Pi$, $b^3\Sigma^+$, $A^1\Pi$, and $C^1\Pi$ electronically excited states are essential for the photoassociation. A pair of colliding Sr and Yb atoms is excited into the triplet states ($\omega_1 \approx 690$ nm). Following stabilization by either spontaneous or stimulated emission, SrYb molecules in their electronic ground state are obtained. The required dipole coupling for photoassociation (stabilization) is provided by the $C^1\Pi$ ($A^1\Pi$) state.

If photoassociation is followed by spontaneous emission, about 24% of the photoassociated molecules will decay into bound levels of the ground electronic state, roughly independent of the detuning of the photoassociation laser. However, *which* ground state rovibrational levels are populated by spontaneous emission depends strongly on the detuning of the photoassociation laser. While most detunings will lead to decay into the last bound levels of the ground electronic states, certain detunings populate excited state levels with strong spin–orbit mixing. The strongly resonant structure of the wavefunctions allows for decay into low-lying vibrational levels. This might be the starting point for vibrational cooling[27,85] if molecules in their vibronic ground state are desired.

Alternatively, the long lifetime of the photoassociated molecules, of the order of 15 µs, allows for stabilization to the electronic ground state *via* stimulated emission, by a sequence of photoassociation and stabilization laser pulses of µs duration. Two schemes are conceivable: (i) a repeated cycle of photoassociation and stabilization pulses is applied with $X^1\Sigma^+(\nu'' = 1)$ as the target level. The duration of the pulses should be of the order of 1 µs. In order to accumulate molecules in $X^1\Sigma^+(\nu = 0)$, a hold period whose duration depends on the density of atoms is required for collisional decay from $\nu = 1$ to $\nu = 0$. For deep optical lattices with corresponding high densities, hold periods in the sub-ms regime can be reached. (ii) The vibronic ground state, $X^1\Sigma^+(\nu = 0)$, is targeted directly by a counter-intuitive sequence of photoassociation and stabilization pulses (STIRAP), either using two long pulses[81] or a train of phase-locked pulse pairs.[82] The timescale for the pulses is determined by the requirement to be adiabatic with respect to the motion in the optical lattice. The largest trapping frequencies feasible to date imply pulse durations at least of the order of 10 µs. Phase coherence between the pulses needs to be maintained over this timescale. Note that STIRAP fails if applied to an unstructured scattering continuum of colliding atoms. A possibility to circumvent this is given by preselecting the initial state for STIRAP with the help of a (Feshbach) resonance.[82–84] Our variant of the scheme is different since STIRAP is enabled by the presence of a deep trap.

Before either of the above discussed molecule formation schemes can be implemented experimentally, our theoretical data need to be corroborated by spectroscopy. In particular, our binding energies come with an error of a few percent, implying a corresponding uncertainty in the transition frequencies. Moreover, the exact position of strongly spin–orbit mixed excited state wavefunctions needs to be confirmed by measuring the excited state level spacings or rotational constants. However, despite the relatively large uncertainties in the energies of the rovibrational levels important for the proposed photoassociation scheme, our *ab initio* methods correctly locate the crossing of the singlet and triplet potential energy curves. This is the key ingredient for the efficient production of ground state SrYb molecules that we are predicting with our study.

Acknowledgements

We would like to thank Tatiana Korona and Wojciech Skomorowski for many useful discussions and help with the MOLPRO program. This work was supported by the Polish Ministry of Science and Education through the project N N204 215539, and by the Deutsche Forschungsgemeinschaft (Grant No. KO 2301/2). MT was supported by the project operated within the Foundation for Polish Science MPD Programme co-financed by the EU European Regional Development Fund.

References

1 H. R. Thorsheim, J. Weiner and P. S. Julienne, *Phys. Rev. Lett.*, 1987, **58**, 2420.
2 A. J. Kerman, J. M. Sage, S. Sainis, T. Bergeman and D. DeMille, *Phys. Rev. Lett.*, 2004, **92**, 033004.
3 D. Wang, J. Qi, M. F. Stone, O. Nikolayeva, H. Wang, B. Hattaway, S. D. Gensemer, P. L. Gould, E. E. Eyler and W. C. Stwalley, *Phys. Rev. Lett.*, 2004, **93**, 243005.

4 K. M. Jones, E. Tiesinga, P. D. Lett and P. S. Julienne, *Rev. Mod. Phys.*, 2006, **78**, 483.
5 T. Köhler, K. Góral and P. S. Julienne, *Rev. Mod. Phys.*, 2006, **78**, 1311.
6 K.-K. Ni, S. Ospelkaus, M. H. G. de Miranda, A. Pe'er, B. Neyenhuis, J. J. Zirbel, S. Kotochigova, P. S. Julienne, D. S. Jin and J. Ye, *Science*, 2008, **322**, 231.
7 J. Deiglmayr, A. Grochola, M. Repp, K. Mörtlbauer, C. Glück, J. Lange, O. Dulieu, R. Wester and M. Weidemüller, *Phys. Rev. Lett.*, 2008, **101**, 133004.
8 C. Haimberger, J. Kleinert, P. Zabawa, A. Wakim and N. P. Bigelow, *New J. Phys.*, 2009, **11**, 055042.
9 J. D. Weinstein, R. de Carvalho, T. Guillet, B. Friedrich and J. M. Doyle, *Nature*, 1998, **395**, 148.
10 H. L. Bethlem, G. Berden and G. Meijer, *Phys. Rev. Lett.*, 1999, **83**, 1558.
11 H. L. Bethlem and G. Meijer, *Int. Rev. Phys. Chem.*, 2003, **22**, 73.
12 M. Schnell and G. Meijer, *Angew. Chem., Int. Ed.*, 2009, **48**, 6010.
13 S. Y. T. van de Meerakker and G. Meijer, *Faraday Discuss.*, 2009, **142**, 113.
14 B. DeMarco and D. S. Jin, *Science*, 1999, **285**, 1703.
15 G. Modugno, G. Ferrari, G. Roati, R. J. Brecha, A. Simoni and M. Inguscio, *Science*, 2001, **294**, 1320.
16 C. Zipkes, S. Palzer, C. Sias and M. Köhl, *Nature*, 2010, **464**, 388.
17 C. Zipkes, S. Palzer, L. Ratschbacher, C. Sias and M. Köhl, *Phys. Rev. Lett.*, 2010, **105**, 133201.
18 S. Schmid, A. Härter, J.H. Denschlag and A. Frisch, private communication.
19 M. Krych, W. Skomorowski, F. Pawłowski, R. Moszynski and Z. Idziaszek, *Phys. Rev. A: At., Mol., Opt. Phys.*, 2011, **83**, 032723.
20 M. Lara, J. L. Bohn, D. E. Potter, P. Soldan and J. M. Hutson, *Phys. Rev. A: At., Mol., Opt. Phys.*, 2007, **75**, 012704.
21 P. S. Żuchowski and J. M. Hutson, *Phys. Rev. A: At., Mol., Opt. Phys.*, 2009, **79**, 062708.
22 S. K. Tokunaga, W. Skomorowski, P. S. Żuchowski, R. Moszynski, J. M. Hutson, E. A. Hinds and M. R. Tarbutt, *Eur. Phys. J. D*, 2011, DOI: 10.1140/epjd/e2011-10719-x.
23 J. M. Sage, S. Sainis, T. Bergeman and D. DeMille, *Phys. Rev. Lett.*, 2005, **94**, 203001.
24 F. Lang, K. Winkler, C. Strauss, R. Grimm and J. H. Denschlag, *Phys. Rev. Lett.*, 2008, **101**, 133005.
25 S. Ospelkaus, A. Pe'er, K.-K. Ni, J. J. Zirbel, B. Neyenhuis, S. Kotochigova, P. S. Julienne, J. Ye and D. S. Jin, *Nat. Phys.*, 2008, **4**, 622.
26 J. G. Danzl, E. Haller, M. Gustavsson, M. J. Mark, R. Hart, N. Bouloufa, O. Dulieu, H. Ritsch and H.-C. Nägerl, *Science*, 2008, **321**, 1062.
27 M. Viteau, A. Chotia, M. Allegrini, N. Bouloufa, O. Dulieu, D. Comparat and P. Pillet, *Science*, 2008, **321**, 232.
28 S. Kraft, F. Vogt, O. Appel, F. Riehle and U. Sterr, *Phys. Rev. Lett.*, 2009, **103**, 130401.
29 S. Stellmer, M. K. Tey, B. Huang, R. Grimm and F. Schreck, *Phys. Rev. Lett.*, 2009, **103**, 200401.
30 Y. N. M. de Escobar, P. G. Mickelson, M. Yan, B. J. DeSalvo, S. B. Nagel and T. C. Killian, *Phys. Rev. Lett.*, 2009, **103**, 200402.
31 S. Stellmer, M. K. Tey, R. Grimm and F. Schreck, *Phys. Rev. A: At., Mol., Opt. Phys.*, 2010, **82**, 041602.
32 P. G. Mickelson, Y. N. M. de Escobar, M. Yan, B. J. DeSalvo and T. C. Killian, *Phys. Rev. A: At., Mol., Opt. Phys.*, 2010, **81**, 051601.
33 T. Fukuhara, S. Sugawa and Y. Takahashi, *Phys. Rev. A: At., Mol., Opt. Phys.*, 2007, **76**, 051604.
34 Y. Takasu, K. Maki, K. Komori, T. Takano, K. Honda, M. Kumakura, T. Yabuzaki and Y. Takahashi, *Phys. Rev. Lett.*, 2003, **91**, 040404.
35 J. Brown and A. Carrington, *Rotational Spectroscopy of Diatomic Molecules*, Cambridge University Press, 2003.
36 R. Ciuryło, E. Tiesinga and P. S. Julienne, *Phys. Rev. A: At., Mol., Opt. Phys.*, 2005, **71**, 030701.
37 S. Tojo, M. Kitagawa, K. Enomoto, Y. Kato, Y. Takasu, M. Kumakura and Y. Takahashi, *Phys. Rev. Lett.*, 2006, **96**, 153201.
38 T. Zelevinsky, M. M. Boyd, A. D. Ludlow, T. Ido, J. Ye, R. Ciuryło, P. Naidon and P. S. Julienne, *Phys. Rev. Lett.*, 2006, **96**, 203201.
39 T. Zelevinsky, S. Kotochigova and J. Ye, *Phys. Rev. Lett.*, 2008, **100**, 043201.
40 D. DeMille, *Phys. Rev. Lett.*, 2002, **88**, 067901.
41 S. Ospelkaus, K.-K. Ni, D. Wang, M. H. G. de Miranda, B. Neyenhuis, G. Qumner, P. S. Julienne, J. L. Bohn, D. S. Jin and J. Ye, *Science*, 2010, **327**, 853.
42 T. Zelevinsky, private communication, 2011.
43 B. Bussery-Honvault, J.-M. Launay and R. Moszynski, *Phys. Rev. A: At., Mol., Opt. Phys.*, 2003, **68**, 032718.
44 B. Bussery-Honvault, J.-M. Launay and R. Moszynski, *Phys. Rev. A: At., Mol., Opt. Phys.*, 2005, **72**, 012702.
45 B. Bussery-Honvault, J.-M. Launay, T. Korona and R. Moszynski, *J. Chem. Phys.*, 2006, **125**, 114315.
46 B. Bussery-Honvault and R. Moszynski, *Mol. Phys.*, 2006, **104**, 2387.
47 C. P. Koch and R. Moszynski, *Phys. Rev. A: At., Mol., Opt. Phys.*, 2008, **78**, 043417.
48 H. Koch and P. Jorgensen, *J. Chem. Phys.*, 1990, **93**, 3333.
49 H. Sekino and R. J. Bartlett, *Int. J. Quantum Chem.*, 1984, **18**, 255.
50 R. J. Bartlett and M. Musiał, *Rev. Mod. Phys.*, 2007, **79**, 291.
51 T. Helgaker, H. J. A. Jensen, P. Jorgensen, J. Olsen, K. Ruud, H. Agren, A. A. Auer, K. L. Bak, V. Bakken and O. Christiansen and *et al.*, , *DALTON, an ab initio electronic structure program, Release 2.0*, 2005.
52 B. Jeziorski, R. Moszynski and K. Szalewicz, *Chem. Rev.*, 1994, **94**, 1887.
53 R. Moszynski, in *Molecular Materials with Specific Interactions—Modeling and Design*, ed. W. Sokalski, Springer, New York, 2007.
54 B. Jeziorski and R. Moszynski, *Int. J. Quantum Chem.*, 1993, **48**, 161.
55 R. Moszynski, P. S. Żuchowski and B. Jeziorski, *Collect. Czech. Chem. Commun.*, 2005, **70**, 1109.
56 T. Korona, M. Przybytek and B. Jeziorski, *Mol. Phys.*, 2006, **104**, 2303.
57 P. R. Bunker and P. Jensen, *Molecular Symmetry and Spectroscopy*, NRC Press, Ottawa, 1998.
58 H.-J. Werner, P. J. Knowles, R. Lindh, F. R. Manby, M. Schaltz, P. Celani, T. Korona, A. Mitrushenkov, G. Rauhut and T. B. Adler and *et al.*, , *Molpro, version 2006.1, a package of ab initio programs*, 2006.
59 H. A. Bethe and E. E. Salpeter, *Quantum Mechanics of One- and Two-Electron Atoms*, Academic Press, New York, 1957.
60 M. Kaupp, P. v. R. Schleyer, H. Stoll and H. Preuss, *J. Chem. Phys.*, 1991, **94**, 1360.
61 I. S. Lim, H. Stoll and P. Schwerdtfeger, *J. Chem. Phys.*, 2006, **124**, 034107.
62 X. Cao and M. Dolg, *J. Chem. Phys.*, 2001, **115**, 7348.
63 S. F. Boys and F. Bernardi, *Mol. Phys.*, 1970, **19**, 553.
64 http://physics.nist.gov/PhysRef Data.
65 S. B. Nagel, P. G. Mickelson, A. D. Saenz, Y. N. Martinez, Y. C. Chen, T. C. Killian, P. Pellegrini and R. Côté, *Phys. Rev. Lett.*, 2005, **94**, 083004.
66 W. B. Brown and D. M. Whisnant, *Mol. Phys.*, 1973, **25**, 1385.
67 A. J. Lacey and W. B. Brown, *Mol. Phys.*, 1974, **27**, 1013.
68 T. G. A. Heijmen, R. Moszynski, P. E. S. Wormer and A. van der Avoird, *Mol. Phys.*, 1996, **89**, 81.
69 K. T. Tang and J. P. Toennies, *J. Chem. Phys.*, 1984, **80**, 3726.
70 E. Czuchaj, M. Krosnicki and H. Stoll, *Chem. Phys. Lett.*, 2003, **371**, 401.
71 V. Kokoouline, O. Dulieu, R. Kosloff and F. Masnou-Seeuws, *J. Chem. Phys.*, 1999, **110**, 9865.
72 K. Willner, O. Dulieu and F. Masnou-Seeuws, *J. Chem. Phys.*, 2004, **120**, 548.
73 S. Kallush and R. Kosloff, *Chem. Phys. Lett.*, 2006, **433**, 221.
74 F. Masnou-Seeuws and P. Pillet, *Adv. At., Mol., Opt. Phys.*, 2001, **47**, 53.
75 C. Amiot, O. Dulieu and J. Vergès, *Phys. Rev. Lett.*, 1999, **83**, 2316.
76 C. M. Dion, C. Drag, O. Dulieu, B. Laburthe Tolra, F. Masnou-Seeuws and P. Pillet, *Phys. Rev. Lett.*, 2001, **86**, 2253.
77 H. K. Pechkis, D. Wang, Y. Huang, E. E. Eyler, P. L. Gould, W. C. Stwalley and C. P. Koch, *Phys. Rev. A: At., Mol., Opt. Phys.*, 2007, **76**, 022504.

78 S. Ghosal, R. J. Doyle, C. P. Koch and J. M. Hutson, *New J. Phys.*, 2009, **11**, 055011.

79 B. E. Londoño, J. E. Mahecha, E. Luc-Koenig and A. Crubellier, *Phys. Rev. A: At., Mol., Opt. Phys.*, 2009, **80**, 032511.

80 A. Fioretti, O. Dulieu and C. Gabbanini, *J. Phys. B: At., Mol. Opt. Phys.*, 2007, **40**, 3283.

81 K. Bergmann, H. Theuer and B. W. Shore, *Rev. Mod. Phys.*, 1998, **70**, 1003.

82 E. A. Shapiro, M. Shapiro, A. Pe'er and J. Ye, *Phys. Rev. A: At., Mol., Opt. Phys.*, 2007, **75**, 013405.

83 E. Kuznetsova, P. Pellegrini, R. Côté, M. D. Lukin and S. F. Yelin, *Phys. Rev. A: At., Mol., Opt. Phys.*, 2008, **78**, 021402.

84 E. Kuznetsova, M. Gacesa, P. Pellegrini, S. F. Yelin and R. Côté, *New J. Phys.*, 2009, **11**, 055028.

85 A. Bartana, R. Kosloff and D. J. Tannor, *Chem. Phys.*, 2001, **267**, 195.

Appendix B

Paper II

"Interatomic potentials, electric properties and spectroscopy
of the ground and excited states of the Rb_2 molecule:
ab initio calculations and effect of a non-resonant field"

Michał Tomza, Wojciech Skomorowski, Monika Musiał,
Rosario Gonzalez-Ferez, Christiane P. Koch, Robert Moszynski

Molecular Physics, **111**, 1781 (2013).

Molecular Physics, 2013
Vol. 111, Nos. 12–13, 1781–1797, http://dx.doi.org/10.1080/00268976.2013.793835

INVITED ARTICLE

Interatomic potentials, electric properties and spectroscopy of the ground and excited states of the Rb_2 molecule: *ab initio* calculations and effect of a non-resonant field*

Michał Tomza[a,b], Wojciech Skomorowski[a], Monika Musiał[c], Rosario González-Férez[d], Christiane P. Koch[b] and Robert Moszynski[a,**]

[a]*Faculty of Chemistry, University of Warsaw, Warsaw, Poland;* [b]*Theoretische Physik, Universität Kassel, Kassel, Germany;* [c]*Institute of Chemistry, University of Silesia, Katowice, Poland;* [d]*Instituto Carlos I de Física Teórica y Computacional and Departamento de Física Atómica, Molecular y Nuclear, Universidad de Granada, Granada, Spain*

(*Received 21 January 2013; final version received 20 March 2013*)

We formulate the theory for a diatomic molecule in a spatially degenerate electronic state interacting with a non-resonant laser field and investigate its rovibrational structure in the presence of the field. We report on *ab initio* calculations employing the double electron attachment intermediate Hamiltonian Fock space coupled cluster method restricted to single and double excitations for all electronic states of the Rb_2 molecule up to $5s+5d$ dissociation limit of about 26,000 cm^{-1}. In order to correctly predict the spectroscopic behaviour of Rb_2, we have also calculated the electric transition dipole moments, non-adiabatic coupling and spin-orbit coupling matrix elements, and static dipole polarisabilities, using the multireference configuration interaction method. When a molecule is exposed to strong non-resonant light, its rovibrational levels get hybridised. We study the spectroscopic signatures of this effect for transitions between the $\mathrm{X}^1\Sigma_g^+$ electronic ground state and the $\mathrm{A}^1\Sigma_u^+$ and $\mathrm{b}^3\Pi_u$ excited state manifold. The latter is characterised by strong perturbations due to the spin-orbit interaction. We find that for non-resonant field strengths of the order 10^9 W/cm^2, the spin-orbit interaction and coupling to the non-resonant field become comparable. The non-resonant field can then be used to control the singlet-triplet character of a rovibrational level.

Keywords: potential-energy curves; coupled-cluster theory; induced-dipole interaction; AC Stark effect; far-off-resonant laser field

1. Introduction

Rubidium was one of the first species to be Bose-condensed [1], and nowadays it can routinely be cooled and trapped. It has therefore become the drosophila of ultracold physics. Its long-range interatomic interactions have extensively been studied, and this has allowed to very accurately determine the scattering length and C_6 coefficient [2–4]. Rb_2 molecules have been formed out of ultracold rubidium atoms using both photo- and magneto-association [5,6]. Photoassociation and Feshbach spectroscopy have also served to measure the low-lying shape resonances of the rubidium dimer [7–9]. Trapping rubidium in an optical lattice has facilitated studies of atom-molecule dark states [10] and transferring the molecules into their vibrational ground state [11]. The Rb_2 molecule continues to draw attention in the context of the coherent control of ultracold collisions [12–16] and femtosecond photoassociation [17–20]. These experiments as well as those employing photoassociation with continuous wave lasers [21–25] require precise spectroscopic knowledge not only of the ground but also the excited states for both interpretation and detection.

The electronic ground and excited states have extensively been studied. According to Huber and Herzberg [26], the Rb_2 molecule was first observed in a spectroscopic experiment by Lawrence and Edlefsen as early as 1929 [27]. Cold molecule studies have led to a renewed interest in the Rb_2 molecule. The ground $\mathrm{X}^1\Sigma_g^+$ state has been investigated in Ref. [28], while the most accurate experimental results for the $\mathrm{a}^3\Sigma_u^+$ state have been reported by Lozeille *et al.* [29], Beser *et al.* [30] and Tiemann and collaborators [31]. The most important excited states corresponding to the $^2\mathrm{S}+^2\mathrm{P}$ dissociation limit, the $\mathrm{A}^1\Sigma_u^+$ and $\mathrm{b}^3\Pi_u$ states, have extensively been analysed in Ref. [21]. Less experimental information is available for other excited states. Notably, the $(1)^3\Sigma_g^+$ state has been studied in Ref. [32], and Ref. [33] reports the experimental observation of the $(2)^2\Pi_g$ state. The pure long-range state of 0_g^- symmetry, which is important for the photoassociation of ultracold Rb atoms, has been analysed in Ref. [34]. Several of these experimental data were successfully employed to derive empirical potentials that reproduce the spectroscopic data with the experimental accuracy (cf. Refs. [28,31] for the ground state $\mathrm{X}^1\Sigma_g^+$ and

---

*This paper is dedicated to Professor Bretislav Friedrich on the occasion of his 60th birthday.
**Corresponding author. Email: robert.moszynski@tiger.chem.uw.edu.pl

Refs. [30,31] for the $a^3\Sigma_u^+$ potential). The coupled manifold of the $A^1\Sigma_u^+$ and $b^3\Pi_u$ states was deperturbed by Bergeman and collaborators [21,35] with the corresponding potential energy curves and spin-orbit coupling matrix elements reported in Ref. [35]. Potential energy curves for other electronic states fitted to the experimental data are older (cf. Ref. [36] for the empirical potential energy curve of the $(1)^1\Pi_g$ state, and Refs. [37] and [38] for those of the $(2)^1\Sigma_g^+$ state and $(2)^1\Pi_u$ states, respectively).

Given this extensive amount of experimental data, it is not surprising that many theoretical calculations have tackled the ground and excited states of the rubidium dimer. The first *ab initio* calculation on the Rb_2 molecule dates back to 1980 and was reported by Konowalow and Rosenkrantz [39]. Three recent studies have reported *ab initio* data of varying accuracy for the potential energy curves and in some cases further properties such as couplings and transition moments of Rb_2. The non-relativistic potentials for all molecular states by Park *et al.* [40] show a root mean square deviation (RMSD) between the theoretical well depths and the available experimental data of $235\,\mathrm{cm}^{-1}$, i.e. 9.9% on the average. The 2003 calculations by Edvardsson *et al.* [41] were devoted to the ground state potential and six excited state potentials of ungerade symmetry. The spin-orbit coupling matrix elements were also reported. The overall accuracy of these results was about the same as in Ref. [40] with a RMSD of $180\,\mathrm{cm}^{-1}$ representing an average error of 25%. Note that since the number of states considered in Refs. [40] and [41] differs, the absolute RMSD may be smaller and the percentage error larger. Finally, in 2012, Allouche and Aubert-Frécon [42] reported calculations of all molecular states and spin-orbit coupling matrix elements corresponding to the dissociation limits $5s+5s$, $5s+5p$ and $5s+4d$. These calculations are much more accurate than any other previously reported in the literature with a RMSD of $129\ \mathrm{cm}^{-1}$, i.e. an error of 5.5% only. However, they do not cover highly excited molecular states that are of interest for conventional spectroscopy experiments [43], for the detection of ultracold molecules [44] as well as photoassociation into states with ion-pair character [45–47].

Photoassociation into highly excited electronic states is at the core of a recent proposal for the production of ultracold Rb_2 molecules [47], aimed at improving earlier femtosecond experiments [17–20]. It is based on multi-photon transitions that can easily be driven by femtosecond laser pulses and allow to fully take advantage of the broad bandwidth of femtosecond laser pulses while driving the narrow photoassociation transition [48]. Moreover, multi-photon photoassociation populates highly excited electronic states with ion-pair character and strong spin-orbit interaction. These features are advantageous for an efficient stabilisation of the photoassociated molecules into deeply bound molecules in the electronic ground state [47]. The theoretical modelling of the proposed photoassociation scheme required the knowledge of precise *ab initio* potential energy curves including those for highly excited states, spin-orbit and non-adiabatic coupling matrix elements, electric transition dipole moments and dynamical Stark shifts. These data were not available in the literature for the highly excited states, and the non-adiabatic couplings and dynamical Stark shifts have been missing even for the lowest states. Moreover, the newly developed tools of electronic structure theory based on the Fock space coupled cluster method [49–51] could possibly allow for reaching a better accuracy of the potentials than reported in Refs. [40–42]. Last but not least, calculations of the electric properties for diatomic molecules in spatially degenerate electronic states are scarce. To the best of our knowledge, only two studies considered this problem, in the context of the dispersion interactions between molecules [52,53] rather than non-resonant interactions with an external field, and a systematic theoretical approach has not yet been proposed. Moreover, the presence of spin-orbit coupling between the electronic states has been neglected in a recent treatment of nuclear dynamics in a non-resonant field [54,55]. Such an approximation does not allow to study the competition between the spin-orbit coupling and the interaction with a non-resonant field, which may both significantly perturb the spectrum.

Here, we fill this gap and report the theoretical framework for a Π state molecule interacting with a non-resonant field and study its rovibrational dynamics in the presence of the field. We also report *ab initio* calculations of all potential energy curves, spin-orbit and non-adiabatic coupling matrix elements corresponding to the dissociation limits up to and including $5s+5d$. We test our *ab initio* results by comparing the main spectroscopic characteristics of the potentials to the available experimental data. We devote special emphasis to the important manifold of the $A^1\Sigma_u^+$ and $b^3\Pi_u$ states, comparing our results to Refs. [21,35]. Since the electric properties of spatially degenerate electronic states were not extensively studied in the literature thus far, we report here, to the best of our knowledge, the first *ab initio* calculation of the irreducible components of the polarisability tensor, including their dependence on the interatomic distance R, for the $A^1\Sigma_u^+$ and $b^3\Pi_u$ states. Finally, we study the effect of a non-resonant field on the spectroscopy in the $A^1\Sigma_u^+$ and $b^3\Pi_u$ manifold. This is motivated by our recent proposal for enhancing photoassociation by controlling shape resonances with non-resonant light [54,55]. In order to significantly modify the scattering continuum of the atom pairs to be photoassociated, rather large non-resonant intensities are required. Since the bound rovibrational levels are much more affected by a strong non-resonant field than continuum states, it is important to investigate how the corresponding spectroscopic features change.

Our paper is organised as follows. In Section 2, we formulate the theory of the interaction of a homonuclear molecule with an external non-resonant field. In Section 3, we provide the theoretical description of the perturbation of spectra by a non-resonant field, using as an example the spin-orbit coupled manifold of the $\mathrm{A}^1\Sigma_u^+$ and $\mathrm{b}^3\Pi_u$ electronic states of Rb_2. We briefly summarise the *ab initio* methods employed in our calculations in Section 4 and discuss the results of these calculations in Section 5. In particular, we compare our data with results available in the literature and discuss the ability of the *ab initio* results to reproduce the high-resolution spectroscopic data for the $\mathrm{A}^1\Sigma_u^+$ and $\mathrm{b}^3\Pi_u$ manifold [21,35]. We then describe the interaction with a non-resonant field and study its spectroscopy signatures on the transitions between the electronic ground state and the $\mathrm{A}^1\Sigma_u^+$ and $\mathrm{b}^3\Pi_u$ manifold. Finally, Section 6 concludes our paper.

2. Diatomic molecule in a non-resonant electric field

We consider the interaction of a diatomic molecule with an electric field with the direction taken along the Z axis of the space-fixed coordinate system, $\vec{\mathcal{E}} = (0, 0, \mathcal{E})$. To the second order, the Hamiltonian for the interaction of the molecule with the electric field in the space-fixed frame can be written as,

$$H_{\mathrm{int}} = -d_Z^{\mathrm{SF}}\mathcal{E} - \frac{1}{2}\alpha_{ZZ}^{\mathrm{SF}}\mathcal{E}^2 , \tag{1}$$

where d_Z^{SF} and $\alpha_{ZZ}^{\mathrm{SF}}$ denote, respectively, the appropriate components of the electric dipole moment and electric dipole polarisability in the space-fixed frame. Since we deal with a homonuclear molecule, only the second term of the above Hamiltonian will be relevant in the present analysis. To evaluate the matrix elements of the Hamiltonian in the electronic and rovibrational basis, we rewrite $\alpha_{ZZ}^{\mathrm{SF}}$ in terms of the polarisability components in the body-fixed frame. The $\alpha_{ZZ}^{\mathrm{SF}}$ dipole polarisability component can be expressed in terms of space-fixed irreducible tensor components $\alpha_m^{(l),\mathrm{SF}}$ [56],

$$\alpha_{ZZ}^{\mathrm{SF}} = -\frac{1}{\sqrt{3}}\alpha_0^{(0),\mathrm{SF}} + \sqrt{\frac{2}{3}}\alpha_0^{(2),\mathrm{SF}} . \tag{2}$$

For the irreducible tensor components, the transformation from the space-fixed to the body-fixed coordinate system is given by the rotation matrices $D_{m,k}^{(l)\star}(\widehat{R})$,

$$\alpha_m^{(l),\mathrm{SF}} = \sum_{k=-l}^{l} D_{m,k}^{(l)\star}(\widehat{R})\ \alpha_k^{(l),\mathrm{BF}} . \tag{3}$$

Hence, we have

$$\begin{aligned} \alpha_0^{(0),\mathrm{SF}} &= D_{0,0}^{(0)\star}(\widehat{R})\ \alpha_0^{(0),\mathrm{BF}} = \alpha_0^{(0),\mathrm{BF}} , \\ \alpha_0^{(2),\mathrm{SF}} &= \sum_{k=-2}^{2} D_{0,k}^{(2)\star}(\widehat{R})\ \alpha_k^{(2),\mathrm{BF}} . \end{aligned} \tag{4}$$

For simplicity, we omit the superscripts SF/BF in the rest of the paper as from now we will use only the body-fixed quantities. We assume in this paper that the molecular axis defines the body-fixed z axis. For a diatomic molecule, the set of the Euler angles $\widehat{R}$ can be chosen as $\widehat{R} = (0, \theta, 0)$, where θ is the angle between the molecular axis and the space-fixed Z axis. This particular choice of the Euler angles is consistent with the requirement that the space-fixed Y and body-fixed y axes coincide. The other possible set would be $\widehat{R} = (3\pi/2, \theta, \pi/2)$ that correspond to the coincidence of the space-fixed X and body-fixed x axes. Note that for our specific choice of the Euler angles, the Wigner D functions appearing in Equation (4) reduce to:

$$D_{0,k}^{(l)\star}(\phi, \theta, 0) = \left[\frac{(l-k)!}{(l+k)!}\right]^{1/2} P_l^k(\cos\theta), \tag{5}$$

where P_l^k are the associated Legendre polynomials. For any diatomic molecule, the non-zero irreducible components of the dipole polarisability are $\alpha_0^{(0)}$ and $\alpha_0^{(2)}$. In addition, for a diatomic molecule in a Π electronic state, the $\alpha_{-2}^{(2)}$ and $\alpha_2^{(2)}$ terms do not vanish. They should be viewed as off-diagonal polarisability tensor components connecting two degenerate electronic states, $|\Pi_1\rangle$ and $|\Pi_{-1}\rangle$, with opposite projection of the total electronic orbital angular momentum on the molecular axis (see, for instance, Equation (16) of Ref. [53]).

The non-vanishing body-fixed polarisability components are most conveniently expressed in terms of the Cartesian tensor elements α_{ii}, $i = x, y, z$. Then $\alpha_0^{(0)}$ is related to the trace of the polarisability,

$$\alpha_0^{(0)} = -\frac{1}{\sqrt{3}}\left(\alpha_{xx} + \alpha_{yy} + \alpha_{zz}\right) , \tag{6}$$

$\alpha_0^{(2)}$ to the anisotropy of the polarisability,

$$\alpha_0^{(2)} = \frac{1}{\sqrt{6}}\left(2\alpha_{zz} - \alpha_{xx} - \alpha_{yy}\right) , \tag{7}$$

and, for a molecule in a Π electronic state, $\alpha_{-2}^{(2)}$ and $\alpha_2^{(2)}$ reflect the difference between two perpendicular components,

$$\alpha_2^{(2)} = \alpha_{-2}^{(2)} = \alpha_{yy} - \alpha_{xx} . \tag{8}$$

For a diatomic molecule in a Σ state, the definitions of the Cartesian components of the polarisability tensor α_{ii} in Equations (6)–(8) are unambiguous. The zz and xx components are simply the parallel and perpendicular components, $\alpha_\parallel$ and $\alpha_\perp$, respectively. Thus, the irreducible tensor components appearing in Equations (6)–(8) are simply related to the trace α and the anisotropy $\Delta\alpha$ of the polarisability tensor,

$$\alpha_0^{(0)} = -\sqrt{3}\alpha, \qquad \alpha_0^{(2)} = \frac{2}{\sqrt{6}}\Delta\alpha\,. \tag{9}$$

Obviously, for a Σ state molecule, the xx and yy components are equal, and $\alpha_2^{(2)} = 0$.

In the case of a molecule in a degenerate electronic state (Π, Δ, etc.), some caution is needed when employing the Cartesian components α_{ii}, since one has to specify the basis of the electronic states, in which these quantities are expressed. Equation (8) assumes the Cartesian components, α_{yy} and α_{xx}, to be calculated for the $|\Pi_x\rangle$ state. However, the Cartesian basis $\{|\Pi_x\rangle, |\Pi_y\rangle\}$ for the Π electronic state is not convenient for the dynamical calculations, since the spin-orbit coupling matrix elements are complex in this basis. Therefore, we prefer to use the spherical basis $\{|\Pi_{-1}\rangle, |\Pi_1\rangle\}$ for the Π state over the Cartesian basis $\{|\Pi_x\rangle, |\Pi_y\rangle\}$ since it avoids complex quantities in the calculations and allows for a simple adaptation of the Hund's case (*a*) wave function to a given symmetry of the rovibrational level. Therefore, we will use the irreducible polarisability components $\alpha_m^{(l)}$ rather than the Cartesian α_{ii}.

Combining Equations (1)–(8) and making use of properties of the rotation matrices $D_{m,k}^{(l)^\star}(\widehat{R})$, one arrives at the following Hamiltonian for the interaction of the homonuclear diatomic molecule with the static electric field,

$$H_{\text{int}} = -\frac{\mathcal{E}^2}{2}\left[-\frac{1}{\sqrt{3}}\alpha_0^{(0)} + \sqrt{\frac{2}{3}}\alpha_0^{(2)}P_2^0(\cos\theta) + \frac{1}{6}\alpha_2^{(2)}P_2^2(\cos\theta) + 4\alpha_{-2}^{(2)}P_2^{-2}(\cos\theta)\right]. \tag{10}$$

The above Hamiltonian is valid for any isolated electronic state of a diatomic homonuclear molecule. Albeit, the last two terms in this equation are relevant only for molecules in a Π electronic state. Let us stress here that although this form of the Hamiltonian seems a bit elaborate at first glance, it simplifies the evaluation of the matrix elements in the symmetry-adapted basis set, and it also avoids any ambiguities when employing the Cartesian polarisability components for degenerate electronic states. Equation (10) also assumes the frequency of the non-resonant field to be far from any resonance that allows for using the static polarisability and the two-photon rotating-wave approximation. Such a field can be produced, for example, by a carbon dioxide laser with a wavelength of about 10 μm.

3. Hamiltonian for the Rb$_2$ molecule in the manifold of the coupled A$^1\Sigma_u^+$ and b$^3\Pi_u$ excited states interacting with a non-resonant field

We construct the Hamiltonian for the nuclear motion in Hund's case (*a*) coupling scheme with the primitive basis functions $|n,\ \Lambda\rangle|S,\ \Sigma\rangle|J,\ \Omega,\ M\rangle$ that are products of the electronic $|n,\ \Lambda\rangle$, electron spin $|S,\ \Sigma\rangle$ and rotational $|J,\ \Omega,\ M\rangle$ functions. Here, J is the total angular momentum quantum number, S is the total electronic spin quantum number, Λ and Σ are the projections of the total electronic orbital and total electronic spin angular momenta onto the molecular axis, and M is the projection of the total angular momentum onto the Z space-fixed axis. n labels the non-relativistic dissociation limit of the molecular state. We also define the projection of the total, electronic orbital plus spin, angular momentum onto the molecular axis, $\Omega = \Lambda + \Sigma$. For the coupled A$^1\Sigma_u^+$ and b$^3\Pi_u$ manifold, we consider the rovibrational levels of the *e* spectroscopic symmetry and odd parity. For simplicity, any hyperfine structure effects are neglected here. The properly symmetry-adapted Hund's case (*a*) wavefunctions read,

$$\begin{aligned}
|\mathrm{A}^1\Sigma_{0_u^+}, J, M, e\rangle &= |\mathrm{A}, 0\rangle|0, 0\rangle|J, 0, M\rangle\ ,\\
|\mathrm{b}^3\Pi_{0_u^+}, J, M, e\rangle &= \frac{1}{\sqrt{2}}\big[|\mathrm{b}, 1\rangle|1, -1\rangle|J, 0, M\rangle\\
&\quad - |\mathrm{b}, -1\rangle|1, 1\rangle|J, 0, M\rangle\big]\ ,\\
|\mathrm{b}^3\Pi_{2_u}, J, M, e\rangle &= \frac{1}{\sqrt{2}}\big[|\mathrm{b}, 1\rangle|1, 1\rangle|J, 2, M\rangle\\
&\quad - |\mathrm{b}, -1\rangle|1, -1\rangle|J, -2, M\rangle\big]\ .
\end{aligned} \tag{11}$$

The first two states have a projection of the total angular momentum onto the molecular axis $|\Omega| = 0$, while the third one has $|\Omega| = 2$. In the field-free case, the state with $|\Omega| = 2$ is decoupled from the states with $|\Omega| = 0$, and it is not accessible from the ground electronic state in the one-photon dipolar transitions considered here. Consequently, the field-free model Hamiltonian H_0 describing the nuclear motion in the manifold of the coupled A$^1\Sigma_u^+$ and b$^3\Pi_u$ states can be represented by following 2 × 2 matrix,

$$H_0 = \begin{pmatrix} T_R + \frac{\vec{j}^2}{2\mu R^2} + V^{\mathrm{A}^1\Sigma_u^+}(R) & \xi_1(R) \\ \xi_1(R) & T_R + \frac{\vec{j}^2}{2\mu R^2} + V^{\mathrm{b}^3\Pi_u}(R) - \xi_2(R) \end{pmatrix}, \tag{12}$$

where $T = T_R + \frac{\vec{j}^2}{2\mu R^2}$ is the sum of the vibrational and rotational kinetic energy operators with $\vec{j} = \vec{J} - \vec{L} - \vec{S}$ being the mechanical angular momentum of the molecule and $V^k(R)$, $k = \mathrm{A}^1\Sigma_u^+$, $\mathrm{b}^3\Pi_u$, denotes the respective potential energy curves in the Born-Oppenheimer approximation. $\xi_1(R) = \langle \mathrm{A}^1\Sigma_u^+|H_{\mathrm{SO}}|\mathrm{b}^3\Pi_u\rangle_{|\Omega|=0}$ and $\xi_2(R) = \langle \mathrm{b}^3\Pi_u|H_{\mathrm{SO}}|\mathrm{b}^3\Pi_u\rangle_{|\Omega|=0}$ are the spin-orbit coupling matrix elements, and only the electronic states with $|\Omega| = 0$ are included. Our model does not account for Coriolis-type angular couplings, i.e. the couplings of the $\Omega = 0$ states with $\Omega = 1$ states because their effect on the rovibrational dynamics is negligible compared to the spin-orbit couplings, the error of the electronic structure data and the influence of the weak non-resonant field. It is not surprising due to large reduced mass of Rb_2 molecules whose inverse enters all coupling matrix elements.

When the electric field is switched on, the $\Lambda = 1$ and $\Lambda = -1$ components of the $\mathrm{b}^3\Pi_u$ state are coupled. The coupling results form the off-diagonal polarisability tensor components in the Hamiltonian of Equation (10). Therefore, not only the interaction H_{int} from Equation (10) has to be added to the Hamiltonian H_0 for the $\mathrm{A}^1\Sigma_u^+$ and $\mathrm{b}^3\Pi_u$ states with $|\Omega| = 0$, but also the matrix (12) has to be extended so as to include the $|\Omega| = 2$ component originating from the $\mathrm{b}^3\Pi_u$ state since it has the Λ projections exactly opposite to those found in the state with $|\Omega| = 0$ while all other quantum numbers are the same. Hence, in the presence of the electric field the rovibrational levels of the A $^1\Sigma_u^+$ and $\mathrm{b}^3\Pi_u$ manifold are obtained by diagonalising the Hamiltonian represented by the following 3 × 3 matrix,

$$H = \begin{pmatrix} T + W^{\mathrm{A}^1\Sigma_u^+}(R,\theta) & \xi_1(R) & 0 \\ \xi_1(R) & T + W^{\mathrm{b}^3\Pi_u}(R,\theta) - \xi_2(R) & W_{0/2}(R,\theta) \\ 0 & W_{0/2}(R,\theta) & T + W^{\mathrm{b}^3\Pi_u}(R,\theta) + \xi_2(R) \end{pmatrix}. \qquad (13)$$

The diagonal elements of the interaction potentials incorporating the interaction with non-resonant field are given by,

$$W^k(R,\theta) = V^k(R) + H^k_{\mathrm{int}}\,, \qquad (14)$$

where $k = \mathrm{A}^1\Sigma_u^+$ or $\mathrm{b}^3\Pi_u$ and H^k_{int} is given by Equation (10) for the electronic state labelled by k. The off-diagonal term due to the non-resonant field, $W_{0/2}(R, \theta)$, couples the $|\Omega| = 0_u^+$ and $|\Omega| = 2_u$ components resulting from the $\mathrm{b}^3\Pi_u$ state. It is proportional to the off-diagonal polarisability of the molecule in the $\mathrm{b}^3\Pi$ state,

$$W_{0/2}(R,\theta) = -\frac{1}{12}\mathcal{E}^2\alpha_2^{(2),\mathrm{b}^3\Pi_u}(R)P_2^2(\cos\theta)\,, \qquad (15)$$

with $\alpha_2^{(2)}$ defined by Equation (8). Analogously to Equations (13) and (14), the Hamiltonian for the molecule in its electronic ground state interacting with a non-resonant field is simply given by $T + W^{\mathrm{X}^1\Sigma_g^+}(R,\theta)$.

4. *Ab initio* electronic structure and dynamical calculations

We adopt the computational scheme successfully applied to the ground and excited states of the calcium dimer [57–61], magnesium dimer [62,63], strontium dimer [64,65], $(\mathrm{BaRb})^+$ molecular ion [66] and SrYb heteronuclear molecule [67]. The potential energy curves for the singlet and triplet gerade and ungerade states of the Rb_2 molecule corresponding to the first seven lowest dissociation limits, $5s+5s$, $5s+5p$, $5s+4d$, $5s+6s$, $5s+6p$, $5p+5p$ and $5s+5d$, have been obtained by a supermolecule method,

$$V^{2S+1|\Lambda|_{g/u}}(R) = E^{\mathrm{SM}}_{\mathrm{AB}} - E^{\mathrm{SM}}_{\mathrm{A}} - E^{\mathrm{SM}}_{\mathrm{B}}\,, \qquad (16)$$

where $E^{\mathrm{SM}}_{\mathrm{AB}}$ denotes the energy of the dimer computed using the supermolecule method (SM), and $E^{\mathrm{SM}}_{\mathrm{X}}$, $X = A$ or B, is the energy of the atom X in the electronic state corresponding to the dissociation limit of the state $^{2S+1}|\Lambda|_{g/u}$. The full basis of the dimer was employed in the supermolecule calculations on the atoms A and B, and the molecule AB, and the Boys and Bernardi scheme was utilised to correct for the basis-set superposition error [68]. The calculations for the excited states employed the recently introduced double electron attachment intermediate Hamiltonian Fock space coupled cluster method restricted to single and double excitations (DEA-IH-FS-CCSD) [49,51]. Starting with the closed-shell reference state for the doubly ionised molecule Rb_2^{2+} that shows the correct dissociation at large interatomic separations, R, into closed-shell subsystems, $\mathrm{Rb}^+ + \mathrm{Rb}^+$, and using the double electron attachment operators in the Fock space coupled cluster ansatz makes our method size-consistent at any interatomic separation R and guarantee the correct large-R asymptotics. Thus, the DEA-IH-FS-CCSD approach overcomes the problem of the standard coupled cluster method restricted to single and double excitations (CCSD) and the equation of motion CCSD method [50] with the proper dissociation into open-shell atoms. The potential energy curves obtained from the *ab initio* calculations were smoothly connected at intermediate interatomic separations with the asymptotic multipole expansion [56]. The C_6 coefficient of the electronic ground state and the C_3 coefficient of the first excited state were fixed at their empirical values derived from high-resolution spectroscopic experiments [4,34], while the remaining coefficients were taken from Ref. [69].

The transitions from the ground $\mathrm{X}^1\Sigma_g^+$ state to the $^1\Sigma_u^+$ and $^1\Pi_u$ states and from the $\mathrm{a}^3\Sigma_u^+$ to the $^3\Sigma_g^+$ and $^3\Pi_g$ states are electric dipole allowed. The transition dipole moments for the electric transitions were computed from the following expression [70],

$$\begin{aligned} d_i(n \leftarrow \mathrm{X}) &= \langle \mathrm{X}^1\Sigma_g^+|\hat{d}_i|(n)^1|\Lambda|_u\rangle \\ d_i(n \leftarrow \mathrm{a}) &= \langle \mathrm{a}^3\Sigma_u^+|\hat{d}_i|(n)^3|\Lambda|_g\rangle, \end{aligned} \qquad (17)$$

where the $\hat{d}_i$, $i = x, y$ or z, denotes the ith component of the electric dipole moment operator. Note that in the first term of Equation (17) $i = x$ or y corresponds to transitions to $^1\Pi_u$ states, while $i = z$ corresponds to transitions to $^1\Sigma_u^+$ states. The transitions from the $a^3\Sigma_u^+$ state connect this state with the $^3\Pi_g$ and $^3\Sigma_g^+$ states, through the x or y and z operators, respectively.

We expect the rovibrational energy levels of the excited electronic states of Rb_2 to show perturbations due to the non-adiabatic couplings between the states. Analysing the pattern of the potential energy curves, we have found that many potential energy curves display avoided crossings, suggesting strong radial couplings between these electronic states. We have therefore computed the most important radial coupling matrix elements, defined by the expression,

$$R(n \leftrightarrow n') = \left\langle (n)^{2S+1}|\Lambda|_{g/u} \left| \frac{\partial}{\partial R} \right| (n')^{2S+1}|\Lambda|_{g/u} \right\rangle , \tag{18}$$

where $n \leftrightarrow n'$ signifies that the electronic states n and n' are coupled. Note that the radial derivative operator couples states with the same projection of the electronic orbital angular momentum on the molecular axis Λ.

Electric transition dipole moments, radial non-adiabatic coupling and spin-orbit coupling matrix elements were obtained using the Multireference Configuration Interaction (MRCI) method restricted to single and double excitations with a large active space. Scalar relativistic effects were included by using the small-core fully relativistic energy-consistent pseudopotential ECP28MDF [71] from the Stuttgart library. Thus, in the present study, the Rb_2 molecule was treated as a system of effectively 18 electrons. The [14*s*14*p*7*d*6*f*] basis set was employed in all calculations. This basis was obtained by decontracting and augmenting the basis set of Ref. [71] by a set of additional functions improving the accuracy of the atomic excitation energies of the rubidium atom with respect to the NIST database [72]. The DEA-IH-FS-CCSD calculations were done with the code based on the ACES II program system [73], while the MRCI calculations were performed with the MOLPRO code [74]. All *ab initio* results reported in the present paper are available from the Authors on request.

The rovibrational levels of the $A^1\Sigma_u^+$ and $b^3\Pi_u$ excited state manifold are computed by diagonalising the Hamiltonian (12) represented on a mapped Fourier grid, employing about $N_R = 512$ radial grid points. For the calculations in the field we complement our Fourier grid representation for the radial part by a basis set expansion in terms of Legendre polynomials for the angular part, taking advantage of the magnetic quantum number m being conserved. We find that $j_{max} = 19$ is sufficient to obtain converged results for $\mathcal{I} \leq 2 \times 10^9$ W/cm^2. Presence of an intense non-resonant field leads to strong hybridisation of the rovibrational levels, and an adiabatic separation of rotational and vibrational motion is not applicable [54,55]. We account for this fact by diagonalising the full two-dimensional Hamiltonian, Equation (13), represented by a $3N_R(j_{max} + 1) \times 3N_R(j_{max} + 1)$ matrix. For $\mathcal{I} \neq 0$, the non-resonant field mixes different partial waves, and j and j' are not good quantum numbers anymore. For the sake of simplicity, we label the field-dressed rovibrational levels by the field-free quantum numbers. Note that the field-dressed levels are adiabatically connected to their field-free counterparts even for very large intensities.

5. Numerical results and discussion

5.1. Potential energy curves

To test the ability of the *ab initio* approach adopted in the present work to reproduce the experimental data, we first check the accuracy of the atomic results. In Table 1, we report the excitation energies at the dissociation limit computed with the DEA-IH-FS-CCSD method and compare the results to non-relativistic excitation energies

Table 1. Asymptotic energies (in cm^{-1}) and molecular states arising from different states of rubidium atoms [26].

Asymptote	Energy (Present)	Energy (Exp.)	Molecular states
$(1)^2S(5s)$+$(1)^2S(5s)$	0	0	$^1\Sigma_g^+$, $^3\Sigma_u^+$
$(1)^2S(5s)$+$(1)^2P(5p)$	12731	12737	$^1\Sigma_g^+$, $^1\Pi_g$, $^1\Sigma_u^+$, $^1\Pi_u$, $^3\Sigma_g^+$, $^3\Pi_g$, $^3\Sigma_u^+$, $^3\Pi_u$
$(1)^2S(5s)$+$(1)^2D(4d)$	19471	19355	$^1\Sigma_g^+$, $^1\Sigma_u^+$, $^1\Pi_g$, $^1\Pi_u$, $^1\Delta_g$, $^1\Delta_u$, $^3\Sigma_g^+$, $^3\Sigma_u^+$, $^3\Pi_g$, $^3\Pi_u$, $^3\Delta_g$, $^3\Delta_u$
$(1)^2S(5s)$+$(2)^2S(6s)$	20126	20133	$^1\Sigma_g^+$, $^1\Sigma_u^+$, $^3\Sigma_g^+$, $^3\Sigma_u^+$
$(1)^2S(5s)$+$(2)^2P(6p)$	23732	23767	$^1\Sigma_g^+$, $^1\Pi_g$, $^1\Sigma_u^+$, $^1\Pi_u$, $^3\Sigma_g^+$, $^3\Pi_g$, $^3\Sigma_u^+$, $^3\Pi_u$
$(1)^2P(5p)$+$(1)^2P(5p)$	25462	25475	$^1\Sigma_g^+(2)$, $^1\Sigma_u^-$, $^1\Pi_g$, $^1\Pi_u$, $^1\Delta_g$, $^3\Sigma_u^+(2)$, $^3\Sigma_g^-$, $^3\Pi_g$, $^3\Pi_u$, $^3\Delta_u$
$(1)^2S(5s)$+$(2)^2D(5d)$	25736	25707	$^1\Sigma_g^+$, $^1\Sigma_u^+$, $^1\Pi_g$, $^1\Pi_u$, $^1\Delta_g$, $^1\Delta_u$, $^3\Sigma_g^+$, $^3\Sigma_u^+$, $^3\Pi_g$, $^3\Pi_u$, $^3\Delta_g$, $^3\Delta_u$
$Rb^+(^1S)$+$Rb^-(^1S)$	29741	29771	$^1\Sigma_g^+$, $^1\Sigma_u^+$

obtained with the Landé rule from the experimental excitation energies. Inspection of Table 1 shows that the agreement between the theoretical and experimental excitation energies is very good. For the $5s+ns$ and $5s+np$ dissociation limits, the RMSD is only 21 cm^{-1}, which represents an error of 0.08%. When the D states are included, this good agreement is somewhat degraded. The RMSD is now 49 cm^{-1}, i.e. 0.26%. This is due to the lack of g symmetry functions in the basis set used in our calculations. Note parenthetically that we could not include g functions in the basis, because the ACESS II program does not support g orbitals in the calculations involving pseudopotentials. Our method reproduces very well the electron affinity of the Rb atom, 3893 cm^{-1} on the theory side versus 3919 cm^{-1} measured in Ref. [75], as well as the ionisation potential, 33630 cm^{-1} versus 33690 cm^{-1} [72]. Finally, we note that the ground state static electric dipole polarisability of the atom obtained from our molecular calculations is 319.5 a_0^3 compared to 318.6 a_0^3 from the most sophisticated atomic calculations by Derevianko *et al.* [76].

The computed potential energy curves are reported in Figure 1 for the $^1\Sigma_g^+$ and $^3\Sigma_g^+$ symmetries, in Figure 2 for the $^1\Sigma_u^+$ and $^3\Sigma_u^+$ symmetries, in Figures 3 and 4 for the $^1\Pi_g$ and $^3\Pi_g$, and $^1\Pi_u$ and $^3\Pi_u$ symmetries, respectively. Finally, Figure 5 shows the potential energy curves for the singlet and triplet gerade and ungerade states of Δ symmetry. The spectroscopic characteristics of the singlet gerade states are reported in Table 2 while Table 3 collects these properties for the triplet gerade states. Tables 4 and 5 present

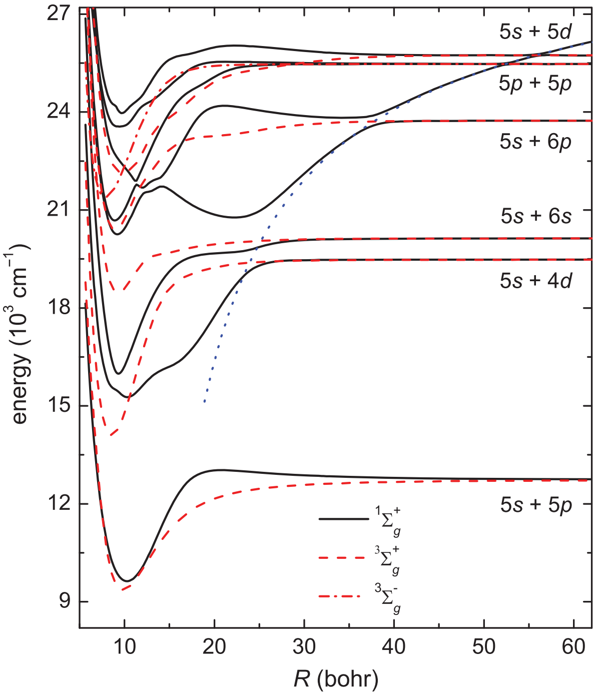

Figure 1. Potential energy curves for the $^1\Sigma_g^+$ and $^3\Sigma_g^\pm$ states of the Rb_2 molecule.

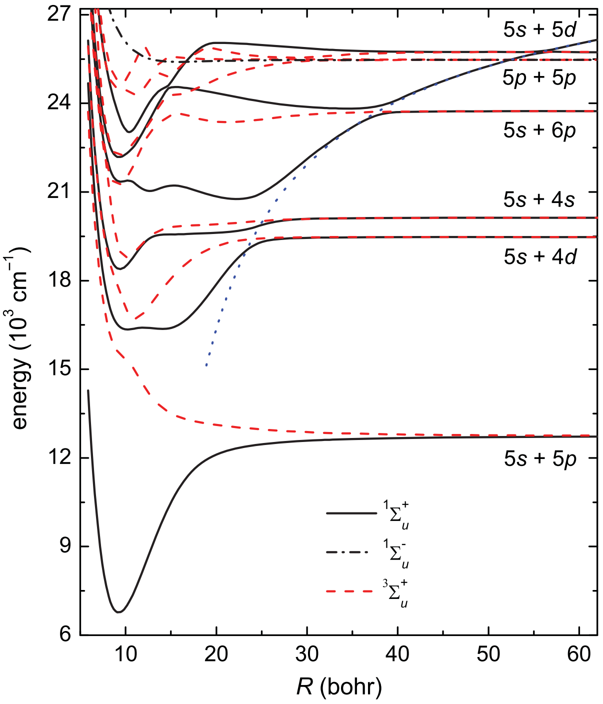

Figure 2. Potential energy curves for the $^1\Sigma_u^\pm$ and $^3\Sigma_u^+$ states of the Rb_2 molecule.

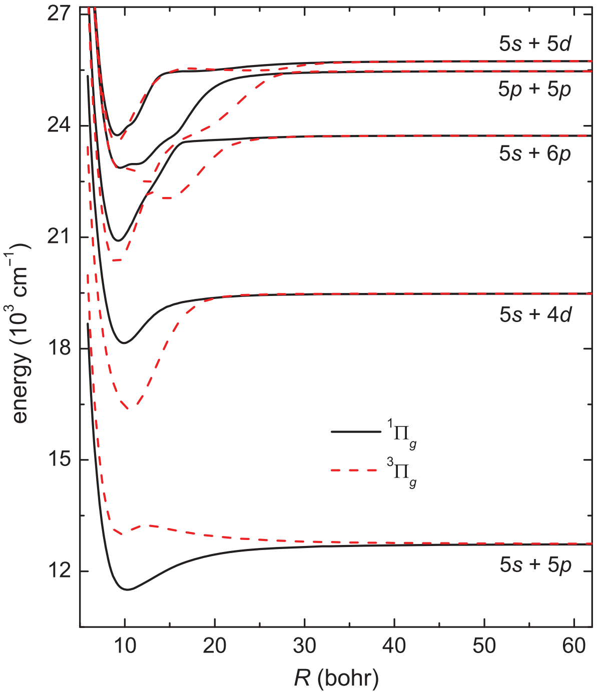

Figure 3. Potential energy curves for the $^1\Pi_g$ and $^3\Pi_g$ states of the Rb_2 molecule.

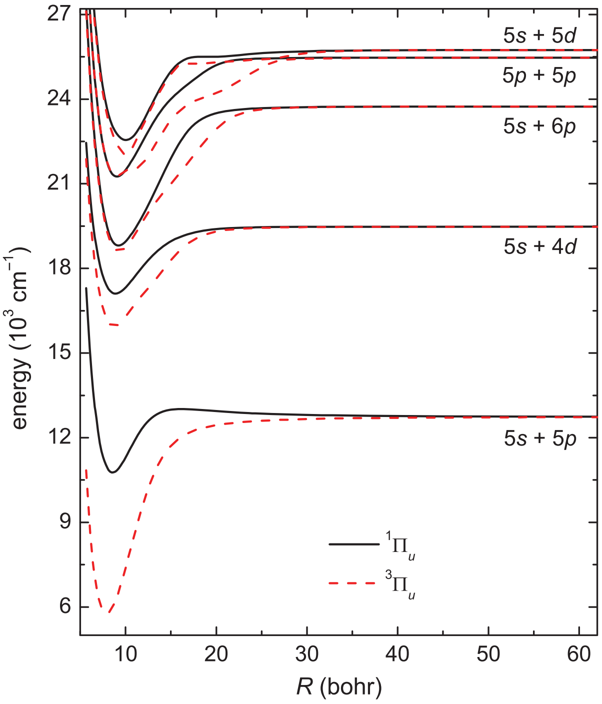

Figure 4. Potential energy curves for the $^1\Pi_u$ and $^3\Pi_u$ states of the Rb_2 molecule.

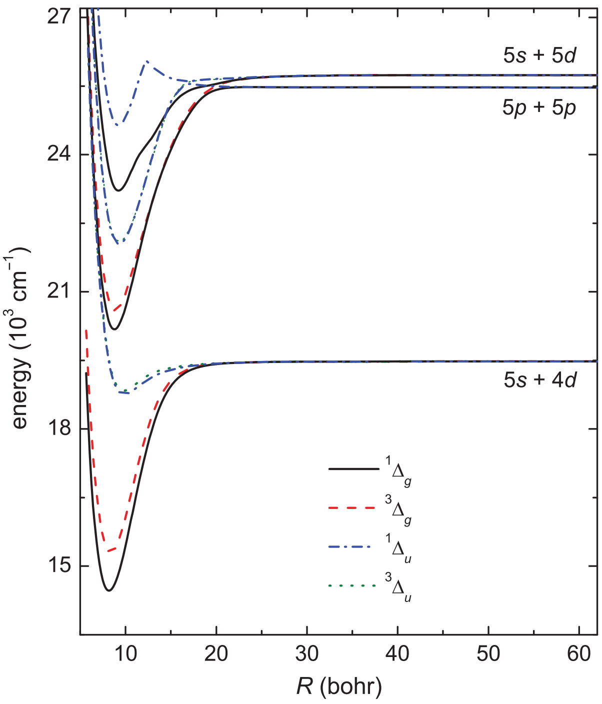

Figure 5. Potential energy curves for the $^1\Delta_{g/u}$ and $^3\Delta_{g/u}$ states of the Rb_2 molecule.

the results for the singlet and triplet states of ungerade symmetry, respectively. Inspection of Figures 1–5 reveals that almost all potential energy curves show a smooth behaviour with well-defined minima. Some higher states display perturbations, mostly in the form of avoided crossings, due to the interaction with other electronic states of the same symmetry that are located nearby. At high energies, the density of states becomes so high that the avoided crossings produce some irregularities in the curves. This is especially true for the singlet and triplet gerade and ungerade states of Σ^+ symmetry. The Π states show less perturbations, except for the avoided crossings between the curves corresponding to the $(3)^1\Pi_g$ and $(4)^1\Pi_g$, and $(3)^3\Pi_g$ and $(4)^3\Pi_g$ states. Interestingly, the Π_u states and the Δ states do not show any irregularity due to non-adiabatic interactions between the states.

The agreement of the present potentials with those derived from the experimental data is very good. This is demonstrated in Tables 2–5, where we compare the potential characteristics with the available experimental data and with the most recent calculations [42]. For all the experimentally observed states, the RMSD of our calculation is only 75.9 cm^{-1}, i.e. the error is 3.2% on average, better than the most recent calculations by Allouche and Aubert-Frécon [42] with a RMSD of 129 cm^{-1} corresponding to an average error of 5.5%. It is gratifying to observe that we reproduce low lying and highly excited electronic states equally well. This is in a sharp contrast to Ref. [42], which reproduces the well depth of the $(2)^1\Pi_u$ state only with an error of 12% compared to 3.5% for our calculation. Such a good agreement between theory and experiment for the highest observed excited electronic state gives us confidence that our predictions for the photoassociative production of ultracold Rb_2 molecules in even higher electronic states [47] are accurate. Tables 2–5 also report the fundamental vibrational frequencies ω_e for all electronic states considered in the present paper. Except for the ground state, the agreement between theory and experiment is within a few tenths of a wavenumber. Similar agreement was found in the calculations by Allouche and Aubert-Frécon [42].

5.2. *Non-adiabatic coupling and spin-orbit coupling matrix elements*

The importance of non-adiabatic interactions between electronic states, resulting in the avoided crossings of the corresponding potential energy curves observed in Figures 1–5, can nicely be explained by analysing the non-adiabatic coupling matrix elements computed according to Equation (18). The non-adiabatic coupling matrix elements are reported in Figure 6 for singlet and triplet states of Σ_g^+ and Σ_u^+ symmetry (top) and the Π states (bottom). As expected, the non-adiabatic coupling matrix elements are smooth, Lorenzian-type functions, which, in the limit of an infinitely close avoided crossing, become a Dirac

Table 2. Spectroscopic characteristics of the non-relativistic $^1|\Lambda|_g$ electronic states of $^{87}Rb_2$ molecule.

State	Ref.	R_e (Bohr)	D_e (cm^{-1})	ω_e (cm^{-1})	T_e (cm^{-1})	Asymptote
$X^1\Sigma_g^+$	Present	7.99	3912	56.1	0	$5s+5s$
	[28] (Exp.)	7.96	3994	57.8	0	
	[42]	7.96	3905	58.4	0	
$(2)^1\Sigma_g^+$	Present	10.29	3102	32.0	13545	$5s+5p$
	[37] (Exp.)	10.28	2963	31.5	13602	
	[42]	10.17	3084	31.2	13559	
$(3)^1\Sigma_g^+$	Present	10.32	4210	32.9	19180	$5s+4d$
	[42]	10.20	4072	31.9	19189	
$(4)^1\Sigma_g^+$	Present	9.34	4144	62.0	19898	$5s+6s$
$(5)^1\Sigma_g^+$	Present	9.21	3483	37.8	24166	$5s+6p$
2nd min.	Present	22.22	2968	11.0	24681	
$(6)^1\Sigma_g^+$	Present	8.93	3055	46.6	24594	$5s+5p$
2nd min.	Present	12.02	2056	50.6	25593	
3rd min.	Present	34.60	86	4.7	27734	
$(7)^1\Sigma_g^+$	Present	11.26	1852	92.8	25797	$5s+5p$
$(8)^1\Sigma_g^+$	Present	9.47	183	41.3	27465	$5s+5d$
$(1)^1\Pi_g$	Present	10.25	1230	21.7	15417	$5s+5p$
	[36] (Exp.)	10.24	1290	22.3	15510	
	[42]	10.24	1198	22.0	15545	
$(2)^1\Pi_g$	Present	9.92	1326	31.0	22063	$5s+4d$
	[42]	9.88	1238	22.0	22023	
$(3)^1\Pi_g$	Present	9.25	2833	43.1	22149	$5s+6p$
$(4)^1\Pi_g$	Present	9.48	2598	37.1	22099	$5p+5p$
$(5)^1\Pi_g$	Present	9.13	1994	42.9	22187	$5s+5d$
$(1)^1\Delta_g$	Present	8.18	5026	48.7	18449	$5s+4d$
	[42]	8.14	4871	50.5	18390	
$(2)^1\Delta_g$	Present	8.76	5291	57.6	24165	$5p+5p$
$(3)^1\Delta_g$	Present	9.22	2528	56.5	27212	$5s+5d$

Table 3. Spectroscopic characteristics of the non-relativistic $^3|\Lambda|_g$ electronic states of $^{87}Rb_2$ molecule.

State	Ref.	R_e (Bohr)	D_e (cm^{-1})	ω_e (cm^{-1})	T_e (cm^{-1})	Asymptote
$(1)^3\Sigma_g^+$	Present	9.91	3367	37.8	13279	$5s+5p$
	[42]	9.73	3345	36.6	13298	
$(2)^3\Sigma_g^+$	Present	8.58	5372	51.1	18017	$5s+4d$
	[42]	8.47	5347	51.5	17914	
$(3)^3\Sigma_g^+$	Present	9.31	1657	38.2	22384	$5s+6s$
$(4)^3\Sigma_g^+$	Present	8.95	3335	46.7	24313	$5s+6p$
$(5)^3\Sigma_g^+$	Present	9.72	3488	19.4	26065	$5p+5p$
$(6)^3\Sigma_g^+$	Present	9.19	3292	43.8	26953	$5s+5p$
$(7)^3\Sigma_g^+$	Present	9.12	3268	38.5	27832	$5s+5d$
$(1)^3\Pi_g$	Present	9.54	−267	30.3	16914	$5s+5p$
	[42]	9.47	−268	30.3	16911	
$(2)^3\Pi_g$	Present	10.56	3104	34.2	20285	$5s+4d$
	[42]	10.53	2927	33.6	20334	
$(3)^3\Pi_g$	Present	9.08	3416	45.4	24232	$5s+6p$
$(4)^3\Pi_g$	Present	9.06	2646	27.4	26735	$5p+5p$
$(5)^3\Pi_g$	Present	9.09	2170	45.8	27484	$5s+5d$
$(1)^3\Delta_g$	Present	8.36	4181	48.3	19284	$5s+4d$
	[42]	8.31	4017	48.9	19244	
$(2)^3\Delta_g$	Present	8.85	5152	46.2	24588	$5s+5d$

Table 4. Spectroscopic characteristics of the non-relativistic $^1|\Lambda|_u$ electronic states of $^{87}\mathrm{Rb}_2$ molecule.

State	Ref.	R_e (Bohr)	D_e (cm^{-1})	ω_e (cm^{-1})	T_e (cm^{-1})	Asymptote
$\mathrm{A}^1\Sigma_u^+$	Present	9.24	5967	44.1	10680	$5s+5p$
	[35] (Exp.)	9.21	5981	44.6	10750	
	[42]	9.20	5896	44.4	10747	
$(2)^1\Sigma_u^+$	Present	10.21	3128	20.5	20261	$5s+4d$
	[42]	10.09	3003	22.1	20258	
2nd min.	Present	14.11	3112	13.5	20277	
	[42]	13.81	2926	11.5	20335	
$(3)^1\Sigma_u^+$	Present	9.37	1737	42.4	22305	$5s+6s$
$(4)^1\Sigma_u^+$	Present	9.46	2390	31.3	25258	$5s+6p$
2nd min.	Present	12.64	2702	24.3	24946	
3rd min.	Present	22.26	2973	10.7	24675	
$(5)^1\Sigma_u^+$	Present	9.28	3565	39.1	26088	$5p+5p$
2nd min.	Present	34.69	1920	5.0	27733	
$(6)^1\Sigma_u^+$	Present	10.38	3308	52.9	26937	$5s+5d$
$(1)^1\Pi_u$	Present	8.57	1971	46.9	14676	$5s+5p$
	[38] (Exp.)	–	1907	47.5	14666	
	[42]	8.48	1989	47.9	14654	
$(2)^1\Pi_u$	Present	8.92	2369	31.6	21021	$5s+4d$
	[38] (Exp.)	–	2454	36.4	20895	
	[42]	8.77	2157	36.1	21104	
$(3)^1\Pi_u$	Present	9.23	4927	40.4	22721	$5s+6p$
$(4)^1\Pi_u$	Present	9.03	4216	43.1	25166	$5p+5p$
$(5)^1\Pi_u$	Present	10.06	3189	31.4	26465	$5s+5d$
$(1)^1\Delta_u$	Present	9.80	639	28.0	22825	$5s+4d$
	[42]	9.78	542	26.9	22718	
$(2)^1\Delta_u$	Present	9.31	3638	48.1	25818	$5p+5p$
$(3)^1\Delta_u$	Present	9.40	2630	34.2	27110	$5s+5d$

Table 5. Spectroscopic characteristics of the non-relativistic $^3|\Lambda|_u$ electronic states of $^{87}\mathrm{Rb}_2$ molecule.

State	Ref.	R_e (Bohr)	D_e (cm^{-1})	ω_e (cm^{-1})	T_e (cm^{-1})	Asymptote
$\mathrm{a}^3\Sigma_u^+$	Present	11.46	250	13.5	3662	$5s+5s$
	[31] (Exp.)	11.51	242	13.5	–	
	[42]	11.45	237	13.3	3669	
$(2)^3\Sigma_u^+$	Present	repulsive	–	–	–	$5s+5p$
$(3)^3\Sigma_u^+$	Present	11.02	2761	40.0	20628	$5s+4d$
	[42]	10.96	2646	40.6	20614	
$(4)^3\Sigma_u^+$	Present	10.06	1340	43.0	22701	$5s+6s$
$(5)^3\Sigma_u^+$	Present	9.18	2493	44.7	25155	$5s+6p$
$(6)^3\Sigma_u^+$	Present	9.29	3235	40.9	26147	$5p+5p$
$(7)^3\Sigma_u^+$	Present	9.09	938	47.2	28444	$5p+5p$
$\mathrm{b}^3\Pi_u$	Present	7.91	6969	57.2	9677	$5s+5p$
	[35] (Exp.)	7.81	7039	60.1	9601	
	[42]	7.88	7015	59.7	9624	
$(2)^3\Pi_u$	Present	8.73	3527	43.5	19862	$5s+4d$
	[42]	8.60	3497	43.3	19764	
$(3)^3\Pi_u$	Present	9.28	5117	40.0	22531	$5s+6p$
$(4)^3\Pi_u$	Present	8.99	4189	43.3	25193	$5p+5p$
$(5)^3\Pi_u$	Present	10.04	3711	56.5	25943	$5s+5d$
$(1)^3\Delta_u$	Present	9.83	719	27.3	22746	$5s+4d$
	[42]	9.86	619	25.8	22641	
$(2)^3\Delta_u$	Present	9.30	3695	40.7	25761	$5s+5d$

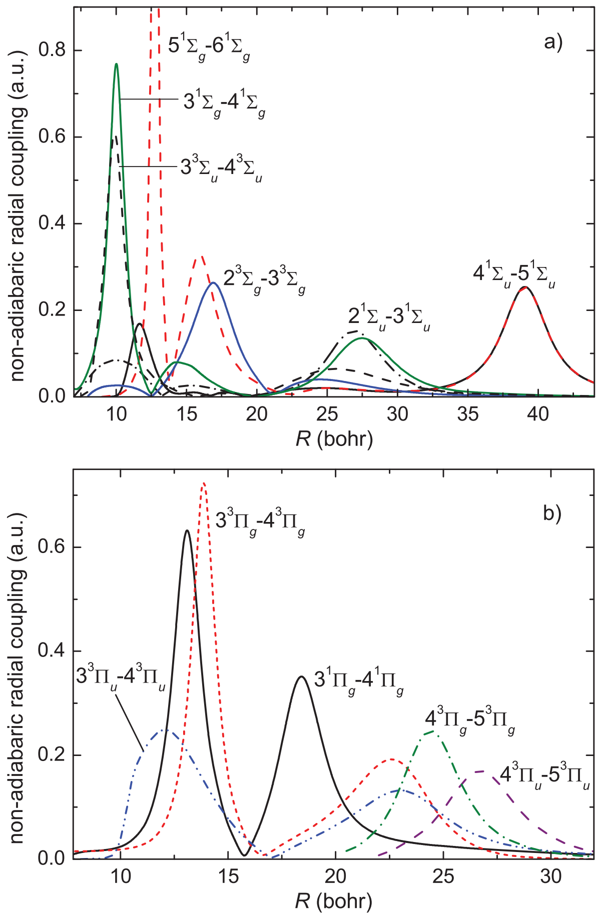

Figure 6. Non-adiabatic radial coupling matrix elements between states of Σ (*a*) and Π (*b*) symmetry.

δ-function. The height and width of the curve depends on the strength of the interaction. The smaller the width and the larger the peak, the stronger is the interaction between the electronic states, and the corresponding potential energy curves are closer to each other at the avoided crossing. It is gratifying to observe that the maxima on the non-adiabatic coupling matrix elements agree well with the locations of the avoided crossing, and this despite the fact that two very different methods were used in *ab initio* calculations. Since the potential energy curves were shown to be accurate, cf. the discussion in Section 5.1, we are confident that also the non-adiabatic coupling matrix elements are essentially correct.

Rubidium is a heavy atom and the electronic states of the Rb_2 molecule show strong couplings due to the relativistic spin-orbit interaction. Figure 7 reports the spin-orbit coupling matrix elements as a function of the interatomic separation. The matrix elements are all represented by smooth curves approaching the atomic limit at large R. The fine splittings of the atomic states are very accurately reproduced by our calculations. For the first excited P state, the theoretical splitting between the 1/2 and 3/2 components is 236.2 cm^{-1} as compared to 237.6 cm^{-1} from the experiment. It is also gratifying to observe that our *ab initio* calculations reproduce very well the spin-orbit coupling functions obtained from fitting analytical functions to high-resolution spectroscopic data for the $A^1\Sigma_u^+$ and $b^3\Pi_u$ manifold of states [35]. This gives us confidence that also perturbations in the molecular spectra due to the spin-orbit interaction will correctly be reproduced from the present *ab initio* data.

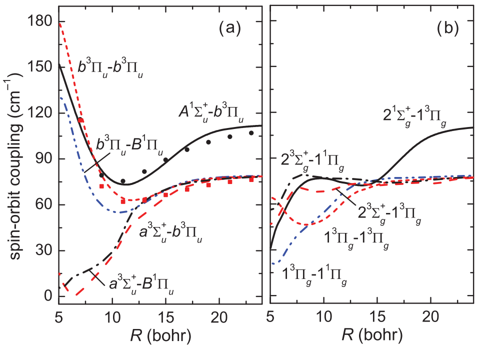

Figure 7. Spin-orbit coupling matrix elements between states of ungerade (*a*) and gerade (*b*) symmetries dissociating into $^2S(5s)$ + $^2P(5p)$. Black circles and red squares are analytical fit to high-resolution spectroscopic data from Ref. [35].

5.3. *Electric transition dipole moments and electric dipole polarisabilities*

A full characterisation of the molecular spectra requires knowledge of the electric transition dipole moments. These were calculated according to Equation (17) and are presented in Figure 8 for transitions from the $X^1\Sigma_g^+$ ground state and in Figure 9 for transitions from the $a^3\Sigma_u^+$ lowest triplet state. The strongest transitions from the ground singlet state are those to the $A^1\Sigma_u^+$ and $(1)^1\Pi_u$ states, i.e. to states corresponding to the first excited dissociation limit. All other transition moments are much smaller, suggesting that the corresponding line intensities in the spectra will be much weaker. The same is true for transitions departing from the $a^3\Sigma_u^+$ state. The transition moments do not show a strong dependence on R, except at small interatomic separations, and smoothly tend to their asymptotic atomic value.

The static electric dipole polarisabilities for the $X^1\Sigma_g^+$ electronic ground state, the $a^3\Sigma_u^+$ state and the relevant excited $A^1\Sigma_u^+$ and $b^3\Pi_u$ states are presented in Figure 9. They show an overall smooth behaviour and also tend smoothly to their asymptotic atomic values. The interaction-induced variation of the polarisability is clearly visible while changing the internuclear distance R. It is significant for excited states, especially for the $A^1\Sigma_u^+$ state for which the isotropic part α reaches 8000 a_0^3, and the anisotropic part $\Delta\alpha$ reaches

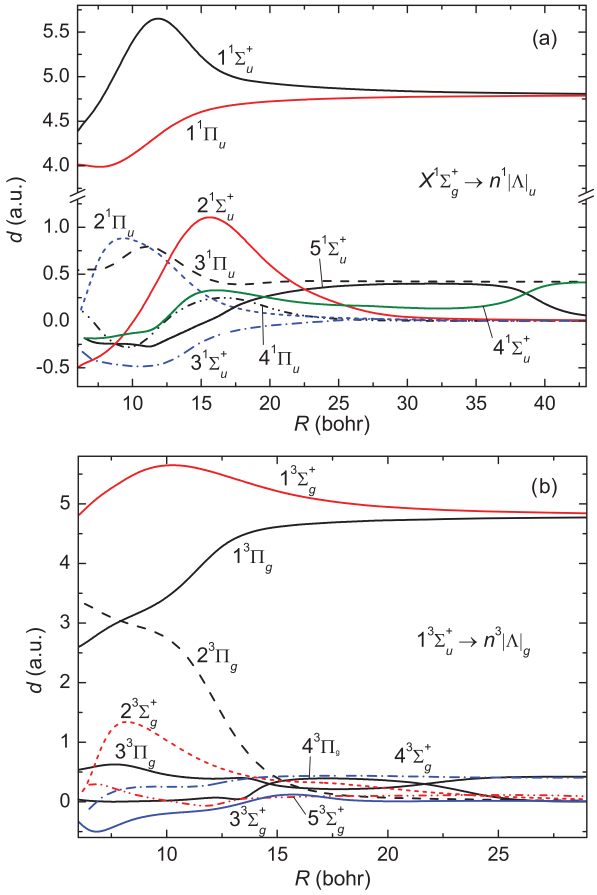

Figure 8. Electric dipole transition moments: (*a*) between the $X^1\Sigma_g^+$ ground state and excited states of $^1\Sigma_u^+$ and $^1\Pi_u$ symmetry, and (*b*) between the $a^3\Sigma_u^+$ lowest triplet state and excited states of $^3\Sigma_g^+$ and $^3\Pi_g$ symmetry.

6000 a_0^3. Such large values of both the interaction-induced variation of isotropic and anisotropic polarisabilities suggest that the influence of the non-resonant laser field on the rovibrational dynamics and transitions between the ground $X^1\Sigma_g^+$ state, and the $A^1\Sigma_u^+$ and $b^3\Pi_u$ states, should be significant even at relatively weak field intensities. Comparing the present polarisabilities of the $X^1\Sigma_g^+$ and $a^3\Sigma_u^+$ states with theoretical results by Deiglmayr *et al.* [77], we find good agreement. For example, the isotropic polarisability α given by trace of the polarisability tensor for the $X^1\Sigma_g$ and $a^3\Sigma_u^+$ states is 522 a.u. and 675 a.u. in the present study and 533 a.u. and 678 a.u. in Ref. [77], respectively.

Note parenthetically that the transition moments and matrix elements of the spin-orbit coupling also change when a DC or non-resonant AC field is applied, but the changes induced on the rovibrational spectrum are expected to be smaller compared to the effects introduced within Equation (13). Therefore, the investigation of the field-induced variation of the transition moments and spin-orbit couplings is out of the scope of the present paper.

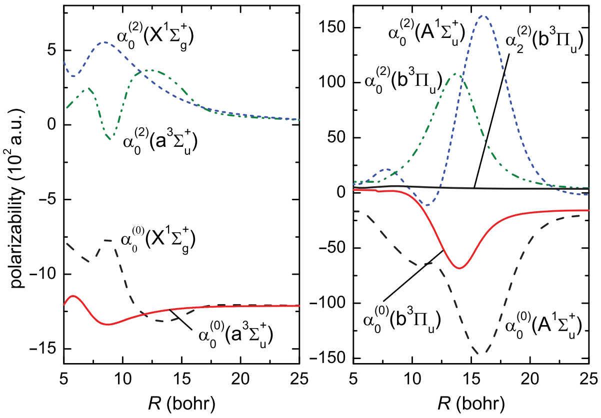

Figure 9. Electric dipole polarisabilities for the electronic ground state (left) and the first excited state (right).

5.4. *Rovibrational spectra in the* $A^1\Sigma_u^+ + b^3\Pi_u$ *manifold without a non-resonant field*

We now compare in more detail the ability of our *ab initio* data to reproduce the fine details of high-resolution experiments of Ref. [35]. In Figure 10(*a*), we report the *ab initio* and empirical potentials for the $A^1\Sigma_u^+$ and $b^3\Pi_u$ states of Rb_2. Inspection of Figure 10(*a*) shows a very good agreement. The *ab initio* calculations reproduce the well depth

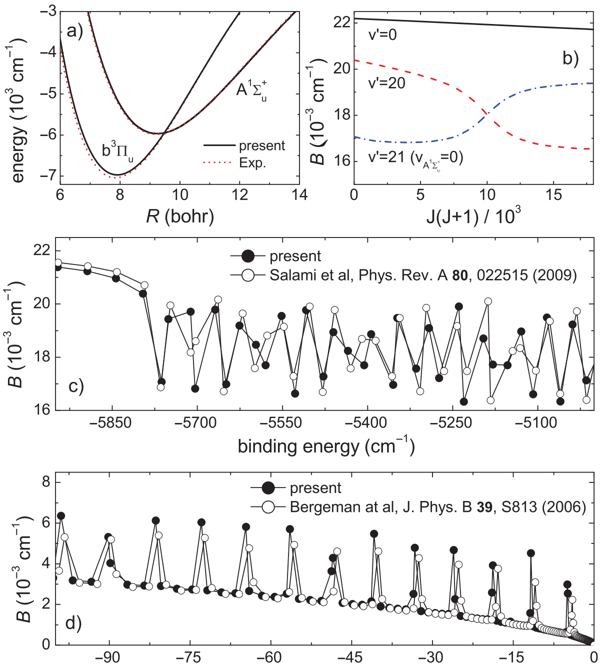

Figure 10. Characteristics of the rovibrational levels for the $|\Omega| = 0_u^+$ component of the coupled $A^1\Sigma_u^+$ and $b^3\Pi_u$ manifold of states in $^{87}Rb_2$: (*a*) present and empirical potential energy curves [35], (*b*) rotational spacings, and $j = 1$ rotational constants for strongly bound levels (*c*) and close to the dissociation limit (*d*).

of the $A^1\Sigma_u^+$ state within 14 cm^{-1} on the overall depth of 5981 cm^{-1}, i.e. within 0.2%. The agreement for the $b^3\Pi_u$ state is slightly less good. The difference in the well depths amounts to 70 cm^{-1} for the well depth of 7039 cm^{-1}. This represents an error of roughly 1%. Such an agreement between theory and experiment should be considered as very good. Also, the crossing of the $A^1\Sigma_u^+$ and $b^3\Pi_u$ potential energy curves is perfectly reproduced. Our dynamical calculations predict the level $v' = 21$ to be the first rovibrational level corresponding to the A state (see the rotational spacings in panel (*b*) of Figure 10). This is one quantum higher than predicted by the experiment [35], but the 70 cm^{-1} disagreement in the well depths fully explains this difference.

Figure 10 also reports the rotational constants for the deeply bound rovibrational levels (panel (*c*)) and levels at the threshold (panel (*d*)). Inspection of Figure 10(*c*) reveals that theory correctly locates all levels that are not perturbed by the spin-orbit interaction, and the first perturbed level. The agreement in the rotational constants for the rovibrational levels in the middle of the potential well is less good, but note the scale on the axis. Overall, we reproduce semi-quantitatively the pattern of the rovibrational levels in this region of the potentials. Also the oscillations of the rotational constants reflecting the perturbations due to the spin-orbit coupling between the $A^1\Sigma_u^+$ and the $b^3\Pi_u$ states are correctly described. This is in accordance with the good agreement between the *ab initio* spin-orbit coupling and the data fitted to the experiment shown in Figure 7. The agreement of the rotational constants for the rovibrational levels near the threshold is very good. This is partly due to the fact that in our calculations we have used the best long-range coefficients from atomic calculations [76]. However, the correct long-range coefficient alone would not be sufficient to obtain such a good agreement between theory and experiment. In fact, panel (*d*) of Figure 10 shows that theory very precisely locates the repulsive walls of the potentials near the zero crossing. This is very gratifying for a theoretical calculation as this region of the potential energy curve is very difficult to describe with *ab initio* methods.

5.5. *Perturbation of the spectra by a non-resonant field*

Bound rovibrational levels are strongly affected by a non-resonant field [55]. We demonstrate in this section that not only are the levels shifted in energy and their rotational motion strongly hybridised, but also, for levels in the coupled $A^1\Sigma_u^+$ and $b^3\Pi_u$ excited state manifold, the singlet-triplet composition may be changed. Note that the non-resonant field mixes different rotational and possibly also vibrational states, and in the presence of the field, v, j, v', j' are not good quantum numbers anymore. However, for simplicity, we do not distinguish between the field-free quantum numbers v, j, v', j' and the corresponding field-dressed labels $\tilde{v}$, $\tilde{j}$, $\tilde{v}'$, $\tilde{j}'$ [55]. The carbon dioxide laser with wavelength of about 10 μm is assumed to be used as a source of a non-resonant field. For that wavelength, the static electric dipole polarisability is good approximation for the dynamic one with a few per cent error both for the ground and excited A+b states.

Comparing three different intensities, Figure 11 illustrates the effect of the non-resonant field on the transition dipole matrix elements for transitions between the $X^1\Sigma_g^+$ ground state and the $A^1\Sigma_u^+$ and $b^3\Pi_u$ excited states. The transition dipole matrix elements are calculated as rovibrational average of Equation (17) for given field-dressed rovibrational levels, i.e. $\sum_{k=A^1\Sigma_u^+,b^3\Pi_u} \langle\varphi^k_{v',j'}|d_z(k \leftarrow \text{X})(R) \cos\theta|\varphi^{X^1\Sigma_g^+}_{v,j}\rangle$, and shown for the $X^1\Sigma_g^+$ state ground level in Figure 11(*a*) and a vibrationally highly excited level in Figure 11(*b*). These levels could be studied using molecules

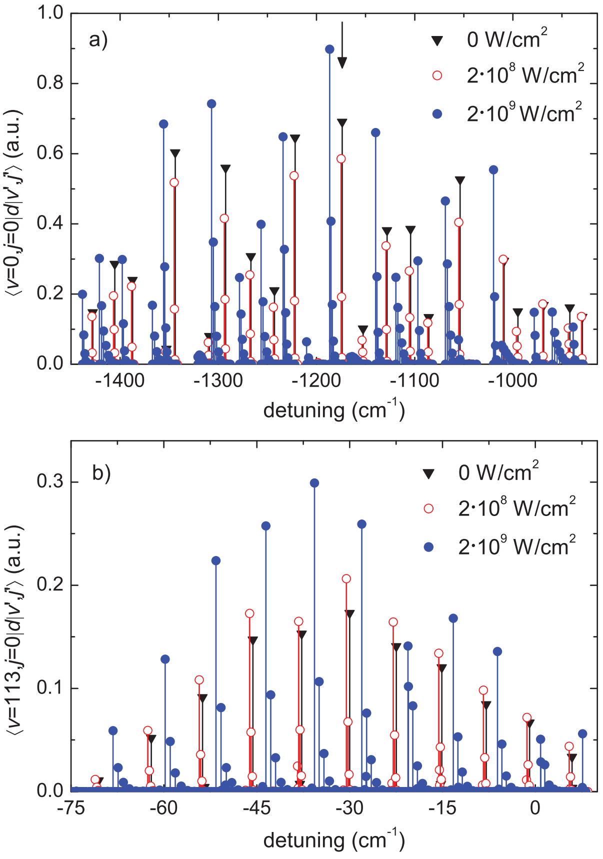

Figure 11. Transition dipole matrix elements between the ground rovibrational level $v = 0, j = 0$ (*a*) and the highly excited level $v = 113, j = 0$ (*b*) of the $X^1\Sigma_g^+$ ground electronic state and rovibrational levels of the $A^1\Sigma_u^+$ and $b^3\Pi_u$ manifold for three intensities of the non-resonant field in $^{87}\text{Rb}_2$. The binding energy of the field-free $X^1\Sigma_g^+$ $v = 113, j = 0$ level is $E_b = 8.3\,\text{cm}^{-1}$. The detuning is computed as $E_{v',J'} - E_{v,J} - (E_{^2P_{1/2}} - E_{^2S})$, with $E_{^2P_{1/2}}$, $E_{^2S}$ the field-free energies of the atomic levels.

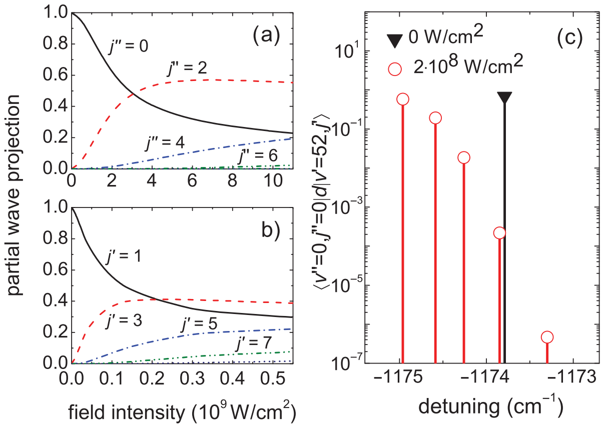

Figure 12. Partial wave decomposition of the field-dressed rovibrational wavefunctions for the $X^1\Sigma_g^+$ state $v = 0, j = 0$ ground level (*a*) and the $v' = 52$, $J' = 1$ level (*b*) of the $A^1\Sigma_u^+$ and $b^3\Pi_u$ manifold in ^{87}Rb$_2$. Also shown are the electric dipole transition moments between the $X^1\Sigma_g^+$ state $v = 0, j = 0$ ground level and the rotational manifold with $v' = 52$ (*c*).

in a molecular beam (*a*) or produced by photoassociation (*b*) [23]. Inspection of Figure 11 reveals that the transitions get shifted as expected, due to the decrease of all eigenenergies in the non-resonant field [54,55]. Moreoever, the transition strengths are strongly modified. This modification is analysed in more detail in Figure 12 for the strongest transition from the $X^1\Sigma_g^+$ state ground level indicated by an arrow in Figure 11(*a*). Due to hybridisation of the rotational motion, illustrated in Figure 12(*a*) and (*b*) in terms of the projections of the rovibrational wavefunctions onto the field-free partial waves, the wavefunctions consist of contributions from several field-free partial waves between which transitions are allowed. This yields a series of rovibrational lines observed in Figure 12(*c*) instead of the single line for $v = 0, j = 0$ to $v' = 52, j' = 1$ in the field-free case. For the largest intensity shown in Figure 11, $\mathcal{I} = 2 \cdot 10^9$ W/cm^2, the transition matrix elements for the strongest lines are clearly larger than in the field-free case. This is rationalised by an alignment of the field-dressed levels in the ground and excited electronic states, with $\langle \cos^2\theta\rangle \gtrsim 0.73$ for $\mathcal{I} = 2 \cdot 10^9$ W/cm^2. Correspondingly, the field-dressed wavefunctions are localised in the angular regions θ close to 0 and π. As a consequence, the field-dressed transition strengths are larger than the field-free ones due to the angular dependence of the matrix elements on $\cos\theta$ [78].

Figure 13 illustrates the effect of a non-resonant field on the transition dipole moments for a weakly bound level in the excited $A^1\Sigma_u^+$ and $b^3\Pi_u$ state manifold. This level is particularly well-suited for the photoassociative production of Rb$_2$ molecules [23], and the analysis of Figure 13 is motivated by a recent proposal for enhancing photoassociation rates using a non-resonant field [55]. While the calculations of Ref. [55] were carried out for Sr$_2$, a somewhat smaller, albeit still significant, enhancement of the photoassociation rate of about one order of magnitude can be expected for Rb$_2$ [54]. The non-resonant field will affect the spontaneous decay of the photoassociated molecules, which is governed by the matrix elements shown in Figure 13. The field-free data represents a rotationally resolved equivalent of Figure 3 of Ref. [23]. The binding energy of 8.3 cm^{-1} in Figure 13 corresponds to the ground state level $v = 113$ (cf. Figure 11(*b*)). A weak non-resonant field splits the two lines originating from the $j' = 1$ level into several ones, similar to Figure 12(*c*). The transition strength for $j = 0$ is almost not affected by the weak field. This behaviour is similar to what has been observed for transitions between weakly bound levels of the strontium dimer [55]. For a strong non-resonant field, the binding energies are shifted and the overall behaviour is similar to Ref. [55]. This implies that a non-resonant field may enhance the photoassociation rate without compromising an efficient stabilisation into bound ground state levels by spontaneous emission as it was observed in Ref. [23].

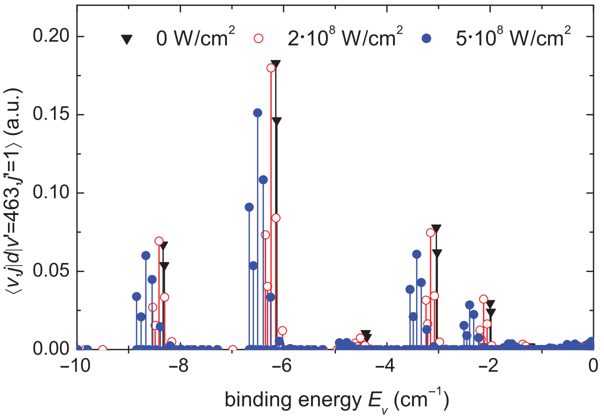

Figure 13. Transition dipole matrix elements for a highly excited rovibrational level ($v' = 463$, $E_{bind}^{v'=463} = 8.3\,\text{cm}^{-1}$) of the $A^1\Sigma_u^+$ and $b^3\Pi_u$ manifold and highly excited $X^1\Sigma_g^+$ state levels in ^{87}Rb$_2$.

Finally, Figure 14 analyses the interplay of the spin-orbit coupling and the interaction with the non-resonant field for several of the rovibrational levels of the $A^1\Sigma_u^+$ and $b^3\Pi_u$ manifold studied in Figures 11(*a*), 12 and 13. Surprisingly, the levels from the middle of the well, $v' = 52, \ldots, 56$, show a remarkable dependence of the singlet-triplet decomposition on the non-resonant field intensity. On the other hand, the singlet-triplet character of weakly bound levels of the $A^1\Sigma_u^+$ and $b^3\Pi_u$ manifold, shown here for the representative $v' = 463$, is hardly affected. This behaviour can be understood by inspection of the *R*-dependence of the polarisability components and the spin-orbit coupling matrix elements (cf. Figures 9 and 7). Weakly bound levels have most of their amplitude at internuclear separations larger than $R = 20\,a_0$. The spin-orbit coupling is strong at large internuclear separations and smaller at intermediate separations, while the opposite is true for the polarisability components. A large dependence of the singlet-triplet

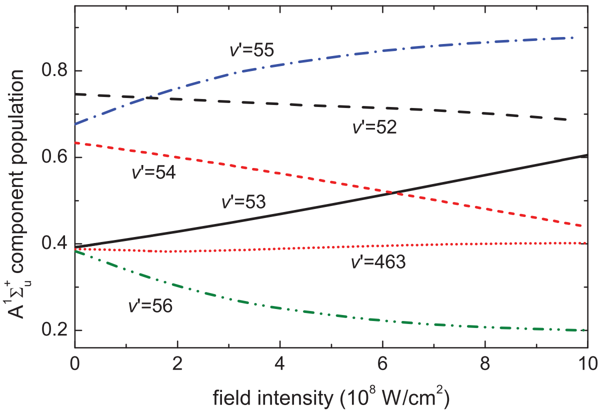

Figure 14. Singlet component of the coupled excited state rovibrational levels versus non-resonant field intensity with v' the field-free vibrational quantum number. Data shown for $j = 1$ (the behaviour for other j is very similar).

character on the non-resonant field intensity is expected when the interaction energy with the field and the spin-orbit coupling become comparable. Due to the R-dependence of the polarisability, for weakly bound levels this requires field intensities in excess of 10^{10} W/cm^2. On the other hand, the more deeply bound levels, $v' = 52, \ldots, 56$, have their outer turning point near $R = 12\,a_0$ where the polarisability is large and the spin-orbit coupling is small. Therefore, intensities of the order of 10^9 W/cm^2 yield an interaction energy with the field that is comparable to the spin-orbit coupling. For example, for 10^9 W/cm^2, the Stark shift of the levels amounts to about 15 cm^{-1}. Their vibrational spacing, of the order of 20 cm^{-1}, is also comparable. The interaction with the non-resonant field will then affect the singlet-triplet character of a rovibrational wavefunction, provided the R-dependence of polarisabilities differs for singlet and triplet states. This is indeed the case, cf. Figure 9, explaining the changes in the singlet-triplet decomposition observed in Figure 14.

6. Summary and conclusions

In the present work, we have investigated how the spectroscopy of the Rb_2 molecule is affected by applying a non-resonant field. Our emphasis has been on the manifold of the spin-orbit coupled $A^1\Sigma_u^+$ and $b^3\Pi_u$ excited states. To this end we have derived the electronic Hamiltonian describing the interaction of a diatomic molecule with a non-resonant field in general and the Hamiltonian describing the nuclear motion in a non-resonant field for the manifold of the coupled $A^1\Sigma_u^+$ and $b^3\Pi_u$ excited electronic states in particular. We have employed the DEA-IH-FS-CCSD for all electronic states of the Rb_2 molecule up to the $5s+5d$ dissociation limit of about 26,000 cm^{-1}. The agreement between the present results and those fitted to high-resolution spectroscopic data is very good, both for the well depths and the vibrational frequencies. The accuracy of the present results for the potential energy curves is much higher than the previous electronic structure calculations in Refs. [40,41] and slightly better than in the most recent study by Allouche and Aubert-Frécon [42].

In order to correctly predict the spectroscopic behaviour, we have also calculated the electric transition dipole moments, non-adiabatic coupling and spin-orbit coupling matrix elements, and static dipole polarisabilities of Rb_2, using the MRCI method. To the best of our knowledge, we have reported in this paper the very first calculation of the irreducible components of the polarisability tensor as a function of R for electronically excited states. For the spin-orbit coupled manifold of the $A^1\Sigma_u^+$ and $b^3\Pi_u$ excited states, we have checked the accuracy of the *ab initio* results with the spectroscopic data. Very good agreement was found.

We have investigated the spectroscopy of Rb_2 in its rovibronic ground state, corresponding to a molecular beam experiment, as well as in highly excited vibrational levels of ground and electronically excited states, typical for photoassociation experiments at ultracold temperatures. In both cases, the spectroscopy is significantly altered by a non-resonant field. Specifically, fields of the order of 10^8 W/cm^2 are found to split a single rovibrational line into several ones and shift the lines by a few cm^{-1}. The splitting is due to rotational hybridisation, i.e. the field-dressed wavefunctions are made up of several field-free partial waves with comparable contributions. For strong non-resonant fields, of the order of 10^9 W/cm^2, alignment leads to an increase of the transition strengths compared to the field-free case, due to localisation of the rotational wavefunctions in regions close to $\theta = 0$ and π, and the dependence of the transition matrix elements on $\cos\theta$ [78]. We have also investigated the effect of a non-resonant field on the transition matrix elements that govern stabilisation by spontaneous emission for photoassociated molecules [23]. Similarly to strontium molecules [55], transitions occur to the same vibrational levels as in the field-free case. This implies that a non-resonant field may be used to enhance the photoassociation rate [55] without deteriorating stabilisation of the photoassociated molecules into bound levels of the electronic ground state. Somewhat surprisingly, we have found a non-resonant field to significantly modify the singlet-triplet character of rovibrational levels in the $A^1\Sigma_u^+$ and $b^3\Pi_u$ excited state manifold for levels in the middle of the potential wells, while weakly bound levels remain rather unaffected. We have identified two conditions for a modification of the singlet-triplet character – the interaction energy with the field needs to be comparable to the spin-orbit coupling and the dependence of the polarisability tensor components on the interatomic separation must differ for singlet and triplet molecules. If both conditions are fulfilled, as was found to be the case for Rb_2 levels of the $A^1\Sigma_u^+$ and $b^3\Pi_u$ manifold with vibrational quantum number around 55, the singlet or triplet character of a rovibrational wavefunction can be controlled by a non-resonant field.

An interesting perspective for coherent control arises when applying a non-resonant field to degenerate excited electronic states. We have shown that, for degenerate states, a non-resonant field introduces a coupling between different states, 0_u^+ and 2_u in the present example. In coherent control based on wavepacket motion, such a coupling between different states can be used to shape the effective potential energy curve governing the wavepacket dynamics [61]. Using a non-resonant field, for example in the far infrared, comes with the advantage of small losses even for strong fields. Non-resonant field control of photoassociation rates [55] or wavepacket dynamics based on field-induced resonant coupling [61] represents a new twist to manipulating molecules with non-resonant fields [79,80].

Acknowledgements

Financial support from the Polish Ministry of Science and Higher Education through the project N N204 215539 and by the Spanish project FIS2011-24540 (MICINN) as well as the Grants P11-FQM-7276 and FQM-4643 (Junta de Andalucía) is gratefully acknowledged. MT was supported by the project operated within the Foundation for Polish Science MPD Programme co-financed by the EU European Regional Development Fund. RGF belongs to the Andalusian research group FQM-207. RM thanks the Foundation for Polish Science for support within the MISTRZ programme. Part of this work was done while the authors were visitors at the Kavli Institute for Theoretical Physics, University of California at Santa Barbara, within the programme Fundamental Science and Applications of Ultra-cold Polar Molecules. Financial support from the National Science Foundation grant no. NSF PHY11-25915 is gratefully acknowledged.

References

[1] E. Cornell, J. Res. Natl. Inst. Stand. Techol. **101**, 419 (1996).
[2] J.L. Roberts, N. Claussen, J.P. Burke, Jr., C.H. Greene, E.A. Cornell, and C.E. Wieman, Phys. Rev. Lett. **81** (23), 5109 (1998).
[3] E.G.M. van Kempen, S.J.J.M.F. Kokkelmans, D.J. Heinzen, and B.J. Verhaar, Phys. Rev. Lett. **88**, 093201 (2002).
[4] A. Marte, T. Volz, J. Schuster, S. Dürr, G. Rempe, E.G.M. van Kempen, and B.J. Verhaar, Phys. Rev. Lett. **89**, 283202 (2002).
[5] C. Gabbanini, A. Fioretti, A. Lucchesini, S. Gozzini, and M. Mazzoni, Phys. Rev. Lett. **84** (13), 2814 (2000).
[6] S. Dürr, T. Volz, A. Marte, and G. Rempe, Phys. Rev. Lett. **92**, 020406 (2004).
[7] H.M.J.M. Boesten, C.C. Tsai, B.J. Verhaar, and D.J. Heinzen, Phys. Rev. Lett. **77**, 5194 (1996).
[8] H.M.J.M. Boesten, C.C. Tsai, J.R. Gardner, D.J. Heinzen, and B.J. Verhaar, Phys. Rev. A **55** (1), 636 (1997).
[9] T. Volz, S. Dürr, N. Syassen, G. Rempe, E. van Kempen, and S. Kokkelmans, Phys. Rev. A **72**, 010704 (2005).
[10] K. Winkler, G. Thalhammer, M. Theis, H. Ritsch, R. Grimm, and J.H. Denschlag, Phys. Rev. Lett. **95**, 063202 (2005).
[11] F. Lang, K. Winkler, C. Strauss, R. Grimm, and J.H. Denschlag, Phys. Rev. Lett. **101**, 133005 (2008).
[12] M.J. Wright, S.D. Gensemer, J. Vala, R. Kosloff, and P.L. Gould, Phys. Rev. Lett. **95**, 063001 (2005).
[13] M.J. Wright, J.A. Pechkis, J.L. Carini, and P.L. Gould, Phys. Rev. A **74**, 063402 (2006).
[14] M.J. Wright, J.A. Pechkis, J.L. Carini, S. Kallush, R. Kosloff, and P.L. Gould, Phys. Rev. A **75**, 051401 (2007).
[15] J.A. Pechkis, J.L. Carini, C.E. Rogers, P.L. Gould, S. Kallush, and R. Kosloff, Phys. Rev. A **83** (6), 063403 (2011).
[16] J.L. Carini, J.A. Pechkis, C.E. Rogers, P.L. Gould, S. Kallush, and R. Kosloff, Phys. Rev. A **87**, 011401 (2013).
[17] W. Salzmann, T. Mullins, J. Eng, M. Albert, R. Wester, M. Weidemüller, A. Merli, S.M. Weber, F. Sauer, M. Plewicki, F. Weise, L. Wöste, and A. Lindinger, Phys. Rev. Lett. **100**, 233003 (2008).
[18] T. Mullins, W. Salzmann, S. Götz, M. Albert, J. Eng, R. Wester, M. Weidemüller, F. Weise, A. Merli, S.M. Weber, F. Sauer, L. Wöste, and A. Lindinger, Phys. Rev. A **80** (6), 063416 (2009).
[19] A. Merli, F. Eimer, F. Weise, A. Lindinger, W. Salzmann, T. Mullins, S. Götz, R. Wester, M. Weidemüller, R. Ağanoğlu, and C.P. Koch, Phys. Rev. A **80**, 063417 (2009).
[20] D.J. McCabe, D.G. England, H.E.L. Martay, M.E. Friedman, J. Petrovic, E. Dimova, B. Chatel, and I.A. Walmsley, Phys. Rev. A **80**, 033404 (2009).
[21] T. Bergeman, J. Qi, D. Wang, Y. Huang, H.K. Pechkis, E.E. Eyler, P.L. Gould, W.C. Stwalley, R.A. Cline, J.D. Miller, and D.J. Heinzen, J. Phys. B **39**, S813 (2006).
[22] Y. Huang, J. Qi, H.K. Pechkis, D. Wang, E.E. Eyler, P.L. Gould, and W.C. Stwalley, J. Phys. B **39**, S857 (2006).
[23] H.K. Pechkis, D. Wang, Y. Huang, E.E. Eyler, P.L. Gould, W.C. Stwalley, and C.P. Koch, Phys. Rev. A **76**, 022504 (2007).
[24] A. Fioretti, O. Dulieu, and C. Gabbanini, J. Phys. B **40** (16), 3283 (2007).
[25] M.A. Bellos, D. Rahmlow, R. Carollo, J. Banerjee, O. Dulieu, A. Gerdes, E.E. Eyler, P.L. Gould, and W.C. Stwalley, Phys. Chem. Chem. Phys. **13**, 18880 (2011).
[26] P.H. Huber and G. Herzberg, *Molecular Spectra and Molecular Structure: IV. Constants of Diatomic Molecules* (Van Nostrand Reinhold, New York, 1979).
[27] E.O. Lawrence and N.E. Edlefsen, Phys. Rev. **34**, 233 (1929).
[28] J.Y. Seto, R.J.L. Roy, J. Vergès, and C. Amiot, J. Chem. Phys. **113** (8), 3067 (2000).
[29] J. Lozeille, A. Fioretti, C. Gabbanini, Y. Huang, H.K. Pechkis, D. Wang, P.L. Gould, E.E. Eyler, W.C. Stwalley, M. Aymar, and O. Dulieu, Eur. Phys. J. D **39**, 261 (2006).
[30] B. Beser, V.B. Sovkov, J. Bai, E.H. Ahmed, C.C. Tsai, F. Xie, L. Li, V.S. Ivanov, and A.M. Lyyra, J. Chem. Phys. **131**, 094505 (2009).
[31] C. Strauss, T. Takekoshi, F. Lang, K. Winkler, R. Grimm, J. Hecker Denschlag, and E. Tiemann, Phys. Rev. A **82**, 052514 (2010).
[32] M. Mudrich, P. Heister, T. Hippler, C. Giese, O. Dulieu, and F. Stienkemeier, Phys. Rev. A **80**, 042512 (2009).
[33] G. Auböck, M. Aymar, O. Dulieu, and W.E. Ernst, J. Chem. Phys. **132**, 054304 (2010).
[34] R.F. Gutterres, C. Amiot, A. Fioretti, G. Gabbanini, M. Mazzoni, and O. Dulieu, Phys. Rev. A **66**, 024502 (2002).
[35] H. Salami, T. Bergeman, B. Beser, J. Bai, E.H. Ahmed, S. Kotochigova, A.M. Lyyra, J. Huennekens, C. Lisdat, A.V. Stolyarov, O. Dulieu, P. Crozet, and A.J. Ross, Phys. Rev. A **80**, 022515 (2009).
[36] C. Amiot, Mol. Phys. **58** (4), 667 (1986).
[37] C. Amiot and J. Verges, Mol. Phys. **61** (1), 51 (1987).
[38] C. Amiot, J. Chem. Phys. **93** (12), 8591 (1990).
[39] D. Konowalow and M. Rosenkrantz, ACS Symp. Ser. **179**, 3 (1982).

[40] S.J. Park, S.W. Suh, Y.S. Lee, and G.H. Jeung, J. Mol. Spectrosc. **207** (2), 129 (2001).

[41] D. Edvardsson, S. Lunell, and C.M. Marian, Mol. Phys. **101**, 2381 (2003).

[42] A.R. Allouche and M. Aubert-Frecon, J. Chem. Phys. **136** (11), 114302 (2012).

[43] W. Jastrzebski (private communication).

[44] P.L. Gould (private communication).

[45] T. Ban, H. Skenderović, R. Beuc, I.K. Bronić, S. Rousseau, A. Allouche, M. Aubert-Frécon, and G. Pichler, Chem. Phys. Lett. **345**, 423 (2001).

[46] T. Ban, R. Beuc, H. Skenderovi, and G. Pichler, Europhys. Lett. **66** (4), 485 (2004).

[47] M. Tomza, M.H. Goerz, M. Musiał, R. Moszynski, and C.P. Koch, Phys. Rev. A **86**, 043424 (2012).

[48] C.P. Koch, M. Ndong, and R. Kosloff, Faraday Disc. **142**, 389 (2009).

[49] M. Musiał, J. Chem. Phys. **136** (13), 134111 (2012).

[50] R.J. Bartlett and M. Musiał, Rev. Mod. Phys. **79**, 291 (2007).

[51] D.I. Lyakh, M. Musiał, V.F. Lotrich, and R.J. Bartlett, Chem. Rev. **112** (1), 182 (2012).

[52] D. Spelsberg, J. Chem. Phys. **111**, 9625 (1999).

[53] W. Skomorowski and R. Moszynski, J. Chem. Phys. **134** (12), 124117 (2011).

[54] R. Ağanoğlu, M. Lemeshko, B. Friedrich, R. González-Férez, and C.P. Koch, arXiv:1105.0761 (2011).

[55] R. González-Férez and C.P. Koch, Phys. Rev. A **86**, 063420 (2012).

[56] T.G.A. Heijmen, R. Moszynski, P.E.S. Wormer, and A. van der Avoird, Mol. Phys. **89**, 81 (1996).

[57] B. Bussery-Honvault, J.M. Launay, and R. Moszynski, Phys. Rev. A **68**, 032718 (2003).

[58] B. Bussery-Honvault, J.M. Launay, and R. Moszynski, Phys. Rev. A **72**, 012702 (2005).

[59] B. Bussery-Honvault, J.M. Launay, T. Korona, and R. Moszynski, J. Chem. Phys. **125**, 114315 (2006).

[60] B. Bussery-Honvault and R. Moszynski, Mol. Phys. **104** (13–14), 2387 (2006).

[61] C.P. Koch and R. Moszyński, Phys. Rev. A **78**, 043417 (2008).

[62] L. Rybak, S. Amaran, L. Levin, M. Tomza, R. Moszynski, R. Kosloff, C.P. Koch, and Z. Amitay, Phys. Rev. Lett. **107**, 273001 (2011).

[63] L. Rybak, Z. Amitay, S. Amaran, R. Kosloff, M. Tomza, R. Moszynski, and C.P. Koch, Faraday Disc. **153**, 383 (2011).

[64] W. Skomorowski, R. Moszynski, and C.P. Koch, Phys. Rev. A **85**, 043414 (2012).

[65] W. Skomorowski, F. Pawłowski, C.P. Koch, and R. Moszynski, J. Chem. Phys. **136**, 194306 (2012).

[66] M. Krych, W. Skomorowski, F. Pawłowski, R. Moszynski, and Z. Idziaszek, Phys. Rev. A **83**, 032723 (2011).

[67] M. Tomza, F. Pawłowski, M. Jeziorska, C.P. Koch, and R. Moszynski, Phys. Chem. Chem. Phys. **13** (42), 18893 (2011).

[68] S. Boys and F. Bernardi, Mol. Phys. **19**, 553 (1970).

[69] M. Marinescu and A. Dalgarno, Phys. Rev. A **52** (1), 311 (1995).

[70] P. Bunker and P. Jensen, *Molecular Symmetry and Spectroscopy* (NRC Press, Ottawa, 1998).

[71] I.S. Lim, P. Schwerdtfeger, B. Metz, and H. Stoll, J. Chem. Phys. **122** (10), 104103 (2005).

[72] NIST Atomic Spectra Database, <http://physics.nist.gov/PhysRefData/ASD>.

[73] J.F. Stanton, J. Gauss, S.A. Perera, J.D. Watts, A. Yau, M. Nooijen, N. Oliphant, P. Szalay, W. Lauderdale, S. Gwaltney, S. Beck, A. Balkov, D. Bernholdt, K. Baeck, P. Rozyczko, H. Sekino, C. Huber, J. Pittner, W. Cencek, D. Taylor, and R. Bartlett, *ACES II: Computer Program* (Quantum Theory Project, University of Florida, Gainesville, FL, 2006).

[74] H.J. Werner, P.J. Knowles, F.R.M.R. Lindh, M. Schütz, P. Celani, T. Korona, A. Mitrushenkov, G. Rauhut, T.B. Adler, R.D. Amos, A. Bernhardsson, A. Berning, D.L. Cooper, M.J.O. Deegan, A.J. Dobbyn, E.G. F. Eckert, C. Hampel, G. Hetzer, T. Hrenar, G. Knizia, C. Köppl, Y. Liu, A.W. Lloyd, R.A. Mata, A.J. May, S.J. McNicholas, W. Meyer, M.E. Mura, A. Nicklass, P. Palmieri, K. Pflüger, R. Pitzer, M. Reiher, U. Schumann, H. Stoll, A.J. Stone, R. Tarroni, T. Thorsteinsson, M. Wang, and A. Wolf, *MOLPRO, version 2008.1, a Package of ab initio Programs* 2008, <http://www.molpro.net>.

[75] P. Frey, F. Breyer, and H. Holop, J. Phys. B: At. Mol. Phys. **11** (19), L589 (1978).

[76] A. Derevianko, S.G. Porsev, and J.F. Babb, At. Data Nucl. Data Tables **96** (3), 323 (2010).

[77] J. Deiglmayr, M. Aymar, R. Wester, M. Weidemuller, and O. Dulieu, J. Chem. Phys. **129** (6), 064309 (2008).

[78] M. Mayle, R. González-Férez, and P. Schmelcher, Phys. Rev. A **75**, 013421 (2007).

[79] B. Friedrich and D. Herschbach, Phys. Rev. Lett. **74**, 4623 (1995).

[80] M. Lemeshko and B. Friedrich, J. Phys. Chem. A 114, 9848 (2010).

Appendix C

Paper III

”Optimized production of ultracold ground-state molecules: Stabilization employing potentials with ion-pair character and strong spin-orbit coupling”

Michał Tomza, Michael H. Goerz, Monika Musiał,
Robert Moszynski, Christiane P. Koch

Physical Review A, **86**, 043424 (2012).

PHYSICAL REVIEW A **86**, 043424 (2012)

Optimized production of ultracold ground-state molecules: Stabilization employing potentials with ion-pair character and strong spin-orbit coupling

Michał Tomza,[1,2] Michael H. Goerz,[2] Monika Musiał,[3] Robert Moszynski,[1] and Christiane P. Koch[2,*]
[1]*Faculty of Chemistry, University of Warsaw, Pasteura 1, 02-093 Warsaw, Poland*
[2]*Theoretische Physik, Universität Kassel, Heinrich-Plett-Str. 40, 34132 Kassel, Germany*
[3]*Institute of Chemistry, University of Silesia, Szkolna 9, 40-006 Katowice, Poland*
(Received 10 August 2012; published 22 October 2012)

We discuss the production of ultracold molecules in their electronic ground state by photoassociation employing electronically excited states with ion-pair character and strong spin-orbit interaction. A short photoassociation laser pulse drives a nonresonant three-photon transition for alkali-metal atoms colliding in their lowest triplet state. The excited-state wave packet is transferred to the ground electronic state by a second laser pulse, driving a resonant two-photon transition. After analyzing the transition matrix elements governing the stabilization step, we discuss the efficiency of population transfer using transform-limited and linearly chirped laser pulses. Finally, we employ optimal control theory to determine the most efficient stabilization pathways. We find that the stabilization efficiency can be increased by one and two orders of magnitude when using linearly chirped and optimally shaped laser pulses, respectively.

DOI: 10.1103/PhysRevA.86.043424 PACS number(s): 33.80.−b, 82.53.Kp, 31.50.−x, 33.90.+h

I. INTRODUCTION

Photoassociation, which is the forming of molecules from ultracold atoms using laser light [1], is a prime candidate for coherent control which utilizes the wave nature of matter in order to steer a process, such as the formation of a chemical bond, toward a desired target [2,3]. At very low temperature, the delicate buildup of constructive and destructive interference between different quantum pathways is not hampered by thermal averaging. The basic tool for coherent control are short laser pulses that can be shaped in their amplitude, phase, and polarization. They can drive both adiabatic and nonadiabatic photoassociation dynamics [4].

A particular feature of photoassociation at very low temperatures is the excitation of an atom pair at fairly large interatomic separations [1]. This results from a compromise between the atom pair density in the electronic ground state, highest at large interatomic separations, and the population of excited-state bound levels with reasonable binding energies, which increase with decreasing interatomic separations. Therefore, the free-to-bound transition matrix elements are largest for photoassociation at separations of $50a_0$ to $150a_0$ with corresponding detunings of less than about 20 cm^{-1}. Although these matrix elements are optimally chosen, they are several orders of magnitude smaller than those for the excitation of atoms. This poses a problem for photoassociation with short laser pulses which inherently have a large bandwidth. As soon as the wings of the pulse spectrum overlap with the atomic resonance, atoms instead of bound levels are excited [5], and subsequent spontaneous emission depletes the trapped sample [6,7]. In photoassociation experiments using broadband femtosecond laser pulses, the pulse spectrum therefore needed to be cut to suppress excitation of the atomic resonance [8]. The sharp spectral cut yields long wings of the temporal pulse profile, and the ensuing photoassociation dynamics were dominated by transient Rabi oscillations of extremely weakly bound molecules caused by the long tail of the pulse [8–11]. While it was gratifying to see that femtosecond photoassociation is feasible [8], larger binding energies and vibrational instead of electronic dynamics are required to produce stable molecules in their electronic ground state [4].

Femtosecond photoassociation at very low temperature corresponds to driving a narrow-band transition with a broadband laser. This can be achieved by employing multiphoton rather than one-photon transitions [12]. The high peak powers of femtosecond laser pulses easily allow for driving multiphoton transitions, and multiphoton control schemes have been demonstrated for both weak [12,13] and strong laser pulses [14–16]. In the weak-field regime, perturbation theory shows that optical interference of two or more photons can be used to completely suppress absorption [12,13]. For intermediate intensities, higher-order perturbation theory can be employed to obtain rational pulse shapes that allow the absorption to be controlled [17–21]. In the strong-field regime, dynamic Stark shifts drive the transition out of resonance. This can be countered by a linear chirp of the pulse which compensates the phase accumulated due to the Stark shift. Additionally, adjusting the amplitude of the pulse to guarantee a π or 2π pulse controls the absorption [14–16]. These control schemes can be applied to femtosecond photoassociation in order to suppress the excitation of atoms [22]. Multiphoton transitions can also be useful for femtosecond photoassociation at high temperature [23,24]. There the main advantage derives from the larger flexibility in transition energies, obtained when combining two or more photons, and the new selection rules. The disadvantage of high temperatures is the low initial coherence, or quantum purity, of the thermal ensemble of atoms. However, femtosecond photoassociation can generate rovibrational coherence by Franck-Condon filtering [23]. The long-standing goal of coherently controlling bond formation [25] has thus become within reach also for high temperatures.

Besides the possibility of driving a narrow-band transition, multiphoton femtosecond photoassociation also allows for accessing highly excited electronic states that may have significant ion-pair character. Such states are expected to

---

[*] christiane.koch@uni-kassel.de

be well suited for the formation of stable molecules in their electronic ground state due to the peculiar shapes of the potential-energy curves obtained when an ion-pair state crosses covalent ones [26,27].

These effects become most significant for heavy atoms with strong spin-orbit interaction. The coupling of two (or more) electronic states leads to strong mixing of the rovibrational levels provided the coupling becomes resonant [28]. The wave functions of such strongly mixed levels display peaks at all the four classical turning points. This leads to large transition matrix elements for both photoassociation and subsequent stabilization to the electronic ground state [29]. For homonuclear diatomics, usually several neighboring vibrational levels are affected by the resonant coupling [30,31], making them particularly suitable for short-pulse photoassociation and stabilization since a laser pulse addresses a wave packet, not just a single level. In the case of heteronuclear molecules, the resonantly perturbed levels are typically isolated within the vibrational spectrum. However, the peaks at the inner turning points are so large that stabilization into deeply bound levels of the ground-state well [32,33] all the way down to $v'' = 0$ for SrYb [34] becomes feasible in a single step. Strong spin-orbit interaction furthermore allows for singlet-triplet conversion [35,36]. Here, we combine all these features in a study of short-pulse multiphoton photoassociation into highly excited states with significant ion-pair character and strong spin-orbit interaction. Our envisioned scheme for off-resonant three-photon photoassociation and subsequent resonant two-photon stabilization is displayed in Fig. 1. The potential-energy curves shown in Fig. 1 as well as the spin-orbit couplings and transition matrix elements were calculated with state of the art *ab initio* methods. The interaction of the atom pair with the laser pulses is modelled nonperturbatively. A photoassociation pulse excites a pair of rubidium atoms, colliding in their lowest triplet state, into the manifold of electronically excited states just below the $5s + 6p_{1/2}$ threshold. The shape of the potential-energy curves close to the Franck-Condon radius for photoassociation is dominated by the $1/R$ behavior of the ion-pair state. Note that excitation into the ion-pair state is dipole forbidden. The three-photon photoassociation indicated in Fig. 1 is facilitated by the covalent states that are coupled to the ion-pair state. Upon its creation by the photoassociation pulse, the wave packet rolls down the $1/R$ slope, being subject to spin-orbit oscillations between different electronic states of the manifold at the same time. Once the wave packet reaches short interatomic separations, a stabilization pulse catches it, transferring it to the electronic ground state via a resonant transition into the intermediate $A\,^1\Sigma_u^+\ b\,^3\Pi_u$ states. The strong spin-orbit coupling in both the highly excited and intermediate state affords a conversion of the molecules to purely singlet character in the final state. Our emphasis in the present study is on the intricate dynamics of the photoassociated wave packet in the electronic manifold below the $5s + 6p_{1/2}$ asymptote and the stabilization to the electronic ground state. We employ rationally shaped laser pulses as well as optimal control theory to determine the maximum stabilization efficiencies, taking standard constraints of pulse shaping experiments into account. The application of optimal control theory to the photoassociation step requires a theoretical description that accounts for the initial incoherent ensemble of atoms and will be presented elsewhere.

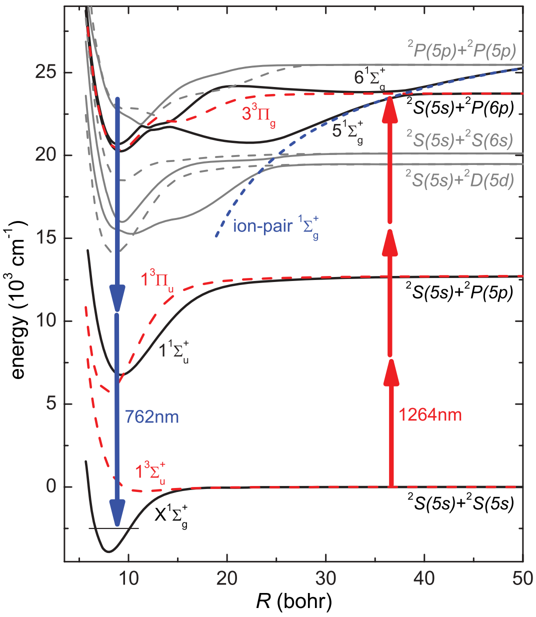

FIG. 1. (Color online) Proposed scheme for multiphoton photoassociation and subsequent stabilization producing ultracold Rb_2 molecules in their electronic ground state.

The plan of our paper is as follows: The theoretical framework is presented in Sec. II, describing the model in Sec. II A, and details of the electronic structure calculations and optimal control theory in Secs. II B and II C, respectively. The creation of the photoassociated wave packet, representing the initial state for the stabilization step, and its dynamics in the coupled manifold of electronic states below the $5s + 6p_{1/2}$ asymptote is studied in Sec. III. The stabilization efficiency of transform-limited and linearly chirped pulses is investigated in Sec. IV. Optimally shaped pulses driving the excited-state wave packet into the electronic ground state and their efficiency are discussed in Sec. V. We conclude in Sec. VI.

II. THEORETICAL FRAMEWORK

A. Hamiltonian

We consider a pair of ^{85}Rb atoms, held at a temperature of 100 μK, typical for magneto-optical traps, colliding in the $a\,^3\Sigma_u^+$ lowest triplet state. The formation of molecules by photoassociation and stabilization of the excited-state molecules to the electronic ground state are treated separately. First, a photoassociation laser pulse drives a three-photon transition, red detuned with respect to the $^2S(5s) + {}^2P_{1/2}(6p)$ asymptote, creating a molecular wave packet in the manifold of the $(5)\,^1\Sigma_g^+$, $(6)\,^1\Sigma_g^+$, $(7)\,^1\Sigma_g^+$, $(3)\,^3\Pi_g$, and $(4)\,^3\Pi_g$ electronically excited states that partially have an ion-pair character (cf. Fig. 2). The states in this manifold are coupled by spin-orbit interaction and nonadiabatic radial coupling matrix elements. In our calculations, only the $(5)\,^1\Sigma_g^+$, $(6)\,^1\Sigma_g^+$, and $(3)\,^3\Pi_g$ components of the photoassociated wave packet turned out to be significant [63]. Neglecting the $(7)\,^1\Sigma_g^+$ and $(4)\,^3\Pi_g$ states, the Hamiltonian describing the three-photon photoassociation reads

$$\hat{\mathsf{H}}_{\mathrm{pump}}(t) = \begin{pmatrix} \hat{\mathsf{H}}^{a\,^3\Sigma_u^+}(R) & 0 & \epsilon^*(t)^3\chi^{(3)}(\omega_L,R) & 0 \\ 0 & \hat{\mathsf{H}}^{(5)\,^1\Sigma_g^+}(R) & \xi_3(R) & A(R) \\ \epsilon(t)^3\chi^{(3)}(R) & \xi_3(R) & \hat{\mathsf{H}}^{(3)\,^3\Pi_g}(R)-\xi_4(R) & \xi_5(R) \\ 0 & A(R) & \xi_5(R) & \hat{\mathsf{H}}^{(6)\,^1\Sigma_g^+}(R) \end{pmatrix} \tag{1}$$

in the (three-photon) rotating-wave approximation. In Eq. (1), $\hat{\mathsf{H}}^{^{2S+1}|\Lambda|}$ denotes the Hamiltonian for the nuclear motion in the $^{2S+1}|\Lambda|$ electronic state,

$$\hat{\mathsf{H}}^{^{2S+1}|\Lambda|} = \hat{\mathsf{T}} + V^{^{2S+1}|\Lambda|}(R) + \omega_S^{^{2S+1}|\Lambda|}(t,R) + \Delta_{\omega_L}, \tag{2}$$

where the kinetic energy operator is given by $\hat{\mathsf{T}} = \frac{\hbar^2}{2\mu}\frac{d^2}{dR^2}$, μ is the reduced mass, and $V^{^{2S+1}|\Lambda|}(R)$ is the potential-energy curve. The three-photon detuning, Δ_{ω_L} is taken with respect to the atomic $^2S(5s) \longrightarrow {}^2P_{1/2}(6p)$ three-photon transition. For strong photoassociation laser pulses, the dynamic Stark shift, $\omega_S^{^{2S+1}|\Lambda|}(t,R)$, will become significant. It arises from the interaction of the $^{2S+1}|\Lambda|$ state with the intermediate off-resonant states and is given by the effective dynamic electric dipole polarizability, $\alpha_{\mathrm{eff}}(\omega_L,R)$,

$$\omega_S^{^{2S+1}|\Lambda|}(t,R) = -\tfrac{1}{2}|\epsilon(t)|^2\alpha_{\mathrm{eff}}(\omega_L,R), \tag{3}$$

where $\epsilon(t) = |\epsilon(t)|e^{i\phi(t)}$ describes the electric field of the laser pulse in the rotating frame with envelope $|\epsilon(t)|$ and $\phi(t)$ denoting the relative phase, taken with respect to the central frequency's phase. $\chi^{(3)}(\omega_L,R)$ is the three-photon electric dipole transition moment, $\xi_i(R)$ $(i = 3,5)$ are the spin-orbit couplings, and $A(R)$ is the nonadiabatic radial coupling matrix element between the $(5)\,^1\Sigma_g^+$ and $(6)\,^1\Sigma_g^+$ states.

In a second step, the initial wave packet created by the three-photon photoassociation is deexcited to the $X\,^1\Sigma_g^+$ ground electronic state via a resonant two-photon electric dipole transition. The intermediate states for the two-photon transition are the $A\,^1\Sigma_u^+$ and $b\,^3\Pi_u$ states, correlating to the $^2S(5s) + {}^2P(5p)$ asymptote and which are also strongly coupled by the spin-orbit interaction. Electric dipole transitions are allowed between all components of the initial wave packet and the intermediate states, whereas the $X\,^1\Sigma_g^+$ ground electronic state is only connected to the $A\,^1\Sigma_u^+$ state by a strong electric dipole transition. The Hamiltonian describing the stabilization of the photoassociated wave packet to the electronic ground state via a resonant two-photon transition reads

$$\hat{\mathsf{H}}_{\mathrm{dump}}(t) = \begin{pmatrix} \hat{\mathsf{H}}^{X\,^1\Sigma_g^+}(R) & \epsilon^*(t)d_1(R) & 0 & 0 & 0 & 0 \\ \epsilon(t)d_1(R) & \hat{\mathsf{H}}^{A\,^1\Sigma_u^+}(R) & \xi_1(R) & \epsilon^*(t)d_2(R) & 0 & \epsilon^*(t)d_4(R) \\ 0 & \xi_1(R) & \hat{\mathsf{H}}^{b\,^3\Pi_u}(R)-\xi_2(R) & 0 & \epsilon^*(t)d_3(R) & 0 \\ 0 & \epsilon(t)d_2(R) & 0 & \hat{\mathsf{H}}^{(5)\,^1\Sigma_g^+}(R) & \xi_3(R) & A(R) \\ 0 & 0 & \epsilon(t)d_3(R) & \xi_3(R) & \hat{\mathsf{H}}^{(3)\,^3\Pi_g}(R)-\xi_4(R) & \xi_5(R) \\ 0 & \epsilon(t)d_4(R) & 0 & A(R) & \xi_5(R) & \hat{\mathsf{H}}^{(6)\,^1\Sigma_g^+}(R) \end{pmatrix}, \tag{4}$$

in a (one-photon) rotating-wave approximation. The Hamiltonian for field-free nuclear motion in the $^{2S+1}|\Lambda|$ electronic state, $\hat{\mathsf{H}}^{^{2S+1}|\Lambda|}$, is now given by

$$\hat{\mathsf{H}}^{^{2S+1}|\Lambda|} = \hat{\mathsf{T}} + V^{^{2S+1}|\Lambda|}(R) + \Delta_{\omega_L}^{np}, \tag{5}$$

with the detunings $\Delta_{\omega_L}^{5p} = \omega_{^2P(5p)} - \omega_L$ and $\Delta_{\omega_L}^{6p} = \omega_{^2P(6p)} - 2\omega_L$ for the states dissociating into the $^2S(5s) + {}^2P(5p)$ and $^2S(5s) + {}^2P(6p)$ asymptotes, respectively. The electric transition dipole moments are denoted by

$$d_1(R) = \langle X\,^1\Sigma_g^+|\hat{\mathsf{d}}|A\,^1\Sigma_u^+\rangle, \quad d_2(R) = \langle A\,^1\Sigma_u^+|\hat{\mathsf{d}}|(5)\,^1\Sigma_g^+\rangle,$$
$$d_3(R) = \langle b\,^3\Pi_u|\hat{\mathsf{d}}|(3)\,^3\Pi_g\rangle, \quad d_4(R) = \langle A\,^1\Sigma_u^+|\hat{\mathsf{d}}|(6)\,^1\Sigma_g^+\rangle,$$

and the spin-orbit coupling matrix elements read

$$\xi_1(R) = \langle A\,^1\Sigma_u^+|\hat{\mathsf{H}}_{\mathrm{SO}}^{\Omega=0_u^+}|b\,^3\Pi_u\rangle,$$
$$\xi_2(R) = \langle b\,^3\Pi_u|\hat{\mathsf{H}}_{\mathrm{SO}}^{\Omega=0_u^+}|b\,^3\Pi_u\rangle,$$
$$\xi_3(R) = \langle (5)\,^1\Sigma_g^+|\hat{\mathsf{H}}_{\mathrm{SO}}^{\Omega=0_g^+}|(3)\,^3\Pi_g\rangle,$$
$$\xi_4(R) = \langle (3)\,^3\Pi_g|\hat{\mathsf{H}}_{\mathrm{SO}}^{\Omega=0_g^+}|(3)\,^3\Pi_g\rangle,$$
$$\xi_5(R) = \langle (6)\,^1\Sigma_g^+|\hat{\mathsf{H}}_{\mathrm{SO}}^{\Omega=0_g^+}|(3)\,^3\Pi_g\rangle,$$

where $\hat{\mathsf{H}}_{\mathrm{SO}}$ denotes the spin-orbit Hamiltonian in the Breit-Pauli approximation. For large interatomic separations R, the transition dipole moments and spin-orbit coupling approach,

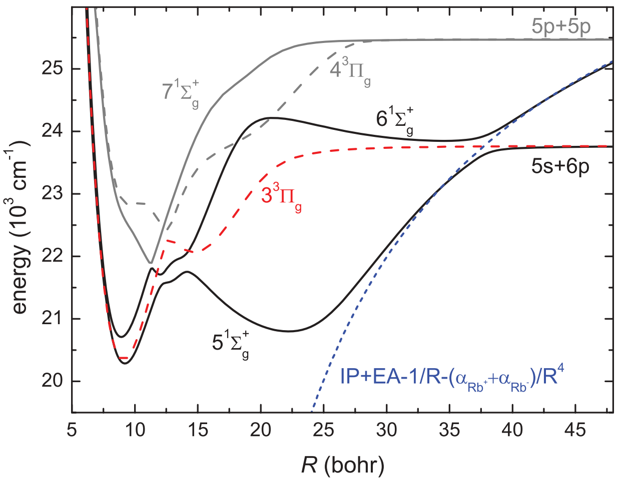

FIG. 2. (Color online) The (5) ${}^1\Sigma_g^+$, (6) ${}^1\Sigma_g^+$, and (3) ${}^3\Pi_g$ electronic states relevant for initial wave packet dynamics and ion-pair curve.

shown in Fig. 3, their atomic values,

$$d_1(R\to\infty)=\sqrt{2}\langle {}^2S(5s)|\hat{\mathsf{d}}|{}^2P(5p)\rangle,$$
$$d_2(R\to\infty)=0,\quad d_3(R\to\infty)=0,$$
$$d_4(R\to\infty)=\sqrt{2}\langle {}^2S(5s)|\hat{\mathsf{d}}|{}^2P(5p)\rangle,$$

and

$$\xi_2(R\to\infty)=\xi_1(R\to\infty)/\sqrt{2}=\Delta_{FS}({}^2P(6p))/3,$$
$$\xi_4(R\to\infty)=\xi_3(R\to\infty)/\sqrt{2}=\Delta_{FS}({}^2P(5p))/3,$$
$$\xi_5(R\to\infty)=0,$$

where $\Delta_{FS}({}^2P(5p))=237.6\ \text{cm}^{-1}$ and $\Delta_{FS}({}^2P(6p))=77.5\ \text{cm}^{-1}$ are the atomic fine structure splittings.

The Hamiltonians (1) and (4) are represented on a Fourier grid with an adaptive step size [37–39] using $N=2048$ grid points. The time-dependent Schrödinger equation for the pump and dump Hamiltonians,

$$i\frac{\partial}{\partial t}|\Psi(t)\rangle=\hat{\mathsf{H}}|\Psi(t)\rangle, \tag{6}$$

is solved by the Chebyshev propagator [40].

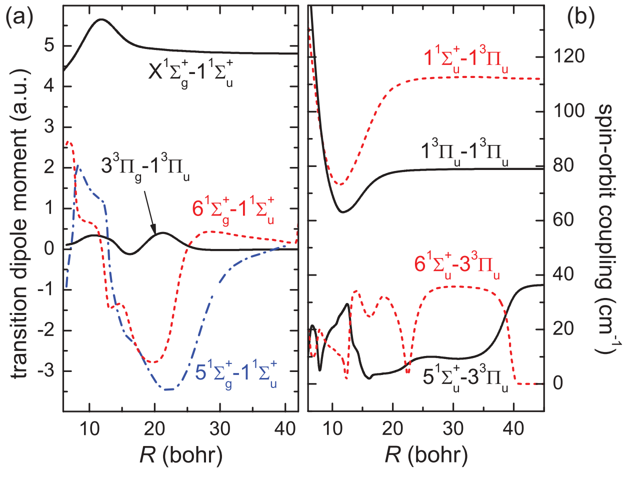

FIG. 3. (Color online) Electric transition dipole moments (a) and spin-orbit coupling matrix elements (b) essential for the dynamics studied.

B. Electronic structure

State-of-the-art *ab initio* techniques have been applied to determine the electronic structure data of the rubidium molecule needed in our dynamical models of the pump and dump processes. The details of the calculations and a thorough discussion of the accuracy by comparison with the most recent high-resolution spectroscopic results will be reported elsewhere [41]. Briefly, all potential-energy curves for the gerade and ungerade singlet and triplet states lying below 26 000 cm^{-1} at the dissociation limit were calculated with the recently introduced double electron attachment intermediate Hamiltonian Fock space coupled cluster method restricted to single and double excitations (DEA-IH-FS-CCSD) [42,43]. Starting with the closed-shell reference state for the doubly ionized molecule $\text{Rb}_2{}^{2+}$ that shows the correct dissociation at large distances R into closed-shell subsystems, $\text{Rb}^+ + \text{Rb}^+$, and using the double electron attachment operators in the Fock space coupled cluster ansatz renders our method size-consistent at any interatomic distance R and guarantees the correct large-R asymptotics. Thus, the DEA-IH-FS-CCSD approach overcomes the problem of the standard CCSD and equation of motion CCSD methods [44] with the proper dissociation into open-shell atoms. The potential-energy curves obtained from the *ab initio* calculations were smoothly connected at intermediate distances to the asymptotic multipole expansion [45]. The C_6 coefficient of the electronic ground state and the C_3 coefficient of the first excited state were fixed at their empirical values derived from high-resolution spectroscopic experiments [46,47], while the remaining coefficients were taken from Ref. [48]. Electric transition dipole moments, radial nonadiabatic coupling, and spin-orbit-coupling matrix elements were obtained by the multireference configuration interaction method (MRCI), restricted to single and double excitations with a large active space. Scalar relativistic effects were included by using the small-core fully relativistic energy-consistent pseudopotential ECP28MDF [49] from the Stuttgart library. Thus, in the present study the Rb_2 molecule was treated as a system of effectively 18 electrons. The $[14s14p7d6f]$ basis set was used in all calculations. This basis was obtained by decontracting and augmenting the basis set of Ref. [49] by a set of additional functions, improving the accuracy of the atomic excitation energies of the rubidium atom with respect to the NIST database. With this basis set, employing the DEA-IH-FS-CCSD method for the nonrelativistic energies and the MRCI approach for the fine structure, we reproduce the experimental excitation energies with a root mean square deviation (rmsD) of 21 cm^{-1}. The DEA-IH-FS-CCSD calculations were done with the code based on the ACES II program system [50], while the MRCI calculations were performed with the MOLPRO code [51].

The accuracy of the computed potential-energy curves is as excellent as that of the atomic excitation energies [41]. Here, we only point out that the rmsD of the well depths of the present potential-energy curves for electronic states that were observed experimentally is 64 cm^{-1}. In particular, the well depths of the ground singlet state and the lowest triplet state are reproduced within 2.7% and 3.7%, respectively. The relative errors for the excited states relevant for the present study, the $A\,^1\Sigma_u^+$ and $b\,^3\Pi_u$ pair, are even smaller at 0.5% and 0.3%, respectively. We expect a similar accuracy for the higher electronic states that have not yet been observed experimentally. The accuracy of the present results for the potential-energy curves is much higher than that of Refs. [52,53] and slightly better than in the recent study by Allouche and Aubert-Frécon [54], which did not consider the electronic states crucial for our photoassociation proposal.

C. Optimal control theory

Optimal control theory (OCT) can be used to calculate the shape of laser pulses that efficiently drive a desired transition. We will employ it here to determine the most efficient stabilization between an initial molecular wave packet and deeply bound levels in the ground electronic state. In principle, this problem is completely controllable such that perfect population transfer can be realized. However, constraints such as limited pulse duration, spectral bandwidth, and pulse intensity will compromise the stabilization process, reducing the transfer efficiency.

The control problem is defined by minimization of the functional

$$J = J_T + \int_0^T g[\epsilon(t)]dt, \tag{7}$$

where the first term denotes the final-time T target and the second one denotes the intermediate-time costs. The final-time target J_T can be chosen to correspond to a single state-to-state transition J_T^{ss} or to the transition into a manifold of final states, J_T^{sm}. For a single state-to-state transition from an initial state $|\Psi_{\text{in}}\rangle$ to a target state, here a vibrational level of the electronic ground state, v'', the final-time functional is written as

$$J_T^{ss} = 1 - |\langle\Psi_{v''}|\hat{\mathsf{U}}(T,0;\epsilon)|\Psi_{\text{in}}\rangle|^2. \tag{8}$$

$\hat{\mathsf{U}}(T,0;\epsilon)|\Psi_{\text{in}}\rangle$ represents the formal solution of the time-dependent Schrödinger equation with $\hat{\mathsf{U}}(T,0;\epsilon)$ being the time evolution operator. J_T^{ss} corresponds to the overlap of the initial state, propagated to the final time T under the action of the laser field $\epsilon(t)$, with the target state. Optimizing a transition into a manifold of states is expressed by the functional

$$J_T^{sm} = 1 - \sum_{v''=v''_{\text{min}}}^{v''_{\text{max}}} |\langle\Psi_{v''}|\hat{\mathsf{U}}(T,0;\epsilon)|\Psi_{\text{in}}\rangle|^2, \tag{9}$$

where any vibrational level of the electronic ground state with quantum number between v''_{min} and v''_{max} can be populated at the final time. Once the optimum is reached, both functionals J_T^{ss} and J_T^{sm} take the value zero.

The intermediate-time cost, $g[\epsilon(t)]$ can in general depend on both the state and the field. Here, we restrict the dependence to one on the laser field only, where we ask that optimization does not change or changes only minimally the integrated pulse energy

$$g[\epsilon(t)] = \frac{\lambda}{S(t)} \sum_{a=\{\text{Re},\text{Im}\}} \left(\epsilon_a^{(k+1)}(t) - \epsilon_a^{(k)}(t)\right)^2, \tag{10}$$

with k labeling the iteration step [55]. The shape function $S(t)$, $S(t) = \sin^2(\pi t/T)$, enforces a smooth switch on and off of the field and λ is a weight. Note that the laser field is complex since we employ the rotating-wave approximation. A nonzero phase indicates a relative phase with respect to the laser-pulse peak center or, in the spectral domain, with respect to the phase of the central laser frequency.

Using the linear variant of Krotov's method [56,57], the update equation for the laser field at iteration step $k+1$ can be derived:

$$\begin{aligned}
&\text{Re}\left[\epsilon^{(k+1)}(t)\right] \\
&\quad = \text{Re}\left[\epsilon^{(k)}(t)\right] - \frac{S(t)}{2\lambda}\text{Im}\Bigg[\sum_{v''=v''_{\text{min}}}^{v''_{\text{max}}} \langle\Psi_{\text{in}}|\hat{\mathsf{U}}^\dagger(T,0;\epsilon^{(k)})|\Psi_{v''}\rangle \\
&\qquad \times \langle\Psi_{v''}|\hat{\mathsf{U}}^\dagger(t,T;\epsilon^{(k)})\frac{\partial\hat{\mathsf{H}}_{\text{dump}}}{\partial\text{Re}[\epsilon]}\bigg|_{\epsilon^{(k+1)}}\hat{\mathsf{U}}(t,0;\epsilon^{(k+1)})|\Psi_{\text{in}}\rangle\Bigg],
\end{aligned} \tag{11}$$

and analogously for $\text{Im}[\epsilon^{(k+1)}(t)]$, where $\hat{\mathsf{U}}(t,0;\epsilon^{(k+1)})|\Psi_{\text{in}}\rangle$ is the initial state forward propagated to time t under the action of the new field, $\epsilon^{(k+1)}$, and $\hat{\mathsf{U}}(t,T;\epsilon^{(k)})|\Psi_{v''}\rangle$ denotes the target state(s) backward propagated to time t under the action of the old field, $\epsilon^{(k)}$. The derivative of the Hamiltonian with respect to the field yields a matrix having as its elements all the transition dipole moments d_i [cf. Eq. (4)]. Optimization of the functionals J_T^{ss} or J_T^{sm} requires repeated forward and backward propagations of the initial and target states.

III. EXCITED-STATE WAVE PACKET REPRESENTING INITIAL STATE FOR STABILIZATION

The initial wave packet for the stabilization step is created by the photoassociation pulse. The simplest pulse that can be employed for the three-photon photoassociation is a transform-limited (TL) Gaussian pulse. The intensity of the laser pulse is chosen to be in the perturbative weak-field regime, where the composition of the photoassociated wave packet reflects the bandwidth of the laser pulse combined with the vibrationally averaged three-photon electric dipole transition moments between the initial scattering state and the excited-state vibrational levels below $^2S(5s) + {}^2P_{1/2}(6p)$ dissociation limit. A pulse duration of 4 ps full width at half maximum (FWHM) is considered, corresponding to a spectral bandwidth of 3.7 cm^{-1}. The pulse is red detuned by 12 cm^{-1} from the $^2S(5s) \longrightarrow {}^2P_{1/2}(6p)$ atomic three-photon transition. In order to utilize broadband femtosecond laser pulses, more elaborate pulse shapes will be required that suppress the excitation of atoms [22] while possibly maximizing free-to-bound transitions. However, the general features of the photoassociated wave packet are determined by the three-photon matrix elements. They are the largest close to the $^2S(5s) + {}^2P_{1/2}(6p)$ dissociation limit, corresponding to a photoassociation window at interatomic separations between

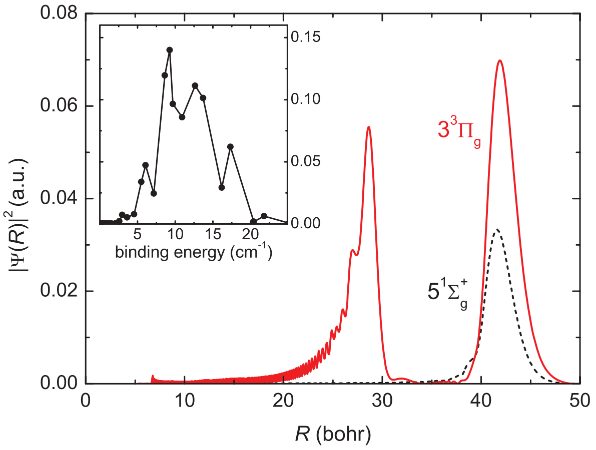

FIG. 4. (Color online) Wave packet obtained after photoassociation with a transform-limited pulse. The pulse duration is 4 ps (FWHM) and a snapshot 2.5 ps after the photoassociation pulse maximum is shown. At this time, the $(6)\,^1\Sigma_g^+$ component is insignificant and not visible on the scale of this figure. Inset shows the decomposition of the wave packet onto the vibrational levels of the coupled $(5)\,^1\Sigma_g^+$, $(6)\,^1\Sigma_g^+$, and $(3)\,^3\Pi_g$ states.

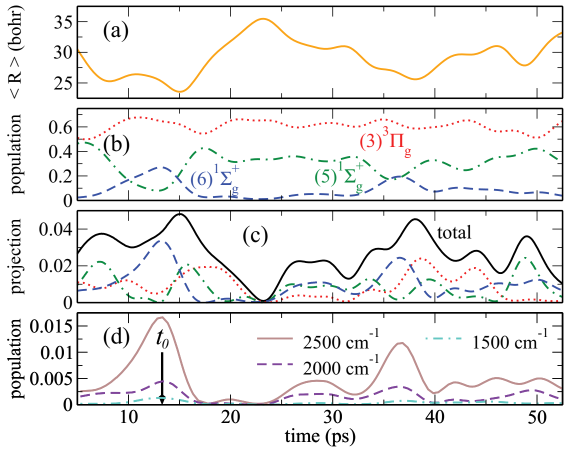

FIG. 5. (Color online) (a) Time evolution of the average bond length of the wave packet. (b) Time evolution of the populations of the $(5)\,^1\Sigma_g^+$, $(6)\,^1\Sigma_g^+$, and $(3)\,^3\Pi_g$ components of the wave packet. (c) Projection of the time-dependent wave packet and its $(5)\,^1\Sigma_g^+$, $(6)\,^1\Sigma_g^+$, and $(3)\,^3\Pi_g$ components onto all vibrational levels of the $X\,^1\Sigma_g^+$ ground electronic states with binding energies up to 1000 cm^{-1}. (d) Population of the $X\,^1\Sigma_g^+$ component of the wave function after stabilization with a TL pulse vs time delay between photoassociation and stabilization pulse for three different detunings, taken with the respect to the $^2P_{1/2}(6p) \longrightarrow {}^2S(5s)$ two-photon transition. The stabilization pulse has a FHWM of 100 fs and an integrated pulse energy of 25.4 nJ corresponding to the weak-field regime. The arrow indicates $t_0 = 13.3$ ps chosen as the time delay between the photoassociation and stabilization pulse peaks.

$30a_0$ and $50a_0$. Transition moments to the vibrational levels detuned by more then 30 cm^{-1} from the $^2S(5s) + {}^2P_{1/2}(6p)$ threshold, corresponding to photoassociation windows at shorter interatomic separations, are significantly smaller. The most important contributions to the photoassociated wave packet will therefore remain the same as in our simple example. It could turn out that, using coherent control, photoassociation into wave packets with binding energies larger than 30 cm^{-1} becomes feasible. In this case, the stabilization of the photoassociated molecules becomes easier, and their faster vibrational dynamics and larger Franck-Condon factors to the deeply bound $X\,^1\Sigma_g^+$ vibrational levels will only improve the predictions of the present study. The initial wave packet for the stabilization step is plotted in Fig. 4. The inset shows the decomposition of the wave packet onto the vibrational levels of the coupled $(5)\,^1\Sigma_g^+$, $(6)\,^1\Sigma_g^+$, and $(3)\,^3\Pi_g$ states. The binding energy of the wave packet amounts to 11.55 cm^{-1}. The snapshot shown in Fig. 4 is taken 2.5 ps after the maximum of the photoassociation pulse (i.e., before the pulse is over). At this time, the Gaussian character of the wave packet is still apparent, while at later times the strongly anharmonic shape of the potential-energy curves leads to strong wave-packet dispersion. Note that the photoassociated wave packet shows a truly mixed character with about 65% of its norm residing on the $(3)\,^3\Pi_g$ triplet component and 35% on the $(5)\,^1\Sigma_g^+$ singlet component. This is despite the fact that electric dipole transitions are allowed only between the atomic pair in the $a^3\Sigma_u^+$ lowest triplet state and the $(3)\,^3\Pi_g$ triplet component of the coupled electronically excited manifold dissociating into $^2S(5s) + {}^2P_{1/2}(6p)$ and illustrates the strong spin-orbit coupling. The role of the spin-orbit coupling is further evidenced by the double-peak structure of the wave packet with the short-range peak corresponding to the outer turning point of the $(3)\,^3\Pi_g$ potential and the long-range peak reflecting the outer turning point of the $(5)\,^1\Sigma_g^+$ potential. The importance of the strong resonant spin-orbit coupling for the stabilization of photoassociated molecules has been discussed extensively [29–34,58]. In the present study, we will not only use it for improved transition matrix elements to deeply bound ground-state levels, but also to convert an atom pair colliding in the triplet state to singlet molecules [35]. The initial wave packet propagates toward shorter interatomic separations under the influence of the excited-state potentials. At large interatomic separations, the potential-energy curve of the $(5)\,^1\Sigma_g^+$ state displays a strong $-1/R$ ion-pair character. The singlet-triplet oscillations are analyzed in Fig. 5(a) displaying the singlet and triplet components of the wave packet evolving after the photoassociation pulse in the manifold of electronically excited states. The population of the $(3)\,^3\Pi_g$ triplet component oscillates around 60%, whereas the population of the $(6)\,^1\Sigma_g^+$ component, that was absent just after photoassociation, reaches a maximum of 27% at $t = 12.7$ ps after the peak of the photoassociating pulse. A second maximum of the $(6)\,^1\Sigma_g^+$ component is observed after a period of 20.1 ps and a third one after another 36.2 ps. The times at which the $(6)\,^1\Sigma_g^+$ component reaches maximal values can be interpreted as moments when the wave packet arrives at its shortest distance and is reflected from the innermost repulsive short-range wall. This observation is confirmed by calculating the average bond length of the wave packet, shown in Fig. 5(b), which allows us to estimate the revival time of the present wave packet to be between 20 and 30 ps. This estimate agrees with the range of revival times, defined by $T_{\mathrm{rev}}(v) = 2h/|E_{v+1} + E_{v-1} - 2E_v|$ [59], for the vibrational levels v that make up a wave packet with binding energies close to 12 cm^{-1}.

The knowledge of the revival time of the wave packet is useful for the interpretation of the projections of the time-dependent wave packet, $|\langle\Psi_{\text{in}}(t)|v''\rangle|^2$, onto the vibrational levels v'' of the $X^1\Sigma_g^+$ ground electronic state, shown in Fig. 5(c) for all ground-state levels with binding energies up to $1000\,\text{cm}^{-1}$. These projections are largest when the wave packet is localized at its inner turning point [cf. Fig. 5(b)]. The time at which the projections show maxima correspond to optimal time delays between photoassociation and stabilization pulse. The times in between these maxima are given by the revival time. However, the transition probability does not only depend on the overlap of initial and final wave function, but also on the dipole moments and the topology of the intermediate state surfaces and their coupling. This is illustrated by the difference between Figs. 5(c) and 5(d) with Fig. 5(b) showing the calculated population on the $X^1\Sigma_g^+$ ground electronic state as a function of the time delay between photoassociation and stabilization pulse for three different detunings of the stabilization pulse. The $X^1\Sigma_g^+$ population is obtained by solving the time-dependent Schrödinger equation for a weak TL stabilization pulse. The positions of the maxima and minima of the final $X^1\Sigma_g^+$ state population correspond to those of the projection of the $(6)\,^1\Sigma_g^+$ component [dashed blue line in Fig. 5(c)] rather than the total projection [black line in Fig. 5(c)]. This suggests that the transition from the $(6)\,^1\Sigma_g^+$ component is the most important one in the stabilization process.

Based on the time-dependence of the projection and the stabilization probability analyzed in Fig. 5, we choose $t_0 = 13.3$ ps for the time delay, taken between the peak of the photoassociating pulse and the center of all pulses used in the following sections.

IV. STABILIZATION TO ELECTRONIC GROUND STATE WITH TRANSFORM-LIMITED AND LINEARLY CHIRPED PULSES

We first study transform-limited and linearly chirped stabilization pulses in order to understand the role of the basic pulse parameters such as intensity and spectral width and to investigate dynamical effects. By comparing projections and actual final-state populations in the previous section, we have shown that a simple two-photon Franck-Condon principle does not correctly capture the stabilization dynamics. A less simplified picture is obtained by taking the structure of the vibrational levels in the initial, intermediate, and final electronic states fully into account, neglecting strong-field effects and a dynamical interplay between pulse and spin-orbit couplings. Specifically, in the weak-field regime and for TL pulses, the probability of the resonant two-photon transition is obtained by perturbation theory. It is determined by the effective two-photon transition moment,

$$D(v'') = \sum_{v'} \left| \sum_{j=2,3,4} \langle\Psi_{\text{in}}|d_j|v'\rangle\langle v'|d_1|v''\rangle \right| e^{\Delta\omega_{v'}^2/2\sigma_\omega^2}, \tag{12}$$

where $\langle\Psi_{\text{in}}|d_j|v'\rangle = \sum_{i,i'}\int \Psi_{\text{in}}^i(R)^* d_j(R)\chi_{v'}^{i'}(R)dR$ denotes the electric transition dipole moment between the initial wave packet with components i in the $(5)\,^1\Sigma_g^+$, $(6)\,^1\Sigma_g^+$, and $(3)\,^3\Pi_g$ manifold and the intermediate vibrational levels v' with components i' in the excited $A^1\Sigma_u^+$ and $b\,^3\Pi_g$. Correspondingly, $\langle v'|d_1|v''\rangle$ is the electric transition dipole moment between the intermediate levels v' of the $A^1\Sigma_u^+$ and $b\,^3\Pi_g$ states and the final ground $X^1\Sigma_g^+$ state vibrational level v''. The exponent accounts for the bandwidth of the laser pulse, σ_ω, and the detuning of the intermediate levels from the laser frequency,

$$\Delta\omega_{v'} = \omega_{^2P_{1/2}(5p)} - \omega_{v'} + \omega_{v''} - \omega_L. \tag{13}$$

The laser frequency ω_L is chosen such that the two-photon transition is resonant for the initial wave packet and the final level v'', $\omega_L = (\omega_{^2P_{1/2}(6p)} - \omega_{\text{in}} + \omega_{v''})/2$. Here, ω_{in} denotes the binding energy of the initial wave packet, defined to be positive, and $\omega_{^2P_{1/2}(np)}$ is the excitation energy of the $^2P_{1/2}(np)$ atomic level. The spectral width is given in terms of the FWHM of the time profile of the pulse τ, $\sigma_\omega = 2\sqrt{2\ln(2)}/\tau$. The two-photon transition moments, defined by Eq. (12), are shown in Fig. 6 for all vibrational levels v'' of the $X^1\Sigma_g^+$ ground electronic state. The large peak around a binding energy of $2650\ \text{cm}^{-1}$ indicates that stabilization of the excited-state wave packet to levels with binding energies in this range is most efficient. The peak maximum in Fig. 6 corresponds to a transition to the vibrational level $v'' = 23$, with a binding energy $E_{v''} = 2651\,\text{cm}^{-1}$. This suggests that the level $v'' = 23$ might be a good choice for the target in the state-to-state optimization of stabilization process below in Sec. V. A standard choice of 100 fs pulse duration for the TL pulse, corresponding to a spectral width of about $150\ \text{cm}^{-1}$ FWHM

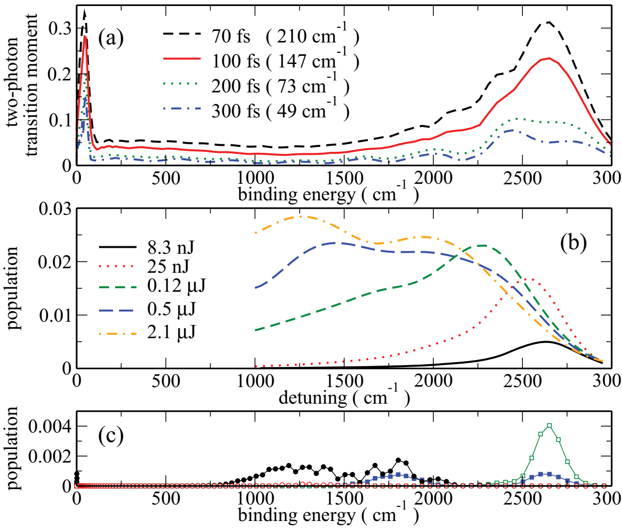

FIG. 6. (Color online) (a) Resonant two-photon transition moments defined by Eq. (12) vs binding energy of the target $X^1\Sigma_g^+$ state levels v'' for four different pulse durations or spectral widths, respectively. (b) Final population of the $X^1\Sigma_g^+$ state after a TL 100 fs pulse vs pulse detuning, taken with the respect to the $^2P_{1/2}(6p) \longrightarrow {}^2S(5s)$ atomic two-photon transition, for five different integrated pulse energies. (c) Vibrational decomposition of the $X^1\Sigma_g^+$ component of the wave function after stabilization with TL 100 fs pulses with different pulse energies and detunings with the respect to $^2P_{1/2}(6p) \longrightarrow {}^2S(5s)$ atomic two-photon transition: □ 25.4 nJ and $2650\ \text{cm}^{-1}$, ■ 2.06 μJ and $2650\ \text{cm}^{-1}$, ○ 25.4 nJ and $1240\ \text{cm}^{-1}$, ● 2.06 μJ and $1240\ \text{cm}^{-1}$.

is sufficient to address a broad distribution of target vibrational levels in the $X^1\Sigma_g^+$ state.

The integrated pulse energy is given by

$$E = \varepsilon_0 c A \int_0^\infty |\epsilon(t)|^2 dt, \tag{14}$$

with $\epsilon(t)$ being the laser field, $A = \pi r^2$ being the area which is covered by the laser ($r = 50$ μm was assumed), c being the speed of light, and ε_0 being the dielectric constant. We use the integrated pulse energy rather than the peak intensity of the pulse since, independently of the pulse duration, it quantifies the energy pumped into the molecule.

The two-photon transition probability can be predicted from the effective two-photon transition moment [cf. Eq. (12) and Fig. 6] only in the weak-field regime when dynamic Stark shifts and other time-dependent effects do not play any role. The dependence of the two-photon transition probability on the pulse intensity and detuning,

$$\Delta\omega_L = 2\omega_L - \omega_{^2P_{1/2}(6p)}, \tag{15}$$

is illustrated in Fig. 6(b). The pulse duration is kept fixed at 100 fs FWHM. For weak and intermediate pulse intensities, with the integrated pulse energy corresponding to 8.3 and 25.4 nJ, the final $X^1\Sigma_g^+$ ground-state population as a function of the pulse detuning reflects the shape of the effective two-photon transition moment [Fig. 6(a)]. On the other hand, the final $X^1\Sigma_g^+$ population decreases for the detuning corresponding to the maximum of the two-photon transition moment and increases for smaller detunings when the integrated pulse energy is increased. This observation is rationalized in terms of the strong dynamic Stark shift by analyzing the vibrational distribution of the final $X^1\Sigma_g^+$ state population in Fig. 6(c) for a detuning $\Delta\omega_L = 2650$ cm^{-1}, corresponding to the maximum of the two-photon transition moment in Fig. 6(a). When increasing the integrated pulse energy from 25.4 nJ to 2 μJ (i.e., from the intermediate- to the strong-field regime), two peaks are observed in the vibrational distribution rather than a single Gaussian around the binding energy of $v'' = 23$, reflecting the bandwidth of the pulse. In the strong-field regime, one peak of the vibrational distribution is still located around the binding energy of the resonant level, while the second one is shifted by 800 cm^{-1} to smaller binding energies. This is due to the positive differential Stark shift caused by the coupling to the intermediate states, which indeed increases the energy separation between ground and excited states by about 800 cm^{-1}. The dynamic Stark shift of the ground-state vibrational level v'' is estimated according to

$$\omega_S^{v''} = -\frac{1}{2}|\epsilon(t)|^2 \sum_{v''} |\langle v''|\hat{\mathsf{d}}_{\mathsf{e}}|v'\rangle|^2 \frac{\omega_{v'v''}}{\omega_{v'v''}^2 - \omega_L^2}, \tag{16}$$

where $\langle v''|\hat{\mathsf{d}}_{\mathsf{e}}|v'\rangle$ is the electric transition dipole moment, $\omega_{v'v''}$ is the transition frequency between levels v' and v'', and ω_L denotes the laser frequency. Figure 6(c) compares the final-state vibrational distribution for two different detunings of the stabilization pulse, $\Delta\omega_L = 2650\,\text{cm}^{-1}$ corresponding to the peak of the two-photon transition probability for weak and intermediate fields [black dotted and red solid curves in Fig. 6(b)] and $\Delta\omega_L = 1240\,\text{cm}^{-1}$ corresponding to the peak of the two-photon transition probability for strong fields [black dot-dashed curve in Fig. 6(b)]. Inspection of the vibrational distributions in Fig. 6(c) reveals that, for $\Delta\omega_L = 1240\,\text{cm}^{-1}$ and 2 μJ integrated pulse energy, a peak at binding energies larger than the detuning appears. Also, this peak is caused by the differential Stark shift which this time is negative, decreasing the energy separation between ground and excited states by about 600 cm^{-1}. In the weak- and intermediate-field regimes, almost no population is transferred for $\Delta\omega_L = 1240$ cm^{-1} [red empty circles in Fig. 6(c)], confirming a strong-field effect.

The total population that is transferred by a TL pulse, with 100 fs FWHM and a detuning in the range of 2500 to 2600 cm^{-1}, from the initial wave packet to the $X^1\Sigma_g^+$ ground electronic state amounts to up to 1.7% in the weak- and intermediate-field regimes. For strong fields, up to 2.9% of the population can be transferred for detunings between 1000 and 1500 cm^{-1} and pulse energies above 1 μJ. The subsequent analysis is restricted to pulses with detunings between 2500 and 2650 cm^{-1}, corresponding to the maximum of the effective two-photon transition moment where the smallest pulse intensities should be required. As apparent from Fig. 6, the dynamic Stark shift is detrimental to efficient population transfer by the stabilization pulse. One option to increase the integrated pulse power while keeping the maximum field intensity and thus the dynamic Stark shift small is to consider a train of short TL pulses. A second option is given by chirping the pulse. The efficiency of the two-photon population transfer to the electronic ground with the first option, a train of 100 fs TL pulses delayed relative to each other by 200 fs and with a sinusoidal envelope, is analyzed in Fig. 7. While increasing the pulse energy of a 100 fs pulse does not improve the population transfer to the electronic ground state beyond 1.7%, a train of pulses yields up to about 6% for pulse energies that are still in the nJ range. The population transfer with a train of short pulses can be interpreted as the cumulative result of many single transitions that accumulate amplitude in the $X^1\Sigma_g^+$ ground state. Using a train of pulses instead of a single pulse with the same bandwidth, one can produce 3.5 times more ground-state molecules. Figure 7 thus confirms that the Stark shift is responsible for the comparatively inefficient population transfer observed for TL pulses. From the coherent control of atomic transitions using strong fields, it is known that the influence of the dynamic Stark shift can be compensated by chirping the pulse [14,15]. We investigate in Fig. 8(a), which shows the final ground-state population vs chirp rate for increasing pulse energy, whether this approach works also for molecular transitions. We use a positive chirp to correct the influence of the dynamic Stark shift since the differential Stark shift for stabilization to vibrational levels with binding energies close to 2650 cm^{-1} is positive. Chirping a weak-field pulse (black dot-dashed curve) deteriorates the population transfer. When more energetic pulses are used, chirping increases the final $X^1\Sigma_g^+$ state population from 1.5% for unchirped pulses to almost 9% for the best-chirped pulses. In total we find that chirping the pulse improves the stabilization process and enhances the amount of ground-state population by a factor of about six. Figure 8(b) showing the final-state

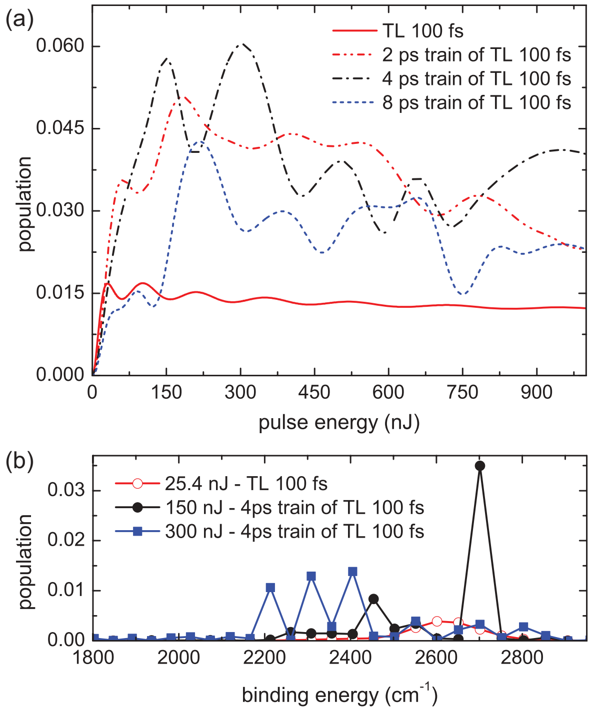

FIG. 7. (Color online) (a) $X^1\Sigma_g^+$ state population after a 100 fs TL pulse (solid line) and a train of 100 fs TL pulses (dashed and dotted lines) vs integrated pulse energy. (b) $X^1\Sigma_g^+$ state vibrational distribution after stabilization with a 100 fs TL pulse and 4 ps train of 100 fs TL pulses. The pulse detuning is 2500 cm^{-1} taken with the respect to the $^2P_{1/2}(6p) \longrightarrow {}^2S(5s)$ atomic two-photon transition.

vibrational distribution confirms that the same mechanism as in the atomic case is at work [14,15]: When increasing the pulse energy from 25.4 to 300 nJ without chirping the pulse, a second peak shifted by 500 cm^{-1} appears. The energies of the levels of this second peak correspond exactly to the detuning corrected by the Stark shift. A linear chirp introduces a time-dependent instantaneous frequency of the pulse, $\omega(t) = \omega_L + \chi t/2$, with χ being the temporal chirp rate. When chosen correctly, the chirp compensates the phase that the molecules accumulate due the Stark shift and thus prevents the transition to shift out of resonance. This leads to the strong enhancement of the stabilization efficiency observed in Fig. 8.

Our investigation of the stabilization dynamics under TL and linearly chirped pulses shows that simply replacing a strong TL pulse by a train of pulses with the same total integrated pulse energy or linearly chirping the pulse can enhance the stabilization probability from 1% up to 9%. The reason for the enhancement is given by the weaker Stark shifts for smaller peak intensities and compensation of the phase accumulated due to the Stark shift by a linear chirp. In the following section we employ optimal control theory to calculate the optimum detunings and pulses shapes. This allows us to determine the maximum number of ground-state molecules that can be produced for a given integrated pulse energy.

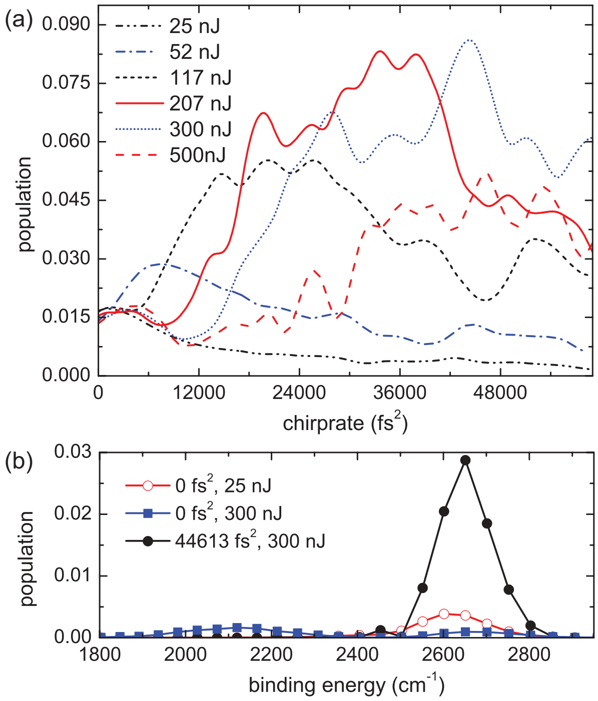

FIG. 8. (Color online) (a) Final $X^1\Sigma_g^+$ state population after linearly chirped pulses with a TL FWHM of 100 fs vs chirp rate for different pulse energies. (b) $X^1\Sigma_g^+$ state vibrational distribution after stabilization with a weak TL pulse, a TL pulse, and a chirped strong pulse. The pulse detuning is 2500 cm^{-1} taken with the respect to the $^2P_{1/2}(6p) \longrightarrow {}^2S(5s)$ atomic two-photon transition.

V. STABILIZATION TO ELECTRONIC GROUND STATE WITH OPTIMALLY SHAPED PULSES

We employ the optimization algorithm described in Sec. II C to find those laser pulses that stabilize the initial wave packet most efficiently to the $X^1\Sigma_g^+$ electronic state. The final $X^1\Sigma_g^+$ state population, shown in Fig. 9(a), converges smoothly to the maximal value that can be obtained with a given pulse duration, displayed in Fig. 9(b). The maximum stabilization probability for a pulse duration of 1 ps is 14%. Increasing the pulse duration, the stabilization probability reaches 26% for 2 ps pulses and 67% for 10 ps pulses. The integrated pulse energies of the optimized pulses vary between 80 and 150 nJ. This is two to three times smaller than the integrated pulse energies for the trains of pulses and the linearly chirped pulses discussed in Sec. IV. The guess pulse for the optimizations shown in Fig. 9 is a TL pulse with a pulse duration of 100 fs and integrated pulse energy of 10 nJ. For all the results presented here, the state-to-manifold-of-states functional, Eq. (9), was employed. The results obtained by using the state-to-state functional, Eq. (8), do not differ significantly. In particular, the same bounds on the maximum stabilization efficiencies are observed. However, for the state-to-state functional, the optimizations were found to converge slower. This is easily rationalized in terms of a single state being a more restrictive optimization target than a manifold. The integrated energy of the optimal pulses presented in Fig. 9(b) does not depend strongly on the

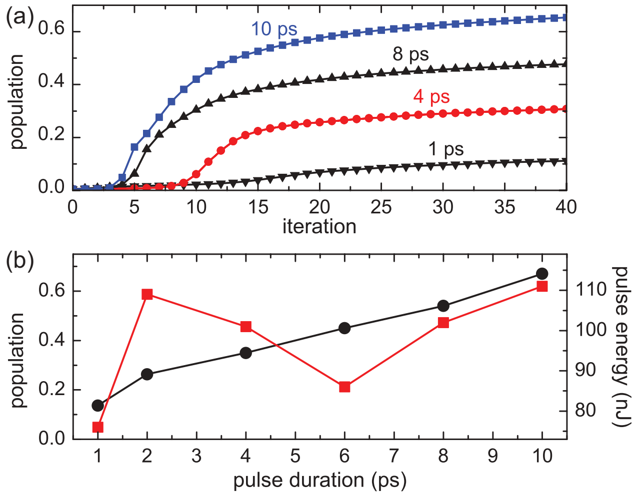

FIG. 9. (Color online) (a) Final $X^1\Sigma_g^+$ state population after optimized pulses of different pulse duration vs number of iteration steps. (b) Final $X^1\Sigma_g^+$ state population (left scale, black circles) and corresponding pulse energy (right scale, red squares) vs pulse duration. The values were collected after 50 iterations, starting with the same weak-field guess pulse ($E = 10$ nJ) and using the same weight, $\lambda = 400$ in all optimizations.

optimal pulse duration. The slightly oscillatory behavior of the integrated pulse energy as a function of pulse duration is observed irrespective of the shape and energy of the guess pulse and the weight λ.

The fact that the maximum population transfer to the $X^1\Sigma_g^+$ state is clearly less than 100% is due to the pulses being too short to drive the complete wave packet to the ground state [60]. When the pulse duration is much shorter than the time scale of the vibrational motion and spin-orbit oscillations, then only that part of the wave packet that shows a favorable overlap with the target state during the optimization window is transferred. For example, the pulse with 1 ps duration essentially reflects the overlap of the initial wave packet. By increasing the pulse duration [cf. Fig. 9(b)], the stabilization efficiency increases monotonically. A stabilization probability of 100% is expected once the pulse duration is longer than the revival time of the wave packet, estimated above to be between 20 and 30 ps. In fact, optimizations with pulse durations of 20 and 30 ps yield stabilization efficiencies of 93% and 99%, respectively, with pulse energies below 150 nJ. However, we restrict our analysis to pulse durations up to 10 ps since stretching a TL 100 fs pulse by more than a factor of 100 due to pulse shaping is not realistic. Analyzing the time evolution of the population on each of the electronic states during an optimized pulse of 10 ps pulse duration, the molecules are found to first accumulate in the intermediate $^1\Sigma_u^+$ and $b\,^3\Pi_u$ states before being dumped to the $X^1\Sigma_g^+$ electronic ground state. The example of an optimized pulse with pulse duration of 8 ps is presented in Fig. 10. Inspection of the optimized pulse during a short interval of 400 fs [Fig. 10(b)], reveals that each peak of the pulse amplitude is correlated to a change of the temporal phase by π. The spectrum, Fig. 10(c), displays two pronounced peaks with maxima at ± 400 cm^{-1} with respect to the central

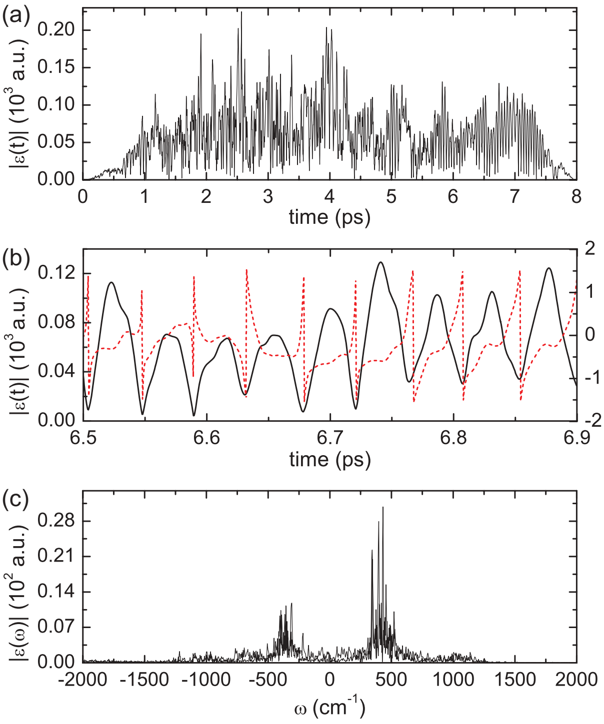

FIG. 10. (Color online) Temporal envelope (a) and spectrum (c) of an optimized pulse. (b) Envelope (left scale, solid black line) and temporal phase (right scale, red dashed line) of the optimized pulse in a short time interval.

laser frequency. The disappearance of the central frequency during the optimization and appearance of two slightly detuned frequencies is somewhat surprising since the central frequency was chosen to maximize the effective two-photon transition moment. There are two possibilities to rationalize this result of the optimization: Either the detuning shifted by the additional 400 cm^{-1} is better and should be chosen for the guess pulse, or the absorption of two photons with different energies is more optimal than that of two identical photons. The latter explains the observed optimal spectrum: Analysis of the electric transition dipole moment between the initial wave packet and the intermediate vibrational levels, $\langle \Psi_{\rm in}|\hat{\mathsf{d}}_{\rm e}|v'\rangle$, reveals that it takes its maximal value for levels v' that are detuned from the frequency corresponding to the maximum of the effective two-photon transition moment, Eq. (12), by 460 cm^{-1}. The electric transition dipole moment between the intermediate and ground-state vibrational level, $\langle v'|\hat{\mathsf{d}}_{\rm e}|v''\rangle$, attains its maximum for a transition frequency that is smaller than the laser frequency corresponding to the maximum of the effective two-photon transition moment by 250 cm^{-1}. Note that the transition moments for absorption of the first photon, $\langle \Psi_{\rm in}|\hat{\mathsf{d}}_{\rm e}|v'\rangle$, are about 7 times smaller than those for absorption of the second photon, $\langle v'|\hat{\mathsf{d}}_{\rm e}|v''\rangle$. The effective two-photon transition moment is obtained as a compromise of the two one-photon transition moments [cf. Eq. (12)]. Allowing for two photons of different energy in the calculation of the effective two-photon transition moment, we still find a peak for a ground-state binding energy of 2650 cm^{-1}, which is at best 40% higher when energies of photons are detuned by ± 390 cm^{-1}. It corresponds to the transition frequency from the initial wave packet to the intermediate state being 390 cm^{-1} larger and that between the intermediate state and the ground electronic state being 390 cm^{-1} smaller than the frequency for a transition with two identical photons. Equipped with this information, we can construct a guess pulse that is the sum of two TL pulses with their central frequencies separated by 780 cm^{-1}. In this case, half of the integrated guess pulse energy is sufficient to reach the same initial stabilization probability, reflecting the stronger effective two-photon transition moment. Optimization with such a guess pulse converges faster and the final integrated pulse energy of the optimized pulse is smaller (data not shown) but the bound for the stabilization efficiency, Fig. 9, remains in place. The spectrum of the optimized pulse with two peaks separated by 780 cm^{-1} is very similar to the one shown in Fig. 10, irrespective of the guess pulse central frequency. In particular, the width of each of the peaks roughly corresponds to the bandwidth of a TL 100 fs pulse.

Optimization of the stabilization pulse reveals that the upper bound of the stabilization efficiency, found to be 9% for linearly chirped pulses, can be increased up to 67% when a TL pulse of 100 fs pulse duration is shaped and stretched to 10 ps. This is significantly more efficient than any existing proposal for short-pulse photoassociation [5,61,62]. At the same time, the integrated pulse energies of the optimized pulses are below 150 nJ, two to three times less than those found for the best linearly chirped pulses or trains of TL pulses in Sec. IV. The shape of the optimized pulse is comparatively simple, characterized by a sequence of short pulses with linear and quadratic chirps.

VI. SUMMARY AND CONCLUSIONS

Based on state-of-the-art *ab initio* calculations, we have studied the optical production of Rb_2 molecules in their electronic ground state using multiphoton transitions that are driven by short laser pulses. Our model includes not only accurate potential-energy surfaces but also spin-orbit couplings, Stark shifts, and transition matrix elements. We have employed a nonperturbative treatment of the light-matter interaction which is crucial to capture the strong-field effects that often accompany multiphoton transitions.

Our proposal for the optical production of molecules using shaped femtosecond laser pulses that drive multiphoton transitions consists, in its first step, of nonresonant three-photon photoassociation of atom pairs colliding in their triplet state. A three-photon transition allows access of electronic states that vary as $1/R^3$ at long range, providing comparatively large free-to-bound transition matrix elements [22]. Strong spin-orbit interaction allows for triplet-to-singlet conversion. The stabilization pulse, time delayed with respect to the photoassociation pulse, transfers the photoassociated wave packet to the electronic ground state in a resonant two-photon transition proceeding via the $A\,^1\Sigma_u^+\ b\,^3\Pi_u$ manifold. It benefits from the intricate excited-state wave packet dynamics resulting from coupled vibrational dynamics in states with partially ion-pair character and singlet-triplet oscillations due to the spin-orbit interaction.

We have studied the transfer of the excited-state wave packet to the electronic ground state using transform-limited, linearly chirped and optimally shaped laser pulses. Linearly, chirped pulses were found to perform much better, by almost an order of magnitude, than transform-limited pulses. This is due to large Stark shifts which drive the transition off resonance for transform-limited pulses. We have confirmed that a strong-field control scheme known for atomic transitions, with a linear chirp compensating the phase accumulated due to the Stark shift [14,15], can also be successfully employed for molecular transitions. In this case, the chirp rate cannot be calculated analytically but needs to be determined numerically.

Surprisingly, for optimally shaped laser pulses, the integrated pulse energy was found to be significantly lower than that of the best transform-limited and linearly chirped pulses, while yielding a much better stabilization efficiency. This is due to the fact that the transform-limited and linearly chirped laser pulses were chosen based on an effective two-photon transition matrix element assuming equal transition frequencies of both photons. Optimization reveals that a two-photon transition with two slightly different transition frequencies allows us to employ two one-photon transitions with significantly larger transition matrix elements.

Overall, the stabilization efficiency is limited by somewhat less than 70% for transform-limited 100 fs laser pulses that are stretched to 10 ps. More than 90% transfer efficiency becomes possible by stretching the pulse to 20 ps. The target level in the electronic ground state that is reached by these stabilization pulses is located more than half way down the ground-state potential well, with a binding energy of about 2600 cm^{-1}. The stabilization efficiencies reported here have to be compared to 20%, respectively 50%, for stabilization with chirped pulses in the presence of strong spin-orbit interaction to very weakly bound levels [5,61] and to a few percent for stabilization to the vibrational ground state using engineered excited-state dynamics [62]. In contrast to these earlier studies, with the current scheme it becomes possible to convert almost all of the weakly bound photoassociated molecules into truly bound ground-state molecules from where a single subsequent Raman step is sufficient to transfer these molecules into their vibronic ground state. Such a significant improvement for comparatively short stabilization pulses is afforded by a speedup of the dynamics due to the partial ion-pair character of the excited-state potential curves and population trapping at short interatomic separations due to the strong spin-orbit interaction. It emphasizes the usefulness of multiphoton transitions, which allow us to access these electronic states, for the photoassociation of ultracold atoms.

Multiphoton transitions, moreover, allow the utilization of the full bandwidth of a femtosecond pulse for photoassociation and stabilization. They also provide more flexibility with respect to the transition frequencies that can be addressed. The basic features of femtosecond laser pulses—their broad bandwidth and pulse shaping capabilities—can then be used to full advantage. Our results thus pave the way toward the coherent control of photoassociation at very low temperature. They are not restricted to rubidium but rather are applicable to any molecule that shows the main features of the dynamics studied here—an ion-pair potential that is coupled to covalent states and strong spin-orbit interaction.

Future work will consider optimization of the photoassociation pulse. This represents a nontrivial control problem since the initial state of photoassociation is the thermally populated continuum of scattering states. While a thermal ensemble is inherently incoherent, quantum effects are already perceptible due to the low temperature. It will be interesting to see whether an optimally shaped pulse can make use of the enhanced quantum purity and the presence of correlations at low temperature.

ACKNOWLEDGMENTS

We would like to thank Ronnie Kosloff for many fruitful discussions. Financial support from the Polish Ministry of Science and Higher Education through the project N N204 215539 is gratefully acknowledged. M.T. is supported by the project operated within the Foundation for Polish Science MPD Programme cofinanced by the EU European Regional Development Fund.

---

[1] K. M. Jones, E. Tiesinga, P. D. Lett, and P. S. Julienne, Rev. Mod. Phys. **78**, 483 (2006).

[2] S. A. Rice and M. Zhao, *Optical Control of Molecular Dynamics* (John Wiley and Sons, New York, 2000).

[3] P. Brumer and M. Shapiro, *Principles and Applications of the Quantum Control of Molecular Processes* (Wiley Interscience, Hoboken, New Jersey, 2003).

[4] C. P. Koch and M. Shapiro, Chem. Rev. **212**, 4928 (2012).

[5] C. P. Koch, R. Kosloff, and F. Masnou-Seeuws, Phys. Rev. A **73**, 043409 (2006).

[6] W. Salzmann, U. Poschinger, R. Wester, M. Weidemüller, A. Merli, S. M. Weber, F. Sauer, M. Plewicki, F. Weise, A. Mirabal Esparza *et al.*, Phys. Rev. A **73**, 023414 (2006).

[7] B. L. Brown, A. J. Dicks, and I. A. Walmsley, Phys. Rev. Lett. **96**, 173002 (2006).

[8] W. Salzmann, T. Mullins, J. Eng, M. Albert, R. Wester, M. Weidemüller, A. Merli, S. M. Weber, F. Sauer, M. Plewicki *et al.*, Phys. Rev. Lett. **100**, 233003 (2008).

[9] T. Mullins, W. Salzmann, S. Götz, M. Albert, J. Eng, R. Wester, M. Weidemüller, F. Weise, A. Merli, S. M. Weber *et al.*, Phys. Rev. A **80**, 063416 (2009).

[10] A. Merli, F. Eimer, F. Weise, A. Lindinger, W. Salzmann, T. Mullins, S. Götz, R. Wester, M. Weidemüller, R. Ağanoğlu *et al.*, Phys. Rev. A **80**, 063417 (2009).

[11] D. J. McCabe, D. G. England, H. E. L. Martay, M. E. Friedman, J. Petrovic, E. Dimova, B. Chatel, and I. A. Walmsley, Phys. Rev. A **80**, 033404 (2009).

[12] D. Meshulach and Y. Silberberg, Nature (London) **396**, 239 (1998).

[13] D. Meshulach and Y. Silberberg, Phys. Rev. A **60**, 1287 (1999).

[14] C. Trallero-Herrero, D. Cardoza, T. C. Weinacht, and J. L. Cohen, Phys. Rev. A **71**, 013423 (2005).

[15] C. Trallero-Herrero, J. L. Cohen, and T. Weinacht, Phys. Rev. Lett. **96**, 063603 (2006).

[16] C. Trallero-Herrero and T. C. Weinacht, Phys. Rev. A **75**, 063401 (2007).

[17] A. Gandman, L. Chuntonov, L. Rybak, and Z. Amitay, Phys. Rev. A **75**, 031401 (2007).

[18] A. Gandman, L. Chuntonov, L. Rybak, and Z. Amitay, Phys. Rev. A **76**, 053419 (2007).

[19] L. Chuntonov, L. Rybak, A. Gandman, and Z. Amitay, Phys. Rev. A **77**, 021403 (2008).

[20] L. Chuntonov, L. Rybak, A. Gandman, and Z. Amitay, J. Phys. B **41**, 035504 (2008).

[21] Z. Amitay, A. Gandman, L. Chuntonov, and L. Rybak, Phys. Rev. Lett. **100**, 193002 (2008).

[22] C. P. Koch, M. Ndong, and R. Kosloff, Faraday Discuss. **142**, 389 (2009).

[23] L. Rybak, S. Amaran, L. Levin, M. Tomza, R. Moszynski, R. Kosloff, C. P. Koch, and Z. Amitay, Phys. Rev. Lett. **107**, 273001 (2011).

[24] L. Rybak, Z. Amitay, S. Amaran, R. Kosloff, M. Tomza, R. Moszynski, and C. P. Koch, Faraday Discuss. **153**, 383 (2011).

[25] R. Kosloff, S. Rice, P. Gaspard, S. Tersigni, and D. Tannor, Chem. Phys. **139**, 201 (1989).

[26] T. Ban, H. Skenderović, R. Beuc, I. K. Bronić, S. Rousseau, A. Allouche, M. Aubert-Frécon, and G. Pichler, Chem. Phys. Lett. **345**, 423 (2001).

[27] T. Ban, R. Beuc, H. Skenderovi, and G. Pichler, Europhys. Lett. **66**, 485 (2004).

[28] C. Amiot, O. Dulieu, and J. Vergès, Phys. Rev. Lett. **83**, 2316 (1999).

[29] C. M. Dion, C. Drag, O. Dulieu, B. Laburthe Tolra, F. Masnou-Seeuws, and P. Pillet, Phys. Rev. Lett. **86**, 2253 (2001).

[30] H. K. Pechkis, D. Wang, Y. Huang, E. E. Eyler, P. L. Gould, W. C. Stwalley, and C. P. Koch, Phys. Rev. A **76**, 022504 (2007).

[31] A. Fioretti, O. Dulieu, and C. Gabbanini, J. Phys. B **40**, 3283 (2007).

[32] S. Ghosal, R. J. Doyle, C. P. Koch, and J. M. Hutson, New J. Phys. **11**, 055011 (2009).

[33] B. E. Londoño, J. E. Mahecha, E. Luc-Koenig, and A. Crubellier, Phys. Rev. A **80**, 032511 (2009).

[34] M. Tomza, F. Pawłowski, M. Jeziorska, C. P. Koch, and R. Moszynski, Phys. Chem. Chem. Phys. **13**, 18893 (2011).

[35] J. M. Sage, S. Sainis, T. Bergeman, and D. DeMille, Phys. Rev. Lett. **94**, 203001 (2005).

[36] M. Ndong and C. P. Koch, Phys. Rev. A **82**, 043437 (2010).

[37] V. Kokoouline, O. Dulieu, R. Kosloff, and F. Masnou-Seeuws, J. Chem. Phys. **110**, 9865 (1999).

[38] K. Willner, O. Dulieu, and F. Masnou-Seeuws, J. Chem. Phys. **120**, 548 (2004).

[39] S. Kallush and R. Kosloff, Chem. Phys. Lett. **433**, 221 (2006).

[40] R. Kosloff, Annu. Rev. Phys. Chem. **45**, 145 (1994).

[41] M. Tomza, M. Musiał, R. Gonzalez-Ferez, C. P. Koch, and R. Moszynski (unpublished).

[42] M. Musiał, J. Chem. Phys. **136**, 134111 (2012).

[43] D. I. Lyakh, M. Musiał, V. F. Lotrich, and R. J. Bartlett, Chem. Rev. **112**, 182 (2012).

[44] R. J. Bartlett and M. Musiał, Rev. Mod. Phys. **79**, 291 (2007).

[45] T. G. A. Heijmen, R. Moszynski, P. E. S. Wormer, and A. van der Avoird, Mol. Phys. **89**, 81 (1996).

[46] A. Marte, T. Volz, J. Schuster, S. Dürr, G. Rempe, E. G. M. van Kempen, and B. J. Verhaar, Phys. Rev. Lett. **89**, 283202 (2002).

[47] R. F. Gutterres, C. Amiot, A. Fioretti, G. Gabbanini, M. Mazzoni, and O. Dulieu, Phys. Rev. A **66**, 024502 (2002).

[48] M. Marinescu and A. Dalgarno, Phys. Rev. A **52**, 311 (1995).

[49] I. S. Lim, P. Schwerdtfeger, B. Metz, and H. Stoll, J. Chem. Phys. **122**, 104103 (2005).

[50] J. F. Stanton, J. Gauss, S. A. Perera, J. D. Watts, A. Yau, M. Nooijen, N. Oliphant, P. Szalay, W. Lauderdale, S. Gwaltney *et al.*, ACES II is a program product of the Quantum Theory Project, University of Florida.

[51] H.-J. Werner, P. J. Knowles, F. R. M. R. Lindh, M. Schütz, P. Celani, T. Korona, G. Rauhut, R. D. Amos, A. Bernhardsson, A. Berning *et al.*, MOLPRO, version 2006.1, a package of *ab initio* programs (2006), see http://www.molpro.net.

[52] S. J. Park, A. W. Suh, Y. S. Lee, and G.-H. Jeung, J. Mol. Spectrosc. **207**, 129 (2001).

[53] D. Edvardsson, S. Lunell, and C. M. Marian, Mol. Phys. **101**, 2381 (2003).

[54] A.-R. Allouche and M. Aubert-Frecon, J. Chem. Phys. **136**, 114302 (2012).

[55] J. P. Palao and R. Kosloff, Phys. Rev. A **68**, 062308 (2003).

[56] S. E. Sklarz and D. J. Tannor, Phys. Rev. A **66**, 053619 (2002).

[57] D. M. Reich, M. Ndong, and C. P. Koch, J. Chem. Phys. **136**, 104103 (2012).

[58] W. Skomorowski, R. Moszynski, and C. P. Koch, Phys. Rev. A **85**, 043414 (2012).

[59] I. S. Averbukh and N. F. Perelman, Phys. Lett. A **139**, 449 (1989).

[60] C. P. Koch, J. P. Palao, R. Kosloff, and F. Masnou-Seeuws, Phys. Rev. A **70**, 013402 (2004).

[61] C. P. Koch, E. Luc-Koenig, and F. Masnou-Seeuws, Phys. Rev. A **73**, 033408 (2006).

[62] C. P. Koch and R. Moszyński, Phys. Rev. A **78**, 043417 (2008).

[63] Specifically, the population of the (7) $^1\Sigma_g^+$ and (4) $^3\Pi_g$ states at an instant in time was smaller by a factor 100 or more than the population of the (5) $^1\Sigma_g^+$, (6) $^1\Sigma_g^+$, and (3) $^3\Pi_g$ states.

Appendix D

Paper IV

”Controlling magnetic Feshbach resonances in polar open-shell molecules with non-resonant light”

Michał Tomza, Rosario Gonzalez-Ferez, Christiane P. Koch,
Robert Moszynski

Physical Review Letters **112**, 113201 (2014).

Controlling Magnetic Feshbach Resonances in Polar Open-Shell Molecules with Nonresonant Light

Michał Tomza,[1,2,3] Rosario González-Férez,[2,4] Christiane P. Koch,[3,*] and Robert Moszynski[1]
[1]*Faculty of Chemistry, University of Warsaw, Pasteura 1, 02-093 Warsaw, Poland*
[2]*Instituto 'Carlos I' de Física Teórica y Computacional and Departamento de Física Atómica, Molecular y Nuclear, Universidad de Granada, 18071 Granada, Spain*
[3]*Theoretische Physik, Universität Kassel, Heinrich-Plett-Straße 40, 34132 Kassel, Germany*
[4]*The Hamburg Center for Ultrafast Imaging, University of Hamburg, 22761 Hamburg, Germany*

(Received 31 July 2013; revised manuscript received 23 December 2013; published 20 March 2014)

Magnetically tunable Feshbach resonances for polar paramagnetic ground-state diatomics are too narrow to allow for magnetoassociation starting from trapped, ultracold atoms. We show that nonresonant light can be used to engineer the Feshbach resonances in their position and width. For nonresonant field intensities of the order of 10^9 W/cm^2, we find the width to be increased by 3 orders of magnitude, reaching a few Gauss. This opens the way for producing ultracold molecules with sizable electric and magnetic dipole moments and thus for many-body quantum simulations with such particles.

DOI: 10.1103/PhysRevLett.112.113201 PACS numbers: 34.50.Cx, 34.50.Rk, 67.85.-d

Ultracold polar molecules are predicted to probe fundamental physics [1] and realize a wealth of many-body phenomena such as exotic quantum phases [2]. They are thus attracting significant interest in both the AMO and condensed matter communities [3]. Polar alkali dimers have already been produced in their absolute internal ground state close to quantum degeneracy [4], opening the way toward ultracold chemistry [5,6] and quantum simulation [7]. Contrary to ground-state alkali dimers which are closed-shell, diatomics consisting of an open-shell and a closed-shell atom possess an unpaired electron, endowing the molecule with spin structure and a significant magnetic dipole moment. Since these molecules have both electric and magnetic dipoles, they are supreme candidates for creating topologically ordered states [8], investigating collective spin excitations [9], and realizing lattice-spin models [7]. While numerous ultracold mixtures of open-shell alkali and closed-shell Yb or Sr atoms have already been studied experimentally [10–15], magnetoassociating the atoms into molecules has remained an elusive goal.

The most successful and widely used routes to producing ultracold dimers utilize magnetically tunable Feshbach resonances (FRs) [16,17] where the hyperfine interaction couples a scattering state to a bound molecular level. Somewhat unexpectedly, FRs have been predicted for diatomics with a $^2\Sigma$ ground electronic state such as RbSr and LiYb [18,19]. The resonances are caused by a modification of the alkali atom's hyperfine structure due to the presence of the other atom [18] or by creating a hyperfine coupling due to the alkali atom polarizing the nuclear spin density of fermionic Yb [19]. However, the width of these resonances does not exceed a few milli-Gauss. This renders their use in magnetoassociation very difficult, if not impossible. A different kind of FR for a closed-shell—open-shell mixture has recently been observed, with one of the atoms in an electronically excited state [20,21]. In this case, the FR is induced by the anisotropy of the interaction between S-state and P-state atoms. Because of the finite excited state lifetime, such a FR is not ideally suited for making molecules. It suggests, however, to harness an anisotropic interaction for magnetoassociation.

Here we show that nonresonant light, which universally couples to the polarizability anisotropy of a molecule, induces FRs and modifies their position and width. This is due to the nonresonant light changing the background scattering length and altering the differential magnetic susceptibility. Our approach is related to dc electric field control of polar molecules [22–24] but comes with much more favorable requirements in terms of experimental feasibility. We find widths of a few Gauss for nonresonant field intensities of the order 10^9 W/cm^2 for a wide range of polar open-shell molecular species. Widths of a few Gauss are sufficient for magnetoassociation. Nonresonant field control thus paves the way to producing ultracold particles with sizable electric and magnetic dipole moments.

Magnetoassociation can employ an adiabatic ramp of the magnetic field across the resonance or a time-dependent magnetic or radio-frequency (rf) field that drives a transition from a scattering state to a molecular level [17]. These two routes imply different requirements on the characteristics of the resonance. In both cases, a broad FR is needed. Adiabatic passage additionally requires a large product of width, Δ, and background scattering length, a_{bg}. This is seen in the atom-molecule conversion efficiency, given by the Landau-Zener formula $1-\exp[-\eta n(\hbar/\mu)|a_{\mathrm{bg}}\Delta/\dot{B}|]$ with n the atomic number density, $\dot{B}$ the magnetic field ramp speed, μ the reduced mass, and η a dimensionless prefactor [25]. Using Fermi's golden rule, the resonance width Δ can be estimated,

$$\Delta \sim |\langle v|H|k\rangle|^2/(a_{\mathrm{bg}}\delta\chi), \tag{1}$$

in terms of the coupling $\langle v|H|k\rangle$ between molecular level $|v\rangle$ and scattering states $|k\rangle$, the background scattering length a_{bg}, and the differential magnetic susceptibility, $\delta\chi$ [26]. The latter is simply the difference in slope of the bound and continuum energies as a function of magnetic field at resonance. When the background scattering length a_{bg} is larger than the mean scattering length $\bar{a}$ [$\bar{a} \approx 0.48(2\mu C_6/\hbar)^{1/4}$ with C_6 the dispersion coefficient], the coupling $|\langle v|H|k\rangle|$ becomes proportional to a_{bg}. The width is then determined by background scattering length and differential magnetic susceptibility, $\Delta \sim a_{\mathrm{bg}}/\delta\chi$ [26]. The key point of our proposal is that both $\delta\chi$ and a_{bg} can be tuned by applying a nonresonant field. This leads to significant changes in the resonance width Δ and the adiabaticity parameter $|a_{\mathrm{bg}}\Delta|$.

The Hamiltonian describing the relative nuclear motion of an open-shell ^2S atom, a, and a closed-shell ^1S atom, b, reads

$$\hat{H} = \frac{\hbar^2}{2\mu}\left(-\frac{1}{r}\frac{d^2}{dr^2}r + \frac{\hat{L}^2}{r^2}\right) + \hat{H}_a + \hat{H}_b + V(r,\theta), \tag{2}$$

where r is the interatomic separation, $\hat{L}$ the rotational angular momentum operator, and θ the angle between the molecular axis and the space-fixed Z axis. The atomic Hamiltonian including Zeeman and hyperfine interactions is given by

$$\hat{H}_j = \zeta_j \hat{i}_j \cdot \hat{s}_j + (g_e\mu_B\hat{s}_{j,z} + g_j\mu_N\hat{i}_{j,z})B, \tag{3}$$

with $\hat{s}_j$ and $\hat{i}_j$ the electron and nuclear spin operators, $g_{e/j}$ the electron and nuclear g factors, and $\mu_{B/N}$ the Bohr and nuclear magnetons. ζ_j denotes the hyperfine coupling constant. For a fermionic closed-shell ^1S atom, Eq. (3) reduces to the nuclear Zeeman term, whereas for a bosonic one it is zero. The interatomic interaction reads

$$\begin{aligned} V(r,\theta) = {} & V_{X^2\Sigma^+}(r) + \Delta\zeta_a(r)\hat{i}_a \cdot \hat{s}_a \\ & - \frac{I}{2\epsilon_0 c}[\alpha_\perp(r) + \Delta\alpha(r)\cos^2\theta] \end{aligned} \tag{4}$$

for magnetic and nonresonant laser fields parallel to the space-fixed Z axis. $V_{X^2\Sigma^+}(r)$ is the potential energy curve for the $X^2\Sigma^+$ ground electronic state, and $\Delta\zeta_a(r)$ the interaction-induced variation of the hyperfine coupling [18,19]. The molecular static polarizability with perpendicular component $\alpha_\perp(r)$ and anisotropy $\Delta\alpha(r)$ couples to nonresonant light of intensity I, linearly polarized along the space-fixed Z axis. We omit spin-rotation couplings as well as the coupling resulting from a nonzero nuclear spin of a fermionic closed-shell atom since they are significantly smaller than $\Delta\zeta_a(r)$.

We focus on RbYb for which spectroscopic and *ab initio* data for the interaction potential are available [27]. The r-dependent isotropic and anisotropic polarizabilities are calculated using state of the art coupled cluster methods, small-core energy consistent pseudopotentials, and large basis sets [28]. They perfectly agree with Silberstein's formula [29,30] evaluated for the atomic polarizabilities of Ref. [31]. The interaction-induced variation of the hyperfine coupling, $\Delta\zeta_a(r)$, is taken from Ref. [26]. The total scattering wave function is constructed in an uncoupled basis set, $|i_a, m_{i,a}\rangle|s_a, m_{s,a}\rangle|L, m_L\rangle$ with m_j the projection of angular momentum j on the space-fixed Z axis, assuming the projection of the total angular momentum of rubidium $m_f = m_{i,a} + m_{s,a}$ to be conserved. The coupled channel equations are solved using a renormalized Numerov propagator [32]. The scattering length and elastic cross section are obtained from the S matrix for the entrance channel, $a = (1 - S_{11})/(1 + S_{11})/(ik)$ and $\sigma_{el} = \pi|1 - S_{11}|/k^2$, with $k = \sqrt{2\mu E}/\hbar$ and E the collision energy, assumed to be 100 nK. The resonance width Δ is determined by fitting the scattering length to $a(B) = a_{\mathrm{bg}}[1 - \Delta/(B - B_{\mathrm{res}})]$ [16,17].

Nonresonant light modifies the energies of rovibrational levels and scattering states alike [33–36]. The latter implies control of scattering properties such as the cross sections. This is illustrated by Fig. 1 which displays a series of maxima and minima of the elastic cross section as a function of nonresonant field intensity. The maxima correspond to a large absolute value of a_{bg} and occur when a scattering state becomes bound; the minima indicate noninteracting atoms. Broad maxima of the elastic cross section are observed when an s-wave scattering state is pushed below threshold, whereas the narrow features in Fig. 1 are caused by higher partial waves. New FRs are created by the nonresonant light shifting bound levels. This happens when a bound level crosses the atomic threshold of a different hyperfine level as indicated by the dots in Fig. 2(a). New resonances, higher than s wave, may also be induced by mixing partial waves or by spin-rotation

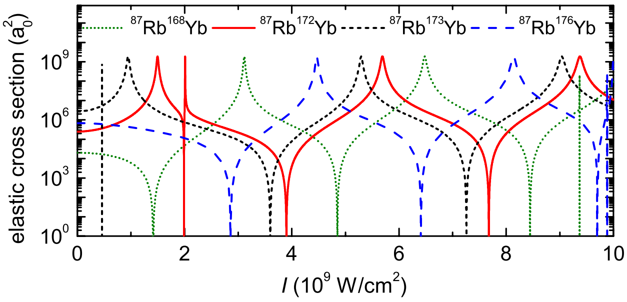

FIG. 1 (color online). Nonresonant light control of scattering properties: Elastic cross section as a function of the nonresonant light intensity ($E/k_B = 100$ nK, $B = 0$).

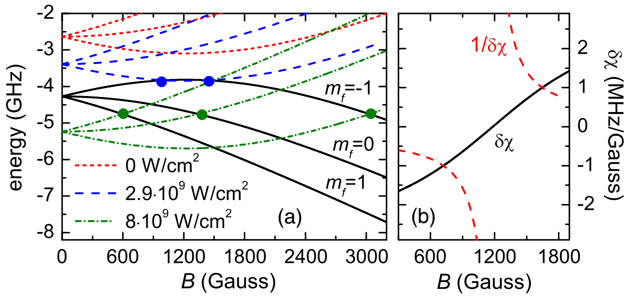

FIG. 2 (color online). Creating a new FR with nonresonant light: (a) Atomic thresholds (solid black lines) start to cross molecular levels (dashed lines) as the nonresonant light shifts the level positions (^{87}Rb^{176}Yb with $|m_f| \le i_a - 1/2$). The dots indicate the position of the new FR. (b) The level shifts are accompanied by a variation of the differential magnetic susceptibility $\delta\chi$ vs magnetic field ($m_f = -1$, $I = 0$).

coupling between higher partial waves. The nonresonant field dependence of the background scattering length observed in Fig. 1 and the creation of a new FR due to the nonresonant light shown in Fig. 2 together with Eq. (1) suggest three mechanisms to increase the width of FRs: (i) $\delta\chi \to 0$, (ii) $|a_{\mathrm{bg}}| \to \infty$, and (iii) $|a_{\mathrm{bg}}| \to 0$. In case (i), $|a_{\mathrm{bg}}\Delta|$ becomes large unless it coincides with case (iii), and large $|a_{\mathrm{bg}}\Delta|$ is guaranteed in case (ii). Then both adiabatic ramping across the resonance and rf association are possible. In contrast, $|a_{\mathrm{bg}}\Delta|$ will always stay small in case (iii), preventing adiabatic passage. Since adiabatic ramping is the most popular technique for magnetoassociation, we focus on cases (i) and (ii) here and will report on case (iii) elsewhere [28].

We find that case (i) yields the largest widths. This is illustrated in Fig. 3(a) for ^{87}Rb^{176}Yb: A pair of resonances is created when the molecular level crosses an atomic threshold close to the maximum of its magnetic field dependence, cf. blue dots in Fig. 2(a). The resonances come with a very large width Δ, of the order of a few Gauss, cf. the left peak in Fig. 3(a), and are separated by several Gauss (by 6G for example for $\Delta \approx 3$G). The large width is rationalized by the broad pole of $1/\delta\chi$ shown in Fig. 2(b) which enters Eq. (1). Not only the width Δ but also the adiabaticity parameter $|a_{\mathrm{bg}}\Delta|$ is found to be large, of the order of 10 $a_0 \cdot$G, whereas the background scattering length remains comparatively small, of the order of 10 a_0. A second peak of the width Δ, of the order of 10 G, is observed in Fig. 3(a), at $I = 2.88 \times 10^9$ W/cm^2. It is caused by a_{bg} going to zero, which can be inferred from the corresponding minimum of the blue dashed curve in Fig. 1. The joint occurrence of $\delta\chi \to 0$ and $a_{\mathrm{bg}} \to 0$ is a coincidence. As can be seen in Figs. 3(a) and 3(b), such a coincidence leads to particularly broad resonances for a range of nonresonant field intensities which at the same time are separated by several hundred Gauss. However, due to $a_{\mathrm{bg}} \to 0$, the adiabaticity parameter $|a_{\mathrm{bg}}\Delta|$ remains small. The adiabaticity parameter is guaranteed to be large in case (ii) when the nonresonant field is used to tune the background scattering length to very large values. This is illustrated in Figs. 3(c) and 3(d). The maximum width Δ which is not limited in theory will depend on the stability of the nonresonant field intensity in practice. For example, an increase by 10^3 requires intensity stabilization of the order 10^{-3} to 10^{-4}. The actual value of Δ that can be obtained also depends on the field-free width. But even for very narrow resonances, with the field-free Δ below 1 mG, the engineered width easily reaches 100 mG, as demonstrated by Fig. 3(c).

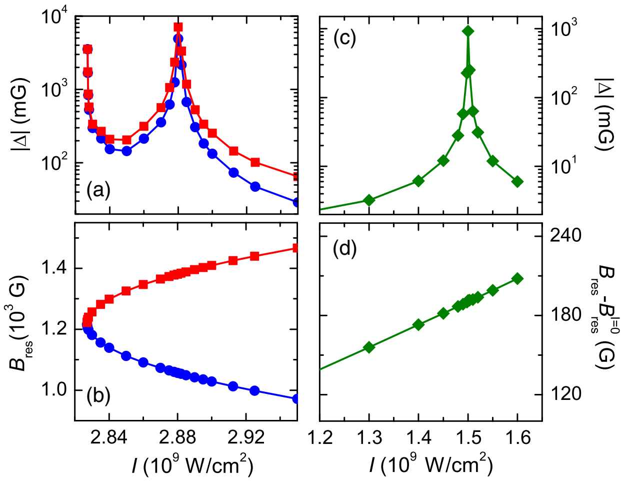

FIG. 3 (color online). Controlling the width of a FR by modifying $\delta\chi$ (a),(b): Resonance width Δ and resonance position B_{res} vs nonresonant light intensity for ^{87}Rb^{176}Yb and the pair of resonances indicated by blue dots in Fig. 2 ($m_f = -1$, $B_{\mathrm{res}} = 1219$G). Controlling the width of a FR by tuning a_{bg} to large values (c),(d): Resonance width Δ and change in resonance position $B_{\mathrm{res}} - B_{\mathrm{res}}^{I=0}$ vs nonresonant light intensity for ^{87}Rb^{172}Yb ($m_f = 1$, $B_{\mathrm{res}}^{I=0} = 1592$G).

We find nonresonant light intensities of the order of 10^9 W/cm^2 to be sufficient to create FRs for all isotopologues of RbYb. The smallest intensity is required for diatomics with a molecular level just above the atomic threshold since the nonresonant field always lowers the energy in the electronic ground state [36]. For example, a pair of broad resonances, as shown in Figs. 3(a) and 3(b), is also observed for ^{85}Rb^{170}Yb (with $\Delta > 0.5$ G at $I = 1.29 \times 10^9$ W/cm^2). When only the rubidium isotope is exchanged, the dependence on the nonresonant light intensity remains essentially unchanged compared to Figs. 3(a) and 3(b). Of course, different hyperfine levels may come into play, e.g., $m_f = -2$ or $m_f = -1$, which imply different magnetic fields ($B_{\mathrm{res}} = 722$G and $B_{\mathrm{res}} = 361$G, respectively, for ^{87}Rb^{176}Yb). The left peak of Δ in Fig. 3(a) and the associated increase in $|a_{\mathrm{bg}}\Delta|$ is found for all RbYb isotopologues. The right peak corresponds to a coincidence of case (i) with case (iii) and is specific to ^{87}Rb^{176}Yb. Case (i) may coincide also with case (ii). This happens for ^{87}Rb^{174}Yb, yielding an adiabaticity parameter $|a_{\rm bg}\Delta|$ of the order of 100 $a_0 \cdot$ G. Case (ii), i.e., large $a_{\rm bg}$, is most easily realized for molecules with a large and negative field-free background scattering length a_s. For ^{87}Rb^{172}Yb shown in Figs. 3(c) and 3(d) for example, $a_s = -131a_0$ [37]. Another good candidate for case (ii) is ^{87}Rb^{173}Yb with $a_s = -431a_0$ [37].

The three mechanisms are generally applicable due to the universal coupling to nonresonant light. Notably, we find the characteristics of controlling the resonance width by tuning the background scattering length, as shown in Figs. 3(c) and 3(d), to be common to all $^2\Sigma$ molecules. When considering closed-shell—open-shell mixtures other than RbYb, different strengths of both magnetic field and nonresonant light might, however, be required. For example, LiYb has a smaller reduced mass than RbYb and Li a smaller polarizability than Rb which implies a larger nonresonant field intensity. The magnetic field strength for which a molecular level crosses the atomic threshold close to the maximum of its magnetic field dependence, relevant for case (i), is determined by the hyperfine splitting [26]. It is thus smaller for mixtures involving Li, Na or K and larger for those involving Cs instead of Rb. Prospects are best for RbSr and CsYb [28] for which the interaction induced variation of the hyperfine structure and the polarizabilities are largest. Together with the tunability of the field-free background scattering length by choice of the Yb isotope, this makes CsYb in particular another very promising candidate.

When tuning nonresonant light and magnetic field for interspecies magnetoassociation, undesired losses may occur due to accidentally hitting an intraspecies FR or shape resonance. For example, for RbYb, depending on the isotope, one to three shape resonances are observed for Yb$_2$ at nonresonant field intensities of the order of 10^9 W/cm^2. The shape resonance found for ^{176}Yb$_2$ at $I = 3.05 \times 10^9$ W/cm^2 is sufficiently far from $I = 2.83 \times 10^9$ W/cm^2, for which the width of the ^{87}Rb^{176}Yb FR is increased to several Gauss, cf. Fig. 3(a). The separation is even slightly larger for ^{174}Yb$_2$. Alkali intraspecies FRs are found to be shifted in position by the nonresonant field. If, as the result, an intraspecies FR is moved too close to the interspecies one, a different Yb isotope should be selected. Similarly, selection of the hyperfine level provides a solution, if a shape resonance approaches the interspecies FR too closely, for example for CsYb. Perturbations due to intraspecies resonances can thus be avoided. Such losses do not occur altogether when working in a double-species Mott insulator state [38].

Our proposal for nonresonant light controlled magnetoassociation requires intensities of the order of 10^9 W/cm^2 and magnetic fields of the order of 1000 G. These requirements are within current experimental capabilities. Intensities of the order 10^9 W/cm^2 can be achieved using intracavity beams with spot sizes of about 10 μm and powers of the order of 1 kW. Such spot sizes could be desirable for creating an additional trap. Larger spot sizes, up to 100 μm, are possible when using an optical buildup cavity [39,40]. The required intensity can be stabilized at a level of 0.001, but even 10^{-4} should be reachable with refined feedback techniques. Magnetic fields can be stabilized at the level 10^{-5}-10^{-6} [41] such that magnetic field stability is not a concern for the resonance widths and separations discussed here. Losses due to photon scattering can be kept minimal by choosing light, such as that of a CO$_2$ laser, that is far off resonance with any molecular transition. Estimating the heating rates for $I = 10^9$ W/cm^2 in terms of the atomic photon scattering rates [42], we find the largest heating rate, that of the alkali atom, to be only of the order of 1 nK/s for a wavelength of 10 μm. Wavelengths in the near infrared, e.g., 1064 nm or 1550 nm, could also be employed. For the telecom wavelength, we find a heating rate of the order of 10 μK/s. This should be sufficiently low to allow for adiabatic ramps whereas for 1064 nm with heating rates below 1 mK/s, the experiment needs to be conducted within 1 ms, better adapted to rf magnetoassociation [17]. The actually required intensities and associated heating rates for these wavelengths might, however, be lower due to the dynamic instead of the static polarizabilities coming into play. This will be studied in detail elsewhere [28].

Compared to electric field control of FRs for polar molecules [22–24], our proposal corresponds to more favorable experimental conditions. For diatomics consisting of an alkali atom and Sr or Yb, we find electric fields of several hundreds kV/cm to be required. This clearly exceeds current experimental capabilities. Compared to the permanent electric dipole moment coupling to a dc electric field, the interaction of Eq. (4) contains diagonal in addition to off-diagonal matrix elements in the basis of field-free rotational eigenstates. This explains the large shifts in level positions which allow in particular for mechanism (i), i.e., $\delta\chi \to 0$. Moreover, the permanent dipole moment vanishes as $1/r^7$ compared to the asymptotic $1/r^3$ behavior of the polarizability. These facts together explain the much better prospects in terms of experimental feasibility of our approach.

In conclusion, we have shown that nonresonant light can be used to control FRs of mixtures of open-shell—closed-shell atoms, engineering their widths to reach up to a few Gauss. Such resonances are sufficiently broad for magnetoassociation. The required field strengths and control are all within current experimental capabilities. Our proposal opens the way for producing ultracold molecules with sizable electric and magnetic dipole moments and thus for many-body quantum simulations with such particles.

We would like to thank Piotr Żuchowski and Axel Görlitz for making their RbYb potentials available to us prior to publication and Michael Drewsen and Jun Ye for providing their expertise on the state of the art of laser technology. The authors enjoyed the hospitality of the Kavli Institute of Theoretical Physics where the work reported here was initiated. M. T. is supported by the Foundation for Polish Science MPD Programme co-financed by the EU European Regional Development Fund. R. G.-F. acknowledges a Mildred Dresselhaus award from the excellence cluster “The Hamburg Center for Ultrafast Imaging—Structure, Dynamics and Control of Matter at the Atomic Scale” of the Deutsche Forschungsgemeinschaft. Financial support by the Spanish Project No. FIS2011-24540 (MICINN), the Grants No. P11-FQM-7276 and No. FQM-4643 (Junta de Andalucía), and Andalusian research group FQM-207, the project N-N204-215539 of the Polish Ministry of Science and Higher Education, the MISTRZ program of the Foundation for Polish Science, and in part by the National Science Foundation under Grant No. NSF PHY11-25915 is gratefully acknowledged.

---

[*] christiane.koch@uni-kassel.de

[1] D. DeMille, S. B. Cahn, D. Murphree, D. A. Rahmlow, and M. G. Kozlov, Phys. Rev. Lett. **100**, 023003 (2008).
[2] N. Y. Yao, A. V. Gorshkov, C. R. Laumann, A. M. Läuchli, J. Ye, and M. D. Lukin, Phys. Rev. Lett. **110**, 185302 (2013).
[3] L. D. Carr, D. DeMille, R. V. Krems, and J. Ye, New J. Phys. **11**, 055049 (2009).
[4] K. K. Ni, S. Ospelkaus, M. H. G. de Miranda, A. Pe’er, B. Neyenhuis, J. J. Zirbel, S. Kotochigova, P. S. Julienne, D. S. Jin, and J. Ye, Science **322**, 231 (2008).
[5] S. Ospelkaus, K.-K. Ni, D. Wang, M. H. G. de Miranda, B. Neyenhuis, G. Quéméner, P. S. Julienne, J. L. Bohn, D. S. Jin, and J. Ye, Science **327**, 853 (2010).
[6] M. H. G. de Miranda, A. Chotia, B. Neyenhuis, D. Wang, G. Quéméner, S. Ospelkaus, J. L. Bohn, J. Ye, and D. S. Jin, Nat. Phys. **7**, 502 (2011).
[7] A. Micheli, G. K. Brennen, and P. Zoller, Nat. Phys. **2**, 341 (2006).
[8] I. Bloch, J. Dalibard, and W. Zwerger, Rev. Mod. Phys. **80**, 885 (2008).
[9] J. Perez-Rios, F. Herrera, and R. V. Krems, New J. Phys. **12**, 103007 (2010).
[10] N. Nemitz, F. Baumer, F. Münchow, S. Tassy, and A. Görlitz, Phys. Rev. A **79**, 061403 (2009).
[11] F. Baumer, F. Münchow, A. Görlitz, S. E. Maxwell, P. S. Julienne, and E. Tiesinga, Phys. Rev. A **83**, 040702 (2011).
[12] H. Hara, Y. Takasu, Y. Yamaoka, J. M. Doyle, and Y. Takahashi, Phys. Rev. Lett. **106**, 205304 (2011).
[13] V. V. Ivanov, A. Khramov, A. H. Hansen, W. H. Dowd, F. Münchow, A. O. Jamison, and S. Gupta, Phys. Rev. Lett. **106**, 153201 (2011).
[14] B. Pasquiou, A. Bayerle, S. M. Tzanova, S. Stellmer, J. Szczepkowski, M. Parigger, R. Grimm, and F. Schreck, Phys. Rev. A **88**, 023601 (2013).
[15] T. Aoki, Y. Yamanaka, M. Takeuchi, Y. Torii, and Y. Sakemi, Phys. Rev. A **87**, 063426 (2013).
[16] T. Köhler, K. Góral, and P. S. Julienne, Rev. Mod. Phys. **78**, 1311 (2006).
[17] C. Chin, R. Grimm, P. S. Julienne, and E. Tiesinga, Rev. Mod. Phys. **82**, 1225 (2010).
[18] P. S. Żuchowski, J. Aldegunde, and J. M. Hutson, Phys. Rev. Lett. **105**, 153201 (2010).
[19] D. A. Brue and J. M. Hutson, Phys. Rev. Lett. **108**, 043201 (2012).
[20] S. Kato, S. Sugawa, K. Shibata, R. Yamamoto, and Y. Takahashi, Phys. Rev. Lett. **110**, 173201 (2013).
[21] A. Khramov, A. Hansen, W. Dowd, R. J. Roy, C. Makrides, A. Petrov, S. Kotochigova, and S. Gupta, Phys. Rev. Lett. **112**, 033201 (2014).
[22] R. V. Krems, Phys. Rev. Lett. **96**, 123202 (2006).
[23] Z. Li and R. V. Krems, Phys. Rev. A **75**, 032709 (2007).
[24] B. Marcelis, B. Verhaar, and S. Kokkelmans, Phys. Rev. Lett. **100**, 153201 (2008).
[25] E. Hodby, S. T. Thompson, C. A. Regal, M. Greiner, A. C. Wilson, D. S. Jin, E. A. Cornell, and C. E. Wieman, Phys. Rev. Lett. **94**, 120402 (2005).
[26] D. A. Brue and J. M. Hutson, Phys. Rev. A **87**, 052709 (2013).
[27] M. Borkowski, P. S. Żuchowski, R. Ciuryło, P. S. Julienne, D. Kedziera, L. Mentel, P. Tecmer, F. Münchow, C. Bruni, and A. Görlitz, Phys. Rev. A **88**, 052708 (2013).
[28] M. Tomza, R. González-Férez, C. P. Koch, and R. Moszynski (to be published).
[29] T. G. Heijmen, R. Moszyński, P. E. Wormer, and A. van der Avoird, Mol. Phys. **89**, 81 (1996).
[30] L. Jensen, P.-O. Åstrand, A. Osted, J. Kongsted, and K. V. Mikkelsen, J. Chem. Phys. **116**, 4001 (2002).
[31] A. Derevianko, S. G. Porsev, and J. F. Babb, At. Data Nucl. Data Tables **96**, 323 (2010).
[32] B. R. Johnson, J. Chem. Phys. **69**, 4678 (1978).
[33] M. Lemeshko and B. Friedrich, Phys. Rev. Lett. **103**, 053003 (2009).
[34] M. Lemeshko and B. Friedrich, J. Phys. Chem. A **114**, 9848 (2010).
[35] R. González-Férez and C. P. Koch, Phys. Rev. A **86**, 063420 (2012).
[36] M. Tomza, W. Skomorowski, M. Musiał, R. González-Férez, C. P. Koch, and R. Moszynski, Mol. Phys. **111**, 1781 (2013).
[37] F. Münchow, Ph. D. thesis, Universität Düsseldorf, 2012.
[38] H. Hara, H. Konishi, S. Nakajima, Y. Takasu, and Y. Takahashi, J. Phys. Soc. Jpn. **83**, 014003 (2014).
[39] D. C. Yost, A. Cingöz, T. K. Allison, A. Ruehl, M. E. Fermann, I. Hartl, and J. Ye, Opt. Express **19**, 23483 (2011).
[40] A. Cingöz, D. C. Yost, T. K. Allison, A. Ruehl, M. E. Fermann, I. Hart, and J. Ye, Nature (London) **482**, 68 (2012).
[41] G. Zürn, T. Lompe, A. N. Wenz, S. Jochim, P. S. Julienne, and J. M. Hutson, Phys. Rev. Lett. **110**, 135301 (2013).
[42] R. Grimm, M. Weidemüller, and Y. B. Ovchinnikov, Adv. At. Mol. Opt. Phys. **42**, 95 (2000).

Appendix E

Paper V

”Prospects for ultracold polar and magnetic
chromium–closed-shell-atom molecules”

Michał Tomza

Physical Review A, **88**, 012519 (2013).

PHYSICAL REVIEW A **88**, 012519 (2013)

Prospects for ultracold polar and magnetic chromium–closed-shell-atom molecules

Michał Tomza[*]
Faculty of Chemistry, University of Warsaw, Pasteura 1, 02-093 Warsaw, Poland

(Received 21 June 2013; published 25 July 2013)

The properties of the electronic ground state of the polar and paramagnetic chromium–closed-shell-atom molecules have been investigated. State-of-the-art *ab initio* techniques have been applied to compute the potential energy curves for the chromium–alkaline-earth-metal-atom, CrX (X = Be, Mg, Ca, Sr, Ba), and chromium–ytterbium, CrYb, molecules in the Born-Oppenheimer approximation for the high-spin $X^7\Sigma^+$ electronic ground state. The spin restricted open-shell coupled cluster method restricted to single, double, and noniterative triple excitations, RCCSD(T), was employed and the scalar relativistic effects within the Douglas-Kroll-Hess Hamiltonian or energy-consistent pseudopotentials were included. The permanent electric dipole moments and static electric dipole polarizabilities were computed. The leading long-range coefficients describing the dispersion interaction between the atoms at large interatomic distances C_6 are also reported. The molecules under investigation are examples of species possessing both large magnetic and electric dipole moments making them potentially interesting candidates for ultracold many-body physics studies.

DOI: 10.1103/PhysRevA.88.012519 PACS number(s): 31.50.Bc, 34.20.−b, 33.15.Kr

I. INTRODUCTION

The research on atoms and molecules at ultralow temperatures addresses the most fundamental questions of quantum mechanics [1]. The field of ultracold matter started with gases of alkali-metal atoms and for many years has been restricted to these species [2]. All ultracold ($T < 1$ mK) molecules in the absolute rovibrational ground state, produced to this day, consist of alkali-metal atoms [3]. Nevertheless, recent success in cooling and Bose-Einstein condensating the highly magnetic ^{52}Cr [4], ^{168}Er [5], and ^{164}Dy [6] atoms or closed-shell ^{40}Ca [7], ^{84}Sr [8,9], ^{86}Sr [10], ^{88}Sr [11], ^{170}Yb [12], and ^{174}Yb [13] atoms allow to consider them as candidates for forming ultracold molecules.

Heteronuclear molecules possessing a permanent electric dipole moment are promising candidates for numerous applications including quantum computing, quantum simulations, many-body physics, ultracold controlled chemistry, precision measurements, and tests of fundamental laws [14]. Heteronuclear molecules formed from atoms with large magnetic dipole moments could possess both magnetic and electric dipole moments that would provide an additional knob to control the quantum dynamics with both magnetic and electric fields [15].

Recently there has been an increased interest in the study of ultracold mixtures of open-shell and closed-shell atoms. Ultracold mixtures of Li and Yb [16,17], Rb and Yb [18,19], Cs and Yb [20], and Rb and Sr [21] atoms have been investigated experimentally. Open-shell Li–alkali-earth-metal-atom [22,23], LiYb [24–26], and alkali-metal-atom–Sr [27] and RbSr [28] molecules have been explored theoretically. Although the properties of the alkali-metal-atom–closed-shell-atom molecules could be tuned with external electric and magnetic fields by controlling the spin-dependent long-range interactions, the intermolecular magnetic dipole-dipole interaction resulting from their magnetic dipole moments is too small to compete against the electric dipole-dipole interaction or short-range chemical forces and to influence the many-body dynamics. To explore the impact of the intermolecular magnetic dipole-dipole interaction on the properties of ultracold molecular gas, molecules formed from the highly magnetic atoms such as Cr(^7S), Eu(^8S), Er(^3H), or Dy(^5I) should be considered.

A high-spin spherically symmetric S-state chromium atom is a natural candidate for the formation of a molecule possessing a large magnetic dipole moment. The properties of the electronic ground state of the chromium–alkali-metal-atom molecules have been investigated theoretically [29,30] and the CrRb molecule was proposed as a candidate for a molecule with both large magnetic and electric dipole moments [29]. The two-species magnetooptical trap (MOT) for the Cr and Rb atoms was realized in 2004 [31], but the operation of superimposed MOTs was limited by the photoionization of the excited state of the Rb atoms by the Cr cooling-laser light. Unfortunately, the same trap losses are expected for the mixtures of chromium with other alkali-metal atoms. Since the ionization potentials of alkali-earth-metal atoms are at least by 10 000 cm^{-1} larger than for alkali-metal atoms of similar size, this problem will not occur for the two-species MOT with chromium and alkali-earth-metal atoms or alkali-earth-metal-like Yb atoms.

There are advantages of using a closed-shell ^1S atom as a partner of ^7S chromium atom for the formation of a highly magnetic open-shell molecule. First of all the resulting electronic structure of such a system is relatively simple. There is only one electronic state dissociating into ground-state closed-shell and ground-state chromium atoms. The zero internal orbital angular momentum of both atoms implies the Σ symmetry of the electronic ground state. Therefore, there is no anisotropy of the interaction between the atoms that could lead to the fast Zeeman relaxation and losses in the formation process of the magnetic molecules from highly magnetic atoms with large orbital angular momentum [32]. Finally, the molecule inherits the large magnetic dipole moment of the chromium atom $d_m = 6\mu_B$.

Until recently, the most efficient method of forming ultracold molecules, that is, magnetoassociation within the vicinity of the Feshbach resonances followed by the stimulated Raman

---

[*] michal.tomza@chem.uw.edu.pl

adiabatic passage (STIRAP), was believed to be restricted to alkali-metal-atom dimers [33,34]. However, recent works by Żuchowski *et al.* [28] and Brue and Hutson [26] suggest that it is possible to form open-shell-atom–closed-shell-atom molecules by magnetoassociation using the interaction-induced variation of the hyperfine coupling constant.

For the above reasons, in the present work we investigate the properties of the electronic ground state of the chromium–alkaline-earth-metal-atom and chromium–ytterbium molecules. To the best of our knowledge, the chromium–closed-shell-atom molecules have not yet been considered theoretically or experimentally, except the recent work on the Feshbach resonances in the Cr and Yb atoms mixture by Żuchowski [35] and buffer gas cooling of the Cr atoms with a cryogenically cooled helium [36]. Here we fill this gap and report the *ab initio* properties of the $^7\Sigma^+$ electronic ground states of the chromium–alkaline-earth-metal-atom and chromium–ytterbium molecules paving the way towards a more elaborate study of the formation and application of these polar and magnetic molecules.

The plan of our paper is as follows. Section II describes the theoretical methods used in the *ab initio* calculations. Section III discusses the potential energy curves and properties of the chromium–alkali-earth-metal-atom and chromium–ytterbium molecules in the rovibrational ground state and analyzes the completeness and accuracy of the applied *ab initio* methods. It also surveys the characteristic length scales related to the intermolecular magnetic and electric dipolar interactions. Section IV summarizes our paper.

II. COMPUTATIONAL DETAILS

The chromium–closed-shell-atom molecules are of open-shell nature, therefore we have calculated the potential energy curves in the Born-Oppenheimer approximation using the spin-restricted open-shell coupled cluster method restricted to single, double, and noniterative triple excitations, starting from the restricted open-shell Hartree-Fock (ROHF) orbitals, RCCSD(T) [37]. The interaction energies have been obtained with the supermolecule method correcting the basis-set superposition error [38]

$$V_{\mathrm{Cr}X} = E_{\mathrm{Cr}X} - E_{\mathrm{Cr}} - E_X, \tag{1}$$

where $E_{\mathrm{Cr}X}$ denotes the energy of the dimer, and E_{Cr} and E_X are the energies of the monomers computed in the dimer basis.

The scalar relativistic effects in the calculations for the CrBe, CrMg, and CrCa molecules were included by employing the second-order Douglas-Kroll-Hess (DKH) Hamiltonian [39], whereas for the CrSr, CrBa, and CrYb molecules the relativistic effects were accounted for by using small-core fully relativistic energy-consistent pseudopotentials (ECP) to replace the inner-shells electrons [40]. We used the pseudopotentials to introduce the relativistic effects for heavier molecules instead of using the DKH Hamiltonian because it allowed to use larger basis sets to describe valence electrons and modeled the inner-shells electrons density as accurately as the high quality atomic calculation used to fit the pseudopotentials.

In all calculations for the CrBe, CrMg, and CrCa molecules the augmented correlation consistent polarized valence quintuple-ζ quality basis sets (aug-cc-pV5Z) were used. The Be and Cr atoms were described with the aug-cc-pV5Z-DK basis sets [41], whereas for the Mg and Ca atoms, the cc-pV5Z-DK and cc-pV5Z basis sets [42], respectively, were augmented at first. In all calculations for CrSr, CrBa, and CrYb the pseudopotentials from the Stuttgart library were employed. The Cr atom was described by the ECP10MDF pseudopotential [43] and the $[14s13p10d5f4g3h]$ basis set with coefficients taken from the aug-cc-pVQZ-DK basis [41]. The Sr atom was described with the ECP28MDF pseudopotential [44] and the $[14s11p6d5f4g]$ basis set obtained by augmenting the basis set suggested by the authors of Ref. [44]. The Ba atom was described with the ECP46MDF pseudopotential [44] and the $[13s12p6d5f4g]$ basis set obtained by augmenting the basis set suggested by the authors of Ref. [44]. The Yb atom was described with the ECP28MDF pseudopotential [45] and the $[15s14p12d11f8g]$ basis set [45]. In all calculations the basis sets were augmented by the set of $[3s3p2d1f1g]$ bond functions [46].

The permanent electric dipole moments

$$d_i = \langle \Psi_{\mathrm{Cr}X} | \hat{d}_i | \Psi_{\mathrm{Cr}X} \rangle = \left. \frac{\partial E_{\mathrm{Cr}X}(F_i)}{\partial F_i} \right|_{F_i=0}, \tag{2}$$

where $\hat{d}_i$, $i = x, y$, or z, denotes the ith component of the electric dipole moment operator and static electric dipole polarizabilities

$$\alpha_{ij} = \left. \frac{\partial^2 E_{\mathrm{Cr}X}(\vec{F})}{\partial F_i \partial F_j} \right|_{\vec{F}=0}, \tag{3}$$

were calculated with the finite field method. The dipole moments and the polarizabilities were obtained with three-point and five-point approximations of the first and second derivatives, respectively. The z axis was chosen along the internuclear axis and oriented from the closed-shell to the chromium atom.

The interaction potential between two neutral atoms in the electronic ground state is asymptotically given by the dispersion interaction of the form [47]

$$V_{\mathrm{Cr}X}(R) = -\frac{C_6}{R^6} + \cdots, \tag{4}$$

where the leading C_6 coefficient given by

$$C_6 = \frac{3}{\pi} \int_0^\infty \alpha_{\mathrm{Cr}}(i\omega) \alpha_X(i\omega) d\omega, \tag{5}$$

is the integral over the dynamic polarizabilities of the Cr and X atoms at an imaginary frequency, $\alpha_{\mathrm{Cr}/X}(i\omega)$. The dynamic electric dipole polarizability is given by

$$\alpha_X(\omega) = \sum_n \frac{f_{0n}^X}{\omega_{X,0n}^2 - \omega^2}, \tag{6}$$

where f_{0n}^X denotes the oscillator strength between the atomic ground state and the nth atomic excited state, and $\omega_{X,0n}$ is the excitation energy to that state.

The dynamic electric dipole polarizabilities at an imaginary frequency of the alkali-earth-metal atoms were taken from the work by Derevianko *et al.* [48], whereas the dynamic polarizability of the ytterbium atom was obtained by using the explicitly connected representation of the expectation

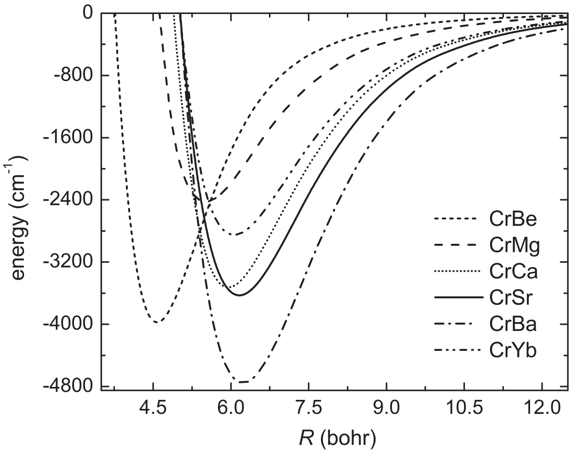

FIG. 1. Potential energy curves of the $X^7\Sigma^+$ electronic ground state of the CrBe, CrMg, CrCa, CrSr, CrBa, and CrYb molecules.

value and polarization propagator within the coupled cluster method [49] and the best approximation XCCSD4 proposed by Korona and collaborators [50]. The dynamic polarizability of the chromium atom was constructed as a sum over states, Eq. (6). The oscillator strengths and energy levels for the discrete transitions were taken from the NIST Atomic Spectra Database [51], whereas the contribution form the bound-continuum transitions were included as a sum over oscillator strengths to quasibound states obtained within the multireference configuration interaction method.

All calculations were performed with the MOLPRO package of *ab initio* programs [52].

III. NUMERICAL RESULTS AND DISCUSSION

A. Potential energy curves

The computed potential energy curves of the $X^7\Sigma^+$ electronic ground state of the CrBe, CrMg, CrCa, CrSr, CrBa, and CrYb molecules are presented in Fig. 1 and the corresponding long-range C_6 coefficients are reported in Table I. The equilibrium distances R_e and well depths D_e are also collected in Table I.

An inspection of Fig. 1 reveals that all potential energy curves show a smooth behavior with well-defined minima. The well depths of the chromium–alkaline-earth-metal-atom and chromium–ytterbium molecules are significantly larger (by a factor of 2 to 4) than those of the Van der Waals type homonuclear alkaline-earth-metal-atom [53–55] or ytterbium molecules [56]. The largest dissociation energy is 4723 cm^{-1} for the CrBa molecule and the smallest one is 2371 cm^{-1} for the CrMg molecule. The equilibrium distances take values between 4.56 bohr for the CrBe molecule up to 6.22 bohr for the CrBa molecule. The dissociation energies and equilibrium distances of the investigated molecules are systematically increasing with the increasing mass of the alkaline-earth-metal atom, except for the dissociation energy of the CrBe molecule which is much larger than expected. However, the much stronger binding energy and shorter equilibrium distance of the CrBe molecule is not surprising when we know that the beryllium dimer has an unexpectedly strong bonding interaction, substantially stronger and shorter than those between other similarly sized closed-shell atoms [57]. The C_6 coefficients are rather small and typical for the Van der Waals type molecules.

The existence of the potential energy crossing between the $X^7\Sigma^+$ state and some lower spin state is very unlikely. The lower spin states are higher in energy because either they are connected with the excited states of chromium and then the interaction energy is of the same order as for the ground state or they are connected with the excited states of the closed-shell atom with excitation energies much larger than the depth of potentially deep potential energy curves. Therefore, the ultracold collisions between the ground-state chromium and close-shell atoms should fully be described on the $X^7\Sigma^+$ potential energy curve.

Ab initio potentials were used to calculate the rovibrational spectra of the $X^7\Sigma^+$ electronic ground states for the molecules consisting of the most abundant isotopes. The harmonic frequencies ω_0 and the numbers of the supported bound states for the angular momentum $J = 0$, N_υ, are reported in Table I. Rotational constants for the rovibrational ground state $\upsilon = 0, J = 0$ were also calculated and are reported in Table I.

B. Permanent electric dipole moments and static electric dipole polarizabilities

Static electric or far-off resonant laser fields can be used to manipulate and control the dynamics of molecules at ultralow temperatures [15]. A static electric field couples with an intrinsic molecular electric dipole moment orienting molecules whereas a nonresonant laser field influences the molecular

TABLE I. Spectroscopic characteristics: Equilibrium bond length R_e, well depth D_e, harmonic frequency ω_0, number of bound vibrational states N_υ, and long-range dispersion coefficient C_6, of the $X^7\Sigma^+$ ground electronic state and rotational constant B_0, electric dipole moment d_0, average polarizability $\bar{\alpha}_0$, and polarizability anisotropy $\Delta\alpha_0$, for the rovibrational ground level of the $X^7\Sigma^+$ ground electronic state of the CrBe, CrMg, CrCa, CrSr, CrBa, and CrYb molecules. $\tilde{C}_6$ is the coefficient for the intermolecular dispersion interaction between molecules in the ground rovibrational level.

Molecule	R_e (bohr)	D_e (cm^{-1})	ω_0 (cm^{-1})	N_υ	B_0 (cm^{-1})	d_0 (D)	$\bar{\alpha}_0$ (a.u.)	$\Delta\alpha_0$ (a.u.)	C_6 (a.u.)	$\tilde{C}_6$ (a.u.)
^{52}Cr^{9}Be	4.56	4018	319	29	0.377	1.43	121.4	102.3	383	1.5×10^4
^{52}Cr^{24}Mg	5.50	2441	141	39	0.121	0.10	170.8	158.3	667	1.1×10^4
^{52}Cr^{40}Ca	5.94	3548	136	62	0.076	−0.76	248.9	178.1	1232	2.7×10^4
^{52}Cr^{88}Sr	6.15	3649	107	75	0.049	−1.48	283.5	176.1	1488	1.2×10^5
^{52}Cr^{138}Ba	6.22	4776	106	94	0.041	−2.67	345.6	121.9	1905	1.1×10^6
^{52}Cr^{174}Yb	6.05	2866	87.8	73	0.041	−1.19	242.9	178.9	1195	6.5×10^4

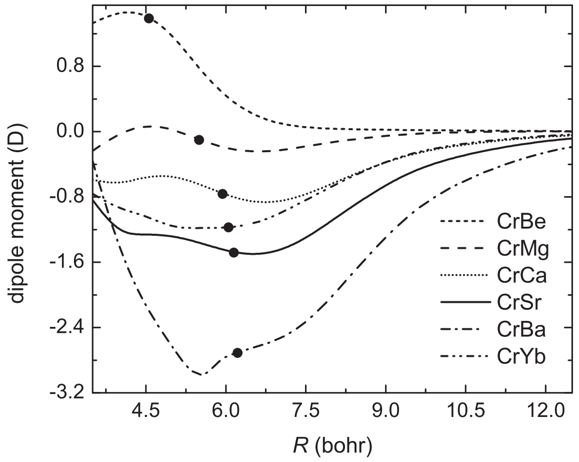

FIG. 2. Permanent electric dipole moments of the $X^7\Sigma^+$ electronic ground state of the CrBe, CrMg, CrCa, CrSr, CrBa, and CrYb molecules. Points indicate the values for the ground rovibrational level.

dynamics by coupling with a dipole polarizability anisotropy aligning molecules. Both can drastically influence the dynamics and enhance intermolecular interaction, therefore the electric dipole moment and electric dipole polarizability are important properties of ultracold molecules.

The permanent electric dipole moments of the $X^7\Sigma^+$ electronic ground state of the CrBe, CrMg, CrCa, CrSr, CrBa, and CrYb molecules as functions of the interatomic distance R are presented in Fig. 2 and the values for the ground rovibrational level are reported in Table I.

We have found that the CrBa molecule has the largest electric dipole moment in the rovibrational ground state, 2.67 D, only slightly smaller than the CrRb molecule with 2.9 D [29]. However, the CrSr and CrYb molecules have also significant dipole moments 1.48 and 1.19 D, respectively. Since cooling techniques for the Sr and Yb atoms are much further established, the CrSr and CrYb molecules should be considered in the first place as candidates for ultracold molecules with both large magnetic and electric dipole moments. The electric dipole moments of the CrSr and CrYb molecules have the values two times larger than the KRb molecule, 0.6 D [58], and similar to the RbCs molecule, 1.2 D [58], or RbSr molecule, 1.36 D [26].

There are two independent components of the polarizability tensor for molecules in the Σ electronic state, i.e., the parallel component $\alpha_\parallel \equiv \alpha_{zz}$ and perpendicular one $\alpha_\perp \equiv \alpha_{xx} = \alpha_{yy}$. Equivalently, the polarizability anisotropy $\Delta\alpha = \alpha_\parallel - \alpha_\perp$ and the average polarizability $\bar{\alpha} = (\alpha_\parallel + 2\alpha_\perp)/3$ can be considered.

The average polarizability and the polarizability anisotropy of the $X^7\Sigma^+$ electronic ground state of the CrBe, CrMg, CrCa, CrSr, CrBa, and CrYb molecules are presented in Fig. 3 and the values for the ground rovibrational level are reported in Table I. The polarizabilities show an overall smooth behavior and tend smoothly to their asymptotic atomic values. The interaction-induced variation of the polarizability is clearly visible while changing the internuclear distance R.

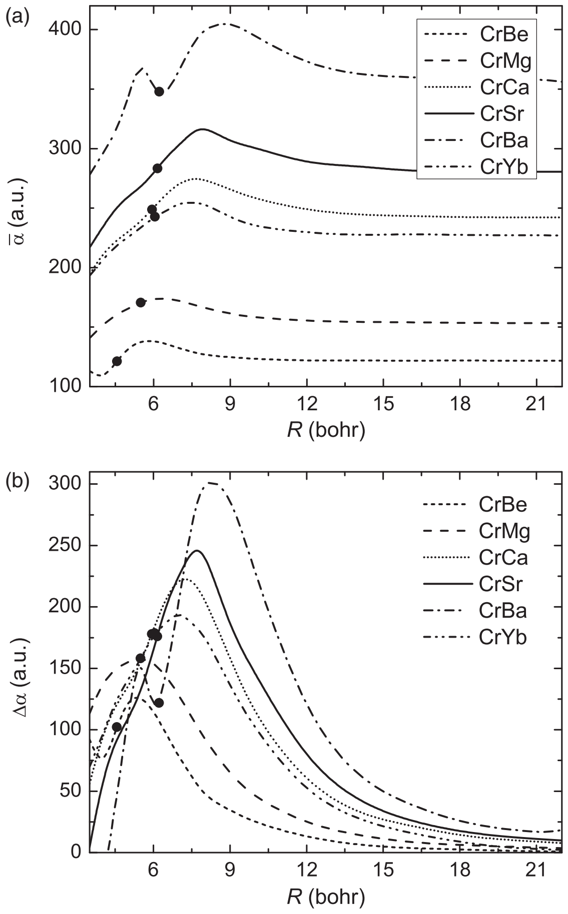

FIG. 3. The average polarizability (upper panel) and polarizability anisotropy (lower panel) of the $X^7\Sigma^+$ electronic ground state of the CrBe, CrMg, CrCa, CrSr, CrBa, and CrYb molecules. Points indicate the values for the ground rovibrational level.

The polarizability anisotropy $\Delta\alpha$ is the quantity responsible for the strength of the alignment and the influence of the nonresonant field on the rovibrational dynamics [59,60]. The larger the average polarizability $\bar{\alpha}$, the easier it is to trap molecules in an optical lattice. The CrSr and CrYb molecules have the largest values of the polarizability anisotropy among the investigated molecules, 176.1 and 178.9 a.u., respectively, in the ground rovibrational state. Therefore, the alignment and control of their dynamics with the nonresonant field should be the easiest and require the lowest field intensity.

In the present work, we have calculated static polarizabilities which describe the interaction of molecules with far nonresonant field from a 10-μm carbon dioxide laser. When the shorter-wavelength field is applied the dynamic polarizabilities have to be used, which usually are larger but of the same order of magnitude as the static ones. Once the wavelength of laser used to control molecules in the experiment will be known, the dynamic polarizabilities can be calculated from linear response theory [61].

C. Accuracy analysis

The discussion of the accuracy of the *ab initio* electronic structure calculations requires addressing the following issues:

(1) the capability of the computational method to reproduce completely the correlation energy,

(2) the completeness of the basis functions set,
(3) the relativistic effects.

The CCSD(T) method is the gold standard of quantum chemistry and a good compromise between the accuracy and the computational cost [62]. It reproduces molecular properties such as equilibrium geometries and dissociation energies with the chemical accuracy [63]. We have used the spin-restricted RCCSD(T) method in contrast to the existing spin-unrestricted UCCSD(T) method [37] because the spin unrestricted version can potentially lead to the spin contamination for high-spin system such as molecules containing a chromium atom. However, the difference in the interaction energy obtained with two methods is insignificant (less than 2% in the present case).

Previous calculations for the ground-state molecules containing closed-shell atoms reveal that the CCSD(T) method reproduces the potential well depths with an error of a few percent comparing to experimental results. For example, an error for Mg_2 is 0.5% [53], for Ca_2 is 1.5% [55], and for Sr_2 is 3.8% [54]. For the two-valence-electron Rb_2 molecule even calculation at the CCSD level gives an error of only 2.7% [64]. However, the chromium atom has six valence electrons in the open shell and we have found that the inclusion of the noniterative triple excitations in the CCSD(T) method accounts for about 30% of the interaction energy in the chromium–closed-shell-atom molecules. The inclusion of full triple or higher excitations in the coupled cluster calculations with high quality basis set for such a large system is computationally unfeasible. Therefore, to estimate the importance of the higher excitations we performed RCCSD(T) and RCCSDT calculation in small aug-cc-pVDZ-DK basis sets for the CrBe, CrMg, and CrCa molecules and we have found that the inclusion of the full triple excitations increases the interaction energy by 7%, on the average. The lack of the higher excitations should be less important and we estimate the uncertainty of the interaction energy due to the incompleteness of the correlation energy is of the order of 10%.

The quintuple-ζ quality basis sets augmented by the midbond functions used in the present calculations are very extensive computational basis sets that should provide results very close to the complete basis set limit [65]. To evaluate the completeness of them we calculated potential energy curves using the series of the aug-pVnZ-DK basis sets with $n = T,Q,5$, with and without bond functions. Based on these results we estimate the uncertainty of the interaction energy due to the incompleteness of the basis sets is smaller than 2%.

The calculation of the atomic electric dipole polarizability is another check for the quality of the used atomic basis sets and completeness of the method. The polarizability of the chromium atom from the present calculations is 86.7 a.u., whereas the polarizabilities of the beryllium, magnesium, calcium, strontium, barium, and ytterbium atoms are 37.87, 71.7, 158.6, 199.0, 275.5, and 143.9 a.u., respectively. These values are in a good agreement with the most sophisticated calculations by Porsev and Derevianko [66]: 37.76, 71.26, 157.1, 197.2, and 273.5 a.u. for Be, Mg, Ca, Sr, and Ba, respectively, and with the value 143 a.u. for the Yb atom recommended by Zhang and Dalgarno [67]. The polarizability of Cr is in agreement with value 85.0 a.u. obtained by Pavlovic *et al.* [68].

To evaluate the importance of the relativistic effects on the properties of the considered molecules we additionally calculated potential energy curves with the standard nonrelativistic Hamiltonian and compared them with the ones obtained using the relativistic DKH Hamiltonian. The well depths are underestimated, on the average by 8%, and the equilibrium lengths are longer when the relativistic effects are not accounted for. This is not surprising since the relativistic contribution to the bonding for the transition metal atoms cannot be neglected even for the comparatively light chromium atom [69]. The relativistic effects in the CrBe, CrMg, and CrCa molecules were accounted for with the DKH Hamiltonian whereas for the CrSr, CrBa, and CrYb molecules by using energy-consistent pseudopotentials. Therefore, to check the performance of the calculations with ECP we compared the potential well depths of the CrBe, CrMg, and CrCa molecules obtained with the DKH Hamiltonian with the ones obtained using energy-consistent pseudopotentials. The difference between the results obtained with these two methods is of the order of 2%, which is much smaller than the relativistic contribution and confirms the validity of the employed approach.

Based on the above analysis, we estimate that the total uncertainty of the calculated potential energy curves and electronic properties is of the order of 10% and the lack of the exact treatment of the triple and higher excitations in the employed CCSD(T) method is a preliminary limiting factor.

The accuracy of the calculated C_6 coefficients is directly related to the accuracy of the input dynamic polarizabilities at an imaginary frequency. For the Be, Mg, Ca, Sr, and Ba atoms they were taken from Derevianko *et al.* [48] with the accuracy estimated by these authors at the level of 1%. The accuracy of the polarizability of the Yb atom is a few percent. Therefore, the uncertainty of the polarizability of the Cr atom, which is of the order of 5%, is a limiting factor for the accuracy of the C_6 coefficients. We estimate that the uncertainty of the computed C_6 coefficients is 5%. The agreement between the raw *ab initio* data and the asymptotic expansion, Eq. (4), is of the order of 1–3% at $R \approx 30$ bohr for all investigated molecules.

D. Characteristic energy and length scales

The investigated molecules have both significant magnetic and electric dipole moments. Therefore, to get a good understanding of their collisional properties at ultralow temperatures and the interplay between the electric dipole-dipole, magnetic dipole-dipole, and long-range dispersion interactions it is important to understand the various length and energy scales associated with them. One can define a characteristic length scale R_i of the given type of interaction by equating the kinetic energy $\hbar^2/\mu R_i^2$ to the interaction potential $V_i(R_i)$ [70]. The characteristic length scales allow to estimate at what distance a given type of interaction starts to affect the dynamics of colliding ultracold molecules and to compare the possible influence of different types of interactions on the collisional properties. For the electric dipole-dipole $d_e^2(1-3\cos\theta)/R^3$, magnetic dipole-dipole $\alpha^2 d_m^2(1-3\cos\theta)/R^3$, and van der Waals $-\tilde{C}_6/R^6$ interactions the characteristic electric dipole R_3^d, magnetic dipole R_3^m, and van der Waals R_6 lengths are given by

$$R_3^d = \frac{2\mu d_e^2(F)}{\hbar^2}, \tag{7}$$

$$R_3^m = \frac{2\mu\alpha^2 d_m^2}{\hbar^2}, \tag{8}$$

$$R_6 = \left(\frac{2\mu\tilde{C}_6}{\hbar^2}\right)^{1/4}, \tag{9}$$

where $\mu = m_{\mathrm{Cr}X}/2$ is the reduced mass of the pair of molecules, each with mass $m_{\mathrm{Cr}X}$, $d_e(F)$ is the induced electric dipole moment at electric field F, $d_m = 6\mu_B$ is the magnetic dipole moment (μ_B is Bohr magneton), and $\tilde{C}_6$ is the van der Waals dispersion coefficient for the intermolecular interaction. The $\tilde{C}_6$ coefficients for the interaction between chromium–closed-shell-atom molecules were obtained using the simple model

$$\tilde{C}_6 \approx \frac{3}{4}U\bar{\alpha}_0^2 + \frac{d_0^4}{6B_0}, \tag{10}$$

where the first term is the electronic contribution estimated with the Unsöld approximation [71] and the second, much larger term, is the contribution from the rotational states calculated assuming molecules in the rovibrational ground state $v = 0, J = 0$. U is the mean excitation energy, $\bar{\alpha}_0 = (\alpha_0^{\parallel} + 2\alpha_0^{\perp})/3$ is the mean dipole polarizability, d_0 is the electric dipole moment, and B_0 is the rotational constant of the molecule in the rovibrational ground state. The computed $\tilde{C}_6$ coefficients are reported in Table I.

Figure 4 presents the characteristic length scales for the chromium–closed-shell-atom molecules in the rovibrational ground state. The chemical bond length R_e is the shortest distance. The magnetic dipole length for all species is larger than the van der Waals length, and for the heaviest CrSr, CrYb, and CrBa, it exceeds 100 bohr and is two times larger than for the atomic chromium and of the same order as for the erbium atoms. The electric dipole lengths for the maximal possible dipole moments are much larger than the magnetic dipole lengths. However, the electric dipole moment for a molecule in the rovibrational ground state has to be induced by an external electric field that allows to tune the electric dipole lengths in a wide range of values. Finally, an inspection of Fig. 4 reveals that the intermolecular magnetic dipole-dipole interaction should affect the properties of an ultracold gas of heavy molecules containing chromium atom to a larger extent than it was observed for the ultracold gas of atomic chromium and a competition between the magnetic and electric dipolar interactions should be an interesting problem in ultracold many-body physics.

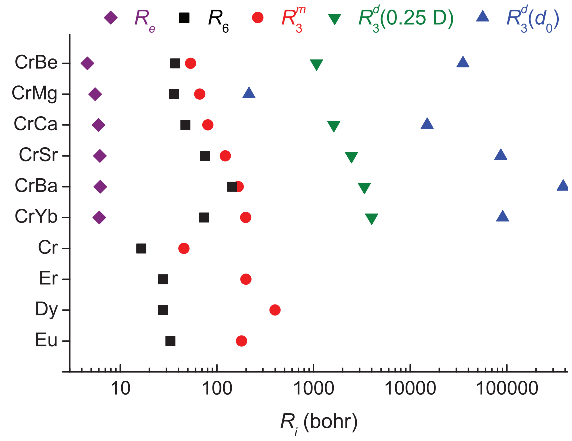

FIG. 4. (Color online) Characteristic length scales R_e, R_6, R_3^m, and R_3^d for the chromium–closed-shell-atom molecules in the rovibrational ground state and for highly magnetic atoms (electric dipole length R_3^d for the maximal possible electric dipole moment and for 0.25 D).

The stability of an ultracold molecular gas against reactive collisions is an important issue. Since the low-spin Cr_2 molecule has a very large binding energy [68], much larger than the binding energy of the chromium–closed-shell-atom molecules, there always exists the reactive channel for the collision of two chromium–closed-shell-atom molecules,

$$2\,\mathrm{Cr}X(^7\Sigma^+) \rightarrow \mathrm{Cr}_2(^{2S+1}\Sigma_g^+) + X_2(^1\Sigma_g^+), \tag{11}$$

yielding to the chromium molecule in the low-spin state. However, the channel leading to the high-spin Cr_2 molecule is closed and one can try to suppress the reactive collisions by applying the magnetic field to restrict molecular dynamics to the maximally spin-stretched electronic potential surface. On the other hand, the reactive collisions can be suppressed by applying static electric field to control the long-range dipolar interaction and by confining molecules in an optical latice to reduce the dimensionality [15].

IV. SUMMARY AND CONCLUSION

In the present work we have investigated the *ab initio* properties of the chromium–alkaline-earth-metal-atom and chromium–yterbium molecules. Potential energy curves, permanent electric dipole moments, and static electric dipole polarizabilities for the molecules in the $X^7\Sigma^+$ electronic ground state were obtained with the spin-restricted open-shell coupled cluster method restricted to single, double, and noniterative triple excitations, RCCSD(T), in the Born-Oppenheimer approximation. The scalar relativistic effects within Douglas-Kroll-Hess Hamiltonian or energy-consistent pseudopotentials were included. The properties of the molecules in the rovibrational ground state were analyzed. The leading long-range coefficients describing the dispersion interaction between the atoms at large interatomic distances, C_6, were also computed.

We have found that CrSr and CrYb are the most promising candidates for the ultracold chromium–closed-shell-atom molecules possessing both relatively large electric and large magnetic dipole moments. This makes them potentially interesting candidates for ultracold collisional studies of dipolar molecules in the combined electric and magnetic fields when the magnetic dipole-dipole interaction can compete with the electric dipole-dipole interaction. An inspection of the characteristic interaction length scales reveals that the magnetic dipole-dipole interaction for the CrSr and CrYb molecules is of the same order as for the highly magnetic erbium atoms, larger than for the chromium atoms due to larger reduced masses. The strength of the electric dipole-dipole interaction is controllable as electric dipole moments have to be induced by an external electric field. At the same time the large polarizability anisotropy of these molecules allows for the nonresonant light control.

The formation of the proposed molecules will be the subject of a future investigation. Nevertheless, in a similar fashion to the proposals by Żuchowski *et al.* [28] and Brue and Hutson [26], the magnetoassociation using the interaction-induced variation of the hyperfine coupling constants can be considered in the case of the fermionic ^{53}Cr atom (provided the widths of the Feshbach resonances are sufficiently broad). On the other hand, a photoassociation near the intercombination line transition of the atomic strontium or ytterbium with the subsequent stabilization into the deeply bound vibrational level of the electronic ground state, similar as predicted for SrYb [72] or Sr_2 [73], can be proposed. To enhance molecule formation, STIRAP with atoms in a Mott insulator state produced by loading the BEC into an optical lattice [74] or nonresonant field control [59] can be employed.

The present paper draws attention to the highly magnetic polar molecules formed from highly magnetic atom and closed-shell atom and paves the way towards a more elaborate study of the magnetoassociation or photoassociation and application of these polar and magnetic molecules in ultracold many-body physics studies.

ACKNOWLEDGMENTS

We would like to thank Robert Moszynski, Piotr Żuchowski, and Jedrzej Kaniewski for many useful discussions. Financial support from the Polish Ministry of Science and Higher Education through the Project No. N204 215539 and from the Foundation for Polish Science within MPD Program cofinanced by the EU European Regional Development Fund is gratefully acknowledged.

[1] *Cold Atoms and Molecules*, edited by M. Weidemüller and C. Zimmermann (Wiley, New York, 2009).
[2] J. Weiner, V. S. Bagnato, S. Zilio, and P. S. Julienne, Rev. Mod. Phys. **71**, 1 (1999).
[3] J. Ulmanis, J. Deiglmayr, M. Repp, R. Wester, and M. Weidemüller, Chem. Rev. **112**, 4890 (2012).
[4] A. Griesmaier, J. Werner, S. Hensler, J. Stuhler, and T. Pfau, Phys. Rev. Lett. **94**, 160401 (2005).
[5] K. Aikawa, A. Frisch, M. Mark, S. Baier, A. Rietzler, R. Grimm, and F. Ferlaino, Phys. Rev. Lett. **108**, 210401 (2012).
[6] M. Lu, N. Q. Burdick, S. H. Youn, and B. L. Lev, Phys. Rev. Lett. **107**, 190401 (2011).
[7] S. Kraft, F. Vogt, O. Appel, F. Riehle, and U. Sterr, Phys. Rev. Lett. **103**, 130401 (2009).
[8] S. Stellmer, M. K. Tey, B. Huang, R. Grimm, and F. Schreck, Phys. Rev. Lett. **103**, 200401 (2009).
[9] Y. N. Martinez de Escobar, P. G. Mickelson, M. Yan, B. J. DeSalvo, S. B. Nagel, and T. C. Killian, Phys. Rev. Lett. **103**, 200402 (2009).
[10] S. Stellmer, M. K. Tey, R. Grimm, and F. Schreck, Phys. Rev. A **82**, 041602 (2010).
[11] P. G. Mickelson, Y. N. Martinez de Escobar, M. Yan, B. J. DeSalvo, and T. C. Killian, Phys. Rev. A **81**, 051601 (2010).
[12] T. Fukuhara, S. Sugawa, and Y. Takahashi, Phys. Rev. A **76**, 051604 (2007).
[13] Y. Takasu, K. Maki, K. Komori, T. Takano, K. Honda, M. Kumakura, T. Yabuzaki, and Y. Takahashi, Phys. Rev. Lett. **91**, 040404 (2003).
[14] *Cold Molecules: Theory, Experiment, Applications*, edited by R. Krems, B. Friedrich, and W. C. Stwalley (CRC Press, Boca Raton, FL, 2009).
[15] G. Quemener and P. S. Julienne, Chem. Rev. **112**, 4949 (2012).
[16] H. Hara, Y. Takasu, Y. Yamaoka, J. M. Doyle, and Y. Takahashi, Phys. Rev. Lett. **106**, 205304 (2011).
[17] V. V. Ivanov, A. Khramov, A. H. Hansen, W. H. Dowd, F. Münchow, A. O. Jamison, and S. Gupta, Phys. Rev. Lett. **106**, 153201 (2011).
[18] F. Baumer, F. Münchow, A. Görlitz, S. E. Maxwell, P. S. Julienne, and E. Tiesinga, Phys. Rev. A **83**, 040702 (2011).
[19] N. Nemitz, F. Baumer, F. Münchow, S. Tassy, and A. Görlitz, Phys. Rev. A **79**, 061403 (2009).
[20] S. L. Cornish (unpublished).
[21] B. Pasquiou, A. Bayerle, S. Tzanova, S. Stellmer, J. Szczepkowski, M. Parigger, R. Grimm, and F. Schreck, arXiv:1305.5935.
[22] S. Kotochigova, A. Petrov, M. Linnik, J. Kłos, and P. S. Julienne, J. Chem. Phys. **135**, 164108 (2011).
[23] G. Gopakumar, M. Abe, M. Kajita, and M. Hada, Phys. Rev. A **84**, 062514 (2011).
[24] P. Zhang, H. R. Sadeghpour, and A. Dalgarno, J. Chem. Phys. **133**, 044306 (2010).
[25] G. Gopakumar, M. Abe, B. P. Das, M. Hada, and K. Hirao, J. Chem. Phys. **133**, 124317 (2010).
[26] D. A. Brue and J. M. Hutson, Phys. Rev. Lett. **108**, 043201 (2012).
[27] R. Guérout, M. Aymar, and O. Dulieu, Phys. Rev. A **82**, 042508 (2010).
[28] P. S. Żuchowski, J. Aldegunde, and J. M. Hutson, Phys. Rev. Lett. **105**, 153201 (2010).
[29] Z. Pavlović, H. R. Sadeghpour, R. Côté, and B. O. Roos, Phys. Rev. A **81**, 052706 (2010).
[30] D.-H. Jeung, D. Hagebaum-Reignier, and M. J. Jamieson, J. Phys. B: At. Mol. Opt. Phys. **43**, 235208 (2010).
[31] S. Hensler, A. Griesmaier, J. Werner, A. Görlitz, and T. Pfau, J. Mod. Opt. **51**, 1807 (2004).
[32] A. Petrov, E. Tiesinga, and S. Kotochigova, Phys. Rev. Lett. **109**, 103002 (2012).
[33] K. K. Ni, S. Ospelkaus, M. H. G. de Miranda, A. Pe'er, B. Neyenhuis, J. J. Zirbel, S. Kotochigova, P. S. Julienne, D. S. Jin, and J. Ye, Science **322**, 231 (2008).
[34] J. Deiglmayr, A. Grochola, M. Repp, K. Mörtlbauer, C. Glück, J. Lange, O. Dulieu, R. Wester, and M. Weidemüller, Phys. Rev. Lett. **101**, 133004 (2008).
[35] P. S. Żuchowski (unpublished).
[36] J. D. Weinstein, R. deCarvalho, J. Kim, D. Patterson, B. Friedrich, and J. M. Doyle, Phys. Rev. A **57**, R3173 (1998).
[37] P. J. Knowles, C. Hampel, and H.-J. Werner, J. Chem. Phys. **99**, 5219 (1993).

[38] S. Boys and F. Bernardi, Mol. Phys. **19**, 553 (1970).
[39] M. Reiher, Theor. Chem. Acc. **116**, 241 (2006).
[40] M. Dolg and X. Cao, Chem. Rev. **112**, 403 (2012).
[41] N. B. Balabanov and K. A. Peterson, J. Chem. Phys. **123**, 064107 (2005).
[42] J. Koput and K. Peterson, J. Phys. Chem. A **106**, 9595 (2002).
[43] M. Dolg, U. Wedig, H. Stoll, and H. Preuss, J. Chem. Phys. **86**, 866 (1987).
[44] I. S. Lim, H. Stoll, and P. Schwerdtfeger, J. Chem. Phys. **124**, 034107 (2006).
[45] Y. Wang and M. Dolg, Theor. Chem. Acc. **100**, 124 (1998).
[46] F.-M. Tao and Y.-K. Pan, J. Chem. Phys. **97**, 4989 (1992).
[47] T. G. A. Heijmen, R. Moszynski, P. E. S. Wormer, and A. van der Avoird, Mol. Phys. **89**, 81 (1996).
[48] A. Derevianko, S. G. Porsev, and J. F. Babb, At. Data Nucl. Data Tables **96**, 323 (2010).
[49] R. Moszynski, P. Zuchowski, and B. Jeziorski, Collect. Czech. Chem. Commun. **70**, 1109 (2005).
[50] T. Korona, M. Przybytek, and B. Jeziorski, Mol. Phys. **104**, 2303 (2006).
[51] NIST Atomic Spectra Database http://physics.nist.gov/PhysRefData/ASD.
[52] H.-J. Werner, P. J. Knowles, F. R. M. R. Lindh, M. Schütz, P. Celani, T. Korona, G. Rauhut, R. D. Amos, A. Bernhardsson, A. Berning, D. L. Cooper, M. J. O. Deegan, A. J. Dobbyn, E. G. F. Eckert, C. Hampel, G. Hetzer, A. W. Lloyd, S. J. McNicholas, W. Meyer, M. E. Mura, A. Nicklass, P. Palmieri, R. Pitzer, U. Schumann, H. Stoll, A. J. Stone, R. Tarroni, T. Thorsteinsson, M. Wang, and A. Wolf, MOLPRO, *version 2012.1, a package of ab initio programs* (2012), see http://www.molpro.net.
[53] L. Rybak, S. Amaran, L. Levin, M. Tomza, R. Moszynski, R. Kosloff, C. P. Koch, and Z. Amitay, Phys. Rev. Lett. **107**, 273001 (2011).
[54] W. Skomorowski, F. Pawlowski, C. P. Koch, and R. Moszynski, J. Chem. Phys. **136**, 194306 (2012).
[55] B. Bussery-Honvault, J.-M. Launay, and R. Moszynski, Phys. Rev. A **68**, 032718 (2003).
[56] A. A. Buchachenko, G. Chalasinski, and M. M. Szczesniak, Eur. Phys. J. D **45**, 147 (2007).
[57] K. Patkowski, V. Spirko, and K. Szalewicz, Science **326**, 1382 (2009).
[58] M. Aymar and O. Dulieu, J. Chem. Phys. **122**, 204302 (2005).
[59] R. González-Férez and C. P. Koch, Phys. Rev. A **86**, 063420 (2012).
[60] M. Tomza, W. Skomorowski, M. Musial, R. Gonzalez Ferez, C. Koch, and R. Moszynski, Mol. Phys. (2013), doi: 10.1080/00268976.2013.793835.
[61] J. Olsen and P. Jorgensen, J. Chem. Phys. **82**, 3235 (1985).
[62] R. J. Bartlett and M. Musial, Rev. Mod. Phys. **79**, 291 (2007).
[63] K. L. Bak, J. Gauss, P. Jorgensen, J. Olsen, T. Helgaker, and J. F. Stanton, J. Chem. Phys. **114**, 6548 (2001).
[64] M. Tomza, M. H. Goerz, M. Musiał, R. Moszynski, and C. P. Koch, Phys. Rev. A **86**, 043424 (2012).
[65] W. Skomorowski, F. Pawlowski, T. Korona, R. Moszynski, P. S. Zuchowski, and J. M. Hutson, J. Chem. Phys. **134**, 114109 (2011).
[66] S. G. Porsev and A. Derevianko, JETP **102**, 195 (2006).
[67] P. Zhang and A. Dalgarno, J. Phys. Chem. A **111**, 12471 (2007).
[68] Z. Pavlović, B. O. Roos, R. Côté, and H. R. Sadeghpour, Phys. Rev. A **69**, 030701 (2004).
[69] M. Pelissier, J. Daudey, J. Malrieu, and G. Jeung, in *Quantum Chemistry: The Challenge of Transition Metals and Coordination Chemistry*, NATO ASI Series, Vol. 176, edited by A. Veillard (Springer, Dordrecht, The Netherlands, 1986), pp. 37–51.
[70] P. S. Julienne, T. M. Hanna, and Z. Idziaszek, Phys. Chem. Chem. Phys. **13**, 19114 (2011).
[71] A. Unsöld, Z. Phys. **43**, 563 (1927).
[72] M. Tomza, F. Pawlowski, M. Jeziorska, C. P. Koch, and R. Moszynski, Phys. Chem. Chem. Phys. **13**, 18893 (2011).
[73] W. Skomorowski, R. Moszynski, and C. P. Koch, Phys. Rev. A **85**, 043414 (2012).
[74] D. Jaksch, V. Venturi, J. I. Cirac, C. J. Williams, and P. Zoller, Phys. Rev. Lett. **89**, 040402 (2002).

Appendix F

Paper VI

"Chemical reactions of ultracold alkali-metal dimers
in the lowest-energy ${}^3\Sigma$ state"

Michał Tomza, Kirk W. Madison, Robert Moszynski, Roman V. Krems

Physical Review A, **88**, 050701(R) (2013).

RAPID COMMUNICATIONS

PHYSICAL REVIEW A **88**, 050701(R) (2013)

Chemical reactions of ultracold alkali-metal dimers in the lowest-energy $^3\Sigma$ state

Michał Tomza,[1,2] Kirk W. Madison,[3] Robert Moszynski,[2] and Roman V. Krems[1]
[1]*Department of Chemistry, University of British Columbia, Vancouver, British Columbia, Canada V6T 1Z1*
[2]*Faculty of Chemistry, University of Warsaw, Pasteura 1, 02-093 Warsaw, Poland*
[3]*Department of Physics, University of British Columbia, Vancouver, British Columbia, Canada V6T 1Z1*

(Received 22 August 2013; published 21 November 2013)

We show that the interaction of polar alkali-metal dimers in the quintet spin state leads to the formation of a deeply bound reaction complex. The reaction complex can decompose adiabatically into homonuclear alkali-metal dimers (for all molecules except KRb) and into alkali-metal trimers (for all molecules). We show that there are no barriers for these chemical reactions. This means that all alkali-metal dimers in the $a^3\Sigma^+$ state are chemically unstable at ultracold temperature, and the use of an optical lattice to segregate the molecules and suppress losses may be necessary. In addition, we calculate the minimum-energy path for the chemical reactions of alkali-metal hydrides. We find that the reaction of two molecules is accelerated by a strong attraction between the alkali-metal atoms, leading to a barrierless process that produces hydrogen atoms with large kinetic energy. We discuss the unique features of the chemical reactions of ultracold alkali-metal dimers in the $a^3\Sigma^+$ electronic state.

DOI: 10.1103/PhysRevA.88.050701 PACS number(s): 34.20.−b, 34.50.Lf, 34.50.Cx, 31.15.ae

The creation of ultracold, deeply bound dimers from laser-cooled alkali-metal atoms can be achieved by photoassociation or by magnetoassociation followed by coherent transfer to a lower-energy state by stimulated Raman adiabatic passage [1,2]. The interaction of two ground-state alkali-metal atoms gives rise to two molecular states: $X^1\Sigma^+$ and $a^3\Sigma^+$. The majority of experiments thus far have focused on the association of alkali-metal atoms into the $X^1\Sigma^+$ state. Fueled by the promise of exciting applications [1,3], the main goal of these experiments is to produce heteronuclear (polar) alkali-metal dimers in the rovibrational ground state. The creation of polar alkali-metal dimers in the rovibrational ground state of the $a^3\Sigma^+$ electronic state [2] is currently emerging as another important research goal. Heteronuclear molecules in the $a^3\Sigma^+$ state offer both the electric and magnetic dipole moments. This can be exploited for a variety of novel applications [1,4,5]. However, alkali-metal dimers in the $a^3\Sigma^+$ state may undergo inelastic collisions and chemical reactions, necessitating the use of an optical lattice to segregate the molecules and suppress losses [6].

For alkali-metal dimers $AB(a^3\Sigma^+)$ in the ground rovibrational state, the following reaction processes may lead to collisional losses:

$$AB(a^3\Sigma^+) + AB(a^3\Sigma^+) \to A_2(a^3\Sigma^+) + B_2(a^3\Sigma^+), \quad (1)$$

$$AB(a^3\Sigma^+) + AB(a^3\Sigma^+) \to A_2B + B, \quad (2)$$

$$AB(a^3\Sigma^+) + AB(a^3\Sigma^+) \to A_2(X^1\Sigma^+) + B_2(T), \quad (3)$$

$$AB(a^3\Sigma^+) + AB(a^3\Sigma^+) \to AB(X^1\Sigma^+) + AB(T), \quad (4)$$

where T is either $X^1\Sigma^+$ or $a^3\Sigma^+$. Reactions (3) and (4) can potentially be suppressed by confining $AB(a^3\Sigma^+)$ molecules in a magnetic trap. Magnetic trapping aligns the electron spin of molecules along the magnetic-field axis, which restricts the total electron spin of the $AB(a^3\Sigma^+)$-$AB(a^3\Sigma^+)$ collision complex to the maximum value $\mathcal{S} = 2$. Reactions (3) and (4) involve transitions to lower spin states mediated by nonadiabatic spin-dependent couplings [7]. These couplings are induced by the long-range magnetic dipole-dipole interaction $V_{\mathrm{d-d}}$ and the spin-dependent fine-structure interactions effective at short intermolecular separations. The effect of $V_{\mathrm{d-d}}$ can generally be ignored [7]. The effect of the short-range couplings depends on the topology of the potential energy surface of the $AB(a^3\Sigma^+)$-$AB(a^3\Sigma^+)$ complex in the $\mathcal{S} = 2$ state. The probability of reactions (1) and (2) is also determined by the $AB(a^3\Sigma^+)$-$AB(a^3\Sigma^+)$ interaction surfaces.

In the present work, we calculate the potential energy for the binary interactions of polar alkali-metal dimers $AB(a^3\Sigma^+)$ in the $\mathcal{S} = 2$ state of the two-molecule complex. The main goal is to explore the possibility of reaction barriers that would prevent molecules from reaching the short-range interaction region. It is known from previous calculations [8–11] that the potential energy of alkali-metal trimers is dominated by nonadditive interactions. The same should be expected for the interaction of four alkali-metal atoms. However, unlike in the atom-diatom case, reactions (1)–(4) involve the dissociation of two molecular bonds. The dissociation energy of these bonds may be expected to give rise to reaction barriers. We find no such barriers, meaning that reaction (1), if energetically allowed, and reaction (2) should be very fast at ultralow temperatures. Our calculations show that the nonadditive three- and four-body interactions are much stronger than the binding energy of alkali-metal dimers in the $a^3\Sigma^+$ state.

The potential-energy surfaces reported here are calculated using the spin-restricted open-shell coupled-cluster method with the single, double, and noniterative triple excitations [RCCSD(T)] method. The Li and Na atoms were described with the augmented core-valence correlation-consistent polarized valence triple-ζ atomic basis sets (aug-cc-pCVTZ) [12], and the H atom was described with the augmented correlation-consistent polarized valence quadruple-ζ atomic basis sets (aug-cc-pVQZ). The relativistic effects in the heavier alkali-metal atoms were accounted for with the fully relativistic small-core energy-consistent pseudopotentials ECP28MDF for Rb and ECP46MDF for Cs from the Stuttgart library [13] and the corresponding basis sets $[13s10p5d3f]/(8s7p5d3f)$ and $[12s11p6d4f]/(8s8p6d4f)$ [13]. The basis set superposition error was eliminated by using the counterpoise correction of Boys and Bernardi [14]. All electronic structure calculations were performed with the MOLPRO package of *ab initio* programs [15].

In order to prove the absence of reaction barriers in reactions (1) and (2), we calculated the potential energy of the four-atom complex along the minimum-energy path of reaction (1). The calculations were performed in two steps. First, the minimum-energy path was found by optimizing the geometries of the reaction complexes using the spin-restricted open-shell coupled-cluster method including single and double excitations (RCCSD) and basis sets as described above but truncated to s, p, and d orbitals only. We defined the intermolecular coordinates R_1 and R_2 that specify the separation between the geometric centers of the heteronuclear molecules and the separations between the centers of the homonuclear molecules, respectively. The geometries were optimized at 20 values of R_1 and R_2 between the position of the global minimum and 40 bohrs by varying all other degrees of freedom. In the second step, the interaction energies for the optimized geometries were calculated using the more accurate RCCSD(T) method and the full basis sets. For a few points we optimized the geometry with the full basis sets and the RCCSD(T) method and found that using the smaller basis set and the lower level of theory introduces negligible errors in the optimized geometry parameters but significantly underestimates the interaction energy.

Figure 1 presents the results of the calculations for the reactive interactions of LiNa, LiCs, and RbCs molecules. These molecules represent three limiting cases of polar alkali-metal dimers: the lightest and most compact molecule, the most polar, and the heaviest. The four-body reactions are clearly barrierless and proceed through the formation of a stable reaction complex corresponding to the deep global minimum of the interaction potential surface. The reaction complex has a tetrahedral geometry, as shown in Fig. 1. The deep minimum of the potential energy is the manifestation of the nonadditive forces in a four-body complex (see inset of Fig. 1). Interestingly, the energy of the reaction paths for LiCs-LiCs and LiNa-LiNa are very similar, while that for RbCs-RbCs is very different. This indicates that the nonadditive interaction forces are largely mediated by the Li atoms. This is consistent with the results of Soldán *et al.* [9–11].

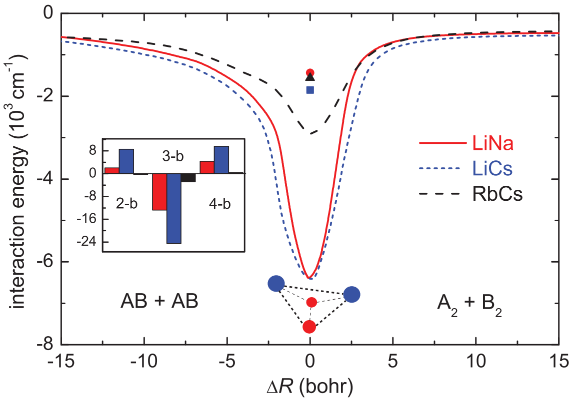

FIG. 1. (Color online) The minimum-energy path of the adiabatic reaction for the LiCs-LiCs, LiNa-LiNa, and RbCs-RbCs reaction complexes in the quintet spin state from the optimized geometry calculations. $\Delta R = (R_{AB} + R_{AB})/2 - (R_{AA} + R_{BB})/2$, where R_{AB} is the separation between atoms A and B. The interaction energy equal to zero corresponds to all atoms being dissociated. The symbols show the most negative values of the potential energy that can be obtained by adding binding energies of the dimers: circles, Li_2Na_2; triangles, Rb_2Cs_2; squares, Li_2Cs_2. The inset shows the decomposition of the interaction energy for the reaction complexes at the minimum-energy geometry into two-, three-, and four-body contributions.

While alkali-metal dimers in the $a^3\Sigma^+$ state form molecules with multiple rovibrational states, the interaction of alkali-metal atoms with hydrogen atoms in the $a^3\Sigma^+$ state gives rise to very shallow potential-energy curves supporting only one bound state [30]. Since the presence of multiple rovibrational states complicates photoassociation of ultracold atoms, alkali-metal hydrides in the $a^3\Sigma^+$ state appear to be attractive candidates for photoassociation experiments [31]. Such an experiment can be carried out, for example, by combining a slow, magnetically decelerated beam of hydrogen atoms with Rb atoms in a magneto-optical trap. In order to analyze the collisional stability of alkali-metal hydrides thus formed, we extended the calculation of Fig. 1 to compute the minimum-energy path for the adiabatic reaction $2\,\mathrm{RbH} \rightarrow \mathrm{Rb}_2 + \mathrm{H} + \mathrm{H}$, as shown in Fig. 2. Although there is no stable intermediate complex for this reaction, the reaction is barrierless. The strong attraction of the Rb atoms appears to pull the interacting molecules down a steep potential slope, resulting in the formation of free H atoms with large kinetic energy. Since most of the energy released as a result of the chemical reaction is carried away by the light hydrogen atoms, this may be used as an alternative way of creating ultracold Rb_2 molecules.

While there are no reaction barriers to prevent reactions (1)–(4), some of the reaction channels may be energetically closed. The relative energies for the reactants and products for reactions (1) and (2) are summarized in Tables I–III. The dissociation energy of alkali-metal dimers in the $a^3\Sigma^+$ state is known from spectroscopic measurements for all polar molecules except LiNa. To complete the data, we calculated the binding energy of LiNa($a^3\Sigma^+$). For this calculation, we used the augmented core-valence correlation-consistent polarized valence quadruple-ζ atomic basis sets (aug-cc-pCVQZ) [12] augmented by bond functions ($3s3p2d1f1g$) [32]. To estimate the error of the computations, we calculated the binding

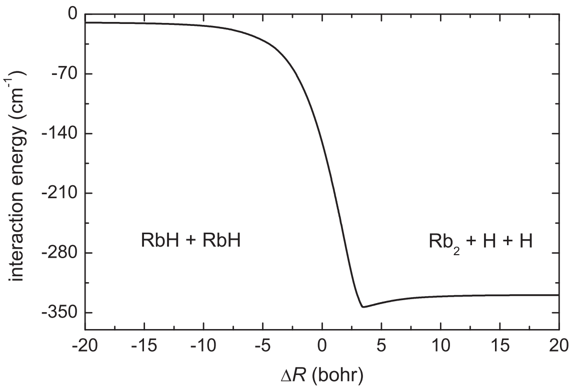

FIG. 2. The minimum-energy path of the adiabatic reaction $\mathrm{RbH} + \mathrm{RbH} \rightarrow \mathrm{Rb}_2 + \mathrm{H} + \mathrm{H}$ in the quintet spin state preserving the total electron spin from the optimized geometry calculations. $\Delta R = R_{AH} - R_{AA}$, where R_{AH} is the separation between atoms A and H.

TABLE I. The dissociation energies D_0 (in cm^{-1}) for alkali-metal dimers in the lowest triplet state $a^3\Sigma^+$.

	Li	Na	K	Rb	Cs
Li	301.829(15) [16]	211(10)	258.8(50) [17]	257.6(40) [18]	287(10) [19]
Na		163.7(12) [20]	196.48(10) [21]	193.365(50) [22]	207.818(10) [23]
K			244.523(50) [24]	239.924(10) [25]	258.769(20) [26]
Rb				234.7641(30) [27]	252.316(30) [28]
Cs					273.532(48) [29]

energies of both Li_2 and Na_2 molecules with the same method and basis sets. The results deviated from the experimental data by 3.5 cm^{-1}.

Tables I–III illustrate three important observations. First, reaction (1) is endothermic, and thus forbidden at ultralow temperatures, for KRb. Second, the change of energy in reaction (1) is very small for any combination of alkali-metal dimers. For example, the reaction KCs + KCs → K_2 + Cs_2 releases less than 1 cm^{-1} of energy, whereas the reaction KRb + KRb → K_2 + Rb_2 requires an activation energy of about 0.6 cm^{-1}. This suggests that the former is bound to form diatomic molecules in the ground vibrational state and the latter can be stimulated by vibrational excitation of the reactants. Given that reaction (1) combines polar species to form nonpolar products, the probability of this reaction must be sensitive to external electric fields. Finally, Table III shows that reaction (2) is exothermic for all combinations of molecules. In combination with the results of Fig. 1, this means that all alkali-metal dimers in the $a^3\Sigma^+$ state are chemically reactive at ultralow temperatures. This is in contrast to alkali-metal dimers in the rovibrational ground state of the $X^1\Sigma^+$ electronic state for which the formation of trimers is always energetically forbidden, making certain combinations of alkali-metal dimers chemically stable [33].

The results of Figs. 1 and 2 and Table IV indicate that ultracold alkali-metal dimers and alkali-metal hydrides in the $a^3\Sigma^+$ state can be used for practical applications only if protected from binary collisions by segregation in an optical lattice [36] or if confined in a quasi-two-dimensional potential with their electric dipoles oriented parallel and perpendicular to the plane of confinement [37]. All applications of molecules in optical lattices rely on the long-range dipole-dipole interactions. The magnitude of the permanent dipole moment is thus a figure of merit for experiments with molecules in optical lattices. Aymar and Dulieu presented a calculation of the potential-energy curves and the dipole moments for all polar alkali-metal dimers [34,35]. Their calculation treated alkali-metal atoms as single-electron species with optimized pseudopotentials. The calculations of Refs. [34,35] included core polarization effects through effective terms and produced accurate results for the dipole moments of the alkali-metal dimers in the $^1\Sigma$ state. However, the dipole moments of the molecules in the $^3\Sigma$ state have a smaller magnitude, so they may be more sensitive to details of the calculations. We computed the dipole moments for the alkali-metal dimers in the $a^3\Sigma^+$ state using the RCCSD(T) approach with the aug-cc-pCVQZ basis for Na and Li, the aug-cc-pVQZ basis for H, and the small-core fully relativistic pseudopotentials ECP*n*MDF [13] and large basis sets for K ([$11s11p5d3f$]), Rb ([$14s14p7d6f1g$]), and Cs ([$12s11p5d3f2g$]). These basis sets were optimized by calculating the energy of the electronic excitations in the individual atoms with the coupled-cluster method [38,39]. In each case, the basis was augmented by the bond functions [32]. The results presented in Fig. 3 and Table IV agree well with the calculations of Refs. [34,35] for light molecules containing Li but not for heavier molecules. Our results for RbCs differ from the previous calculations by a factor of 10, while agreeing within 5%–10% with an independent calculation by Stolyarov [40]. For KRb, our results agree to within 4% with the experimental data [2] and the theoretical prediction by Kotochigova *et al.* [41], whereas the calculation in Refs. [34,35] underestimates the dipole moment for this molecule in the triplet state by 50%.

In summary, we have shown that the interaction of heteronuclear alkali-metal dimers in the lowest-energy $a^3\Sigma^+$ state leads to the formation of a deeply bound reaction complex. The reaction complex, which has a nearly symmetric tetrahedral configuration, can decompose adiabatically into homonuclear alkali-metal dimers (for all molecules except KRb) and into alkali-metal trimers (for all molecules). There are no barriers for these chemical reactions. The absence of reaction barriers indicates the unique possibility to study interesting chemistry at ultralow temperatures. For example, measurements of the

TABLE II. The energy change ΔE (in cm^{-1}) for the reactions $2AB \rightarrow A_2 + B_2$ of alkali-metal dimers in the rovibrational ground state of the $a^3\Sigma^+$ electronic state.

	Li	Na	K	Rb	Cs
Li	0	−44(10)	−28.7(50)	−21.4(40)	−1.4(10)
Na		0	−15.3(10)	−11.7(10)	−21.6(10)
K			0	0.561(60)	−0.52(10)
Rb				0	−3.66(10)
Cs					0

TABLE III. The energy change ΔE (in cm^{-1}) for the reactions $2AB \rightarrow A_2B + B$ of alkali-metal dimers in the rovibrational ground state of the $a^3\Sigma^+$ electronic state. The energies of the trimers were taken from Ref. [11].

A	Li	Na	K	Rb	Cs
Li	−3647	−2035	−2280	−2214	−2609
Na	−953	−489	−587	−556	−685
K	−1316	−745	−803	−748	−858
Rb	−1158	−643	−678	−620	−707
Cs	−1579	−901	−907	−825	−897

TABLE IV. The experimental equilibrium distance R_e, the value of the permanent dipole function d_e at $R = R_e$, the permanent dipole moment of the molecule in the rovibrational ground state d_0, the rotational constant B_0, and the vibrational frequency ω_0 of the alkali-metal dimers in the $a^3\Sigma^+$ state. The reduced masses used in the calculations are for the most abundant isotopes.

Molecule	R_e (a_0)	d_e (D)	d_0 (D)	B_0 (GHz)	ω_0 (cm^{-1})
LiNa	8.918	0.186	0.175	4.10	38.1
LiK	9.433	0.321	0.312	3.35	40.6
LiRb	9.713	0.372	0.359	2.89	37.6
LiCs	9.916	0.475	0.462	2.70	41.1
NaK	10.34	0.0283	0.0269	1.16	21.7
NaRb	10.58	0.0592	0.0594	0.879	19.2
NaCs	10.86	0.0911	0.0914	0.772	18.7
KRb	11.15	0.0508	0.0540	0.540	17.5
KCs	11.44	0.101	0.101	0.454	16.4
RbCs	11.78	0.0348	0.0344	0.251	13.8
LiH	11.28	0.0061	0.00051	–	–
RbH	13.37	0.0061	0.00061	–	–

relative probabilities of reactions (1)–(4) in a magnetic trap would reveal the role of the nonadiabatic spin-dependent interactions. The spin-dependent interactions are sensitive to external electric and magnetic fields [42,43], which can be used to manipulate the branching ratios with external fields. The relative energies of the reactants and products for reaction (1) were found to be very close. This implies that the contribution of the reaction channel (1) can be studied by measuring the chemical decay of molecules in different rovibrational states. This also suggests that the branching ratios of reactions (1) and (2) should be sensitive to external electric fields that can be used to shift the energy levels of the reactants by the amount of energy similar to the energy change in the chemical reaction [44].

Our calculations illustrate the role of strong nonadditive forces in four-body interactions of alkali-metal atoms. We find that, as in the case of alkali-metal trimers [9–11], these forces are much stronger for Li-containing molecules, making the minimum-energy reaction paths of Li-containing molecules very similar. In addition, we calculated the minimum-energy path for the chemical reactions of alkali-metal hydrides. Since the binding energy of the alkali-metal hydrides in the $a^3\Sigma^+$ state is very small, the reaction of two molecules is accelerated by a strong attraction between the alkali-metal atoms, leading to a barrierless process that produces hydrogen atoms with large kinetic energy.

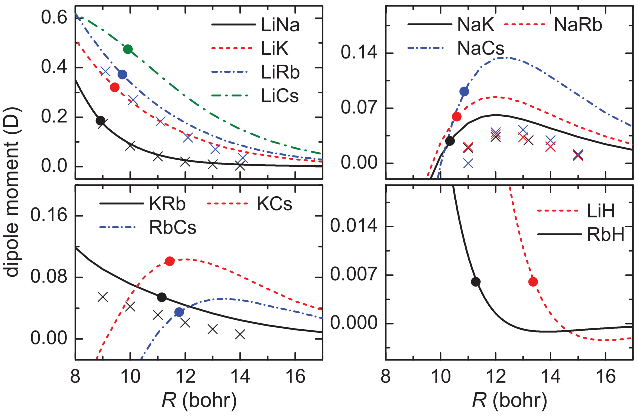

FIG. 3. (Color online) The permanent dipole moments of the heteronuclear alkali-metal dimers and alkali-metal hydrides in the $a^3\Sigma^+$ state. The solid circles indicate the value of the dipole moment at the equilibrium distance of the corresponding molecule, and the crosses are the results from Refs. [34,35]. The internuclear axis is oriented from the lighter atom to the heavier one.

Finally, we presented accurate calculations of the dipole moment functions for all alkali-metal dimers as well as RbH and LiH in the $a^3\Sigma^+$ state. These calculations reveal that Li-containing alkali-metal dimers have a substantial dipole moment in the ground rovibrational state, while the dipole moment of alkali-metal hydrides LiH and RbH appears to be too small to be of practical use.

We acknowledge useful discussions with Professors Alexei Buchachenko, Andrei Stolyarov, and Olivier Dulieu. The work reported here was initiated while the authors were visitors at the Kavli Institute for Theoretical Physics, University of California, Santa Barbara, within the program Fundamental Science and Applications of Ultracold Polar Molecules. Financial support from NSERC of Canada, the Polish Ministry of Science and Higher Education through Project No. N N204 215539, and National Science Foundation Grant No. NSF PHY11-25915 is gratefully acknowledged. M.T. is supported by the project operated within the Foundation for Polish Science MPD Programme cofinanced by the EU European Regional Development Fund. R.M. thanks the Foundation for Polish Science for support within the MISTRZ program.

---

[1] L. D. Carr, D. DeMille, R. V. Krems, and J. Ye, New J. Phys. **11**, 055049 (2009).

[2] K. K. Ni, S. Ospelkaus, M. H. G. de Miranda, A. Pe'er, B. Neyenhuis, J. J. Zirbel, S. Kotochigova, P. S. Julienne, D. S. Jin, and J. Ye, Science **322**, 231 (2008).

[3] J. Doyle, B. Friedrich, R. V. Krems, and F. Masnou-Seeuws, Eur. Phys. J. D **31**, 149 (2004).

[4] A. Micheli, G. K. Brennen, and P. Zoller, Nat. Phys. **2**, 341 (2006).

[5] R. V. Krems, Phys. Chem. Chem. Phys. **10**, 4079 (2008).

[6] A. Chotia, B. Neyenhuis, S. A. Moses, B. Yan, J. P. Covey, M. Foss-Feig, A. M. Rey, D. S. Jin, and J. Ye, Phys. Rev. Lett. **108**, 080405 (2012).

[7] L. M. C. Janssen, A. van der Avoird, and G. C. Groenenboom, Phys. Rev. Lett. **110**, 063201 (2013).

[8] J. Higgins, T. Hollebeek, J. Reho, T.-S. Ho, K. K. Lehmann, H. Rabitz, G. Scoles, and M. Gutowski, J. Chem. Phys. **112**, 5751 (2000).

[9] P. Soldán, M. T. Cvitaš, and J. M. Hutson, Phys. Rev. A **67**, 054702 (2003).

[10] P. Soldán, Phys. Rev. A **77**, 054501 (2008).
[11] P. Soldán, Phys. Rev. A **82**, 034701 (2010).
[12] T. H. Dunning, Jr., J. Chem. Phys. **90**, 1007 (1989).
[13] I. S. Lim, P. Schwerdtfeger, B. Metz, and H. Stoll, J. Chem. Phys. **122**, 104103 (2005).
[14] S. Boys and F. Bernardi, Mol. Phys. **19**, 553 (1970).
[15] H.-J. Werner *et al.*, MOLPRO, version 2012.1, a package of *ab initio* programs, 2012, http://www.molpro.net
[16] C. Linton, F. Martin, A. Ross, I. Russier, P. Crozet, A. Yiannopoulou, L. Li, and A. Lyyra, J. Mol. Spectrosc. **196**, 20 (1999).
[17] E. Tiemann, H. Knöckel, P. Kowalczyk, W. Jastrzebski, A. Pashov, H. Salami, and A. J. Ross, Phys. Rev. A **79**, 042716 (2009).
[18] M. Ivanova, A. Stein, A. Pashov, H. Knockel, and E. Tiemann, J. Chem. Phys. **134**, 024321 (2011).
[19] P. Staanum, A. Pashov, H. Knöckel, and E. Tiemann, Phys. Rev. A **75**, 042513 (2007).
[20] T.-S. Ho, H. Rabitz, and G. Scoles, J. Chem. Phys. **112**, 6218 (2000).
[21] A. Gerdes, M. Hobein, H. Knoeckel, and E. Tiemann, Eur. Phys. J. D **49**, 67 (2008).
[22] A. Pashov, O. Docenko, M. Tamanis, R. Ferber, H. Knöckel, and E. Tiemann, Phys. Rev. A **72**, 062505 (2005).
[23] O. Docenko, M. Tamanis, J. Zaharova, R. Ferber, A. Pashov, H. Knckel, and E. Tiemann, J. Phys. B **39**, S929 (2006).
[24] A. Pashov, P. Popov, H. Knoeckel, and E. Tiemann, Eur. Phys. J. D **46**, 241 (2008).
[25] A. Pashov, O. Docenko, M. Tamanis, R. Ferber, H. Knöckel, and E. Tiemann, Phys. Rev. A **76**, 022511 (2007).
[26] R. Ferber, I. Klincare, O. Nikolayeva, M. Tamanis, H. Knöckel, E. Tiemann, and A. Pashov, Phys. Rev. A **80**, 062501 (2009).
[27] C. Strauss, T. Takekoshi, F. Lang, K. Winkler, R. Grimm, J. Hecker Denschlag, and E. Tiemann, Phys. Rev. A **82**, 052514 (2010).
[28] O. Docenko, M. Tamanis, R. Ferber, H. Knöckel, and E. Tiemann, Phys. Rev. A **83**, 052519 (2011).
[29] F. Xie, V. B. Sovkov, A. M. Lyyra, D. Li, S. Ingram, J. Bai, V. S. Ivanov, S. Magnier, and L. Li, J. Chem. Phys. **130**, 051102 (2009).
[30] N. Geum, G.-H. Jeung, A. Derevianko, R. Cote, and A. Dalgarno, J. Chem. Phys. **115**, 5984 (2001).
[31] R. Côté, E. Juarros, and K. Kirby, Phys. Rev. A **81**, 060704 (2010).
[32] F.-M. Tao and Y.-K. Pan, J. Chem. Phys. **97**, 4989 (1992).
[33] P. S. Żuchowski and J. M. Hutson, Phys. Rev. A **81**, 060703(R) (2010).
[34] M. Aymar and O. Dulieu, J. Chem. Phys. **122**, 204302 (2005).
[35] J. Deiglmayr, M. Aymar, R. Wester, M. Weidemuller, and O. Dulieu, J. Chem. Phys. **129**, 064309 (2008).
[36] I. Bloch, Nat. Phys. **1**, 23 (2005).
[37] M. de Miranda, A. Chotia, B. Neyenhuis, D. Wang, G. Quemener, S. Ospelkaus, J. Bohn, J. Ye, and D. Jin, Nat. Phys. **7**, 502 (2011).
[38] M. Tomza, W. Skomorowski, M. Musial, R. Gonzalez Ferez, C. P. Koch, and R. Moszynski, Mol. Phys. **111**, 1781 (2013).
[39] K. Kosc and R. Moszynski (unpublished).
[40] A. V. Stolyarov (private communication).
[41] S. Kotochigova, P. S. Julienne, and E. Tiesinga, Phys. Rev. A **68**, 022501 (2003).
[42] T. V. Tscherbul and R. V. Krems, Phys. Rev. Lett. **97**, 083201 (2006).
[43] T. V. Tscherbul and R. V. Krems, J. Chem. Phys. **125**, 194311 (2006).
[44] E. R. Meyer and J. L. Bohn, Phys. Rev. A **82**, 042707 (2010).

Acknowledgements

First of all, I would like to thank my thesis supervisors Professor Robert Moszyński and Professor Christiane P. Koch for giving me the opportunity to join the ultracold molecules community and to work on the exciting projects. I am very grateful for their guidance, patience, constant encouragement, and understanding throughout years of my doctoral studies.

I would like to thank Professor Rosario González-Férez (University of Granada, Spain) and Professor Roman Krems (University of British Columbia, Canada) for giving me the opportunity to work in their groups in the beautiful surroundings of Andalusia and British Columbia.

I would also like to thank all the members of the Quantum Chemistry Laboratory at Warsaw University for creating highly supportive and stimulating atmosphere in the Lab.

Finally, and most importantly, I would like to thank my family for their limitless support.

Michał Tomza

Project was cooperated within the Foundation for Polish Science MPD Programme MPD/2008/1 "International Scholarship Program for Graduate Studies in Faculty of Chemistry University of Warsaw" co-financed by the EU European Regional Development Fund.

INNOWACYJNA GOSPODARKA
NARODOWA STRATEGIA SPÓJNOŚCI

WCh Wydział Chemii

FNP
Fundacja na rzecz Nauki Polskiej

UNIA EUROPEJSKA
EUROPEJSKI FUNDUSZ ROZWOJU REGIONALNEGO

Curriculum Vitae

Name:	Michał Tomza
Date of birth:	September 27, 1987
Place of birth:	Żary, Poland

Education:

2009 - 2014	International Ph.D. Studies in Quantum Chemistry/Theoretical Physics at University of Warsaw and University of Kassel
2009	**MSc in Quantum Chemistry** (*summa cum laude*), Faculty of Chemistry, University of Warsaw, Poland
2006 - 2010	Inter-faculty Individual Studies in Mathematics and Natural Sciences (double major Physics + Chemistry), University of Warsaw, Poland

Research experience:

Jun-Sept 2013	**Visiting PhD student**, University of British Columbia, Vancouver, Canada
Apr-Jul 2013	**Visiting PhD student**, University of Granada, Spain
Mar 2013	**Associate PhD student**, University of California in Santa Barbara, CA
2011 - 2013	**PhD student**, University of Kassel, Germany
2009 - 2014	**PhD student**, University of Warsaw, Poland
2008 - 2010	**MSc student**, University of Warsaw, Poland
Sept-Oct 2008	**Visiting researcher**, Swiss Federal Institute of Technology, Lausanne, Switzerland
2007 - 2008	**Research student**, Institute of Physical Chemistry PAS, Warsaw, Poland

List of publications

1. **M. Tomza**, F. Pawłowski, M. Jeziorska, C.P. Koch, R. Moszynski
   Formation of ultracold SrYb molecules in optical lattices by photoassociation spectroscopy: theoretical prospects
   Phys. Chem. Chem. Phys. 13, 18893 (2011)
2. L. Rybak, Z. Amitay, S. Amaran, R. Kosloff, **M. Tomza**, R. Moszynski, C. P. Koch
   Femtosecond coherent control of thermal photoassociation of magnesium atoms
   Faraday Discussion 153, 383 (2011)
3. L. Rybak, S. Amaran, L. Levin, **M. Tomza**, R. Moszynski, R. Kosloff, C. P. Koch, Z. Amitay
   Generating Molecular Rovibrational Coherence by Two-Photon Femtosecond Photoassociation of Thermally Hot Atoms
   Phys. Rev. Lett. 107, 273001 (2011)
4. **M. Tomza**, M. H. Goerz, M. Musiał, R. Moszynski, C. P. Koch
   Optimized production of ultracold ground-state molecules: Stabilization employing potentials with ion-pair character and strong spin-orbit coupling
   Phys. Rev. A 86, 043424 (2012)
5. **M. Tomza**, W. Skomorowski, M. Musiał, R. González-Férez, C. P. Koch, R. Moszynski
   Interatomic potentials, electric properties, and spectroscopy of the ground and excited states of the Rb_2 *molecule: Ab initio calculations and effect of a non-resonant field*
   Mol. Phys. 111, 1781 (2013)
6. S. Amaran, R. Kosloff, **M. Tomza**, W. Skomorowski, F. Pawlowski, R. Moszynski, L. Rybak, L. Levin, Z. Amitay, J. M. Berglund, D. M. Reich, C. P. Koch
   Photoassociation of Mg_2 *by two-photon femtosecond pulse: A time dependent quantum dynamics study*
   J. Chem. Phys. 139, 164124 (2013)
7. **M. Tomza**
   Prospects for ultracold polar and magnetic chromium–closed-shell-atom molecules
   Phys. Rev. A 88, 012519 (2013)
8. **M. Tomza**, K. W. Madison, R. Moszynski, R. V. Krems
   Chemical reactions of ultracold alkali-metal dimers in the lowest-energy $^3\Sigma$ *state*
   Phys. Rev. A 88, 050701(R) (2013)

9. **M. Tomza**, R. González-Férez, C. P. Koch, R. Moszynski
   Controlling magnetic Feshbach resonances in polar open-shell molecules with non-resonant light
   Phys. Rev. Lett. 112, 113201 (2014)
10. **M. Tomza**, C. P. Koch, R. Moszynski
    Cold interactions and collisions of the Yb$^+$ *ions with the Li atoms: Prospects for sympathetic cooling, radiative association, and Feshbach resonances*
    manuscript in preparation
11. **M . Tomza**, D. M. Reich, R. Moszynski, C. P. Koch
    Opimal control of femtosecond multi-photon photoassociation of ultracold atoms
    manuscript in preparation